SANDIA REPORT SAND84—0771 • Unlimited Release • UC—25
Printed May 1984

Radiation Effects in Optoelectronic Devices

C. E. Barnes, J. J. Wiczer

Prepared by
Sandia National Laboratories
Albuquerque, New Mexico 87185 and Livermore, California 94550
for the United States Department of Energy
under Contract DE-AC04-76DP00789

This work was performed at Sandia National Laboratories supported by the Air Force Weapons Laboratory (AFWL), the Air Force Wright Aeronautical Laboratories (AFWAL), and by the U. S. Department of Energy under contract #DE-AC04-76DP00789.

When printing a copy of any digitized SAND Report, you are required to update the markings to current standards.

SF2900Q(8-81)

Issued by Sandia National Laboratories, operated for the United States Department of Energy by Sandia Corporation.

NOTICE: This report was prepared as an account of work sponsored by an agency of the United States Government. Neither the United States Government nor any agency thereof, nor any of their employees, nor any of their contractors, subcontractors, or their employees, makes any warranty, express or implied, or assumes any legal liability or responsibility for the accuracy, completeness, or usefulness of any information, apparatus, product, or process disclosed, or represents that its use would not infringe privately owned rights. Reference herein to any specific commercial product, process, or service by trade name, trademark, manufacturer, or otherwise, does not necessarily constitute or imply its endorsement, recommendation, or favoring by the United States Government, any agency thereof or any of their contractors or subcontractors. The views and opinions expressed herein do not necessarily state or reflect those of the United States Government, any agency thereof or any of their contractors or subcontractors.

Printed in the United States of America
Available from
National Technical Information Service
U.S. Department of Commerce
5285 Port Royal Road
Springfield, VA 22161

NTIS price codes
Printed copy: A15
Microfiche copy: A01

PREFACE

In early 1977 a Sandia National Laboratories Report (SAND 76-0726) was issued by the first author under the title "Radiation Effects in Optoelectronic Devices." In the ensuing six years a significant amount of work has been done in our laboratory and elsewhere in this area of research. It is therefore appropriate at this time to update this report. Since the supply of SAND 76-0726 is now exhausted, we have retained most of the material from the earlier report in the present document. The basic format and the background discussions have been retained essentially intact with new material appearing primarily in the discussions of recent results.

The research work accomplished at Sandia National Laboratories (SNL) in the field of radiation effects in optoelectronics which is summarized in this Report was carried out while under contract to Air Force Laboratories. Radiation effects studies of Plessey AlGaAs LEDs were done for the Air Force Avionics Laboratory, Wright-Patterson AFB, Dayton, Ohio. The Air Force Project Officer at the Avionics Laboratory was Ken Trumble. The majority of the work presented herein was performed while under contract to the Air Force Weapons Laboratory (AFWL), Kirtland AFB, Albuquerque, New Mexico. This latter contract extended over a period of several years from the early 1970's until recently (1982). Because of the length of this contract, several Air Force personnel at the AFWL have played an important role and provided valuable assistance beginning with Ken Soda and Jake Tausch up to the

present Project Officer, Bob Simon. Others on this list include John Mullis, Ed Taylor, Bob Dunn and Hilmer Swenson.

In addition to Air Force personnel, the authors are indebted to many SNL colleagues for their advice and assistance. We wish to thank Roger Chaffin, Ralph Dawson, Errol EerNisse, John Galt, Len Hansen, Ray Hibray, Russ Keefe, Greg Lyons, Kim Mitchell, Gordon Osbourn, Tom Plut, Ben Rose, George Samara, Jay Snelling, Fred Vook, and Tom Zipperian. In addition, we are indebted to the staff of the following radiation facilities at SNL: The Annular Core Research Reactor (ACRR), the Gamma Irradiation Facility (GIF), the High-Energy Radiation Megavolt Electron Source II (HERMES II), the Relativistic Electron Beam Accelerator (REBA), and the Sandia Pulsed Reactor (SPR). We are also indebted to others outside of SNL for their advice and their important contributions to this field of research. This list, while not complete, includes George Sigel, Jr., Joe Friebele, Peter Lyons, Roger Greenwell, Stewart Share, and Jim Wall.

An important point to be made concerning this document is that this is not a "final report" in the usual sense of the phrase. Rather, it was written to satisfy one of the task requirements in the final year of the AFWL Contract. Consequently, the purpose of this report is to provide not only a summary of radiation damage studies at Sandia National Laboratories, but also of those in the literature on the components of optoelectronic systems: light emitting diodes (LEDs), laser diodes, photodetec-

tors, optical fibers, and optical isolators. Because the report also serves as a final summary of our work for the Air Force, we have emphasized our studies at the expense of the discussion of the work of others. This is especially the case in the Section on fibers where the number of Sandia studies has been relatively limited. To those who have made contributions to this field, we apologize for our lack of balance.

This review of radiation damage in optoelectronic components is structured according to device type. In each section, a brief discussion of those device properties relevant to radiation effects is given. These preliminary discussions are brief, however, and one should consult other sources in the literature for more general treatments.

TABLE OF CONTENTS

Section		Page
I	LIGHT EMITTING DIODES	1
	1. RELEVANT PREIRRADIATION PROPERTIES	1
	a. Radiative transition	2
	b. Nature of recombination center	4
	c. Concentration and distribution of recombination centers	6
	d. Radiative and total current flow mechanisms	12
	e. Semiconductor material	26
	2. PERMANENT RADIATION EFFECTS	28
	a. Silicon carbide	30
	b. Gallium phosphide	33
	c. Gallium arsenide phosphide	45
	d. Gallium arsenide, gamma and electron irradiation	50
	e. Gallium arsenide, neutron irradiation	58
	f. Amphoterically Si doped GaAs LEDs	67
	g. Aluminum gallium arsenide	84
	h. Long wavelength emitting LEDs	98
	3. TRANSIENT RADIATION EFFECTS	103
	4. PROTON IRRADIATION EFFECTS	110
	5. SUMMARY	119
	6. REFERENCES	139
II	SEMICONDUCTOR LASER DIODES	149
	1. RELEVANT PREIRRADIATION PROPERTIES	149
	2. RADIATION DAMAGE IN LASER DIODES	159
	3. SUMMARY	173
	4. REFERENCES	174
III	OPTICAL FIBERS	178
	1. RELEVANT PREIRRADIATION PROPERTIES	178
	a. Operating characteristics	179
	b. Fiber dispersion	180
	c. Fiber attenuation	184
	d. Mechanical properties	193
	e. LED and laser selection	194

2. RADIATION DAMAGE EFFECTS 199

a. Permanent damage effects 199

(1) Defects in glasses 199
(2) Pure silica core fibers 207
(3) Complex and doped silica fibers 214
(4) Plastic fibers 220

b. Transient damage effects 222

(1) Luminescence 222
(2) Transient attenuation in pure silica core fibers 224
(3) Transient attenuation in doped silica core fibers 231
(4) Bleaching effects 236

3. SUMMARY 249
4. REFERENCES 252

IV PHOTODETECTORS 264

1. TYPES OF PHOTODETECTORS 264
2. SILICON DETECTORS 273
3. GERMANIUM DETECTORS 277
4. III-V COMPOUND SEMICONDUCTOR DETECTORS 279
5. RADIATION EFFECTS 282

a. Permanent Damage effects 283
b. Transient effects 293

6. SUMMARY 306
7. REFERENCES 308

V. MULTI-COMPONENT DEVICES AND SYSTEMS CONSIDERATIONS 317

1. OPTICAL ISOLATORS 317
2. PIGTAILED DEVICES 326
3. SYSTEMS CONSIDERATIONS 331
4. SUMMARY 336
5. REFERENCES 339

I. LIGHT-EMITTING DIODES

Light emission from semiconductors can be produced by several excitation methods in a large variety of materials. However, our discussion will be restricted to electroluminescence that results from forward bias of a p-n junction. Further details and more general discussions of electroluminescence can be found in several excellent reviews on this subject which have appeared in recent years (Refs.1-3). In addition, we will cover only the more common types of LEDs which are generally commercially available and which have been subjected to radiation effects investigations.

1. RELEVANT PRE-IRRADIATION PROPERTIES

In our previous review (Ref.4) of radiation damage in LEDs, the basic characteristics of these devices were discussed. Because of this previous paper and excellent reviews which have appeared in the literature (Refs.1-3) and because of the widespread use of LEDs today, it is valid to assume that the reader is familiar with the properties of LEDs. Therefore, we will discuss only those characteristics which are affected by radiation damage. Prior to detailed discussion, we list the more important properties which determine device radiation sensitivity:

a. Nature of the radiative transition.

b. Nature of the radiative recombination center.

c. Concentration and distribution of radiative and non-radiative centers within the device.

d. Radiative and total (including nonradiative) current flow mechanisms.

e. The particular semiconductor from which the LED is made.

a. Radiative transition - Several types of radiative transitions can be responsible for the light output of LEDs. For example, donor-acceptor pair (DAP) transitions, free-to-bound transitions, radiative-tunneling transitions, band-to-band recombination, and exciton recombination are often observed in the electroluminescence spectra of LEDs (Refs. 1-3). Generally speaking, radiation damage is believed to degrade the output of LEDs through the introduction of non-radiative recombination centers which compete with the radiative recombination centers for excess carriers. The effect of this relatively simple superposition of additional recombination centers is usually independent of the details of the radiative transitions. Important exceptions do exist, however. For example, certain types of transitions occur over relatively large distances, such as distant DAP recombination, and tunneling between deep localized tails in the conduction and valence bands. If a radiation-induced recombination center is interposed between the DAP or tail states, then overlap between the wavefunctions will be perturbed or destroyed and recombination may very well take place at the radiation-induced center. On the other hand, if the transition is highly localized, this effect would not occur and once the carriers were trapped at a close DAP, radiative recombination would be highly probable.

Another characteristic of transitions which occur over long distances is that they are relatively slow. This fact will be brought out in more detail in our discussion of the GaAs:Si LEDs. If such a transition is a two-step process where the final recombination step is rate limiting, then the effect of radiation damage may be quite different than it is on an ordinary free-to-bound transition. To illustrate, consider a distant DAP recombination event in which the carriers are quickly trapped at the DAP but the recombination takes place some time later. The lifetime for the total process would be quite long, but would be unaffected by radiation-induced recombination centers except in the manner mentioned in the previous paragraph. This is true because the lifetime is a spatially localized lifetime for the carriers trapped at respective members of the DAP and is not associated with a diffusion length. As we will show, the competing effect of the radiation-induced centers is expressed quantitatively as a reduction in carrier diffusion length or minority carrier lifetime. However, when the carrier spends most of its life in a localized center, the diffusion length-associated lifetime characteristic of the initial trapping process will be only a small fraction of the total recombination time so that radiation-induced degradation will be minor. Experimental verification of this effect will be given in our discussion of damage effects in gamma-irradiated GaAs:Si LEDs.

For a radiative recombination process which is slow, it is also highly probable that one will observe saturation of the centers through which this process occurs if the initial trapping

is fairly rapid and the concentration of the centers is low. Such saturation effects can reduce the rate of degradation produced by irradiation relative to a simpler, unsaturable transition. Suppose, for example, that the radiative centers in a particular LED are well-saturated at a given LED current. Following irradiation the excess carrier density may still be large enough to saturate the centers giving the same light output despite the presence of additional non-radiative centers. Later, in our review of experimental work, the effects of neutron damage on saturation in GaP:Zn, O LEDs will be discussed.

b. Nature of recombination center - The nature of the radiative recombination center is important for several reasons. First. there is the possibility that irradiation-induced mobile defects will interact with the radiative centers directly, resulting in annihilation or modification of the centers. The probability of such an interaction will depend in part on the properties of the radiative center, such as its net electrical charge, important for Coulombic interactions, and whether or not the center, itself, is associated with a lattice defect. The latter property is important for another reason. If the radiative center is a defect or a defect associated with an impurity there is the possibility that irradiation will actually increase the light output through the creation of additional radiative centers. As will be shown, this effect has been observed in SiC LEDs.

The capture cross sections of the radiative recombination center are also important. If these cross sections are small, a

relatively larger concentration of radiative centers will be required to effectively compete with the radiation-induced non-radiative centers for excess carriers.

The depth of the energy level of the recombination center may also affect the degradation produced by irradiation. If the level is shallow, resulting in near-edge electroluminescence, irradiation-induced self-absorption which is strongest near the absorption edge (Ref.5) may add to the degradation of light output. The proximity of the level to either band will determine, in part, the mode of radiative current flow which, as we will see, has an effect on the rate of degradation.

An important special case is for band-to-band recombination in which the carrier concentration replaces the recombination center density in the determination of the radiative recombination rate, R_R.

$$R_R = B_r \, \Delta n_p p_o \quad , \ cm^{-3} \ s^{-1} \tag{1.1}$$

where B_r is a recombination coefficient, Δn_p is the excess injected electron density on the p side of the junction, and p_o is the hole density on the p-side. This mode of radiative recombination is often dominant in direct-gap materials such as GaAs and AlGaAs. Experimental values of B_r for GaAs are near $1 \times 10^{-10} cm^3/s$ while for an indirect material like GaP, B_r is typically $1 \times 10^{-14} cm^3/s$ (Ref.2). The significant point to note is that R_R, and hence the light output of the LED, can be enhanced, within limits, by increasing the doping level.

With regard to competing non-radiative recombination, in addition to recombination via deep levels which dominates in indirect gap materials such as Si and GaP, the Auger process also constitutes an important recombination path in heavily doped regions. In this process the energy resulting from recombination of an electron-hole pair is given to a third carrier. The Auger process can be band-to-band or impurity related. A distinctive feature of this non-radiative mechanism, often used to indentify its presence, is that the Auger lifetime decreases as the square of the carrier concentration. In very heavily doped LED and laser diodes the Auger recombination rate can be significant.

c. Concentration and distribution of recombination centers - The relative concentration of radiative recombination centers within the LED is obviously an important parameter with regard to radiation damage. Here, we use the word, "relative", to emphasize the importance of the variety of other recombination centers present in the device due to residual defects and impurities. Indeed, in all but the most efficient LEDs the majority of the carriers recombine non-radiatively at room temperature. Intuitively, one can expect that in a high-quality LED, such as a liquid phase epitaxially (LPE) grown GaAs device containing a low concentration of non-radiative centers, N_{NR}, due to residual defects and impurities, and doped with a relatively low concentration of radiative recombination centers, N_R ($10^{16} cm^{-3}$, for example), the irradiation-induced degradation will proceed rapidly. In such a device the pre-irradiation minority carrier diffusion length and, hence,

lifetime, τ_o, will be very long and it will not take many irradiation-induced competing recombination centers to significantly affect the lifetime. On the other hand, in a device containing large values of both N_R and N_{NR} prior to irradiation, large numbers of defects will have to be introduced to significantly affect the expected small value of τ_o. Hence, the radiation sensitivity of the device varies with the pre-irradiation lifetime.

This can be seen in a more quantitative fashion by noting that the pre-irradiation radiative and non-radiative lifetimes, τ_{oR} and τ_{oNR}, respectively, are given by[6]

$$\frac{1}{\tau_{o_R}} = \sigma_R \, v_{th} \, N_R \quad , \quad s^{-1} \tag{1.2}$$

$$\frac{1}{\tau_{o_{NR}}} = \sigma_{NR} \, v_{th} \, N_{NR} \quad , \quad s^{-1} \tag{1.3}$$

where σ_R and σ_{NR} are the capture cross-sections for minority carriers at radiative and non-radiative centers, respectively, and v_{th} is the thermal velocity of the carriers. As indicated earlier, band-to-band recombination is a special case since N_R is replaced by the carrier concentration. In this case, if the radiative recombination occurs on the p side (Ref.2),

$$\frac{1}{\tau_{o_R}} = B_r \, (p_o + \Delta n_p) \quad , \quad s^{-1}, \tag{1.4}$$

At modest injection levels $\Delta n_p \ll p_o$ in heavily doped LEDs so that

τ_{oR} is controlled by p_o as one would expect from Equation 1.1. However, in high radiance LEDs in which the injected current density is very high, one can have $\Delta n_p > p_o$ and the lifetime varies inversely with excess carrier density. This is called the bimolecular recombination region because

$$R_R = \frac{\Delta n_p}{\tau_{o_R}} \simeq B_r \, (\Delta n_p)^2 \quad , \; cm^{-3} \; s^{-1} \tag{1.5}$$

Note that in this region the lifetime is controlled by Δn_p and can therefore be decreased merely by increasing the LED current.

The lifetimes for the various recombination paths add in a reciprocal manner so that the total pre-irradiation minority carrier lifetime is given by

$$\frac{1}{\tau_o} = \frac{1}{\tau_{o_R}} + \frac{1}{\tau_{o_{NR}}} \quad , \; s^{-1} \tag{1.6}$$

Since irradiation-induced increases in N_R are rarely observed, the usual effect of irradiation is to add non-radiative recombination centers so that the post-irradiation non-radiative lifetime, τ_{NR}, decreases as

$$\begin{aligned} \frac{1}{\tau_{NR}} &= \sigma_{NR} \, v_{th} \, N_{NR} + \sigma_{NRI} \, v_{th} \, N_{NRI} \quad , \; s^{-1} \\ &= \frac{1}{\tau_{o_{NR}}} + \sigma_{NRI} \, v_{th} \, C_I \, \Phi \end{aligned} \tag{1.7}$$

where the irradiation-induced centers are denoted by the subscript, NRI, and the proportionality constant, C_I, is defined by

the rate at which the radiation fluence, Φ, introduces recombination centers: $N_{NRI} \equiv C_I \Phi$, cm^{-3}. The post-irradiation minority carrier lifetime, τ, is then given by

$$\frac{1}{\tau} = \frac{1}{\tau_{o_R}} + \frac{1}{\tau_{NR}} = \frac{1}{\tau_o} + \sigma_{NRI} v_{th} C_I \Phi , \quad s^{-1} \tag{1.8}$$

This equation indicates that τ will not differ significantly from τ_o until the second term on the right is comparable to $1/\tau_o$. Therefore, the effectiveness of the radiation in reducing the lifetime is dependent on the relative value of the reciprocal of the pre-irradiation lifetime.

To correctly judge the sensitivity of a device one must also know the probability of producing a non-radiative recombination center through interaction of the solid making up the LED with the impinging radiation; that is, the proportionality "constant", C_I. Several factors play a role in determining C_I: (1) the type and intensity of the radiation, (2) the irradiation temperature, (3) the relative level of ionization in the device during irradiation, and (4) various material characteristics of the device, itself, such as the cross section for interaction with the radiation. All of these factors are usually lumped phenomenologically into a parameter called the damage constant, K, which essentially gives the number of non-radiative centers introduced per unit fluence or dose of radiation, and also contains the factors σ_{NRI} and v_{th} so that

$$\frac{1}{\tau} = \frac{1}{\tau_o} + K\Phi , \quad s^{-1} \tag{1.9}$$

Hence, the sensitivity of the LED is also dependent on K. We see, then, that the lifetime-damage constant product, $\tau_o K$, is an "inverse" figure of merit for radiation damage in LEDs. This is clearly shown by a slight modification of Equation 1.9:

$$\frac{\tau_o}{\tau} = 1 + \tau_o K \Phi \tag{1.10}$$

As our review of the literature will show it has been common practice to express the radiation sensitivity of LEDs using this product.

With regard to the relative concentration of radiative centers, N_R, the most desirable situation would be a large value of N_R (or of p_o) but a small value of N_{NR}. In such a case, as indicated by Equation 1.6, it might be possible to control τ_o with the radiative lifetime, τ_{o_R} , if τ_{o_R} could be made small enough. One would then have the attractive combination of high light output but a small value of $\tau_o K$. As we will show later, LEDs fabricated in our laboratory and elsewhere approach these characteristics and, hence, are relatively insensitive to irradiation.

For the opposite case where N_{NR} is large and $N_{NR} >> N_R$, one would expect the LED to be highly inefficient but insensitive to irradiation. However, it is usually not feasible to purposely make the LED of poor quality (high N_{NR}) in order to achieve radiation hardness, because the initial light output at reasonable LED currents may be too small to be of practical use. There is a tendency in the literature to report the results of radiation damage studies on LEDs in terms of normalized light output or efficiency; that is,

the light output at a given fluence or dose is divided by the pre-irradiation value. This procedure essentially removes from consideration the initial output of the device. Indeed, it is not that difficult to make an LED which is quite insensitive to irradiation. The SiC devices mentioned later are a case in point. However, the light output of such devices at reasonable currents is usually too low to be of any practical value.

In addition to the relative values of N_R and N_{NR}, the location in the LED of the radiative centers is important for damage considerations. For most LEDs the light output originates in the p-region through the radiative recombination of minority electrons with holes at the radiative centers. In some LEDs there is also a significant concentration of radiative centers in the space-charge region. This is especially true at low temperatures where freeze-out can cause widening of the space-charge layer. The presence of radiative centers in the space-charge region is noteworthy because light emission due to space-charge recombination (SCR) is insensitive to irradiation for constant LED forward bias assuming that the irradiation does not increase or decrease the concentration of radiative centers. This is true because the recombination rate through a particular type of center in the space-charge layer is governed by the quasi-Fermi levels which do not change with irradiation until significant majority carrier removal occurs in the neutral regions.

The distribution of radiative centers (or the majority carrier concentration for band-to-band recombination) in the neutral region

near the junction is also of importance in determining the degradation rate. In later paragraphs it will be shown quantitatively that the rate of degradation is smallest for the radiative center (majority carrier) profile which changes the least with distance into the neutral region away from the junction; that is, for a step increase at the junction to a constant concentration level of radiative centers (majority carriers). The more rapidly the profile changes, the faster the irradiation-induced degradation will proceed. That this is plausible from a physical point of view can be seen by recalling that the effect of radiation-induced recombination centers is to reduce the minority carrier lifetime and, hence, the diffusion length. If N_R is increasing rapidly over the order of a few diffusion lengths, then a reduction in diffusion length through irradiation will mean that significant excess carrier densities will exist only over a range where N_R is much smaller relative to the pre-irradiation condition. On the other hand, if N_R is constant over the range of interest a reduction in diffusion length will not affect the concentration of radiative centers seen by the excess carriers. Thus, one expects that an LED with a step profile in N_R (or p_o) will be more radiation-resistant than a device with a distance-dependent N_R (or p_o) such as a linearly-graded profile.

d. Radiative and total current flow mechanisms - The mode of carrier injection which prevails in LEDs, as in most p-n junction devices, depends critically on the material parameters, the applied voltage, and the temperature. At high temperature and high bias, thermal injection usually dominates while at low tem-

perature and low bias, tunneling processes are often observed. Since most LED materials are wide band gap semiconductors, other types of current mechanisms become much more probable relative to the usual thermally injected diffusion current.

As already indicated, at high temperatures the radiative efficiency is usually quite low so that the light intensity, L, produced by the radiative current flow does not determine the total current-voltage characteristic. For example, as shown in Figure 1.1 for a typical GaAs diode at 300 K, the total current at low voltages is often due to non-radiative recombination in the space-charge layer while those few carriers which are injected into the neutral region recombine radiatively so that the radiative current is diffusion limited (Ref.7). As the applied voltage, V, is increased, the total current, I, also begins to flow by diffusion but this change is often masked in data such as those in Figure 1.1 by Ohmic losses which cause a bend-over in the L-V and I-V curves.

An expression for the light intensity, L, due to a diffusion current can be obtained by integrating the differential recombination rate over the neutral region in which radiative recombination occurs (Ref.8).

$$L = C\int_{0}^{\infty} \Delta n_p \, N_R \, dx, \text{ arbitrary units} \qquad (1.11)$$

where Δn_p is the excess minority carrier density, C is a constant, and x is the distance into the p-region. This equation describes the electroluminescence due to diffusion for an LED in which the light emission is due to recombination of electrons and holes at

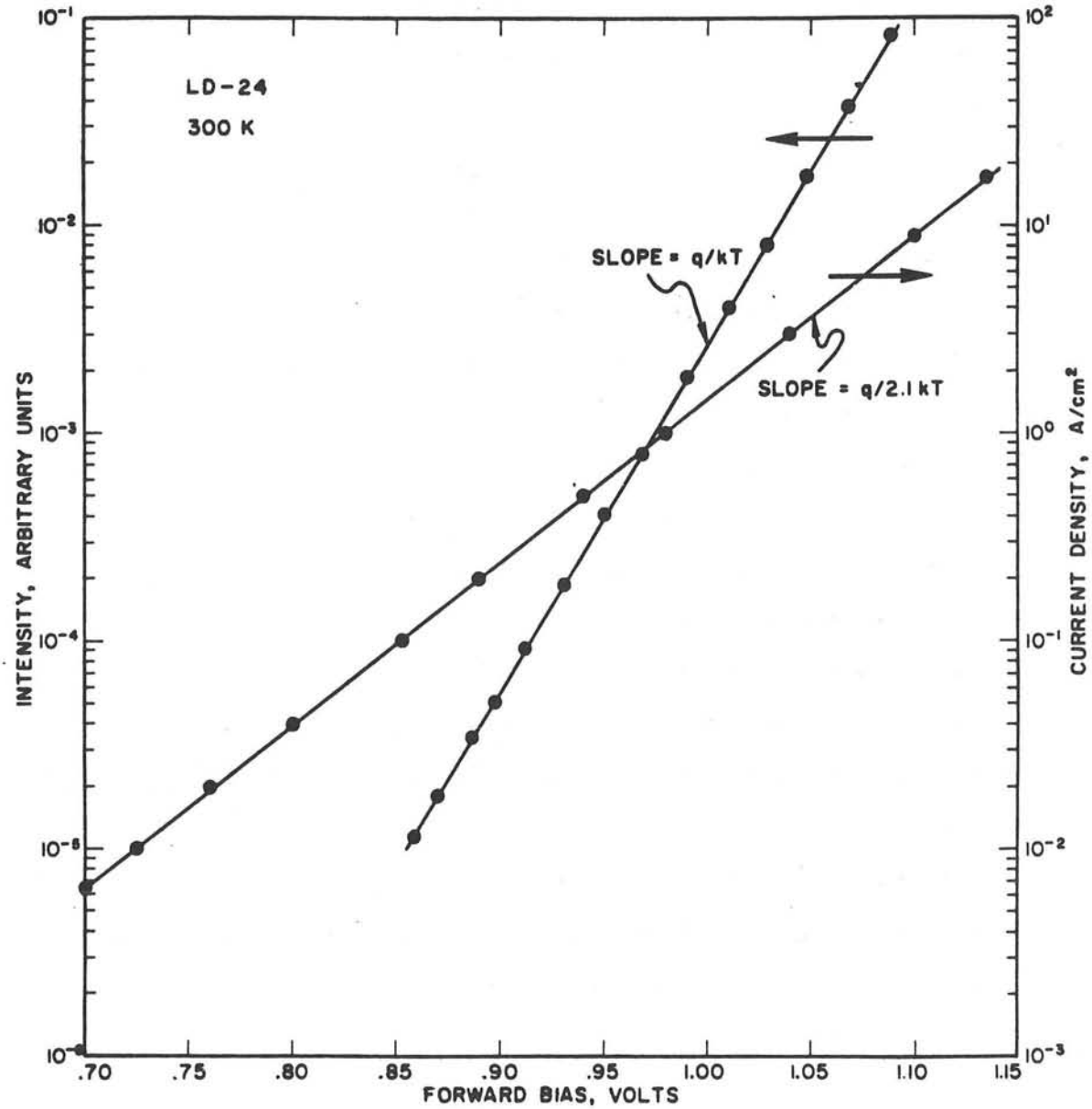

Fig. 1.1 Typical current-voltage and total light intensity-voltage curves for a GaAs LED at low voltages. Note that the differing slopes indicate different current flow mechanisms for the radiative and total currents.

the N_R radiative centers. Note that for band-to-band recombination, N_R is replaced by p_o (or N_A) the majority carrier (or acceptor dopant) concentration. Assuming a profile of the form, $N_R \equiv ax^n$, for the radiative centers, and using the usual expression for Δn_p due to diffusion (Ref.9) with $e^{qV/kT} >> 1$, we have

$$L = Cn_{po}ae^{qV/kT} \int_o^\infty x^n e^{-x/L_e} dx, \text{ arbitrary units} \quad (1.12)$$

where n_{po} is the equilibrium electron density at the edge of the depletion region on the p side, and L_e is the electron diffusion length in the p region. The value of the integral is

$$\int_o^\infty x^n e^{-x/L_e} dx = n!\ L_e^{n+1}\ ,\ cm^{n+1} \quad (1.13)$$

so that

$$L = Cn_{po}an!(D_e\tau)^{(n+1)/2}e^{qV/kT}, \text{ arbitrary units} \quad (1.14)$$

In Equation 1.14 we have used the fact that $L_e = D_e\tau$ where D_e is the electron diffusion coefficient. With regard to radiation damage the dependence of L on τ should be noted. For a flat profile of radiative centers $L \propto \tau^{1/2}$, while for a linearly-graded N_R, $L \propto \tau$. Substituting Equation 1.9 into Equation 1.14

$$\left(\frac{L_o}{L}\right)^{\frac{2}{n+1}} = 1 + \tau_o K\Phi \quad (1.15)$$

where L_o is the pre-irradiation light intensity. Equation 1.15 gives the radiation-induced degradation of the diffusion-controlled

light output when measured at constant LED voltage. As discussed earlier from a physical point of view, the lifetime-damage constant product, $\tau_o K$ is an "inverse" figure of merit for the radiation hardness of LEDs. This fact is readily apparent in Equation 1.15 since the product $(\tau_o K\Phi)$ must be of the order of one before significant degradation of L_o is observed.

Equation 1.15 can be rewritten as

$$\frac{L_o}{L} = \left[1 + \tau_o K\Phi\right]^{\frac{n+1}{2}} \tag{1.16}$$

in order to show the dependence of the degradation on the radiative center (or majority carrier) profile expressed as $N_R = ax^n$. Equation (1.16) indicates that L_o/L changes more rapidly for larger values of n. Therefore, for a step profile with n = 0 one should observe the least amount of degradation for a diffusion-controlled radiative current at constant voltage.

As will be shown later, Equation 1.15 has been successfully employed by several authors in their analysis of radiation-induced degradation. The analysis is fairly simple in that all that is required is a plot of $(L_o/L)^{2/(n+1)} - 1$ versus Φ for L values taken at constant voltage in order to test the validity of Equation 1.15 and obtain a value of $\tau_o K$. This procedure is most easily carried out at low LED voltages where resistive losses across the neutral regions are insignificant. As we will show, however, this can lead to problems if there is a significant change in the radiative current flow mechanism in going from low bias to

the higher currents and voltages required for practical operation of the devices.

The total current, I, observed in LEDs at low voltages usually varies with voltage as $e^{qV/2kT}$, as shown in Figure 1.1, indicating a space-charge recombination (SCR) mechanism (Ref.1). This is not surprising since one can show that the ratio of SCR current to diffusion current increases with the energy gap, E_G (Ref.10), and many of the LED materials possess relatively wide band gaps. Using the total SCR current, an analysis similar to that given above for the diffusion-controlled radiative current can be carried out to obtain $\tau_o K$ values characteristic of damage effects in the space-charge region. The total current, I, due to SCR is given by (Ref.11)

$$I = \frac{qn_i wA}{2\tau_{SCR}} e^{qV/2kT} \quad , A \qquad (1.17)$$

where w is the space-charge region width, A is the device area, n_i is the intrinsic carrier density, and τ_{SCR} is the effective lifetime in the space-charge region. Unlike the radiative current which flows only through recombination at a particular type of center, the total current is due to recombination at all centers. Therefore, a reduction in lifetime through the addition of radiation-induced recombination centers will result in an increase in I as shown in Equation 1.17 by the inverse dependence of I on τ_{SCR}. The effect of radiation-induced recombination centers is introduced by substituting Equation 1.9 with τ_{SCR} replacing τ into Equation 1.17:

$$\frac{I}{I_o} = 1 + \tau_{SCR_o} K_{SCR} \Phi \qquad (1.18)$$

Note that K_{SCR} has replaced K in order to emphasize possible differences in net defect introduction rates between the neutral regions and the space-charge region. Equation 1.18 like its analogue, Equation 1.15, has been used successfully to account for the additional radiation-induced currents observed in damage studies. This is especially true for neutron damage which almost always manifests itself as additional SCR current.

The analysis of light intensity degradation using Equations 1.14 and 1.15 is done at constant forward bias. It is also possible to study the degradation rate at constant forward current. Since the external efficiency, η, of the device is proportional to the radiative current or light intensity, L, divided by the total current, I, the constant current analysis is essentially the same as an efficiency degradation analysis. To obtain an equation for L in terms of I instead of V, the relationship describing the total current in terms of voltage is solved for V and substituted in Equation 1.14. Since radiation-induced current is usually due to SCR we use Equation 1.17 for this purpose and, assuming $\tau_{SCR} \approx \tau$, obtain

$$L = C'\tau^{\frac{n+5}{2}} I^2, \text{ arbitrary units} \qquad (1.19)$$

where C' contains the remainder of the terms in Equations 1.14 and 1.17. Substituting Equation 1.9 into Equation 1.19,

$$\left(\frac{L_o}{L}\right)^{\frac{2}{n+5}} = 1 + \tau_o K \Phi \qquad (1.20)$$

at constant I. Since the efficiency, η, is merely L normalized by I, Equation 1.20 is equally valid when η_o/η is substituted for L_o/L.

At larger forward bias, I is often due to diffusion as is the radiative current. If the radiation fluence is not too large, I will still be due to diffusion following irradiation. To derive equations similar to Equations 1.19 and 1.20 but for I due to diffusion we use, rather than Equations 1.17, the following (Ref.12).

$$I = \frac{qAD^{\frac{1}{2}}n_{po}}{\tau^{\frac{1}{2}}} e^{qV/kT} \quad , \text{ A} \tag{1.21}$$

and obtain the following analogues to Equations 1.19 and 1.20:

$$L = C''\tau^{\frac{n+2}{2}} I \quad , \text{ arbitrary units} \tag{1.22}$$

and

$$\left(\frac{L_o}{L}\right)^{\frac{2}{n+2}} = 1 + \tau_o K\Phi \tag{1.23}$$

at constant I. Comparison of Equations 1.19 and 1.22 with Equation 1.14 indicates that L varies with τ to a larger power for constant current than for constant voltage. Therefore, the radiation-induced degradation of τ will cause a stronger reduction in L at constant current than at constant voltage. Intuitively, this is plausible since, at constant voltage, additional current can be supplied to partially make up for the greater number of recombination centers. However, at constant current this cannot be done and the additional centers have a stronger effect.

Comparison of Equations 1.19 and 1.22 shows that the dependence on τ differs by a factor of $\tau^{1.5}$ between I due to SCR and I due to diffusion. Therefore, care must be taken in analyzing constant current data because of the variation in total current flow mechanisms. Usually, there is a significant intermediate I-V range where I flows by both SCR and diffusion. In this case, one could not use simple equations such as Equations 1.19 or 1.22. Of greater concern, especially for neutron damage, is the fact that irradiation can alter the total current flow mechanism. For example, in neutron-irradiated LEDs one observes a greater and greater fraction of I due to SCR as Φ increases. An additional problem with efficiency measurements is that when there is a significant SCR component of I, η is not independent of the current as one can see by dividing both sides of Equation 1.19 by I. This, combined with the possibility that the SCR fraction of I can change with Φ, means that one must exercise caution in obtaining $\tau_o K$ products using efficiency measurements. Statements concerning the measured $\tau_o K$ values should be accompanied by ranges of I over which these numbers are valid and a discussion of the effect of irradiation on total current flow mechanisms.

Radiative current flow mechanisms other than diffusion-controlled flow are possible. These other modes of current flow can differ drastically from diffusion currents in their response to irradiation. Therefore, they merit some discussion.

It was noted earlier that when there are radiative centers within the space-charge region, one can observe radiative SCR currents. Further, it was pointed out that such currents are insensi-

tive to irradiation at constant voltage and at fluences or doses where majority carrier removal does not occur. Usually, radiative SCR currents are observed at low temperatures where there is insufficient thermal energy for injection into the neutral regions and where the space-charge region has broadened due to freeze-out. In large band gap materials, such as SiC, radiative SCR can be seen at room temperature. If this mechanism was efficient at room temperature, one would have a highly radiation-hardened LED. Unfortunately, there are usually many types of recombination centers in the space-charge region. In addition, the very large gap materials such as SiC and GaN are less pure than GaAs and LEDs from such materials are more difficult to manufacture.

The possible existence of radiative SCR can pose difficulties in deciding whether or not the light output of a particular LED is due to diffusion or SCR. This is due to the fact that the detailed theory (Ref.10) of SCR currents shows that m in exp qV/mkT can be either 1 or 2. Gershenzon, et al. (Ref.13), have shown that the green light output from certain GaP LEDs is due to SCR. In addition, Nelson (Ref.14), has demonstrated that over a large range of injection levels for radiative diffusion currents, m can equal 2 rather than 1 as in Equation 1.14. Thus, the values of m = 1 for diffusion and m = 2 for SCR are not unique and do not provide a completely reliable method of discerning the two types of radiative current flow. Here, then, is one instance where radiation damage studies can provide confirming evidence for the characteristics of an LED prior to any irradiation. The drastic difference between the susceptibilities of SCR and diffusion-controlled radiative

currents to irradiation easily demonstrates whether a given light output is due to an SCR or diffusion mechanism.

Because of the large energy gaps and narrow space-charge regions often encountered in LEDs, tunneling mechanisms can play an important role in radiative current flow, especially at low temperatures and low voltages. The tunneling probability, P_t, for an LED can be written as (Ref.15)

$$P_t = P_{to} \exp\left[-\frac{P_e E_b^{3/2}}{\varepsilon}\right] \tag{1.24}$$

where P_{to} and P_e are slowly varying "constants", E_b is the height of the energy barrier and ε is the electric field across the junction. For a given type of junction, E_b and ε can be expressed in terms of the junction voltage so that one obtains the following equation for total current or light intensity (Ref.15):

$$I \text{ or } L = B\, e^{\alpha_t V} \tag{1.25}$$

where B is a constant which contains the dopant concentration (or gradient). The coefficient in the exponential, α_t, does not depend on temperature and also contains the dopant concentration. The form of α_t depends on the shape of the junction and for linearly graded diodes is weakly voltage dependent (Ref.15). The temperature independence of α_t is an important clue in the observation of tunneling currents since it is in marked contrast with the temperature dependence of the voltage coefficient for SCR and diffusion currents.

In addition to the temperature independence of α_t, radia-

tive tunneling currents possess a second important property. The peak energy of the emission band shifts with applied voltage leading to the observation of "shifting peak" spectra. The peak shift arises because the tunneling probability is highest for carriers near their respective quasi-Fermi levels, the separation of which is determined by the junction voltage.

The various models (photon-assisted tunneling, band-filling) employed to explain light emission due to tunneling in LEDs have been discussed in detail by several authors (Refs. 16-20) and will not be reviewed in this report.

As in the case of light emission due to SCR, one would not expect irradiation to significantly affect the light intensity due to recombination of carriers tunneling into the space-charge layer. In the various models used to describe tunneling currents the only radiation sensitive quantity is the dopant concentration which usually enters as a square root or cube root dependence. Since LEDs are usually heavily doped (10^{17} cm^{-3} to 10^{19} cm^{-3}), large amounts of radiation would be required to produce significant carrier removal and accompanying decreases in radiative tunneling.

On the other hand, if the excess carriers tunnel all the way through the space-charge layer to either the conduction band or valence band in the neutral region and then recombine there, the radiation-induced degradation of the diffusion length will once again govern the light output as a function of fluence or dose.

Recently, we have found that radiative space-charge-limited

current (SCLC) flow can exist in commercially available LEDs at practical operating currents. The experimental details of this work will be given later. Here, we wish to briefly present some background for this current flow mechanism. SCLC is usually observed in highly compensated or low-doped semiconductor materials. When a voltage is applied across such a material and a sufficient number of carriers have been injected, the carriers themselves create a space-charge cloud as they drift across the material. For example, in a highly compensated p-region of an LED, voltage drops across this region will become significant at relatively low currents and injected electrons will begin to drift across the p-region resulting in the buildup of a space charge. The SCLC theory of Ashley and Milnes (Ref.21) and Lampert (Ref.22) gives the drift current, I_{SCLC}, for this process as

$$I_{SCLC} = \frac{9}{8} Aq\tau \ \mu_n \mu_p p_o \frac{(V - V_j)^2}{\ell^3} \ , \ A \qquad (1.26)$$

where V_j is the voltage drop across the junction, μ_n and μ_p are the electron and hole mobilities, respectively, p_o is the hole density in the p-region and ℓ is the thickness of the p-region. Two important points are to be noted about Equation 1.26. First, I_{SCLC} varies as the square of the voltage drop across the neutral region, $(V - V_j)$. Second, in contrast with SCR (Equation 1.17) and diffusion (Equation 1.21) where the current is inversely proportional to τ, I_{SCLC} is directly proportional to τ. This difference occurs because in SCLC flow, the electrons must drift all the way across the p-region to contribute to I_{SCLC}. If they recombine on the way across, the chance of

which is inversely proportional to τ, they will not contribute to I_{SCLC}.

With regard to radiative output in the SCLC range, Byer (Ref.23) found a sublinear dependence of the light intensity, L, on current in correspondence with the $L \propto I^{1/2}$ dependence predicted by the SCLC theory. The sublinear dependence occurs because many of the electrons reach the p-region electrode before they can recombine resulting in a decreasing quantum efficiency as I is increased. In a later examination of GaAs:Mn LEDs, Ashley (Ref.24) and Ashley, et al. (Ref.25), showed that L can vary linearly with I in the SCLC range. This dependence agrees with the theory if one assumes that double injection is occurring in the p-region. In this case, the reduction in quantum efficiency due to the loss of electrons at the electrode is compensated for by hole injection. For the double injection case, L is given by (Ref.25)

$$L = \eta I_{SCLC} \frac{(1 + b)}{q} \text{ , arbitrary units} \qquad (1.27)$$

where η is the external quantum efficiency and b is the ratio of the electron mobility to the hole mobility. In the derivation of Equation 1.27, diffusion was neglected and only drift was considered. In addition, it was assumed that the hole capture cross section of the recombination center was much larger than the electron capture cross section. Implicit in the quantum efficiency is the fraction, f, of carriers which recombine radiatively:

$$f = \frac{1/\tau_R}{(1/\tau_{NR}) + (1/\tau_R)} = \frac{1/\tau_R}{1/\tau} = \frac{\tau}{\tau_R} \quad . \qquad (1.28)$$

Recall that the effect of irradiation is to decrease τ_{NR} by adding nonradiative recombination centers. Equation 1.27 then becomes

$$L = C_\eta \frac{\tau}{\tau_R} I_{SCLC} \frac{(1 + b)}{q} \text{ , arbitrary units,} \qquad (1.29)$$

where $\eta \equiv C_\eta f$.

Finally, Equation 1.26 for I_{SCLC} is substituted in Equation 1.29 in order to obtain an expression for L in terms of $(V - V_j)$:

$$L = C_L \tau^2 (V - V_j)^2 \text{ , arbitrary units} \qquad (1.30)$$

where

$$C_L = \frac{9}{8} C_\eta \frac{\mu_n p_o}{\tau_R \ell^3} (\mu_n + \mu_p) \quad .$$

The important point to note is that L varies as the square of the electron lifetime. Recall that for a diffusion-limited radiative current, Equation 1.14 indicates that L varies as τ for a linearly-graded profile (n = 1) and as $\tau^{1/2}$ for a step profile (n = 0), the two most common profiles. Consequently, one can expect that radiative output due to SCLC will degrade faster with irradiation than the light output due to diffusion near the junction. Therefore, these results suggest that LEDs containing radiative SCLC components should not be used in a radiation environment.

e. Semiconductor material - As one would expect, the particular semiconductor from which an LED is made will affect the amount of degradation produced by a given amount of radiation. First of all, the interaction cross section between the material and the radiation can vary. For example, the Compton scattering

cross section for gamma rays depends on the atomic number of the material. In addition, the net defect concentration created in a particular material depends on defect mobilities, thermal annealing temperatures, and sensitivity to ionization, all of which vary between materials. These various factors, as stated earlier, appear as differences in damage constants between materials.

The variation in response to irradiation from one material type to another depends critically on the type of radiation. Consider for example, the dependence on mass and atomic number of the ratio of the proton to neutron degradation rates in the two important semiconductor materials, Si and GaAs. For neutrons and protons of the same energy, the ratio of the average energy transferred to the primary knock-on by a proton to that imparted by a neutron is given by (Refs.26 and 27)

$$R \equiv \frac{E_p}{E_n} = \frac{2}{r} \ln r \qquad (1.31)$$

where $r \equiv E_m/E_d$, E_m is the maximum energy transferred, and E_d is the displacement energy of the lattice atom. When the mass of the target atom differs markedly from the irradiating particle mass, as in the case of proton or neutron irradiation of semiconductors, the ratio r varies inversely with the mass of the semiconductor elements, M. Therefore, ignoring the slowly varying $\ln$ function, R increases with M. Consequently, the value of R for GaAs will be greater than for Si since the atomic masses for GaAs are somewhat more than twice that for Si. It should be noted,

however, that since r is a large number for bombarding particles in the MeV range, R is always much less than one. In addition, while the neutron scattering cross section is relatively independent of target mass, the Rutherford scattering cross section α, for protons varies as the square of the atomic number of the target (Ref.27). Therefore, α, for Ge or GaAs ($Z \approx 32$) is four times that for Si($Z = 14$) (Ref.27). One can then anticipate that the ratio of the proton-induced degradation rate to the neutron-induced degradation rate will be greater for a GaAs device than for a Si device since both R and α increase with target mass.

Other material properties could be listed such as the quality of the material, but most of these have been mentioned earlier. In addition, more important factors such as maximum possible light output and wavelength range of light output, will dictate the selection of an LED rather than the inherent sensitivity of the material to irradiation.

2. PERMANENT RADIATION EFFECTS

Generally speaking, the effect of radiation on LEDs is similar to that in Si devices in that pure device materials of high quality are most sensitive to irradiation while materials with large numbers of impurities such as SiC are least sensitive. This is illustrated in Figure 1.2 in which light output for various types of LEDs is plotted versus electron fluence (Ref.28). Notice that high quality (epitaxial) GaAs is most sensitive while SiC actually shows an increase in output with irradiation. With the exception of SiC

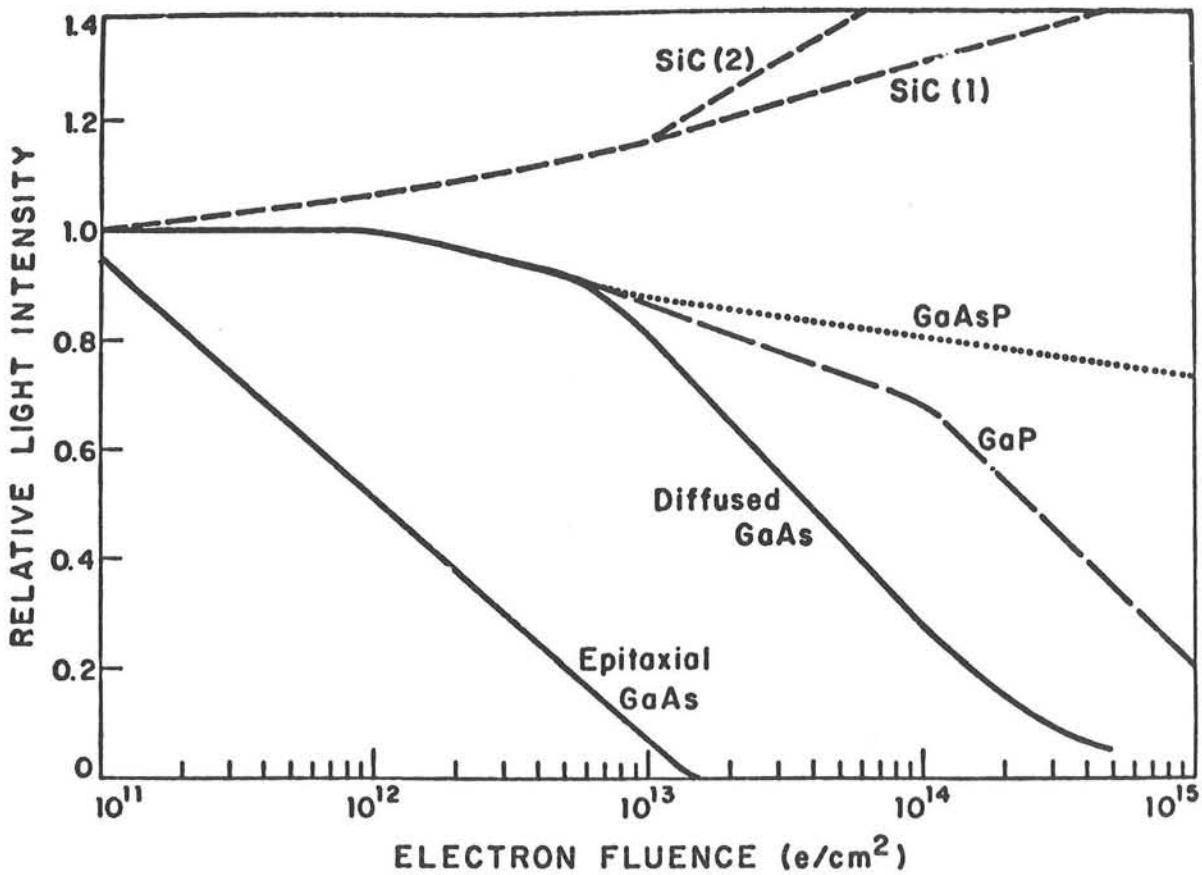

Fig. 1.2 Comparison of relative light intensities of different types of LEDs after correcting for transmission loss of lens (from A. G. Stanley, IEEE Trans. Nucl. Sci. NS-17, No. 6, 239 (1970)).

one usually observes that the light output decreases and the total current increases with irradiation for electrons, gamma rays, and neutrons.

a. Silicon carbide - Although elegant photoluminescence experiments have been conducted on SiC (Ref.29), little is known about the characteristics of unirradiated SiC LEDs in comparison with LEDs made from other materials. This statement is even more applicable to radiation effects in SiC LEDs. We have already referred to the interesting results obtained by Stanley (Ref.28) and shown in Figure 1.2 which indicate that light output increases with electron irradiation. Similar increases in luminescence intensity following electron irradiation have been obtained in bulk samples of SiC (Refs.30 and 31). Several papers on ion implanted SiC have demonstrated that intense luminescence can be produced in SiC by annealing the ion-implanted material at approximately 1000°C (Refs. 32-37). All of these studies lead to the conclusion that radiation-induced defects can act as radiative recombination centers in SiC.

Although these LEDs are not in widespread use at this time, the radiation damage study (Ref.38) briefly reviewed below is of interest because it centers on radiative tunneling into the space charge region. This type of radiative current flow responds in a unique way to irradiation.

We have studied the effects of neutron damage on SiC LEDs in our laboratory (Ref.38). Devices obtained from Norton Co. were irradiated at 300 K in the Sandia Annular Core Research Reactor

(ACRR). The results for one diode are shown in Figure 1.3 in which integrated light intensity is plotted versus diode voltage for five different temperatures. At low voltages, the pre-irradiation curves (and also the post-irradiation curves in most cases) are parallel straight lines indicating that

$$L \sim e^{\alpha_t V} \quad \text{, arbitrary units} \qquad (1.32)$$

where α_t has the value 30 V^{-1}. Recall that for a thermal injection mechanism, α_t should depend on temperature while for tunneling, α_t is independent of temperature. Consequently, the results suggest that radiative tunneling currents persist in these diodes up to 300 K. This is consistent with the fact that E_G for SiC is fairly large (2.9 eV) so that thermal injection would only become significant at temperatures higher than those required for GaAs. A radiative tunneling current with recombination in the space-charge region is consistent with the insensitivity of the light intensity in the low voltage regions to the large neutron fluence of 10^{15} n/cm^2.

At higher voltages the light intensity decreased significantly with irradiation. This is especially true for the 300 K case where one might expect thermal injection to start at voltages lower than for the low temperature curves. The type of thermal injection cannot be ascertained from these curves without correcting them for the series resistance voltage drop.

More recent work (Ref.39) in our laboratory on the same SiC diodes used in the neutron damage study (Ref.38) confirmed the

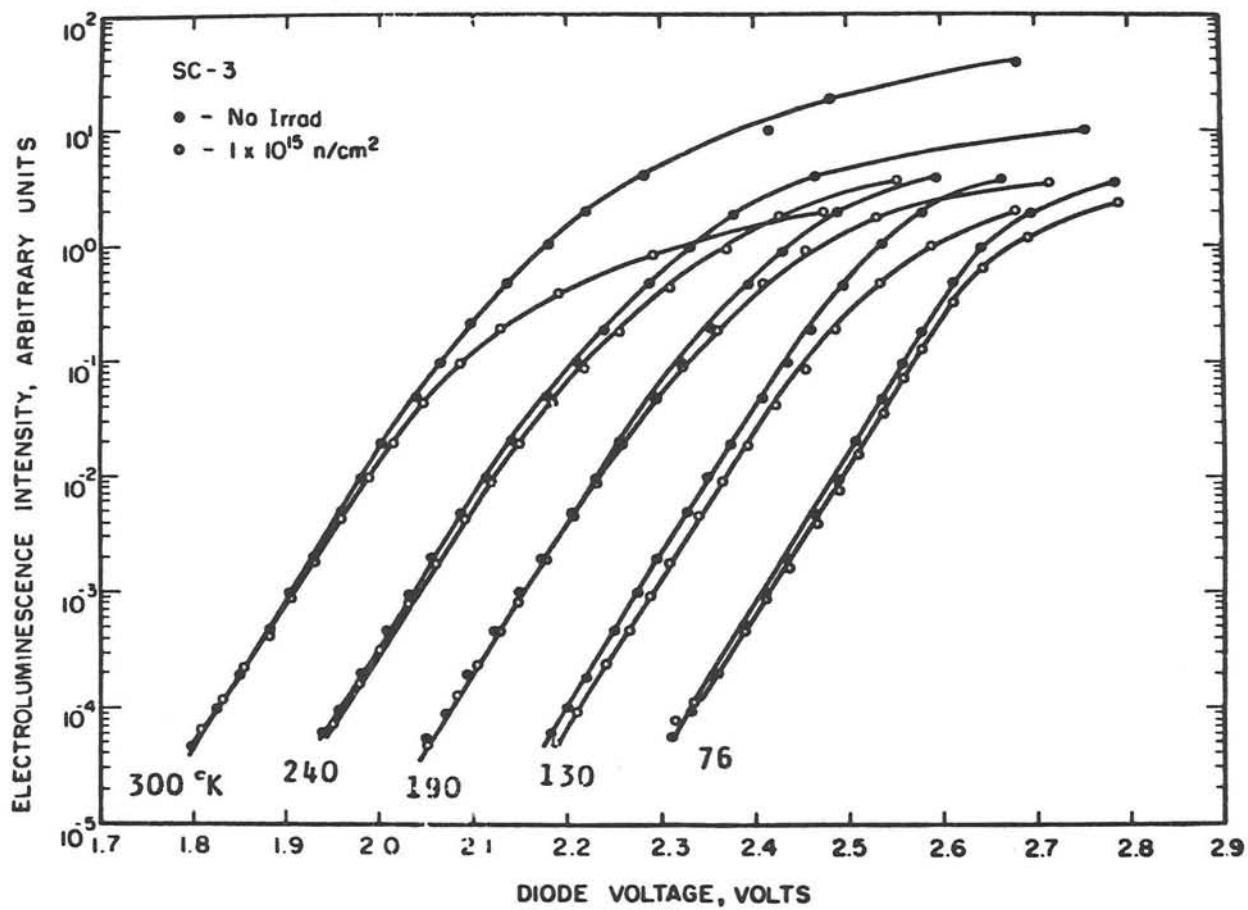

Fig. 1.3 The effect of neutron damage on the light output of a SiC LED at various temperatures. The slope of the curves in the low voltage region is 30 V^{-1}.

presence of radiative tunneling at temperatures as high as 300 K. This conclusion was based on the observation of shifting peak spectra, the temperature-independent slope of the L-V curves and the agreement between the experimental α_t and that calculated from capacitance data.

Figures 1.2 and 1.3 suggest that SiC LEDs are good candidates for applications involving exposure to radiation environments. However, other factors tend to negate the attractive radiation hardness characteristics of these devices. First, they are simply not commercially available because of the very difficult materials problems associated with the growth of good crystals and subsequent formation of p-n junctions (Refs. 40 and 41). Even in the case of vapor or liquid epitaxial growth of SiC, the processing temperatures are often greater than 1700°C (Ref.41). SiC LEDs are also characterized by low light output efficiencies and high defect densities relative to III-V LEDs. In addition, while the short, visible wavelength emission may be attractive for display applications, it is undesirable for use with Si detectors and glass fibers exposed to nuclear radiation.

b. Gallium phosphide - Logan, et. al. (Ref.42) have studied the effects of gamma irradiation on GaP LEDs. Exposure to gamma rays reduced the intensity of both the green and red electroluminescence bands and also the minority carrier lifetime. Because of the similarity in lifetime and light output degradation, they concluded that both the green and red emission bands were due to recombination in the neutral region and, hence, were diffusion-

controlled. From the data presented in their paper an approximate $\tau_o K_\gamma$ value of 2×10^{-8} $rads^{-1}$ can be calculated.

The annealing of the GaP diodes observed by Logan, et. al., (Ref. 42) is interesting in that it appeared to be athermal. Little recovery was found upon annealing to 125°C but a 40% recovery was observed following a 50 mA forward bias at room temperature. This annealing was not due to Joule heating in the device. Logan, et. al., (Ref. 42) suggested that it resulted from the movement of impurities under forward bias.

More recent work on athermal defect annealing in electron-irradiated GaP diodes by Lang and Kimerling (Ref. 43) has established a different annealing mechanism than that suggested by Logan, et. al. (Ref. 43). Under forward bias, six deep levels observed by capacitance spectroscopy following irradiation, annealed at greatly enhanced rates. It was shown that electron-hole recombination at the defects was responsible for the annealing enhancement. The mechanism for this process is the transfer of recombination energy into highly localized vibrational energy at the defect which promotes defect motion. Lang and Kimerling (Ref. 43) also demonstrated that this process is more effective in materials with large energy gaps. This is in accord with their (Ref. 44) earlier observation of recombination-enhanced defect motion in electron-irradiated GaAs diodes in which the enhancement was less than that seen in GaP.

Recently, (Ref. 45) we have examined the effects of gamma irradiation on GaP:Zn,O red-emitting LEDs. At low constant voltage the degradation of the diffusion-controlled light output led to

an average value of $\tau_o K_\gamma \approx 3.6 \times 10^{-8}$ rads^{-1} for five LEDs. This is somewhat higher than that found by Logan, et. al. (Ref. 42). The difference can probably be attributed to a greater lifetime in our devices because they were made at Bell Laboratories by advanced liquid phase epitaxial (LPE) techniques whereas Logan, et. al.'s (Ref. 42) work was done earlier in 1964.

Forward bias-enhanced recovery of the light output, analogous to the effects observed by Logan, et. al., (Ref. 42) and Lang and Kimerling (Ref. 43), was also observed in our diodes (Ref. 45). However, the degree of recovery depended strongly on the operating conditions under which the light output was observed following bias recovery. At low constant voltage and 300 K, the effect was minimal even for attempted bias enhancement with large DC currents applied over 20 to 30 hours. At high constant current and 300 K, however, the forward bias-induced recovery was somewhat device-dependent but always fairly strong, as much as 50% of L_o for a DC current density of 2.8 A/cm^2 applied for 24 hours at 300 K.

In our study (Ref. 45) of gamma irradiation effects in GaP:Zn, O LEDs, the technique of deep level transient spectroscopy (DLTS) was used in addition to the measurement of light output. Several traps were observed including the Zn-O radiative recombination center present prior to irradiation. The DLTS peak due to the Zn-O center is shown in Figure 1.4 along with an irradiation-induced trap with an energy level depth of 0.55 eV. Note that neither irradiation nor room temperature forward bias affect the Zn-O band. However, the 0.55 eV trap is sensitive to

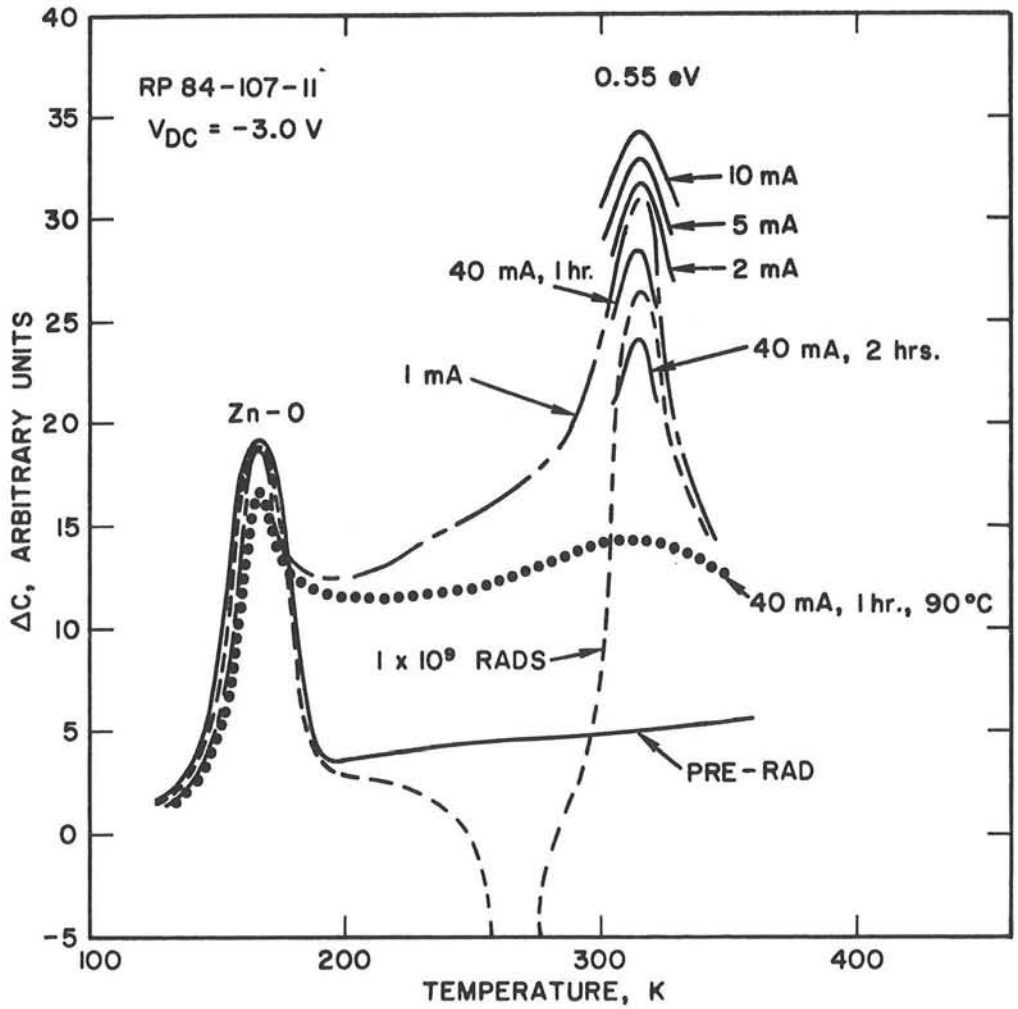

Fig. 1.4 Typical DLTS spectra due to minority carrier traps prior to and following gamma irradiation and forward bias of a GaP:Zn,O LED. The 1, 2, 5, and 10 mA bias currents were applied for 10 min at room temperature.

forward current. In addition it was shown that the Zn-O band could be reduced by forward bias at elevated temperatures as shown in Figure 1.4. Thermal anneal below 160° C without bias did not affect the Zn-O centers. These results definitively show that gamma-induced light output degradation was not due to an irradiation-induced reduction in Zn-O concentration. They also show that the mechanism for forward bias induced light output degradation at elevated temperatures is quite different; the Zn-O centers appear to be directly affected.

Investigation of the GaP:Zn,O LEDs also included a study (Ref. 46) of the effects of forward bias-enhanced recovery on the light emission spectra at 76 K. At this temperature, spectral measurements show that at low currents the spectrum is dominated by green emission rather than the usual red emission due to recombination at the Zn-O pair center. Following gamma irradiation and extended forward bias at 300 K, the 76 K value of the total light output, L at constant voltage often exceeded L_o, the pre-irradiation value. As shown in Figure 1.5, a portion of this increased light output is due to the appearance of two unique sets of triplets in the electroluminescence spectrum. Note that the intensity is greater than that prior to any irradiation. These triplets cannot be produced at this intensity by forward bias of an unirradiated diode or by thermal annealing of an irradiated diode. Thus, the formation of the centers responsible for this emission is very likely the result of athermal recombination-enhanced defect motion as observed by Lang and Kimerling (Ref. 43) in similar LEDs. These luminescence lines have been observed

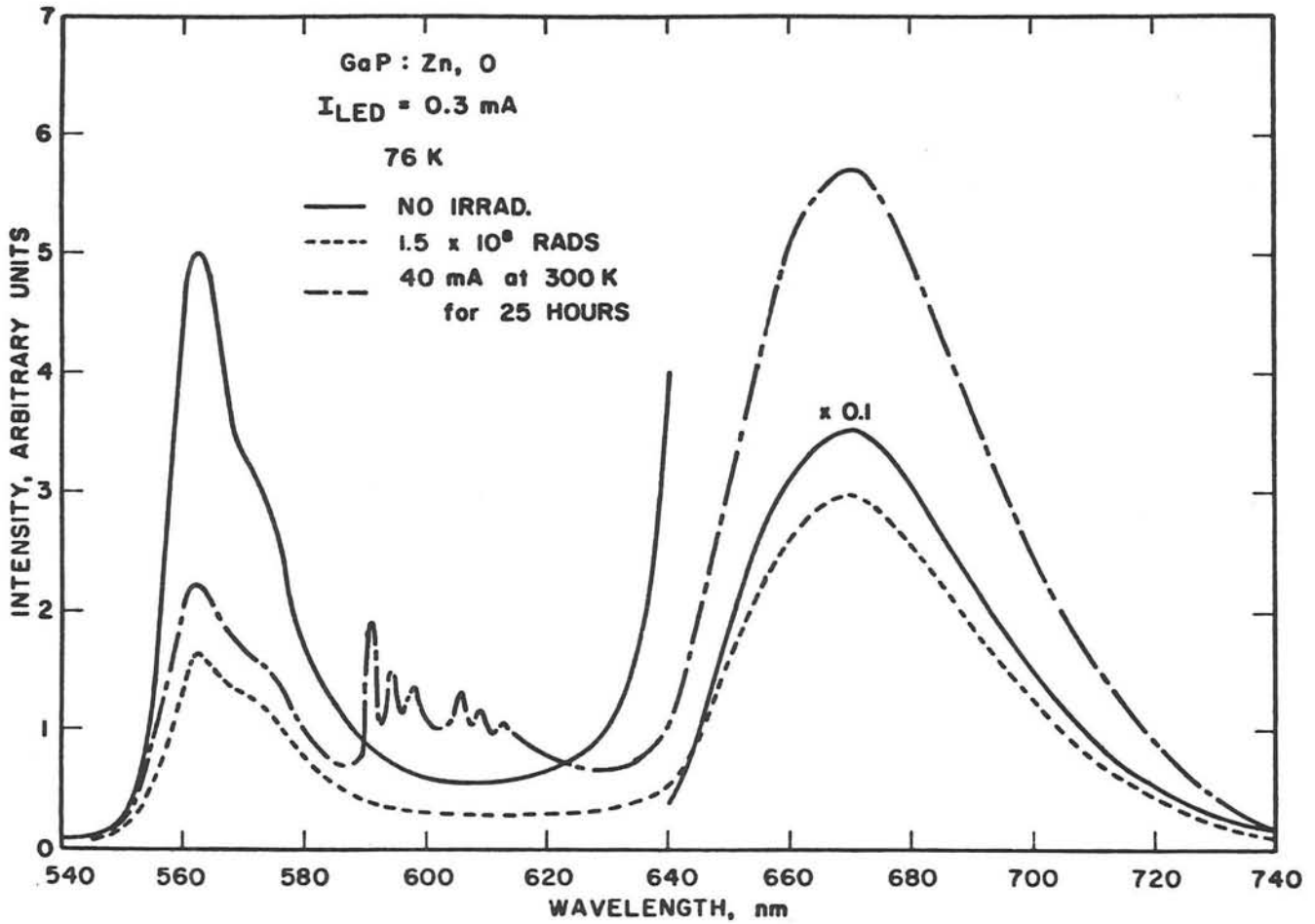

Fig. 1.5 Electroluminescence at 76K as a function of wavelength for a GaP:Zn,O LED operated at a constant current of 0.3 mA. Both gamma irradiation and long-term forward bias at 300K are necessary to produce the two sets of triplet emission between 590 nm and 620 nm.

previously (Ref. 47) in Zn diffused GaP but are very weak, as in our case, in LPE GaP (Refs. 48 and 49). Dean (Ref. 49) has associated this emission with bound exciton recombination at a Zn-associated center. The explanation of the growth of these bands following forward bias of gamma irradiated LEDs would then center on the recombination-enhanced motion of the defect with subsequent trapping of the defect at a Zn-associated complex resulting in the formation of the recombination center responsible for the triplet emission.

Epstein, et. al. (Ref. 50) have also examined the effect of gamma irradiation on GaP LEDs except that their diodes were heavily doped with nitrogen. These GaP:N devices emit the characteristic green light associated with the isoelectronic N center. A $\tau_o K_\gamma$ product of 4×10^{-8} $rads^{-1}$ was found for these diodes, a value very close to that found in our GaP:Zn,O LEDs. While Epstein, et. al., (Ref. 50) observed a recovery of 75% for thermal annealing between 250°C and 500°C, no forward bias induced recovery was observed following the application of 10 A/cm^2 for several hours at room temperature.

Measurements done in our laboratory on gamma irradiated green emitting GaP:N LEDs reveal an average $\tau_o K_\gamma$ of 1.1×10^{-7} $rads^{-1}$, somewhat larger than Epstein, et. al.'s (Ref. 50) result. We also differ with their results in that considerable forward bias induced recovery of light output has been observed at constant high voltage.

Turning our attention to neutron damage in GaP LEDs, previous studies (Ref. 51) in our laboratory illustrate the dramatic

difference between damage effects on radiative diffusion current and radiative SCR current. GaP LEDs obtained from Electro-Nuclear Labs, Inc., were measured at 300 K and then irradiated at the same temperature in the Sandia Annular Core Research Reactor (ACRR). The red and green emission bands were measured prior to and following each irradiation. The green band intensity, L_G, was proportional to exp [qV/ kT] and decreased drastically following irradiation. These results indicated that L_G was diffusion controlled. In contrast, the red emission intensity, L_R, varied as exp [qV/2kT] at low voltage and was unaffected by a neutron fluence of 3×10^{14} n/cm^2 below a voltage of about 1.75 V. On the basis of previous discussion, both of these facts suggest that the red band is due to radiative recombination in the space-charge region. Above 1.75 V, L_R decreased significantly with Φ suggesting that the red emission above this voltage contained a significant diffusion component. However, this was not obvious from the L_R-V curves because neutral region voltage drops also became significant above 1.75 V and distorted the L_R-V characteristic.

The dependence of the effect of damage on the radiative current flow mechanism was confirmed by plotting log L_R versus log L_G. Assuming that L_G is $\propto$ exp [qV/kT] at all voltages the log of L_G is a measure of the junction voltage. Therefore, a plot of log L_R versus log L_G is essentially a semi-log plot of log L_R versus V with a slope of 1/m where m is defined by $L_R \propto$ exp [qV/mkT]. A plot constructed in this manner for an unirradiated LED is shown in Figure 1.6. Note that there is break point at 1.75 V to 1.80 V

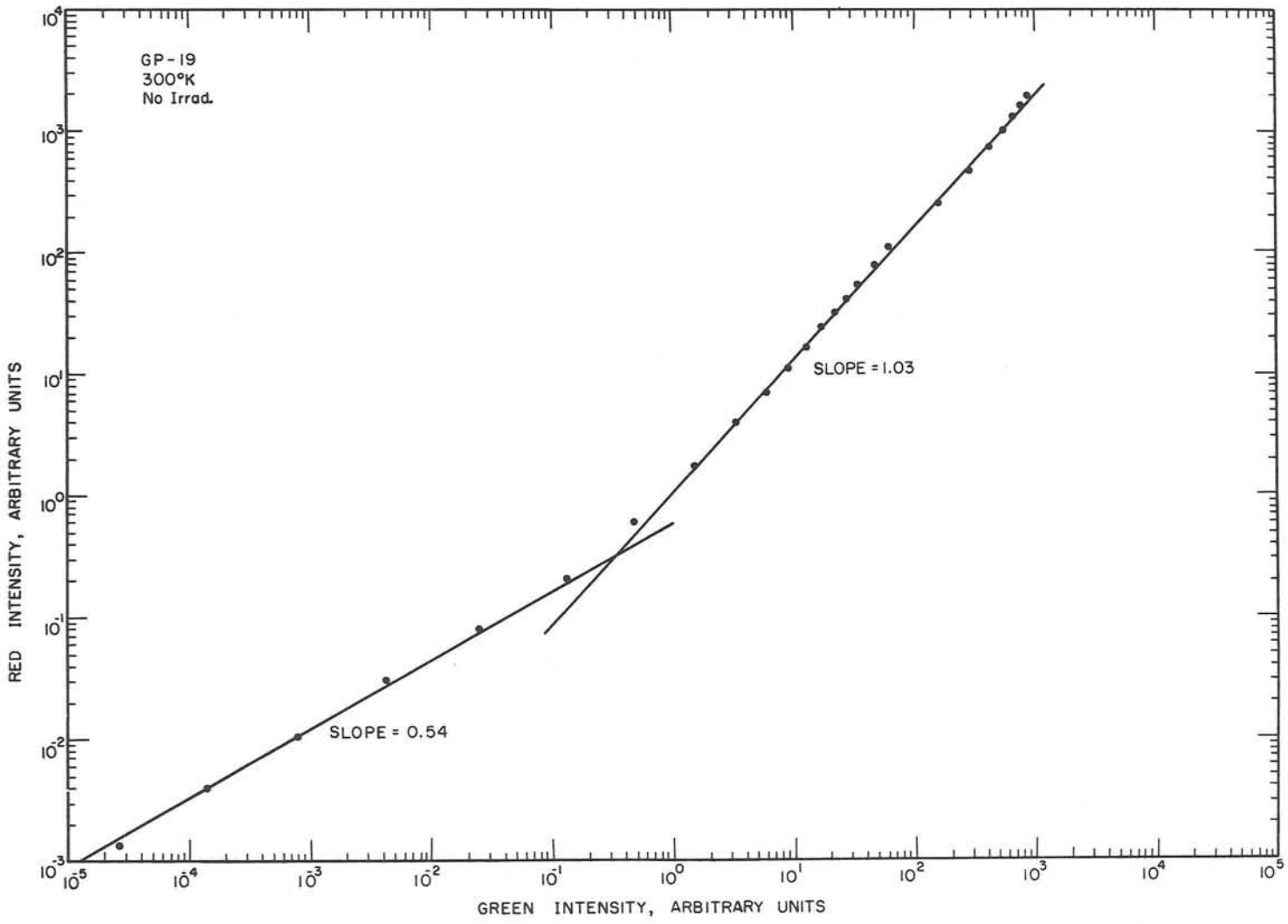

Fig. 1.6 Red intensity vs green intensity for an unirradiated GaP LED at 300°K. The lower-voltage portion indicates space-charge recombination for the red band, while the higher-voltage portion indicates diffusion in the neutral region.

above which m ≈ 1.0 indicating L_R was due to diffusion above this voltage. Below 1.75 V, m is approximately 2 indicating that at lower voltages L_R was due to recombination within the space charge region. Note that the break point voltage agrees with the voltage at which neutron-induced degradation of L_R becomes significant.

Epstein, et. al. (Ref. 52) have examined the effect of neutron damage on the quantum efficiency and minority carrier lifetime in green emitting GaP LEDs. The diodes were formed by diffusing Zn into vapor phase epitaxial n-type GaP doped with Te and nitrogen. Following irradiation to a fluence of $\Phi = 3.5 \times 10^{13}$ n/cm^2, a $\tau_o K_n$ of 4.7×10^{-14} cm^2/n was found for lifetime degradation as expressed by Equation 1.9.

Following our earlier study (Ref. 51) of GaP LEDs, a more detailed investigation (Ref. 53) of neutron damage was carried out at 300 K on red emitting GaP:Zn,O LEDs obtained from Bell Laboratories (Ref. 54). In these devices, the red emission is due to recombination at Zn-O pairs present in concentrations of approximately 10^{16} cm^{-3}, about an order of magnitude less than the Zn dopant concentration (Ref. 1). Because of their relatively low concentration, the Zn-O centers can become saturated at high currents. The emphasis in this work (Ref. 53) was placed on the study of the effects of neutron damage on the Zn-O saturation. Prior to the analysis of the saturation effects, $\tau_o K_n$ values were calculated for the total neutron-added SCR current, I, and the degradation of light intensity, L, at low constant voltage. Using Equation 1.18, $\tau_{SCR} K_{SCR}$ was found to be 2.2×10^{-14} cm^2, while Equation 1.15 was found to fit the degradation of the

diffusion controlled light output for a linearly graded radiative center profile with $\tau_o K_n = 2.7 \times 10^{-14}$ cm^2. This value is close to that (4.7×10^{-14} cm^2) found for the green emitting GaP diodes by Epstein, et. al (Ref. 52).

In order to examine the saturation effects, the results were plotted as the ratio L/I, which we refer to as the efficiency, η, versus I as shown in Figure 1.7 for a typical diode. Note that each curve possesses a maximum due to the saturation of the Zn-O centers. This occurs because as the Zn-O levels become saturated, additional current must flow by recombination through other centers. After successive neutron irradiations, the efficiency maxima decrease in magnitude and move to higher currents. These results were analyzed by writing an expression for L which takes saturation into account (Ref. 55). The efficiency was then taken as the ratio L/I and calculated by using Equation 1.17 for the neutron-induced SCR current. An expression for I_m, the current at the efficiency maximum, η_m, was then found by differentiating the equation for η with respect to I and setting it equal to zero. The resulting I_m's were then used to calculate η_m's. For a linearly graded Zn-O profile the following result was obtained:

$$\eta_m = 3.41 \frac{D^2 qa}{\tau_R G} \tau^2 \sqrt{\frac{n_{p_o}}{n_t}} \qquad (1.33)$$

where τ_R is the radiative lifetime of an electron trapped at a Zn-O center, n_t is the excess electron density required to fill half of the Zn-O centers, G is a constant, and a is defined by the

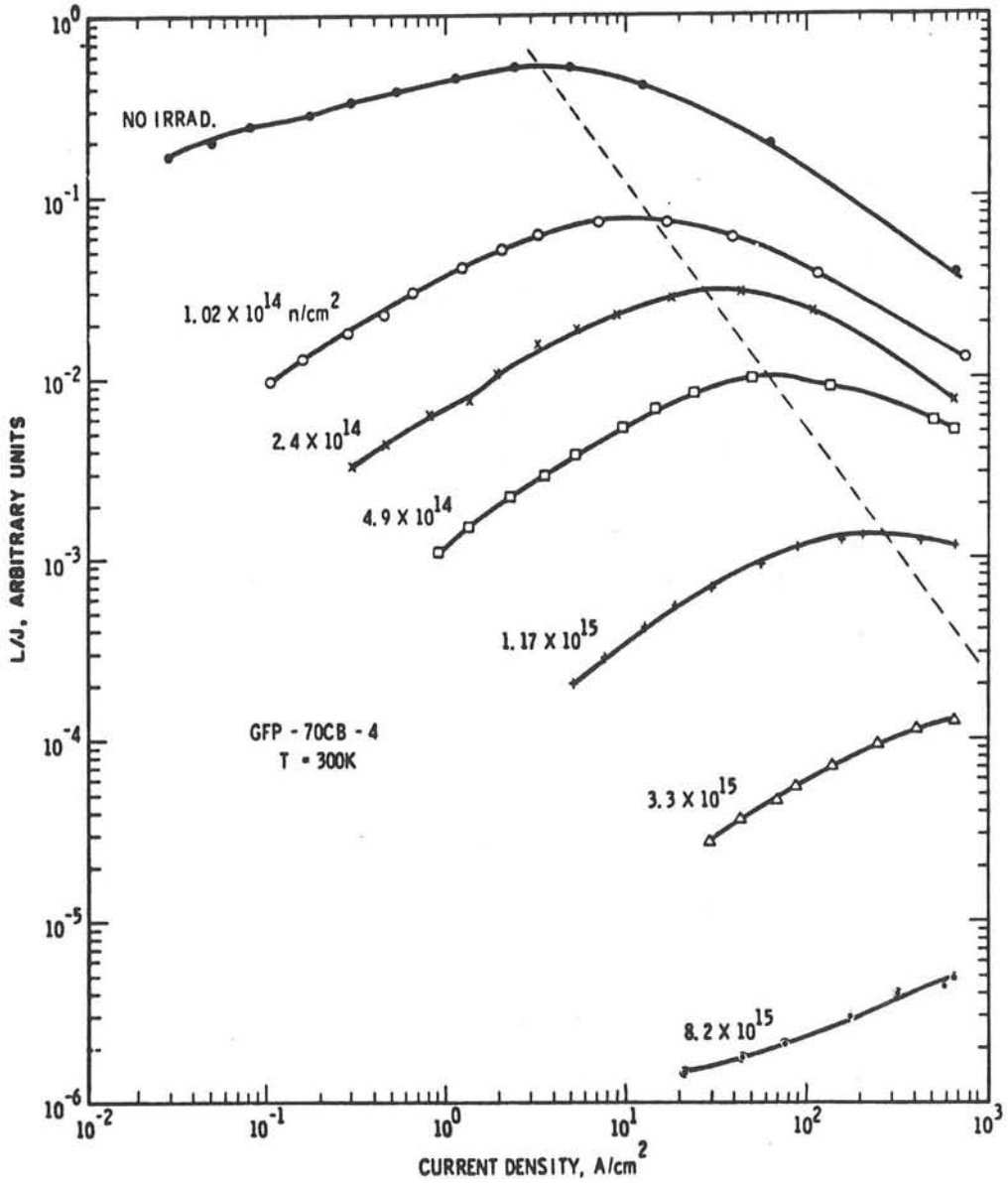

Fig. 1.7 Electroluminescence efficiency, defined as the ratio of total light output to current density, as a function of current density and neutron fluence for a GaP:Zn,O LED operated at 300K. The existence of maxima is indicative of saturation of the Zn-O radiative centers.

linearly graded Zn-O profile: $N_{Zn-O} \equiv ax$. Since measurement of τ is a constant current measurement and we have used an SCR current for I, we can compare Equation 1.33 with Equation 1.19 which gives the degradation of L at constant SCR current. For a linearly graded profile Equation 1.19 indicates that L is proportional to τ^3 so that L will decrease more rapidly than $\eta_m \propto \tau^2$ with irradiation because of the stronger dependence on τ. This result agrees with our earlier qualitative conclusion that saturation of radiative centers reduces the degradation rate.

The effect of neutron irradiation on τ was taken into account by substituting Equation 1.9 for $1/\tau$ into Equation 1.33:

$$\left(\frac{\eta_{m_o}}{\eta_m}\right)^{1/2} - 1 = \tau_o K \Phi \qquad (1.34)$$

where η_{m_o} is the maximum efficiency (L/I ratio) prior to irradiation. Using results such as those shown in Figure 1.7, it was found that Equation 1.34 provided a satisfactory fit to the data and gave an average $\tau_o K_n$ for 5 LEDs of 2.0×10^{-14} cm^2 in good agreement with the values derived from the low voltage total current ($\tau_{SCR} K_{SCR} = 2.2 \times 10^{-14}$ cm^2) and the low voltage light output ($\tau_o K_n = 2.7 \times 10^{-14}$ cm^2).

c. <u>Gallium arsenide phosphide</u> - Schade and co-workers (Refs. 56 and 57) have studied the effects of electron irradiation on $GaAs_{1-x}P_x$ LEDs. Irradiation to $\Phi = 1 \times 10^{17}$ e^-/cm^2 drastically reduced the light output of the devices. As in most of the

studies discussed thus far, the light emission originated in the neutral p-region and the radiation-induced degradation was due to the introduction of nonradiative recombination centers. The center primarily responsible for the decrease in emission is an acceptor center whose influence on light degradation is independent of alloy composition. In the second paper (Ref. 57), the authors described a second type of radiation-induced center, found by thermally stimulated current measurements, which is a trapping center 0.20 to 0.35 eV away from a band. Unlike the first center mentioned, the trapping center concentration increases with alloy composition, that is, with increasing x. It was found that both types of defects anneal below 550°C with most of the annealing occurring between 200 and 300°C. The defects responsible for light output degradation were found to anneal out faster for larger values of x.

Epstein, et. al. (Ref. 52), examined the effects of neutron damage on the external efficiency, η, and the minority carrier lifetime, τ, in $GaAs_{1-x}P_x$ LEDs as a function of alloy composition, x. The pre- and post-irradiation efficiency results for $\Phi = 3.5 \times 10^{13}$ n/cm^2 are shown in Figure 1.8. These data are characterized by a sharp drop in η, both before and after irradiation, at a value of $x \approx .4$ to .5 which corresponds to the transition from a direct band gap characteristic of GaAs to an indirect band gap characteristic of GaP. Neutron irradiation decreases η over the entire range of x. If the data is replotted as η/η_o, where η_o is the pre-irradiation value, this ratio is a maximum for intermediate values of x. The authors therefore conclude

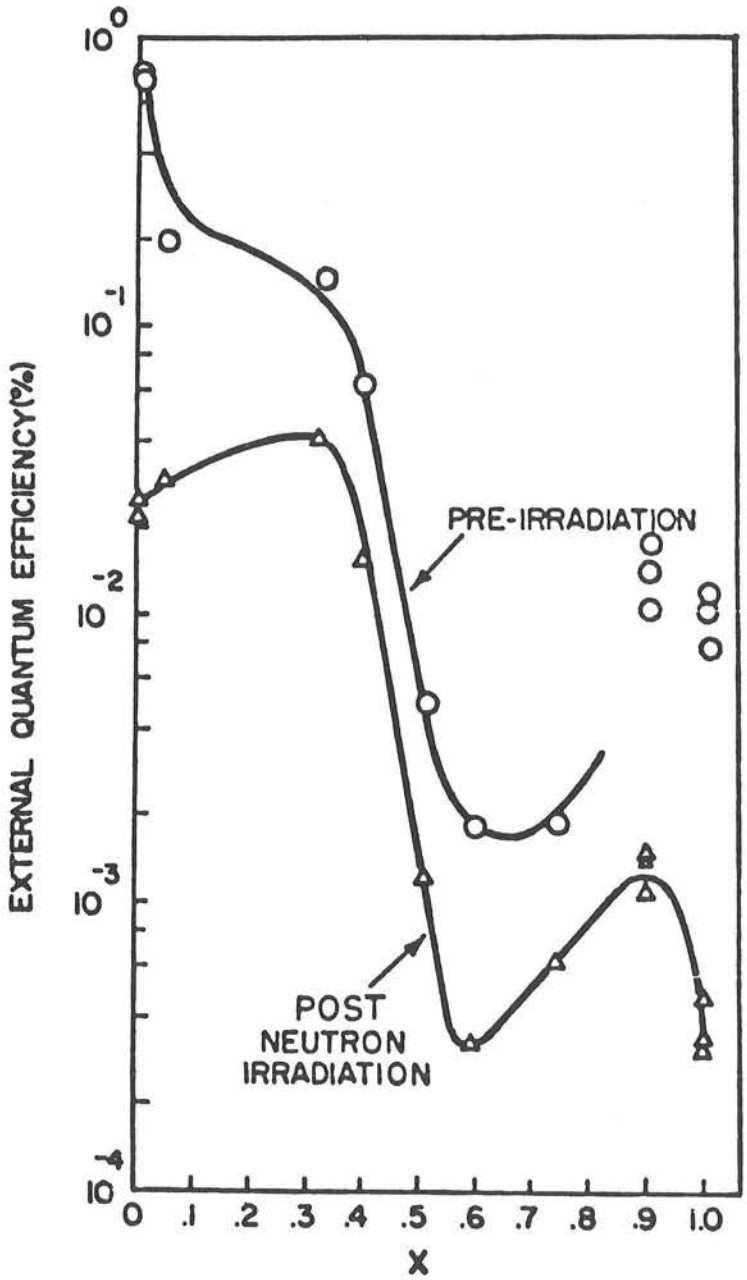

Fig. 1.8 Quantum efficiency at 295K prior to and following neutron irradiation with 3.5×10^{13} n/cm^2 versus fractional concentration of phosphorus, x, in $GaAs_{1-x}P_x$ LEDs. The sharp drop in efficiency at x = 0.4 to 0.5 corresponds with the transfer from a direct to an indirect energy gap (From A. S. Epstein, S. Share, R. A. Polimadei and A. H. Herzog, Appl. Phys. Lett. 23, 472 (1973)).

that degradation is less for such values of x. It is interesting to note, however, that if one does not include the data for x = 0, 0.9, and 1.0, then the remaining results do not really show a maximum. We point this out because the LEDs for these three x values were different from the remaining devices. The GaAs (x = 0) LED was made from boat grown, Si doped material whereas the intermediate x value devices were made by diffusing Zn into Se doped VPE n-type material. For x = 0.9 and 1.0, while the growth method was the same, the substrate was doped with Te rather than Se, and the devices contained nitrogen which produces an efficient radiative center. This latter fact is reflected in the pre-irradiation data in Figure 1.8 by the large increase in η for x = 0.9 and 1.0 relative to x values between 0.5 and 0.7. Based on these differences and our previous discussion of the influence of device properties on the degradation rate, it is possible that the maximum in η/η_0 seen at intermediate x values may be due to factors other than the change in alloy composition. This is supported by later work by Epstein, et. al. (Ref. 58), in which $\tau_0 K_\gamma$ for gamma irradiated GaAs devices was found to depend on the donor dopant and was larger for Te than for Se. Included in this recent study (Ref. 58) are measurements of damage constant as a function of x which show that K_γ decreases with increasing x and levels off at a constant value of 0.3 $(\text{rads} \cdot \text{s})^{-1}$ for x greater than 0.5. The authors (Ref. 58) concluded that the dopant and alloying effects sufficiently perturb the lattice so that the effects of damage are minimized. Isochronal annealing results for the gamma irradiated devices were also quite dependent

on the value of x. For alloy compositions near GaAs a large annealing stage near 250°C was observed. However, this stage rapidly disappeared so that for $x > .15$ annealing at this temperature was minimal.

In the earlier study already mentioned in the discussion of GaP, Epstein, et. al. (Ref. 50), measured various properties of yellow-emitting $GaAs_{0.1}P_{0.9}$ LEDs following gamma irradiation to 10^8 rads (Si). As in several other studies cited thus far, the efficiency for yellow light emission and the minority carrier lifetime both were degraded. Therefore, an equation similar to Equation 1.23 was used with $n = 0$ (step profile) to determine a $\tau_o K_\gamma$ value of 3×10^{-8} $rads^{-1}$. This value is approximately the same as other $\tau_o K_\gamma$ values previously mentioned for GaP and $GaAs_{1-x}P_x$. As in the case of the $GaAs_{1-x}P_x$ diodes with $x > .15$ the thermal annealing of the damaged yellow emitting diodes was insignificant below 250°C. However, annealing to 500°C did produce recovery to 75% of pre-irradiation levels.

In a more recent study, Lambert, et. al. (Ref. 59) examined a variety of GaAsP LEDs prior to and following a series of neutron irradiations. These devices contained from 40% to 100% P with electroluminescence peaks varying from 0.59 μm to 0.69 μm. Spectra were measured at room temperature and at low temperatures. For all of the LEDs the light output degradation was less at the lower temperatures. At all temperatures, the 87% P LEDs (yellow emitting) were the most sensitive to irradiation, the 39% P devices (red emitting) were the least sensitive, and the 100% P (green) and 65% P (orange) LEDs had intermediate sensitivities.

The data were successfully analyzed with an equation of the form of Equation 1.23 for measurements taken at constant current.

d. Gallium arsenide, gamma and electron irradiation - Most of the investigations of radiation effects in LEDs have been concerned with GaAs primarily because more is known about the physics of GaAs than the other LED materials. Aukerman and coworkers were responsible for the early work in this area (Refs. 8,60-62). These studies, again demonstrate the usefulness of radiation damage as a tool in determining the basic characteristics of LEDs.

In the first of these papers, Millea and Aukerman (Ref. 60) studied the effect of electron irradiation on the near edge emission band in moderately doped (2×10^{17} cm^{-3}) GaAs LEDs. Although the dependence of total current on voltage was complex in these diodes, the light intensity, L, was proportional to $e^{qV/kT}$ over several orders of magnitude between 78 K and 298 K. This fact, combined with the observed radiation-induced decrease in L at constant voltage led to the conclusion that L was diffusion controlled. Using Equation 1.9 a $\tau_o K_e$ value of 2×10^{-15} cm^2/electron was found.

In a second paper, Aukerman and Millea (Ref.61) examined the near-edge emission band in heavily doped (2×10^{18} cm^{-3}) GaAs LEDs at 77 K before and after electron irradiation. They observed a substantial increase in total current, I, following irradiation but only a small decrease in L. In our discussion of tunneling phenomena, it was pointed out that low temperatures and heavy doping both enhance the tunneling probability. On the basis of

such reasoning and additional experimental results, the authors concluded that the electroluminescence was due to tunneling of carriers to band tail states within the space-charge region with subsequent radiative recombination in this region.

In later work, Millea and Aukerman (Ref. 62) studied the effect of electron irradiation on two low energy emission bands at 1.0 eV and 1.28 eV in GaAs LEDs. These bands responded similarly to the near-edge electroluminescence studied earlier (Ref. 60). It was concluded that the 1.28 eV band was due to donor-acceptor pair recombination in the neutral region.

The last in this series of papers (Ref. 8) summarized earlier work and provided a more detailed examination of the effects of electron irradiation on both moderately and heavily doped GaAs LEDs. The authors reached conclusions similar to those in the earlier papers concerning diffusion controlled light output in the moderately doped devices and tunneling in the heavily doped devices. In the devices used for this study, the Te doping level in the n-type substrate was varied between $N_{Te} \approx 5 \times 10^{16}$ cm^{-3} and $N_{Te} \approx 2 \times 10^{18}$ cm^{-3}. The LEDs were formed by diffusing Zn into these substrates. The value of $\tau_o K_e$ was inversely proportional to N_{Te} varying from 1.0×10^{-13} cm^2/electron for 5×10^{16} Te/cm^3 to 3.9×10^{-15} cm^2/electron for 2×10^{18} Te/cm^3. These $\tau_o K_e$ values characterize the degradation of light output from the p-region. Unfortunately, Zn doping levels, N_{Zn}, in the p-regions were not obtained for the various n-type dopant concentrations. However, if the profiles are sharp, one can reasonably

assume that N_{Zn} is about the same as N_{Te} since N_{Zn} must approximately equal N_{Te} when the junction is formed and the material becomes p-type. Consequently, one can assume that $\tau_o K_e$ is also inversely proportional to N_{Zn}, a fact we have used as a basis for hardening GaAs LEDs. The experimental work concerning this hardening technique will be discussed in the next section.

Later work (Ref. 7) in our laboratory on the sub-threshold properties of GaAs laser diodes was primarily concerned with the annealing characteristics of defects introduced by Co^{60} gamma irradiation. These defects were studied by observing the degradation and recovery of the near-edge emission following irradiation and subsequent thermal and forward bias annealing. The diodes examined were heavily doped, and the effect of irradiation on the intensity and total current was similar to that observed by Aukerman and Millea (Ref. 61) on their heavily doped diodes. At room temperature the intensity degradation followed Equation 1.15 for a linearly graded profile indicating a diffusion mechanism, while at 76 K, a tunneling mechanism was apparent. The $\tau_o K_\gamma$ value obtained at 300 K was 3.3×10^{-8} $rads^{-1}$. The nonradiative recombination centers which caused a decrease in radiative recombination in the diffusion region annealed out in a single stage centered at 237°C. The annealing kinetics were first order with an activation energy of 1.70 eV and a preexponential factor of 1.2×10^{13} s^{-1}.

As in the case of studies (Refs. 42 and 43) mentioned earlier on GaP, these defects could be removed at room temperature by heavily forward biasing the diode. The injection annealing was

studied as a function of temperature, injection level, and time after an injection annealing pulse. These results led to the proposal of an injection annealing model based on charge state dependent defect stability. However, in view of the more recent results of Lang and Kimerling (Ref. 44) it now appears that the injection annealing was due to recombination-enhanced defect re-ordering.

On the basis of the injection annealing and the kinetics of the thermal annealing, a complex defect was proposed in which an As interstitial is one component and an impurity is the other. The rate limiting step in the thermal annealing of the defects is the breakup of the complex. For the case of injection annealing, the dissociation of the complex is due to the transfer of non-radiative recombination energy to lattice energy near the complex.

In a study of gamma irradiation effects in optical isolators, Epstein and Trimmer (Ref. 63) also examined degradation of a GaAs LED similar to the emitter contained in the optical isolator. Relatively slow degradation of the LED efficiency was observed up to a dose of 10^7 rads with a sudden drop in output by a factor of 200 in going from 10^7 rads to 10^8 rads. Thermal annealing recovery of the light output was noted between 225°C and 300°C. A similar type of degradation of the efficiency was seen in a later study (Ref. 64) of gamma irradiated GaAs LEDs. Herein, minority carrier lifetime measurements were also made and the efficiency was observed to decrease at a faster rate than τ. The efficiency degradation rate was found to be exponential in nature and this rapid reduction in η was attributed to the introduction

of so-called "killer" centers which actually reduce the number of active radiative centers. It is interesting to note that these changes were accompanied by large increases in the diffusion component of the total current. Efficiency measurements inherently contain the efficiency of electron injection into the p-region; that is, they are essentially light output divided by total current. Therefore, it is not clear whether or not part of the rapid efficiency degradation could be due to gamma-induced increases in total current.

Share, et. al. (Ref. 64), developed a quantitative model to account for both the exponential degradation due to radiative center annihilation and the more usual degradation due to competing nonradiative centers. This analysis gave a $\tau_o K_\gamma$ value of 9×10^{-8} rads^{-1} for the non-exponential portion of the degradation.

Similar effects were examined in more detail in a later paper by Share, et. al. (Ref. 65) in which the exponential efficiency degradation was again observed in closely compensated Zn diffused GaAs LEDs. These results were explained as before by postulating the annihilation of radiative centers so that following irradiation, N_R is decreased while τ_R, the radiative lifetime, is increased. In this paper (Ref. 65) the authors also present L-V and I-V curves. Interestingly, at constant voltage there is very little decrease in light intensity, L, following an irradiation of 10^8 rads. This small decrease fits in with the observation that the degradation of the minority carrier lifetime, τ, is small relative to the efficiency, η, degradation. It is also

interesting to note that the increase in total current, I, following 10^8 rads is about the same as the difference between the τ degradation and the η degradation after 10^8 rads. This result suggests that the gamma induced increase in I is responsible for the observed decrease in η rather than a decrease in the radiative recombination rate. In fact, it would seem just as plausible to attempt to explain the results on the basis that there is essentially no change in relative light output, as the L-V measurements show, and the only damage effect is an increase in I. This would eliminate the need to invoke the somewhat controversial killer center model.

In their study of gamma irradiation effects in $Ga_{1-x}Al_xAs$ LEDs, Polimadei, et. al. (Ref. 66), included a Zn diffused GaAs LED. Unlike the previously mentioned work (Refs. 64 and 65), the efficiency degradation in this case was not exponential and could be described by Equation 1.23 with n = 1 for a linearly graded radiative center profile. This difference was apparently due to the close compensation present in the diodes which showed exponential degradation. The $\tau_o K_\gamma$ value found for the GaAs LEDs using Equation 1.23 was 4.5×10^{-7} $rads^{-1}$, a value considerably larger than that found by Barnes (Ref. 7) for laser diodes. Aukerman, et. al.'s (Ref. 8) results which showed that $\tau_o K_e$ was inversely proportional to the doping concentration, agree with the difference between Polimadei, et. al.'s (Ref. 66) results and Barnes' (Ref. 7) results since the laser diodes were very heavily doped.

Included in Soda, et. al.'s (Ref. 67) study of gamma irradiation effects on optical isolators and their separate emitters and detectors, was a Hewlett-Packard GaAs LED with a Zn doped p-region. As is often the case, pre-irradiation L-V and I-V measurements indicated that the light output was diffusion controlled and L was $\propto \exp [qV/mkT]$ with m = 1, while I was due to SCR at low voltages with a diffusion component growing in at higher voltages. Following irradiation, the m = 1 component of I increased and L decreased at a rate described by Equation 1.15 for a linearly graded diode, as confirmed by capacitance measurements. The determination of $\tau_o K_\gamma$ is illustrated in Figure 1.9 for these LEDs. Here the quantity $(L_o/L) - 1$ is plotted for two diodes at different constant voltages. The straight line drawn through the data with slope ≈ 1.0 confirms the applicability of Equation 1.15 and results in a value of $\tau_o K_\gamma = 9 \times 10^{-8}$ $rads^{-1}$. This value agrees with that found by Share, et. al. (Ref. 64) for the non-exponential portion of their gamma induced efficiency degradation. It should be emphasized, however, that Soda, et. al. (Ref. 67) did not observe any exponential degradation of L with dose, Φ. This can be accounted for, in part, by the difference in measurements. Soda, et. al.'s (Ref. 67) degradation rate was determined by constant voltage measurement of L whereas the efficiency measurements of Share, et. al. (Ref. 64) included the effects of gamma irradiation on the total current. In order to check for the presence of exponential degradation in Soda, et. al.'s (Ref. 67) LEDs, measurements of lifetime as a function of dose were made by the reverse recovery

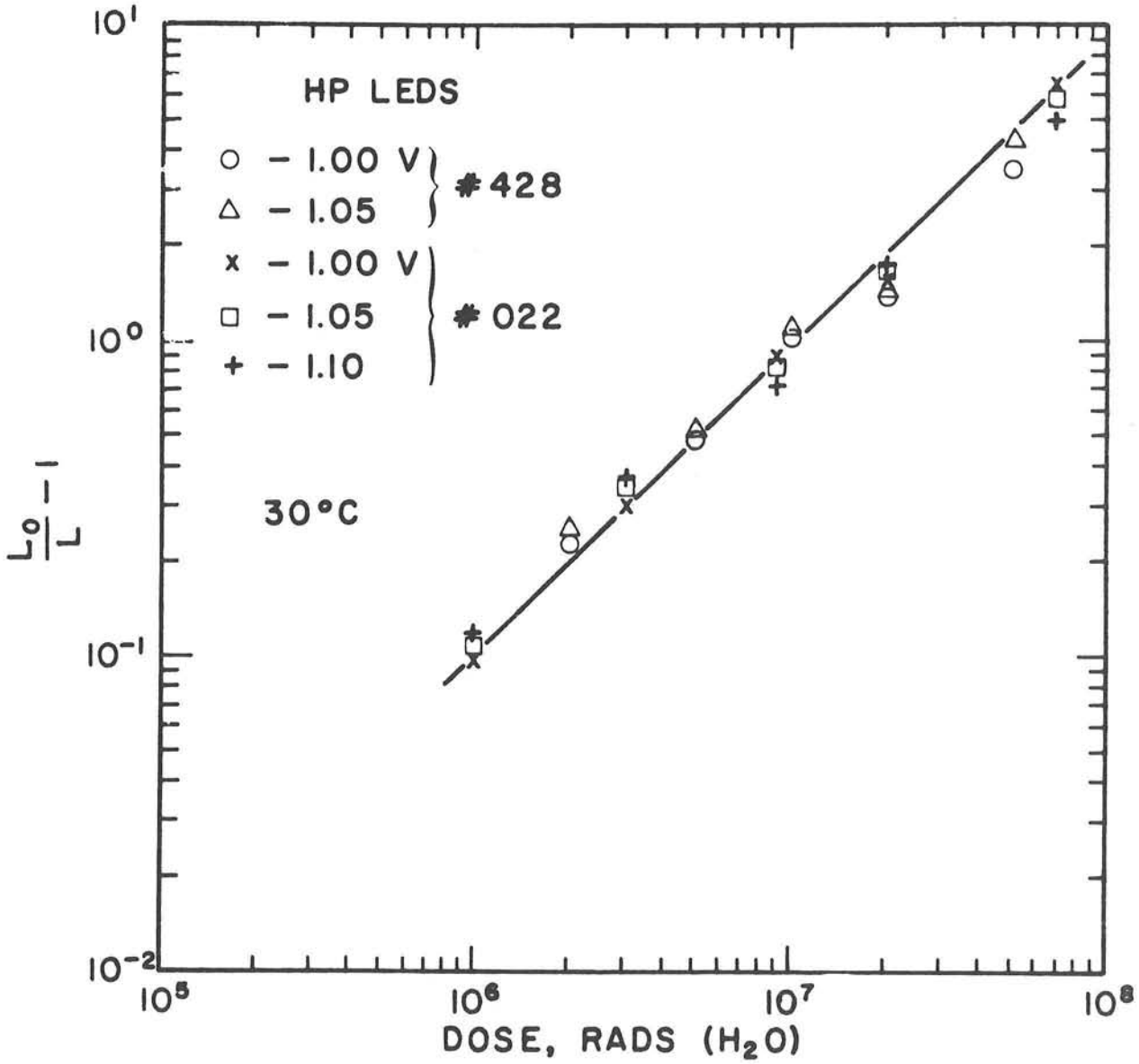

Fig. 1.9 A typical analysis of constant voltage light intensity data using Eq. (12) for linearly graded LEDs. In this case the LEDs are Hewlett-Packard GaAs devices which have been subjected to Co^{60} gamma irradiation. (From K. J. Soda, C. E. Barnes, and R. A. Kiehl, IEEE Trans. Nucl. Sci. NS-22, 2475 (1975)).

method and by observation of the radiative decay time. Both of these quantities decreased with dose at a rate that agreed with the degradation rate predicted by the $\tau_o K_\gamma$ value of 9×10^{-8} $rads^{-1}$ further indicating that exponential degradation was not present.

In another study, Epstein, et. al. (Ref. 58) have examined the effect of varying the type of donor dopant in GaAs LEDs on the gamma induced efficiency degradation. The $\tau_o K_\gamma$ values were calculated from Equation 1.23 with η_o/η substituted for L_o/L and $n = 1$ (linearly graded N_R). Their results are reproduced in Table I, presented in the summary on damage in LEDs, which shows that Se gives the smallest $\tau_o K_\gamma$ while the amphoterically Si doped devices give the largest $\tau_o K_\gamma$'s. This latter result agrees agrees with our experiments on GaAs:Si LEDs as we will show in detail in a later section. Epstein, et. al. (Ref. 58) did not find any dependence of $\tau_o K_\gamma$ on donor dopant concentration N_D. No information was given on what the corresponding p-type dopant concentrations were as a function of N_D. This result contrasts with that of Aukerman, et. al. (Ref. 8) who found an inverse dependence of $\tau_o K_e$ on N_D.

e. <u>Gallium arsenide, neutron irradiation</u> - Turning our attention to neutron irradiation effects in GaAs LEDs, Petree (Ref. 68), in the first investigation of these effects, found a threshold for light output degradation at 1×10^{12} n/cm^2. In a later study, Noel, et. al. (Ref. 69) examined the effects of neutron damage on various sub-threshold properties of diffused GaAs laser diodes.

Pre-irradiation measurements indicated that the total current, I, was due to SCR at room temperature and the light output was due to diffusion-controlled radiative current flow in the p-region. Spectral data showed that in addition to the main, near-edge emission band, there was a prominent lower energy band centered at 1.28 eV as seen earlier by Millea and Aukerman (Ref. 62). Following irradiation the total SCR current increased and the constant voltage light intensity from the main band decreased at a rate such that Equation 1.15 with n = 1 (linearly graded) provided a satisfactory fit to the data with $\tau_o K_n = 3.2 \times 10^{-15}$ cm^2/n.

Pre- and post-irradiation results obtained by Noel, et. al. (Ref. 69) for the 1.28 eV band are shown in Figure 1.10. We present these results because they are quite interesting for two reasons. First, they illustrate the fact that it is possible to have a radiative SCR current with m in exp [qV/mkT] equal to 1.0 in accordance with the detailed SCR theory (Ref. 10). Note that a change in m from 1 to 2 occurs at about 1.19 V. This so-called "kink" voltage, V_K, is approximately proportional to the distance in energy of the recombination center energy level from the center of the energy gap (Ref. 13). Consequently, for the deep levels usually observed in the space-charge region, V_K is very small and only the portion with m = 2 is seen. However, if the recombination center is relatively shallow as for the main near-edge emission and also for the 1.28 eV emission band, V_K will be large and one can observe a significant range of forward bias over which m = 1.0 for an SCR current.

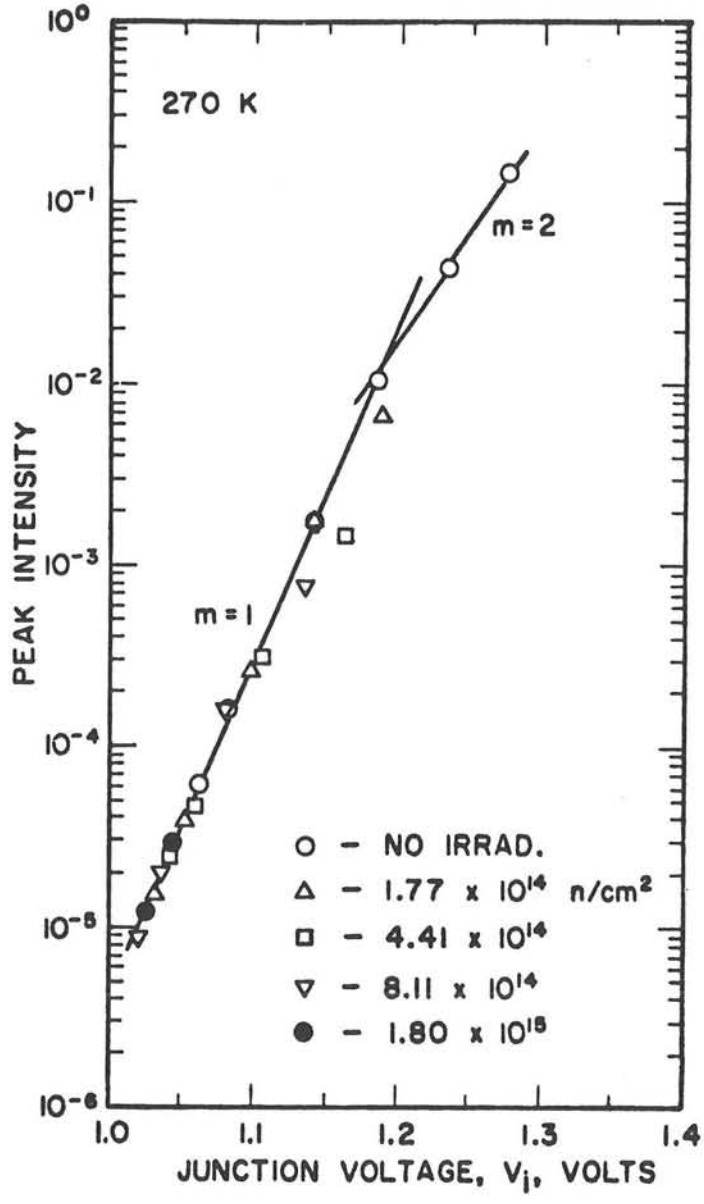

Fig. 1.10 Peak intensity of the 1.28 eV emission from a GaAs LED versus junction voltage prior to and following neutron irradiation. The light output is due to radiative recombination in the space-charge region (from B. W. Noel, C. E. Barnes and H. D. Southward, IEEE Trans. Nucl. Sci. NS-18, No. 6, 378 (1971)).

The second important feature of Figure 1.10 is the insensitivity of the 1.28 eV emission to neutron irradiation. After $\Phi = 1.8 \times 10^{15}$ n/cm^2, the intensity still has not decreased. As we have pointed out earlier, this behavior is expected for a radiative SCR current in which the number of radiative centers is unaffected by the irradiation.

The results in Figure 1.10 are similar to those obtained by Share, et. al. (Ref. 69) for gamma irradiated, closely compensated GaAs LEDs. Recall that the L-V curve, for which m = 1 as in Figure 1.10, did not change significantly after 10^8 rads. With a closely compensated diode, it is reasonable to assume that N_R, in this case, N_{Zn}, is significant in the space-charge region. An analogy with Noel, et. al.'s (Ref. 69) work in Figure 1.10 would then explain the insensitivity of the light output in Share, et. al.'s (Ref. 65) experiments to gamma irradiation.

In our laboratory, similar studies (Ref. 70) were conducted on the effects of neutron damage on the sub-threshold properties of epitaxially grown GaAs laser diodes. As in Noel, et. al.'s (Ref. 69) case, the total current at room temperature was due to SCR, and this current increased following neutron irradiation due to the introduction of nonradiative recombination centers in the space-charge region. Analysis of the increase in SCR current with Φ using equations similar to Equations 1.17 and 1.18 gave a $\tau_{SCR} K_{SCR}$ value of 1.3×10^{-15} cm^2/n. A somewhat larger value larger value of $\tau_o \overset{\circ}{K}_n = 7.1 \times 10^{-15}$ cm^2/n was obtained for the constant voltage degradation of L using Equation 1.15 with n = 1. This difference may be accounted for by variations in lifetime

between the space-charge and neutral regions. The value of $\tau_o K_n$ is roughly twice as large as that obtained by Noel, et. al. (Ref. 69) (3.2×10^{-15} cm^2/n) for diffused laser diodes. This difference is probably due to a greater lifetime in the higher quality epitaxial material used in constructing the diodes measured in our study.

In general, the effects of neutron irradiation on the diode properties at 76 K in our study (Ref. 70) were smaller than the corresponding changes at room temperature. Irradiation to fluences of 10^{15} n/cm^2 did not significantly decrease the light intensity at constant low voltage. This result suggested that the radiative current at 76 K was due to tunneling into the space-charge region. This was verified by the observation of "shifting-peak" spectra.

In their study of gamma and neutron damage in optical isolators, Epstein and Trimmer (Ref. 63) also briefly examined neutron irradiated Zn diffused GaAs LEDs similar to those contained in the isolators. After an irradiation of $\Phi = 3.7 \times 10^{13}$ n/cm^2, the efficiency of the LEDs decreased by about a factor of 30 at an LED current of 50 mA.

Share, et. al. (Ref. 64) also included neutron damage studies in their examination of radiation effects in closely compensated, Zn diffused LEDs. As indicated earlier, gamma irradiation resulted in an exponential decrease in efficiency with dose. In contrast, neutron irradiation did not produce this effect, presumably due to the "killer" center properties of the relatively simple gamma-induced defects. Rather, the neutron-induced degra-

dation of the efficiency was adequately described by Equation 1.23 with n = 1 resulting in $\tau_o K_n = 2.5 \times 10^{-13}$ cm^2/n, a value much larger than those obtained for the laser diodes (Refs. 69 and 70). However, Epstein, et. al. (Ref. 52) in a later study of neutron damage in $GaAs_{1-x}P_x$ LEDs included a GaAs LED very similar to those examined in the earlier work (Ref. 64). In this later study (Ref. 52) they obtained a value of 4.7×10^{-15} cm^2/n, significantly smaller than the previous value. It is possible that the difference is due to the different experimental methods used in each case. In their later work (Ref. 52), rather than measuring the efficiency and using Equation 1.23, the authors measured τ before and after neutron irradiation and used Equation 1.9 directly to calculate $\tau_o K_n$. In a third study, when the efficiency degradation method was used to determine $\tau_o K_n$, Polimadei, et. al. (Ref. 66) obtained a value of 4.0×10^{-13} cm^2/n in good agreement with the previous determination of 2.5×10^{-13} cm^2/n.

Experiments (Ref.71) were conducted in our laboratory, the objective of which was to develop efficient, radiation insensitive GaAs:Zn LEDs. We have noted repeatedly that the $\tau_o K$ product is an inverse figure of merit for LEDs. The central idea behind this study was to reduce $\tau_o K$ by decreasing τ_o through the introduction of large concentrations of radiative centers so that the radiative lifetime, τ_R, is so small that it controls τ_o. In GaAs this essentially means increasing the concentration of the p-type dopant, in this case Zn, since the Zn acceptor level can participate in the radiative recombination process. This technique is also appropriate if the light output is due to band-to-band recombina-

tion without the involvement of the shallow acceptor center. As indicated by Equation 1.4, τ_R is inversely proportional to p_o so that an increase in doping level will decrease τ_R. As we will show in our summary of $\tau_o K$ values for GaAs LEDs, there is evidence in the literature which shows that $\tau_o K$ decreases with increasing p-type dopant concentration. For example, recall the work of Aukerman, et. al. (Ref.8) discussed earlier, and the comparison of $\tau_o K$ values for heavily doped laser diodes with those for other LEDs. The possibility of decreasing τ_o by increasing N_{Zn} is supported by the measurements of Casey, et. al. (Ref.72) of the electron diffusion length, L_e, in p-type GaAs as a function of dopant concentration. In Ge-doped, p-type GaAs, L_e was constant with increasing Ge concentrations, N_{Ge}, up to $N_{Ge} \approx 1 \times 10^{18}$ cm^{-3}. However, above this concentration, L_e was observed to decrease with increasing N_{Ge}. This was attributed to a decrease in the radiative lifetime at large hole concentrations. Below 10^{18} cm^{-3}, L_e was controlled by nonradiative recombination centers, but above 10^{18} cm^{-3}, the radiative lifetime decreased to the point where it determined L_e and hence τ_o.

If, indeed, τ_R can be reduced to the point where it controls τ_o, this would mean that the majority of the electrons would recombine radiatively giving a greater radiative efficiency, and hence a greater light output while at the same time, achieving a smaller value of $\tau_o K$. This is to be contrasted with radiation hardening of many types of Si devices in which shortening of the lifetime to achieve radiation resistance results in poorer device performance. Similar problems are expected with ternary LEDs,

such as GaAlAs, in which $\tau_o K$ is small but the radiative efficiencies are low (Ref.66).

In order to test this hardening technique, four sets of ten epitaxially grown GaAs LEDs each were purchased from Texas Instruments. In three of the sets, the n-type region was doped with 3×10^{18} Te/cm^3. The p-type regions contained the following varying amounts of Zn between the three sets: 2×10^{18} Zn/cm^3, 7×10^{18} Zn/cm^3, and 2×10^{19} Zn/cm^3. In addition to LEDs from these three sets, measurements were also performed on the fourth set with 3×10^{17} Te/cm^3 and 2×10^{18} Zn/cm^3 and on amphoterically Si doped GaAs LEDs which are quite sensitive to irradiation because of the large value of τ_o found in these devices.

Pre-irradiation results agreed with the proposed hardening mechanism in that the radiative decay time was shortest ($\approx$ 15 ns) in the most heavily doped devices while the light output at typical operating currents (10-50 mA) was greatest in the devices with largest N_{Zn} and was comparable with that from the highly efficient GaAs:Si LEDs.

Pre- and post-irradiation measurements of light output at a constant typical operating current of 50 mA for the various LEDs are shown in Figure 1.11. The post-irradiation results also tend to confirm the hardening technique in that the light output, as shown in Figure 1.11, of the GaAs:Si devices, has been strongly reduced relative to that in the heavily Zn doped devices. Similar observations were made for radiative decay time degradation. Smaller, but significant reductions were also noted in the most lightly Zn doped devices, but, in contrast, the most heavily doped GaAs:Zn LEDs do not show significant reduction in light output below

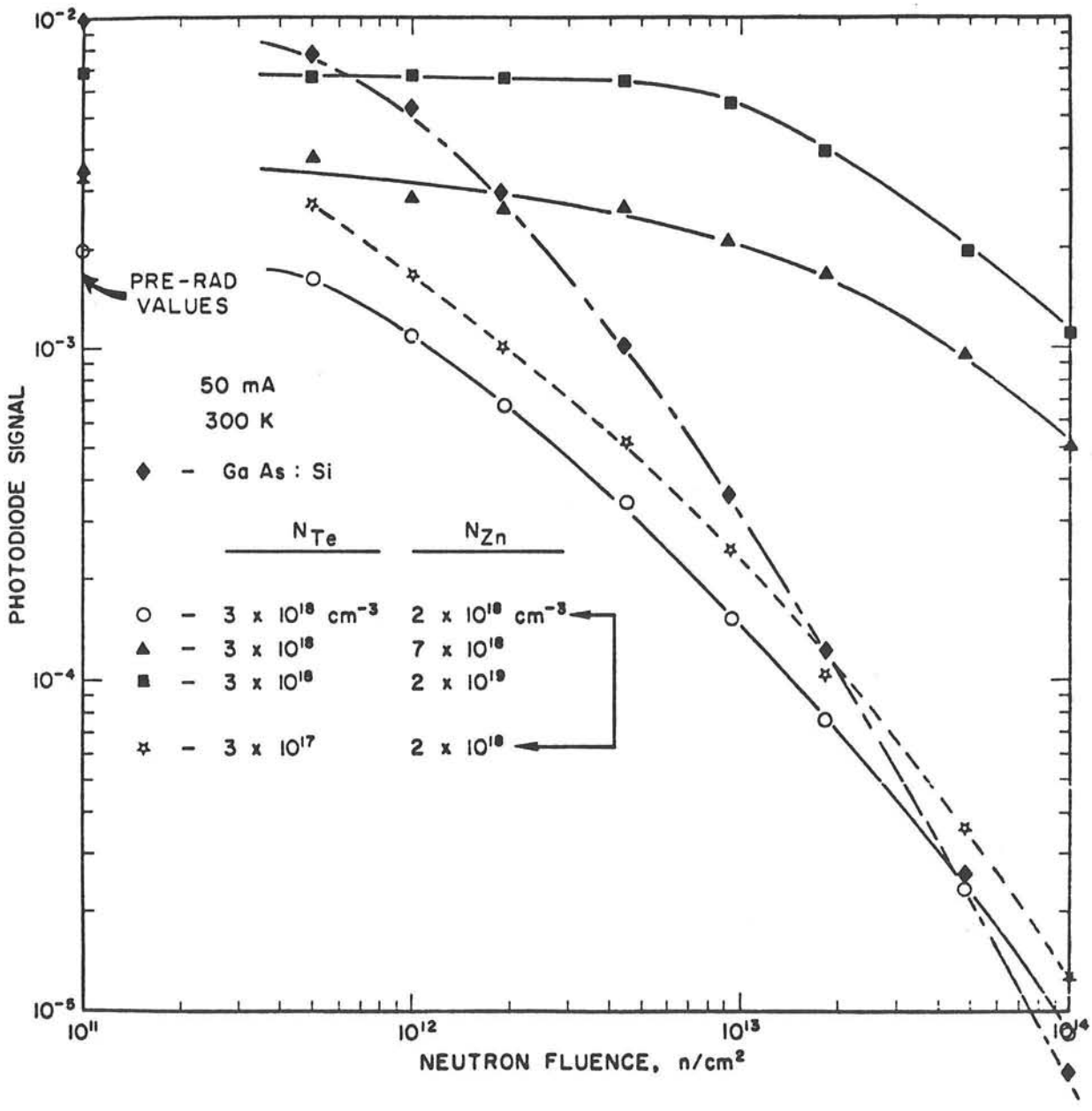

Fig. 1.11 Constant current light output as a function of neutron fluence for GaAs LEDs containing varying amounts of Zn and Te and also for an amphoterically Si doped GaAs LED. The data are averages for three LEDs at each concentration. Note that the more heavily doped devices have greater pre-irradiation light outputs and are also less sensitive to irradiation.

fluences of 10^{13} n/cm^2. Additional support for this model in which the p type doping level is the principal determining factor for the pre-irradiation light output and the radiation sensitivity is provided by the similarity in behavior for the LEDs containing the same $N_{Zn} = 2 \times 10^{18}$ cm^{-3} but N_{Te}'s differing by a factor of 10 (3×10^{18} cm^{-3} and 3×10^{17} cm^{-3}). Values of $\tau_o K_n$ for each set of LEDs are given in Table III.

More recently, we have examined neutron damage effects in both planar and high radiance GaAs LEDs in which the p side was heavily doped with Ge (Refs.73 and 74). These devices were included as part of a study of GaAlAs LEDs which will be discussed in more detail later. Typical results of efficiency (L/I) as a function of neutron fluence and LED current are shown in Figure 1.12. The planar devices are the Texas Instruments (TI) LEDs, while the high radiance LEDs are from Plessey, Inc. (PL). These data demonstrate the importance of using high radiance LEDs to minimize damage effects. As will be shown in more detail later, such LEDs exhibit almost no neutron-added current at high currents. This is shown in Figure 1.12 by the decreased sensitivity to neutrons of the PL GaAs devices at the higher currents of 50 mA and 100 mA. Note that at 10 mA both LED types degrade at the same rate.

f. <u>Amphoterically Si doped GaAs LEDs</u> - We have chosen to devote a separate section to GaAs:Si LEDs because they are unique for several reasons. First, because of their high efficiency relative to other devices, they have dominated the commercial market for GaAs LEDs. Therefore, their radiation sensitivity must be carefully evaluated since the designer may be restricted

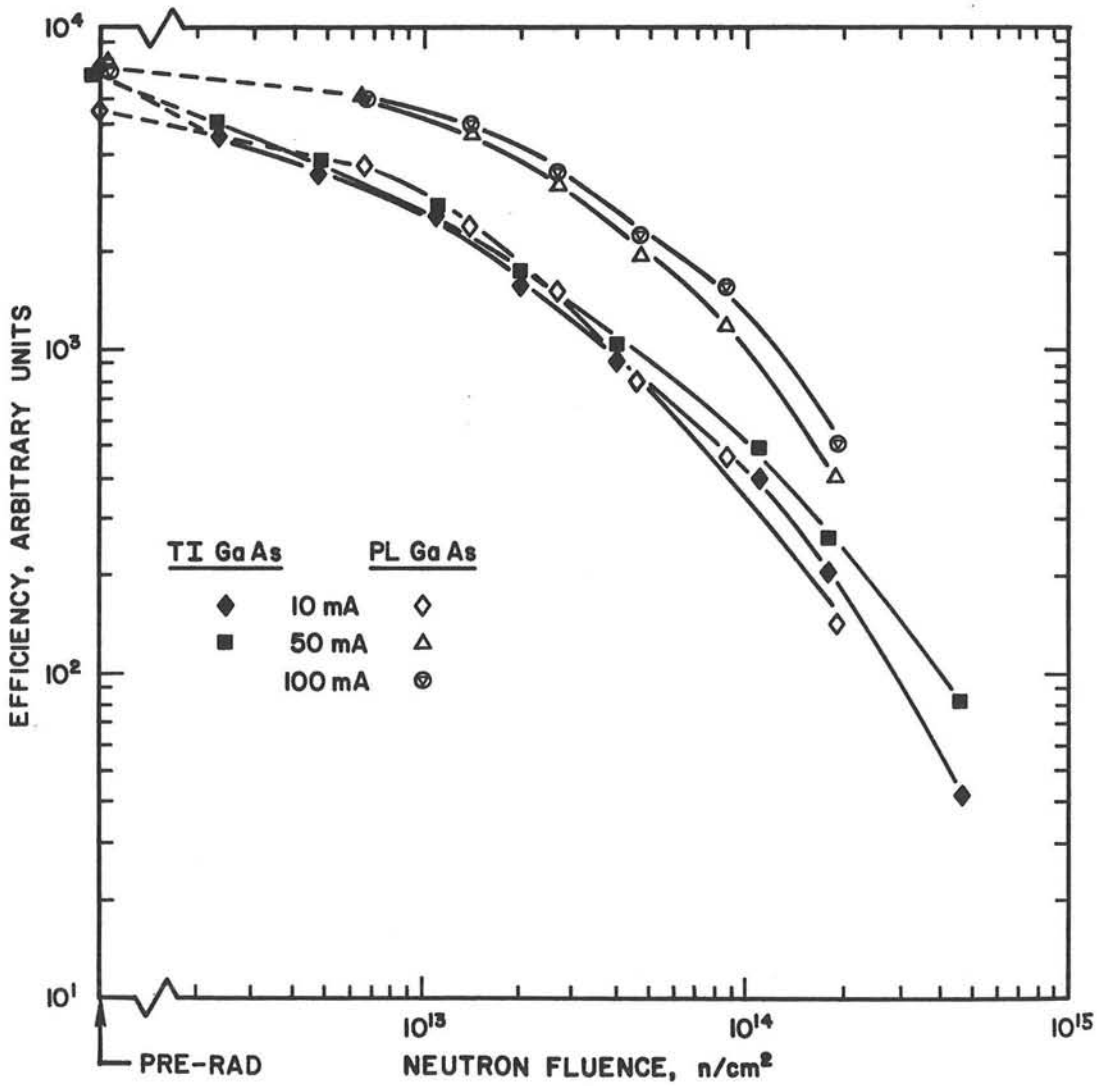

Fig. 1.12 A comparison of efficiency (L/J) degradation at different LED currents between planar Texas Instruments (TI) GaAs LEDs and Plessey (PL) high radiance GaAs LEDs.

in his choice of LEDs to this particular type of device. Second, the GaAs:Si LEDs possess unique properties, both at low and high currents, which are a result of the growth method used in making the devices. As will be shown in some detail, these properties significantly affect the GaAs:Si LEDs response to irradiation. The minority carrier lifetime τ, in these devices is typically quite long (hundreds of nanoseconds) and is inversely proportional to LED current and emitted photon energy. The peak photon energy can be varied by changing the Si doping level. A typical commercial device has an emission wavelength peak at .93 to .94 μm, 30-40 nm above that for LEDs not amphoterically doped. At large currents, space-charge limited currents (SCLC) are observed and light is emitted from the entire p-region. Because of the long lifetimes, the radiative rise and fall times of these LEDs as specified in a typical catalogue of LEDs are quite long. Further discussion of these properties and the structure of the devices is postponed until our review of current work in our laboratory. First, we will review past work on both gamma and neutron damage in the GaAs:Si LED.

Share, et. al. (Ref.64) in their study of compensated GaAs LEDs examined gamma and neutron damage effects in amphoterically Si doped devices. In contrast with the Zn diffused LEDs, no gamma induced exponential degradation was observed. Rather, the efficiency degradation was due to the introduction of competing non-radiative centers whose effect was successfully explained using Equation 1.23 with n = 1. A value of $\tau_o K_\gamma = 8.4 \times 10^{-7}$ rads^{-1} was obtained from this analysis and is quoted in a later paper by these authors (Ref.58). A similar analysis of neutron degradation

resulted in $\tau_o K_n = 3.5 \times 10^{-13}$ cm^2/n. The value of $\tau_o K_\gamma$ is larger than any mentioned previously because of the large values of τ_o in these devices. For example, Share, et. al. (Ref.64) measured a value of $\tau_o = 270$ ns, whereas typical values of τ_o in other GaAs LEDs are 10 to 20 ns.

In a later report, Polimadei, et. al. (Ref.75) studied the effects of both gamma and neutron irradiation on high power (> 200 mW) GaAs:Si LEDs. External quantum efficiency, power output, minority carrier lifetime, and power efficiency were measured after both types of irradiation. Typical results are shown in Figure 1.13 which gives power output at an LED current of 1 A. Note that neutron degradation begins at about 1×10^{12} n/cm^2 while gamma degradation begins at about 10^6 rads. Lifetime-damage constant products were calculated from the efficiency degradation using Equation 1.23 with n = 1 and the following values were obtained: $\tau_o K_\gamma = 8.4 \times 10^{-7}$ $rads^{-1}$ and $\tau_o K_n = 3.5 \times 10^{-13}$ cm^2/n. Lifetime measurements were also used to determine $\tau_o K$ values by way of Equation 1.19 yielding the value, $\tau_o K_\gamma = 1.2 \times 10^{-6}$ $rads^{-1}$ and $\tau_o K_n = 1.1 \times 10^{-12}$ cm^2/n. While the $\tau_o K_\gamma$ values determined by the two methods are in fairly good agreement, there is a significant difference between the two $\tau_o K_n$ products.

Hum and Barry (Ref.76) studied damage due to 100 MeV protons, gamma rays, and 2 MeV neutrons in GaAs:Si LEDs. Special care was taken to avoid injection annealing during the measurements and the $\tau_o K$ values were determined at low constant voltages using Equation 1.15 for light intensity degradation with n = 1 for linearly graded diodes. The following values were obtained

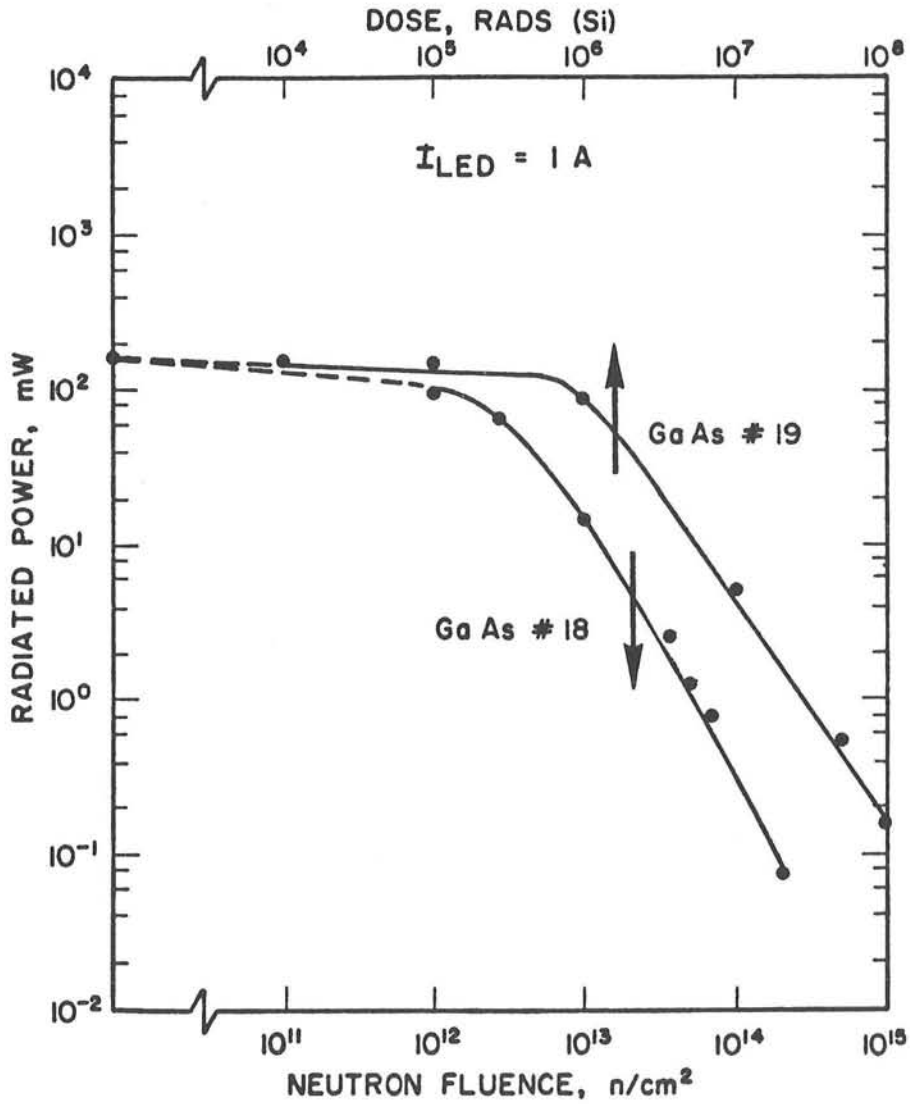

Fig. 1.13 The effect of gamma and neutron irradiation on the power output of high power amphoterically Si doped GaAs LEDs (from R. A. Polimadei, G. E. Gowins, S. Share and A. S. Epstein, Harry Diamond Labs Report No. HDL-TR-1650, Feb. 1974, available from National Tech. Information Service).

for the three types of irradiation: $\tau_o K_p = 1.2 \times 10^{-12}$ cm^2/proton, $\tau_o K_\gamma = 6.1 \times 10^{-7}$ rads^{-1}, and $\tau_o K_n = 3.6 \pm 0.8 \times 10^{-13}$ cm^2/n (the uncertainty in $\tau_o K_n$ is due to the fact that the authors give a value for K_n but not for τ_o for the LED used in the neutron irradiation experiment). The authors also measured degradation of light intensity, L, at high currents and observed that the rate was about the same as that for the low voltage degradation of L. Therefore, they concluded that it was valid to use the $\tau_o K$ values at both high and low currents.

Hum and Barry (Ref.76) also observed radiation-induced increases in total current. Measurements of radiative decay time and of lifetime by the reverse recovery method, revealed that these two parameters decreased at different rates with gamma dose. The rate of degradation of the radiative-decay time matched that of the light intensity degradation while the reverse recovery lifetime decreased more rapidly than L. The authors attributed this more rapid decrease to problems with the reverse recovery measurements due to an SCR component of the forward current whose relative magnitude depended on Φ.

In their study of gamma damage in optical isolators, Soda, et. al. (Ref.67) included the TIL-26 amphoterically Si-doped LED which made up the emitter portion of the TIL-107 optical isolator. Analysis of the constant voltage light intensity using Equation 1.15 revealed a $\tau_o K_\gamma = 7.5 \times 10^{-7}$ rads^{-1} which is between the values found by Hum and Barry (Ref.76) and Share, et. al. (Ref.64). This value is almost a factor of ten greater than the $\tau_o K_\gamma$ found for the Zn diffused device in the same study. This difference is due to the comparatively long initial lifetime in the GaAs:Si device.

We now wish to turn our attention to a series of experiments that have been conducted in our laboratory on damage effects in amphoterically Si doped GaAs LEDs. Before discussing this work we will provide additional background material on the properties of these devices.

Explanation of the properties mentioned earlier of the GaAs:Si LEDs is based on a model developed through studies of photoluminescence in n- and p-type bulk GaAs:Si material (Refs. 77-80) and of the amphoteric LEDs themselves (Refs.23,81-84). During the growth of the epitaxial p-layer of the device, a lower growth temperature is used so that Si will substitute for As and act as an acceptor rather than for Ga which produces the donor activity required for deposition of the n-layer. However, even at the lower growth temperature Si continues to substitute for Ga to a certain degree so that the end result is a compensated p-region containing 10^{18} to 10^{19} Si atoms/cm^3 but only 10^{16} to 10^{17} holes/cm^3 (Ref.23). The high concentration of Si leads to a merging of shallow donor and acceptor states with the conduction and valence bands, respectively, resulting in the creation of deep band "tails". Because the Si atoms are randomly distributed, random clustering of Si atoms occurs causing regions of unusually low or high potential which, in turn, creates localized fluctuations in the energy bands. These conditions lead to the so-called "wavy band" model shown in Figure 1.14 for both low and high current conditions. Figure 1.14 is a hybrid band diagram with energy plotted vertically against distance in the compensated p-region. Since the deepest conduction band tails occur in regions of low potential and the highest valence band states

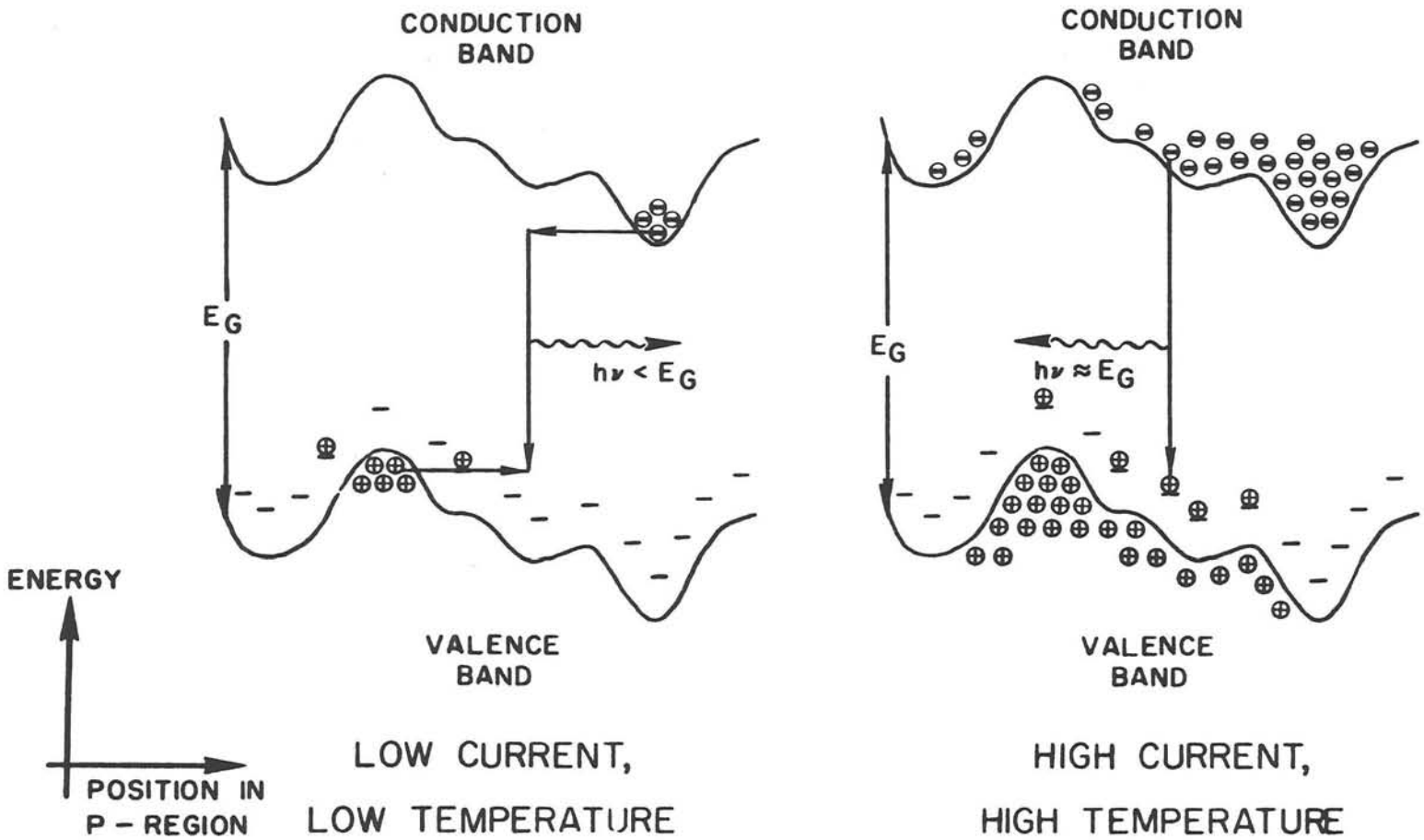

Fig. 1.14 Hybrid energy band picture of the "wavy-band" model. Fluctuations in the band structure are caused by random clustering of Si atoms. The acceptor level shown is the Si radiative recombination center.

are in regions of high potential, the deep valence and conduction band tails are, by necessity, spatially separated from each other as shown in Figure 1.14. In addition to the shallow donor and acceptor levels, Si introduces deeper levels and the radiative recombination in these devices is generally thought to occur through a Si acceptor level at E_V + 0.1 eV (Ref.81). As shown in Figure 1.14, this level is assumed to follow the fluctuations in the valence band. The "wavy band" model has been used successfully by Byer (Refs 23 and 82) and Redfield, et. al. (Ref.80) to explain the properties of amphoterically Si-doped GaAs LEDs. At low currents, as in the left hand portion of Figure 1.14, only the deepest tail states in the conduction and valence bands are filled. Since these states are spatially separated, recombination requires long-range tunneling which leads to long recombination times. In addition, recombination through the deepest states gives low energy photons. Consequently, at low currents the recombination times are long and the photon energies are small. As the current is increased, the deep tails are saturated and the electrons and holes occupy normal, delocalized band states as shown on the right in Figure 1.14. Note that an increased hole density is also shown implying the presence of double injection; a result which is confirmed by our experimental data. As shown, the increased carrier densities lead to vertical, nontunneling recombination which is characterized by shorter recombination times and higher photon energies. Taken together, the low and high current conditions in the wavy band model lead to the observed inverse dependence of radiative decay time (recombination time) on LED current and emitted photon energy.

The properties mentioned above have interesting implications for the study of radiation damage in these devices. We have studied (Ref.85) the effect of gamma irradiation on the low temperature properties of the TIL-26 amphoterically Si doped LED. A temperature of 76 K was chosen because the effect of the deep band tails is most pronounced at low temperatures where thermal excitation out of these states is minimal. In addition to measuring light intensity and total current as a function of voltage, radiative decay time was measured as a function of LED current. As one would expect for a distribution in depth of the band tails, the radiative decay cannot be described by a single exponential. Various methods can be chosen for displaying the radiative decay time. In Figure 1.15 we use the concept of an "initial lifetime," τ_i, calculated from the slope of the radiative decay curve at time, $t = 0$. The quantity, τ_i, is then a measure of the lifetime in the fastest states at any given current. Note that in agreement with the wavy band model, the curves in Figure 1.15 show that τ_i is inversely proportional to I. The most interesting result illustrated in Figure 1.15 is that the longest τ_i's seen at low I, are the least affected, in a multiplicative sense, by gamma irradiation. This is just the opposite of what we have shown to be the case with a diffusion controlled radiative current where the degradation of lifetime and light intensity is successfully described by Equations 1.9, 1.15 and 1.23. In all the work cited thus far, a longer lifetime is more sensitive to irradiation than a short lifetime. Recall, however, that in the wavy band model the long lifetimes at low currents are due to carriers trap-

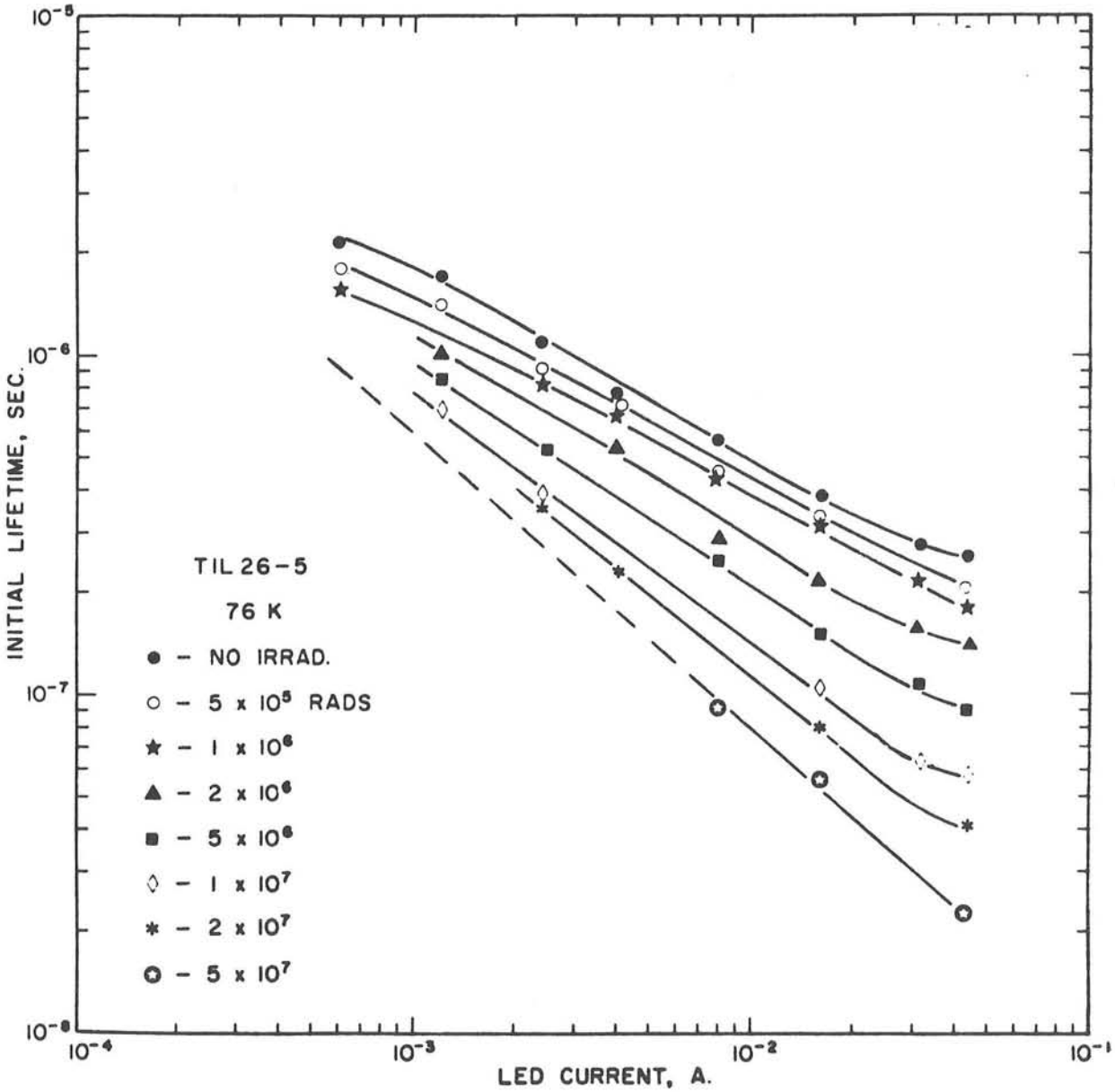

Fig. 1.15 Initial lifetime, τ_i, calculated from the slope of the radiative decay curves at t = 0 and 76K, versus diode pulse current before and after successive gamma irradiations of a typical GaAs:Si LED. Note that gamma irradiation has a greater effect, in a multiplicative sense, on the shorter lifetimes at large currents.

ped in localized, deep states and therefore, these lifetime are not associated with a diffusion length and should not be as severely affected by competition from irradiation-induced recombination centers. However, at larger currents the deep tail states become saturated and τ_i is controlled by the minority carrier lifetime which is sensitive to irradiation. In addition, if one examines the time decay at large currents, but a long time after the forward bias pulse, the results are the same as for τ_i at low currents. Consequently, the results in Figure 1.15 tend to confirm the wavy band model of the GaAs:Si LEDs. Therefore, this work then demonstrates another example of how radiation damage studies can provide information about the pre-irradiation device physics of LEDs.

Of more importance to the user are the properties of GaAs:Si LEDs at higher current levels and temperatures which correspond to the practical operating range of these devices. Byer (Refs. 23 and 82) has shown that radiative SCLC flow exists in amphoterically Si doped LEDs and that the presence of the electron space-charge cloud throughout the p-region explains the unusually wide emitting region seen in these devices. Our studies (Ref.86) of gamma irradiation effects on the room temperature, high current properties of GaAs:Si LEDs show that radiative SCLC flow is also present in our devices. Earlier, it was shown (see Equation 1.30) that the light intensity is more sensitive to irradiation for a radiative SCLC than for diffusion-controlled light output. This increased sensitivity is clearly illustrated in Fig. 1.16 which gives the

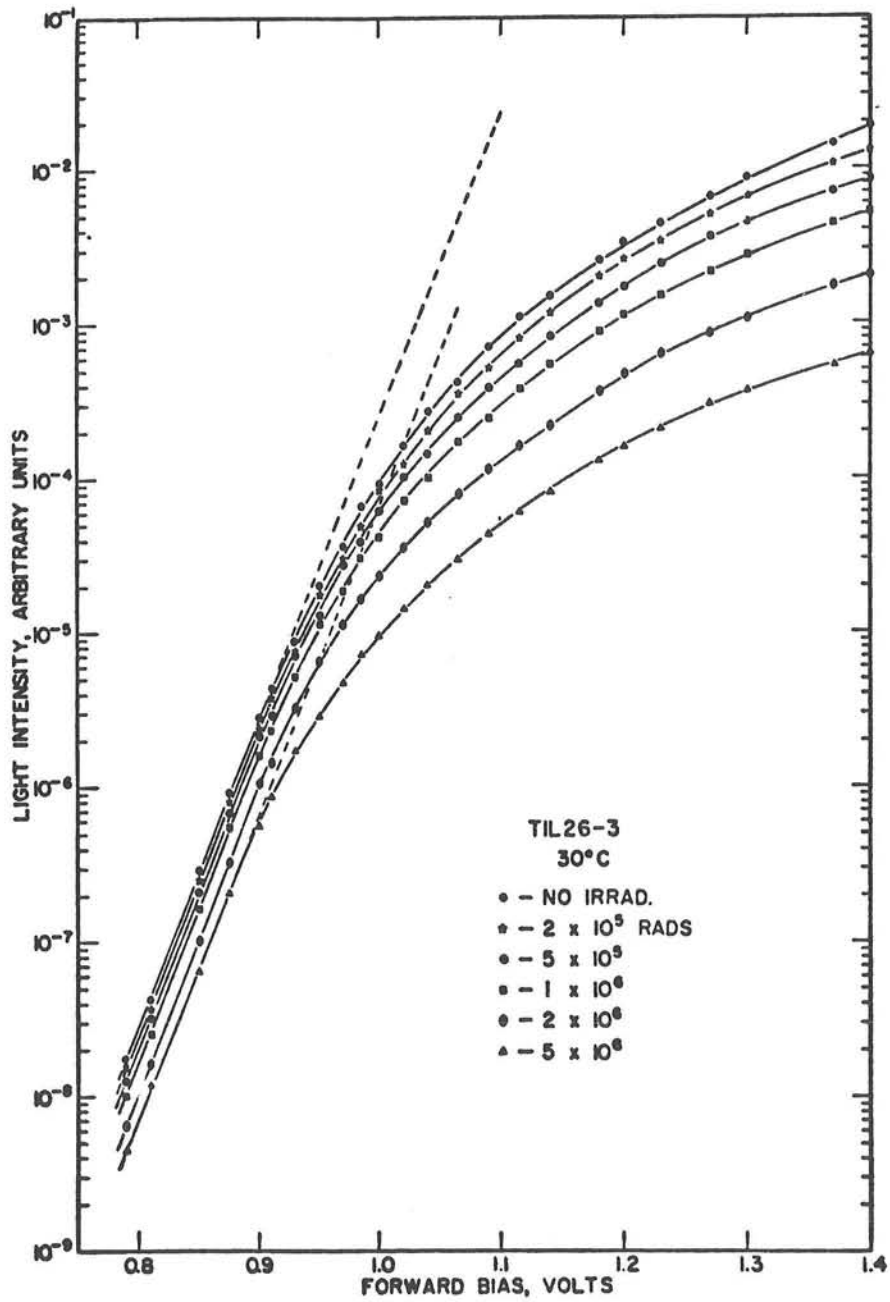

Fig. 1.16 Light intensity at 30°C as a function of forward bias prior to and following successive gamma irradiations of an amphoterically Si doped GaAs LED. Note that the light intensity deviates from the diffusion-controlled exponential behavior at relatively low voltages. The dashed lines are used to calculate junction voltage, V_j.

L-V curves taken at 30°C before and after gamma irradiation. At low voltages the light output is due to diffusion, and analysis in this range gives $\tau_o K_\gamma = 7.5 \times 10^{-7}$ rads^{-1} as indicated earlier in the study by Soda, et. al. (Ref. 67). Figure 1.16 shows that the degradation at large voltages where the devices are typically operated, is much greater. Consequently, as one would expect, the use of $\tau_o K_\gamma = 7.5 \times 10^{-7}$ rads^{-1} in Equation 1.15 gives erroneously large values of L for a given dose, Φ, at large voltages.

In order to correctly analyze the gamma degradation at large currents, the radiative current due to voltage drop, $V-V_j$, in the p-region bulk must be separated from the radiative junction current. The junction voltage, V_j, is obtained by extending the straight line, exponential portions of the L-V curves as shown by the dashed lines in Figure 1.16. The resultant $L-(V-V_j)$ curves show a definite square law behavior. Recalling that I is $\propto (V-V_j)^2$ in the SCLC region, L is then $\propto$ I as for the double injection LEDs studied by Ashley (Ref.24). The presence of a radiative SCLC current at large I is confirmed by analysis of current-voltage and light intensity-current data for our diodes, and also by analysis of L-V data taken at 76 K. Having established the existence of radiative SCLC flow one can then use Equation 1.30 to analyze the gamma induced degradation of L. Substituting Equation 1.9 in Equation 1.30 yields

$$\left(\frac{L_o}{L}\right)^{1/2} - 1 = \tau_o K_\gamma \Phi \quad , \qquad (1.35)$$

for L at constant $(V-V_j)$. Using the L - $(V-V_j)$ data it was shown that Equation 1.35 satisfactorily fits the data when $\tau_o K_\gamma = 7.8 \times 10^{-7}$ rads^{-1} in good agreement with the value of 7.5×10^{-7} rads^{-1} obtained at low voltages. Consequently, the inability to predict the degradation at high voltages by using $\tau_o K_\gamma$ in Equation 1.15 is due to a change in the mode of radiative current flow rather than to a value of $\tau_o K_\gamma$ which applies only over a limited range. The results therefore imply that one must use care in predicting degradation with damage constants; not only must one know the value of $\tau_o K_\gamma$ but also the radiative current flow mechanism.

A third experiment on GaAs:Si LEDs conducted in our laboratory concerned neutron damage in optical isolators and their components with the GaAs:Si LEDs included as one of the components (Ref. 87). Results at an LED current of 3 mA indicate $\tau_o K_n$ values of 3.8×10^{-13} cm^2/n using Equation 1.20 (total current due to SCR) with n = 1 or 9.1×10^{-13} cm^2/n using Equation 1.23 (total current due to diffusion) with n = 1. Yet a third value of $\tau_o K_n$ can be calculated assuming that a major portion of I is due to SCLC. In this case we use Equation 1.29 for constant I along with Equation 1.9 to obtain $\tau_o K_n = 1.6 \times 10^{-12}$ cm^2/n. It is interesting to note that this range of values, 3.8×10^{-13} cm^2/n to 1.6×10^{-12} cm^2/n, corresponds approximately to the range of $\tau_o K_n$'s found in the previous papers on GaAs:Si LEDs: 3.5×10^{-13} cm^2/n to 1.1×10^{-12} cm^2/n. Therefore, it may be possible to explain the variations in $\tau_o K_n$ by taking into

account the method by which it was determined, constant current (efficiency) or constant voltage, and the dominant total current flow mechanism. In our case, a current of 3 mA is still low enough so that SCR dominates, especially after neutron irradiation which creates additional SCR current. Therefore, of the three calculated values, 3.8×10^{-13} cm^2/n is the most plausible.

In this work (Ref.87), we also compared the performance of the TIL-26 with a commercially available Zn diffused LED, the TIXL-36 from Texas Instruments. The TIXL-36 has a power output of 1.2 mW at 50 mA compared to a 1 mW output power at 35 mA for the TIL-26 GaAs:Si LED. Typical results from this study are shown in Figure 1.17 where current transfer ratio (CTR), defined as the ratio of detector current to LED current, is plotted versus gamma dose at LED currents of 1 mA and 20 mA. Note that the CTR from the TIXL-36 is actually larger prior to irradiation and that the TIXL-36 is not nearly as sensitive to irradiation as the TIL-26. These results indicate that in the range of 1 mW power output, GaAs devices are commercially available which have comparable outputs to the GaAs:Si LEDs but which are much less sensitive to irradiation. Following completion of the maximum dose irradiation, 2×10^8 rads, these devices were used in a comparative forward bias annealing study. The bias induced recovery is shown on the right hand side of Figure 1.17. Note that the TIXL-36 device recovers to nearly its pre-irradiation CTR, while the TIL-26 does not respond to bias recovery. The bias annealing results provide an additional incentive for selecting the Zn diffused LED over the GaAs:Si LED.

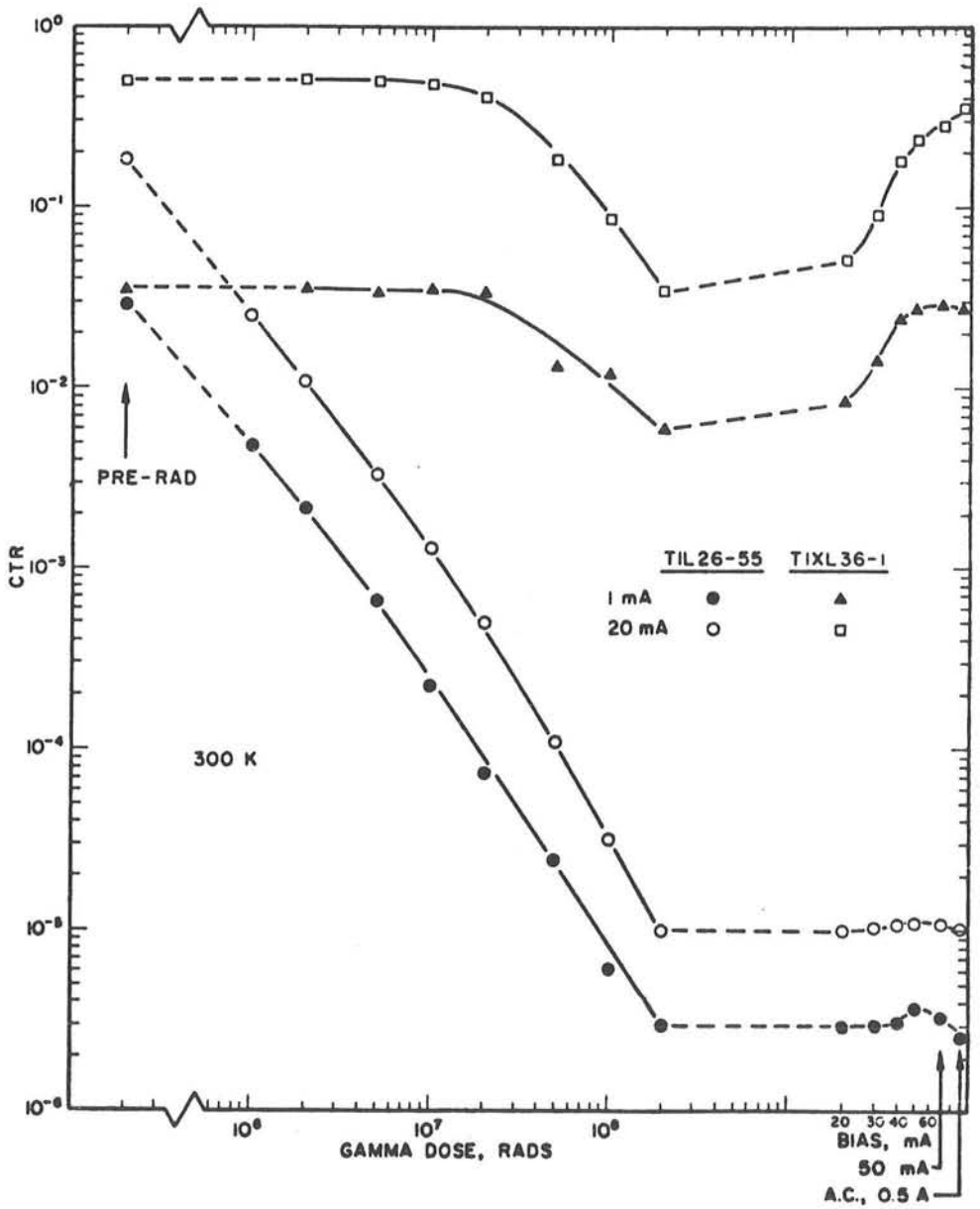

Fig. 1.17 Room temperature current transfer ratio with a phototransistor detector versus gamma dose for an amphoterically Si doped GaAs LED (TIL26) and a Zn diffused GaAs LED (TIXL36) at two LED current levels. Data on the right side are for forward bias induced recovery at the current levels shown for bias periods of 10 min. Also shown are an additional 30 min. bias at 50 mA and a pulse bias at 0.5 amps.

g. Aluminum gallium arsenide - Previous work (Refs. 58 and 66) on radiation damage in ternary LEDs such as AlGaAs and GaAsP suggests that ternary devices are inherently less sensitive to radiation than the related binary LED materials. Our recent studies (Refs. 73 and 74) on $Al_xGa_{1-x}As$ LEDs, however, indicate that addition of the ternary element is not the primary determinant for radiation sensitivity. Indeed, the most sensitive LED we have examined is an amphoterically Si doped AlGaAs LED fabricated at Bell Laboratories. The summary given below of our $Al_xGa_{1-x}As$ work (Refs. 73 and 74) indicates that while addition of the ternary can have a hardening effect, the two most important characteristics are heavy doping of the active region and high current density operation.

Investigation (Refs. 73 and 74) of neutron damage effects in the $Al_xGa_{1-x}As$ LEDs included electroluminescence (EL) spectra before and after irradiation. Representative room temperature spectra for the planar Texas Instruments (TI) $Al_xGa_{1-x}As$ LEDs are shown in Figure 1.18 while EL spectra for a typical etched well, high radiance Plessey $Al_{.05}Ga_{.95}As$ LED are shown in Figure 1.19. In addition to spectra for various alloys, typical attenuation spectra are shown in Figure 1.18 for a glass optical fiber. These latter curves convey two important points which will be discussed in much greater detail in a later chapter. First, in general, the radiation-induced attenuation in fibers is less at longer wavelengths, and second, the intrinsic attenuation in most glass fibers has a "window" near 0.83 μm. These factors must be kept in mind when examining the effects in LEDs. With

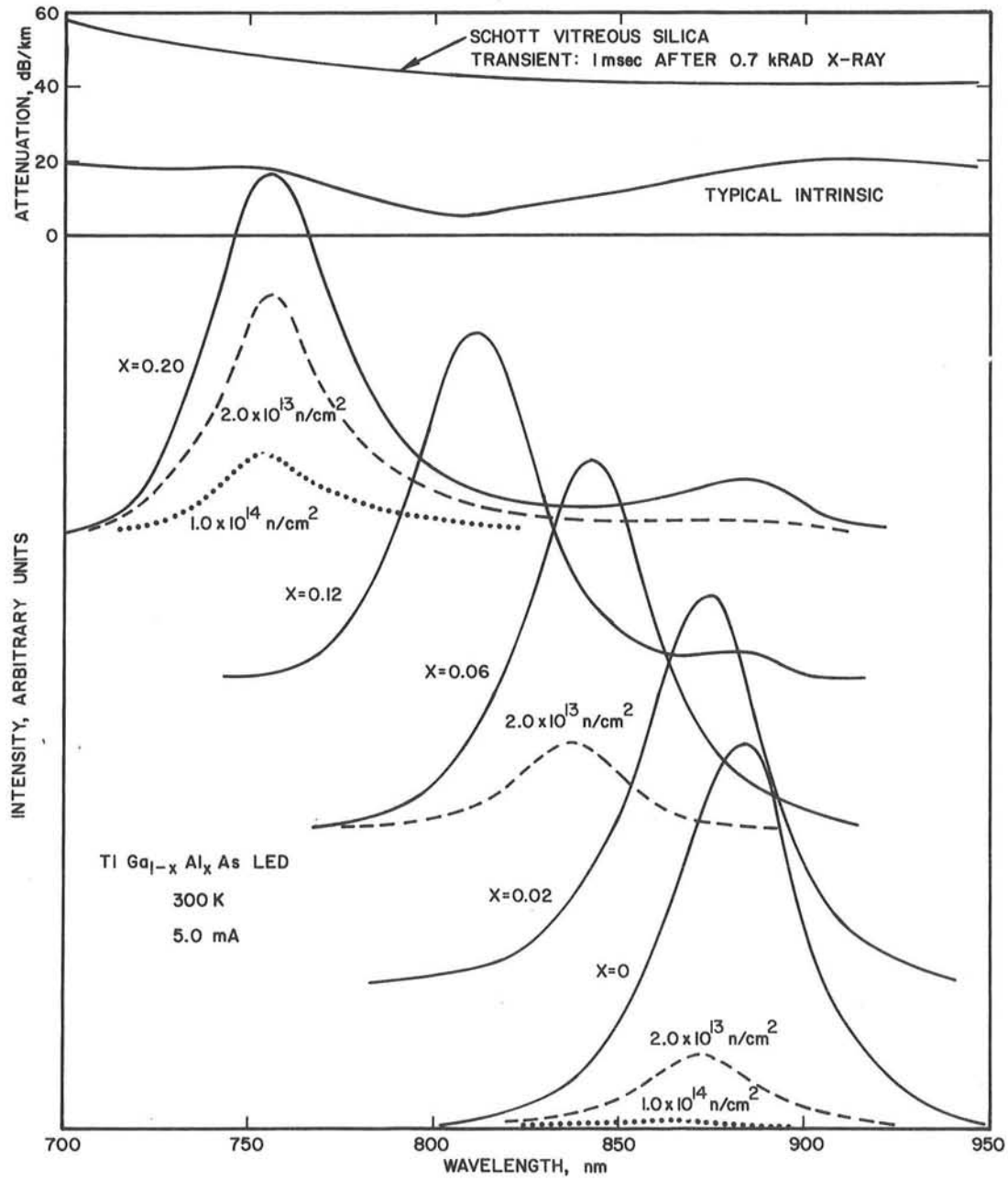

Fig. 1.18 Electroluminescence spectra for a set of $A\ell_xGa_{1-x}As$ planar LEDs from Texas Instruments at an operating current of 5 mA. Also shown are spectra after irradiation, and typical intrinsic and induced attenuation spectra for a pure silica core optical fiber.

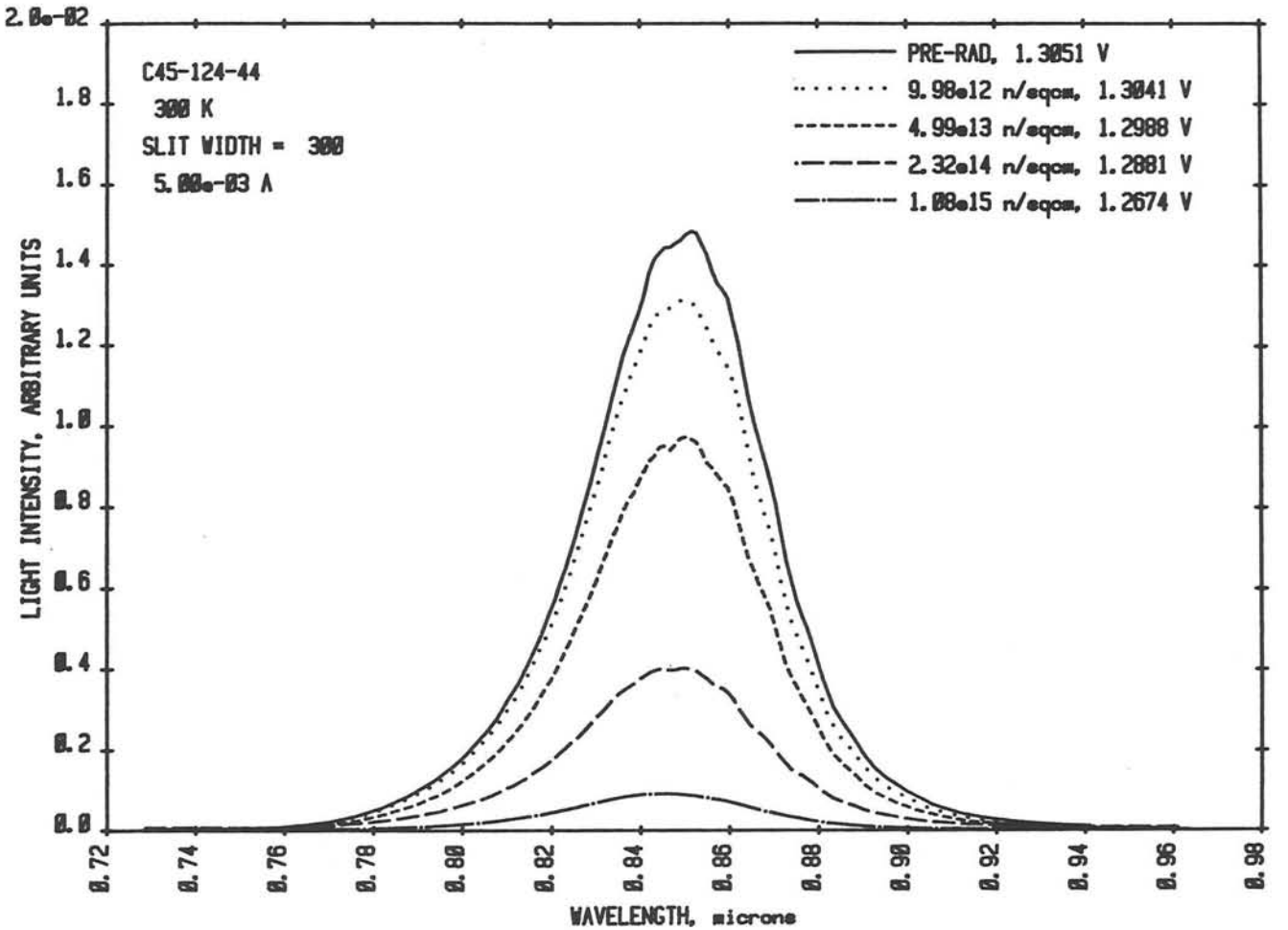

Fig. 1.19 Neutron-induced degradation of the room temperature electroluminescence spectra from a pigtailed Plessey GaAℓAs LED at a constant current of 5.0 mA. Note the absence of the long wavelength band found in earlier LEDS, and the lack of any peak shift with fluence.

regard to wavelength selection, it is important to note that neutron irradiation does not significantly affect either the spectral shape or the peak location of the spectra in Figures 1.18 or 1.19. With the exception of the 20% Al LEDs, the planar TI LEDs for all other x values are equally sensitive to irradiation as shown by the dashed and dotted curves in Figure 1.18. In addition, comparison of these data with Figure 1.19 demonstrates that the Plessey LEDs are much less sensitive for an equal LED operating current of 5.0 mA.

One reason for the reduced sensitivity of the Plessey LEDs is illustrated in Figure 1.20 which shows the current density-voltage characteristics of representative TI and PL AlGaAs LEDs. Because the area of the high radiance PL devices is 100 times less than that for the TI LEDs, typical operating currents correspond to much higher current densities in the Plessey LEDs. As shown in Figure 1.20, the neutron added current is negligible for the PL devices over much of the voltage range. In contrast, even at the maximum permissible operating current of the TI LEDs, there is a significant shift to lower voltages after about $5 \times 10^{14} n/cm^2$. The lack of neutron added current in high radiance LEDs is a particularly significant characteristic of these LEDs with regard to radiation hardness.

To further investigate the effect of high current density operation on LED radiation hardness, we have recently measured the light output degradation in four types of LEDs which differ only in structure. All four are AlGaAs heterostructure devices emitting near 0.82 μm. They were obtained from the same supplier, M/A-COM Laser Diode, Inc. The normalized light output degradation at

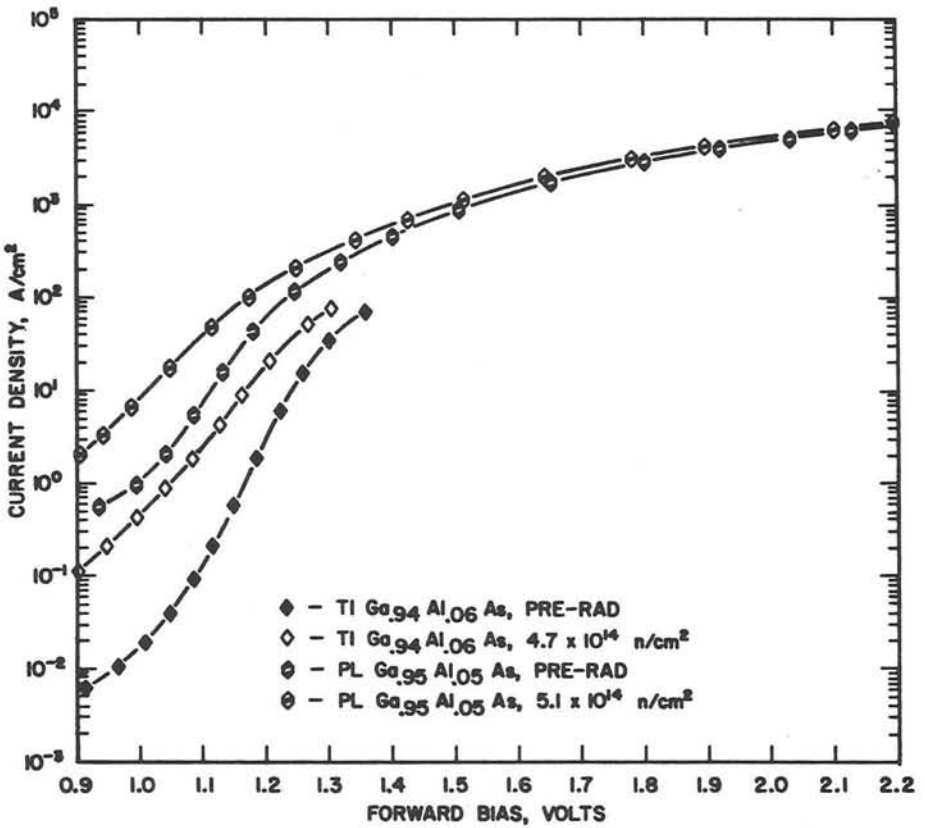

Fig. 1.20 Pre- and post- irradiation room temperature current density - voltage curves for a bare, high radiance Plessey GaAℓAs LED (P65B) and a planar TI GaAℓAs LED (SLH-5-5). Note the lack of excess current at large current densities.

various constant current densities near the corresponding maximum operating currents is shown in Figure 1.21. The structural differences are as follows: the IRE-140 is a relatively large area surface emitting LED, the IRE-151 is an edge emitting device with an area somewhat smaller than the IRE-140, the IRE-160 is an etched well, high radiance LED with a small area, and the IRE-103 is a high radiance edge emitting LED. The important result to note is that the two high radiance LEDs operating well in excess of 1000 A/cm^2 are much less sensitive to irradiation than the other two LEDs. This is true in spite of the fact that at low constant current or voltage the degradation rate is similar in all four LED types.

A similar type of contrast is shown in Figure 1.22 in which we compare the light output degradation as a function of current for the same Plessey and TI devices in Figure 1.20. The degradation is much greater at constant current in the large area TI LED than it is at constant maximum current in the PL device.

These results are to be compared with constant voltage operation wherein the neutron-added non-radiative current can be accommodated by the voltage. Consequently, the degradation rate is less than at constant current for those LEDs which show appreciable neutron-induced excess currents. An example of this behavior is shown in Figure 1.23 for the same TI and PL LEDs as in Figures 1.22 and 1.20. For the high radiance Plessey LED (P65B-13) the degradation at large constant voltage is the same as that at large constant current shown in Figure 1.22. However, the constant voltage light degradation of the planar TI device (SLH5-5), which is not

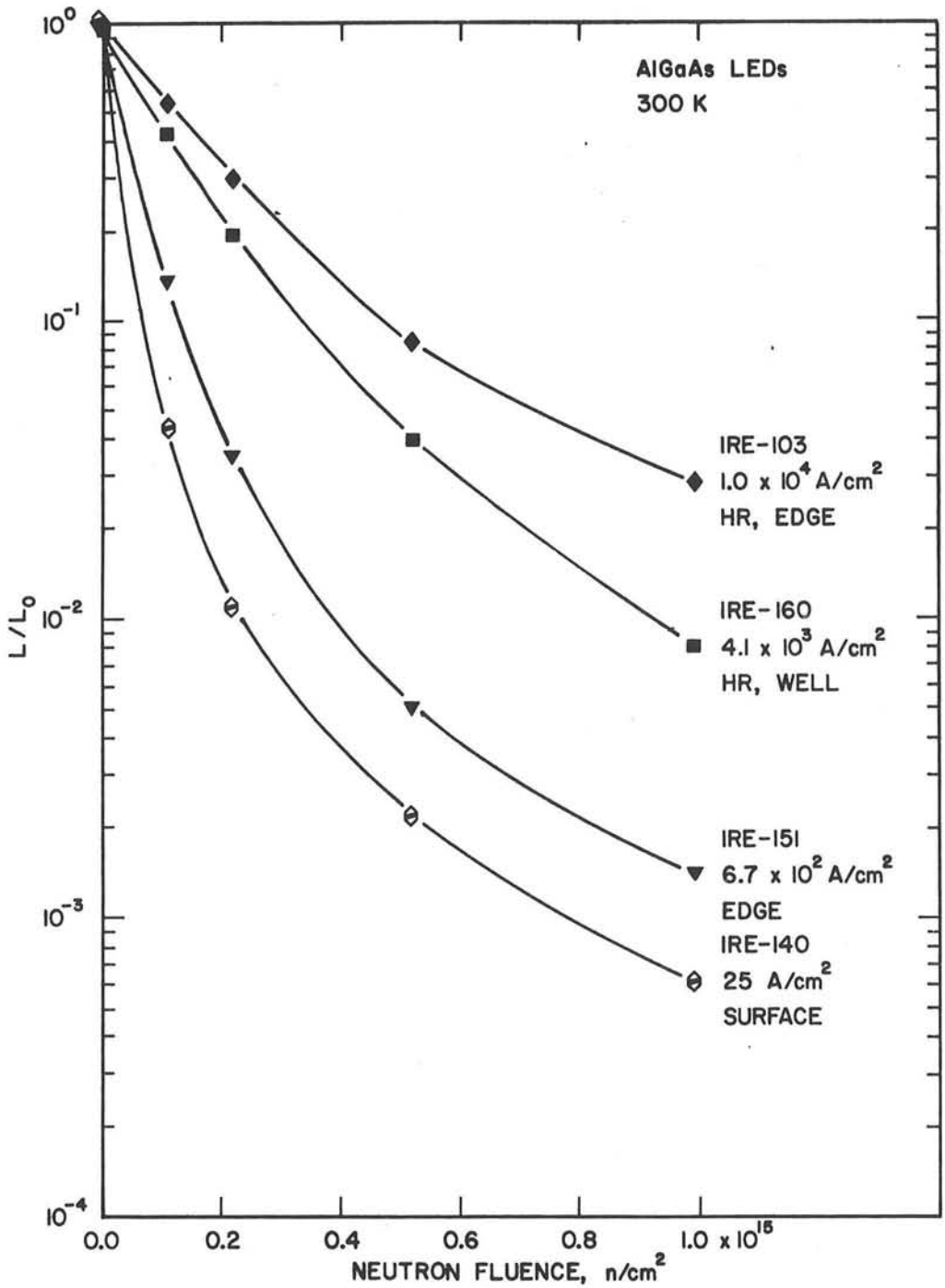

Fig. 1.21 Normalized light output degradation in four types of heterostructure LEDs all with the same Aℓ content and the same peak wavelength (.82 μm). All LEDs were from the same supplier. The following terms are used: HR-high radiance, Edge-edge emitter, Well-etched well emitter, Surface: surface emitter.

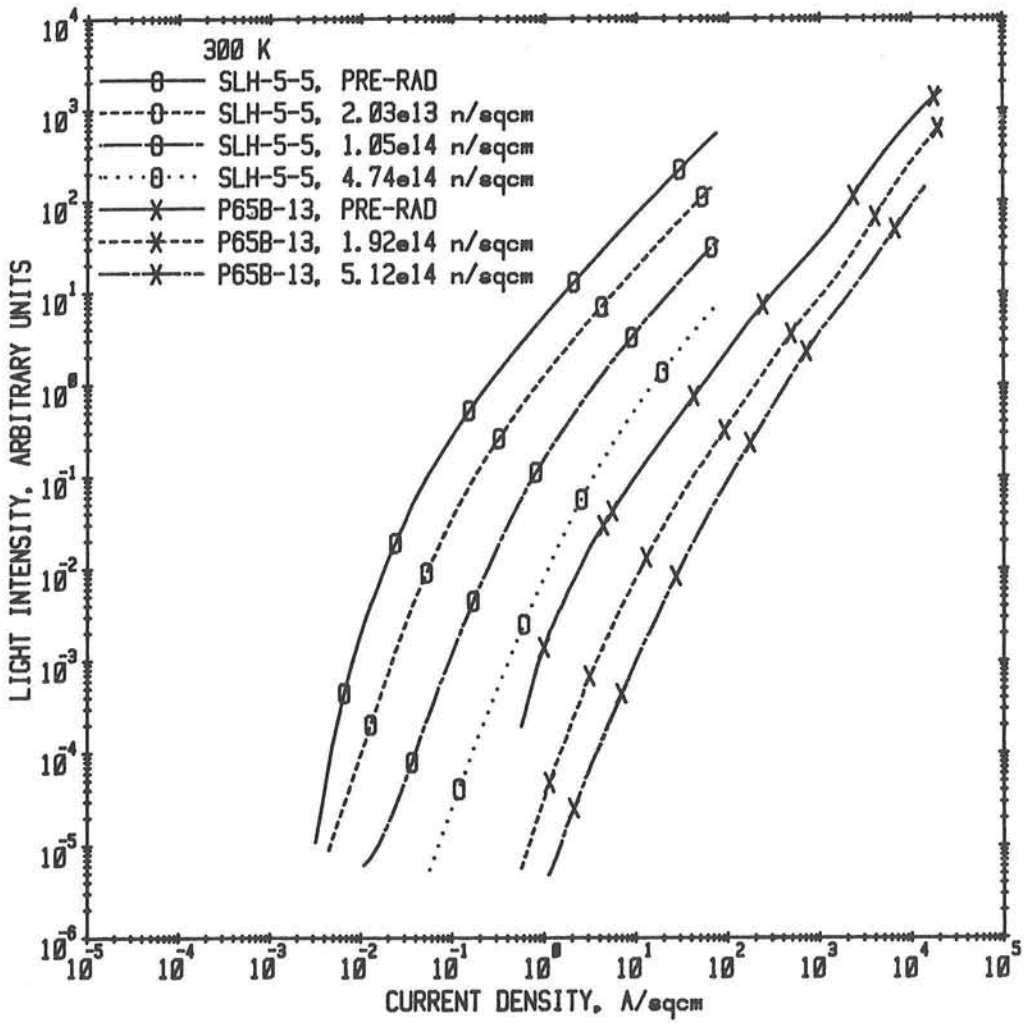

Fig. 1.22 Neutron-induced reduction in total light output as a function of current density for two GaAlAs LEDs: SLH-5 is a planar TI device, and P65B is a high radiance Plessey LED. Note that the Plessey device degrades significantly less than the TI LED.

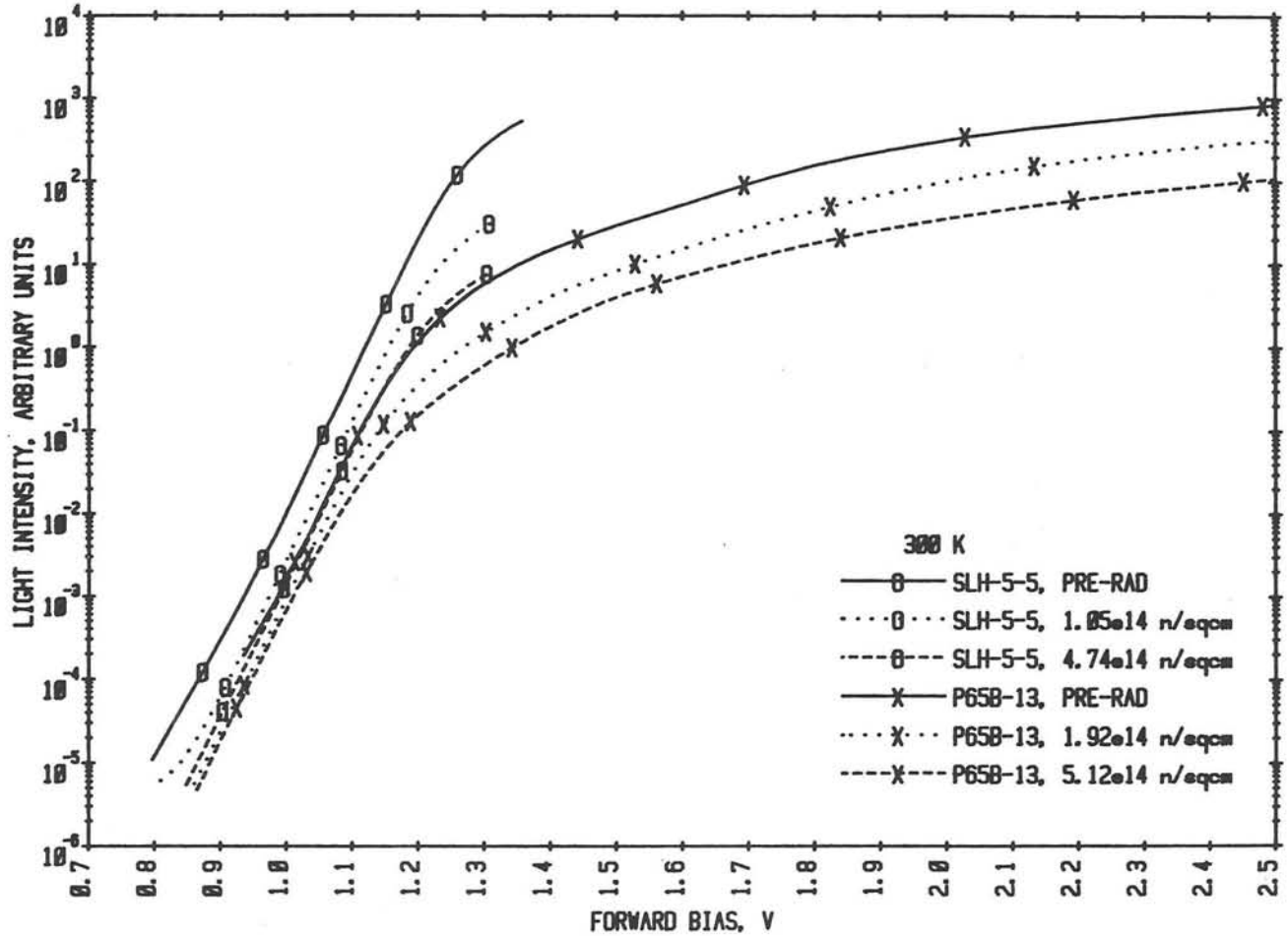

Fig. 1.23 A comparison of neutron-induced degradation of total room temperature light output as a function of voltage in a bare Plessey GaAlAs LED (P65B) and a planar TI GaAlAs LED (SLH-5-5). Note that the Plessey device degrades less than the TI LED.

significantly larger than that for P65B-13, is significantly less than the constant current degradation shown in Figure 1.22 for the SLH5-5. As we have seen through repeated applications by a variety of authors of the equations given herein, light output degradation at constant voltage minimizes the effect of radiation-induced excess current and emphasizes the reduction in minority carrier lifetime through competing recombination at radiation-induced centers in the active region. We have also shown that this type of radiation sensitivity can be minimized without sacrificing initial output power by heavily doping the active region in order to reduce τ_R. This effect is illustrated for the TI and PL LEDs in Figure 1.24 which gives a variety of constant voltage degradation curves. Returning for the moment to GaAs, recall that as shown in Figure 1.12, the Plessey GaAs LEDs were less sensitive to irradiation at large constant currents compared with the planar TI devices. However as shown in Figure 1.24 quite the opposite is true at constant voltage. In fact, the PL GaAs LED degrades more rapidly than any of the other devices in Figure 1.24. The reason for this is that this LED is more lightly doped ($\sim 5 \times 10^{17} cm^{-3}$) than any of the others. The same effect can be seen by comparing the two TI $Al_{.06}Ga_{.94}As$ LED curves. The LED designated "heavy doping" has a five times higher Ge doping level ($5 \times 10^{18} cm^{-3}$) than the other LED. Note that the more heavily doped device does not degrade nearly as rapidly. In addition, the TI (heavy doping) LED is very similar in its behavior to the Plessey $Al_{.05}Ga_{.95}As$ LED which has approximately the same doping level but which is a

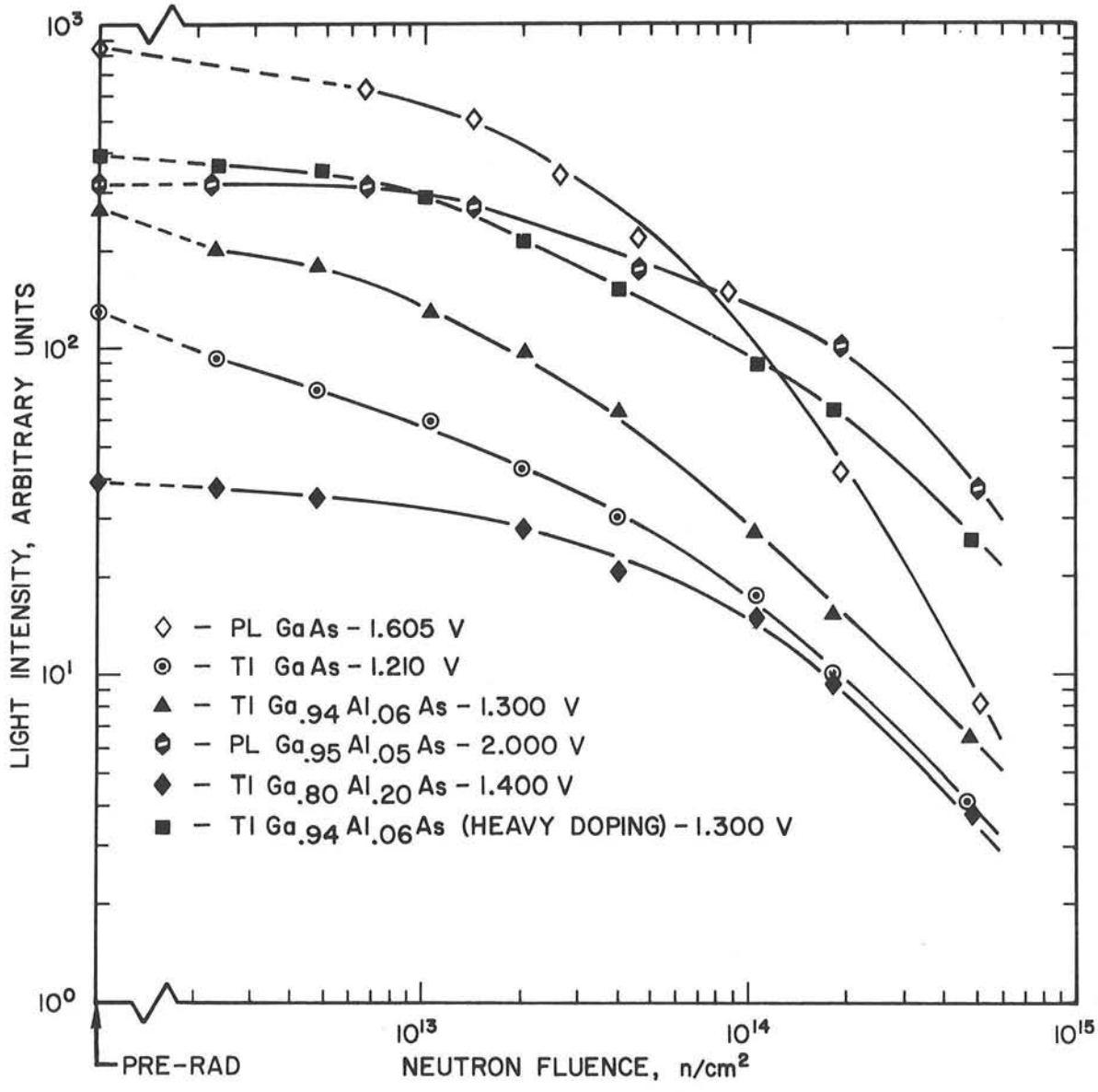

Fig. 1.24 Constant voltage light output degradation curves for various AℓGaAs and GaAs LEDs. PL (Plessey) LEDs are high radiance while TI (Texas Instruments) LEDs are planar devices.

high radiance device. Lastly, we show in Fig. 1.24 a degradation curve for a 20% Al containing TI LED. As indicated in this figure and also in Figure 1.18, this LED has a comparatively low degradation rate similar to those for the heavily doped TI 6% Al LED and the PL 5% Al device. The important difference, however, is that the curve for the 20% Al LED is displaced downward to light intensities an order of magnitude less. Thus, while the addition of a large fraction of Al hardens the LED, it is of no practical value because of the low initial light output of these 20% Al LEDs.

The hardening techniques of heavy doping and high current density operation are further illustrated and compared in Figure 1.25 for 5% Al PL and 6% Al TI LEDs. Note that for constant current operation at 50 mA as one would expect, the more heavily doped TI device degrades less than the other TI LED. In addition, the heavily doped TI LED degrades at about the same rate as the PL LED when the PL LED is operated at the same current density of 75.6 A/cm^2. However, because the Plessey LED is a high radiance device, 75.6 A/cm^2 corresponds to a very low operating current of 0.54 mA. When this LED is operated in its practical operating range of 50 mA to 150 mA its degradation rate is much less due to the lack of neutron-induced excess currents.

As part of our radiation effects study (Ref.74) of Plessey GaAs and AlGaAs LEDs for the Avionics Laboratory, we also examined neutron induced degradation at temperatures other than room temperature for irradiations all at room temperature. Typical data for a 5% Al LED are shown in Figure 1.26 for room temperature

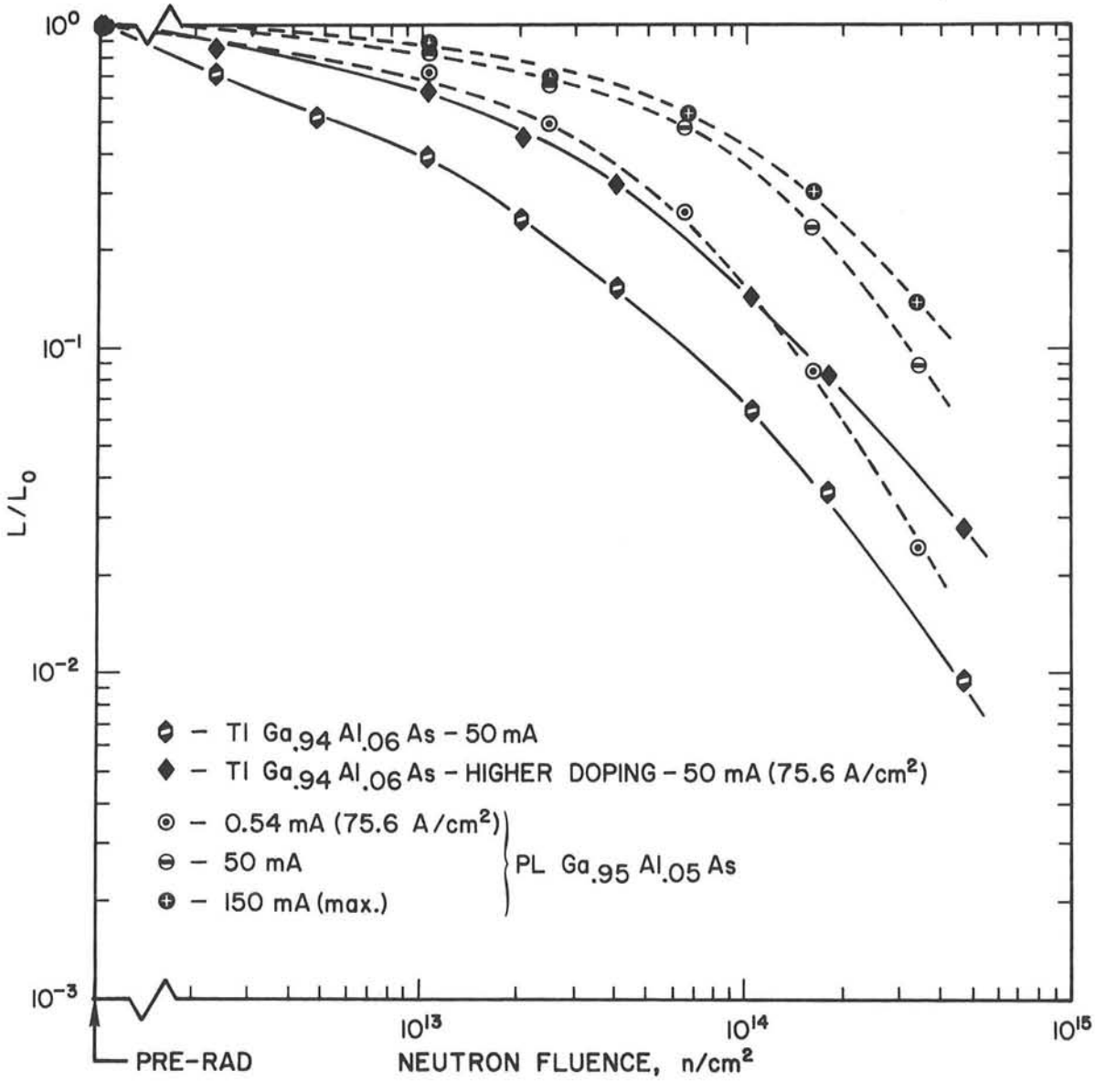

Fig. 1.25 Normalized constant current light output degradation curves for TI (Texas Instruments) planar LEDs and PL (Plessey) high radiance LEDs. Note the reduced degradation at high currents for the PL LEDs.

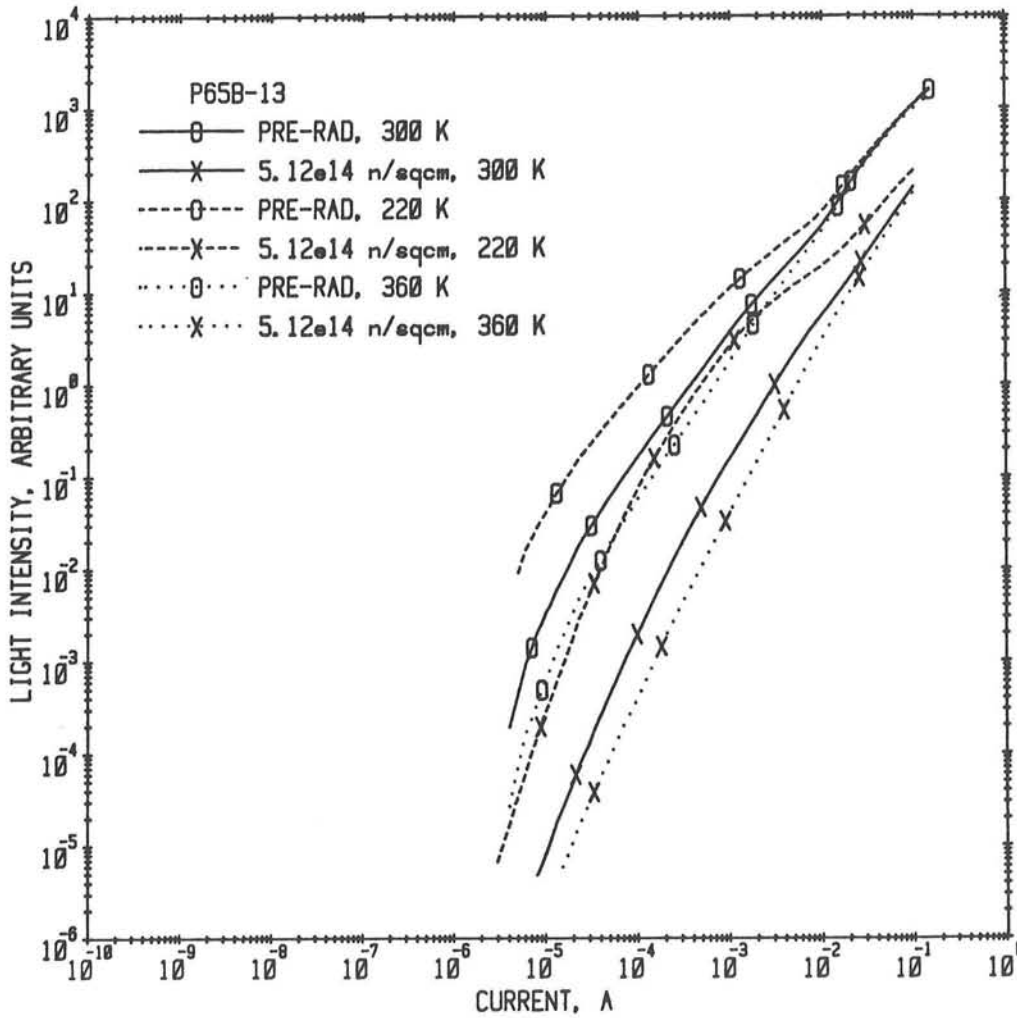

Fig. 1.26 Reduction in light output as a function of current at three different temperatures for a bare Plessey GaAlAs LED irradiated to a fluence of 5.1 x 10^{14} n/cm^2. Degradation is somewhat greater at higher temperatures.

(300 K) and also 220 K and 360 K. For the Al containing LEDs there is less degradation at lower temperatures although this is not a large effect. The temperature dependence of the degradation is even less in the GaAs LEDs.

Lastly, we note that gamma irradiation-induced light output degradation was also studied in the set of planar, TI $Al_{1-x}Ga_xAs$ LEDs. Generally, these devices were relatively insensitive to gamma irradiation with no significant effects occurring until the dose exceeded 10^7 rads. The $\tau_o K_\gamma$ values varied between 2.1×10^{-9} $rads^{-1}$ and 2.5×10^{-8} $rads^{-1}$. These values are given in Tables I and II.

h. Long wavelength emitting LEDs - As will be shown in a later chapter, both the intrinsic properties of optical fibers and their radiation response characteristics provide considerable motivation for operating a fiber optic link at wavelengths in excess of 1.0 μm as opposed to the region near 0.82 μm. Consequently, it is important to study the effects of radiation on LEDs which operate above 1.0 μm. This is especially true for wavelengths near 1.3 μm which is rapidly becoming a popular operating point for state-of-the-art fiber optic systems. In this section we briefly summarize our radiation effects studies (Ref. 88) of InGaAs LEDs and InGaAsP LEDs.

The 1.06 μm emitting InGaAs LEDs subjected to both neutron and gamma irradiations were obtained from RCA (C30116/F) where they were fabricated on GaAs substrates using vapor phase epitaxy. The effect of neutron irradiation on the light output as a function of

LED current is shown in Figure 1.27. These curves have a slope of 2.0 over most of the range as one would expect for a diffusion controlled radiative current in the presence of an SCR controlled total current. Based on these data, a $\tau_o K_n$ value of 1.0×10^{-14} cm^2/n was calculated. This value is relatively small and indicates that these LEDs are insensitive to neutron irradiation. One reason for this is that these LEDs exhibit a minimal neutron-induced increase in total current even at 9×10^{14} n/cm^2. This is also true for the gamma exposures for which the maximum dose of 5×10^8 rads had no effect on the I-V characteristic. The $\tau_o K_\gamma$ value derived from light output degradation at constant current was $1.7 \pm 1 \times 10^{-9}$ $rads^{-1}$, also quite a small value.

As shown in Figure 1.28, the gamma induced degradation was susceptible to forward bias induced recovery. A forward current of 50 mA applied for 45 min at room temperature brought the light intensity back to within a factor of 2 of the pre-irradiation output.

The Plessey 1.3 μm emitting InGaAsP high radiance LEDs are also relatively insensitive to neutron irradiation as demonstrated by the data in Figure 1.29. These light intensity-current curves indicate that the degradation rate depends significantly on current and is less at higher current levels as one might expect for a high radiance device. At the maximum current of 100 mA the $\tau_o K_n$ value is 1.0×10^{-14} cm^2/n.

Neutron damage effects in InGaAs LEDs emitting at 1.06 μm were also studied by Arimura and Caldwell (Ref. 89) as part of an overall development program for radiation hardened fiber optic links. The Plessey GAL-103 LEDs examined were also found to be relatively

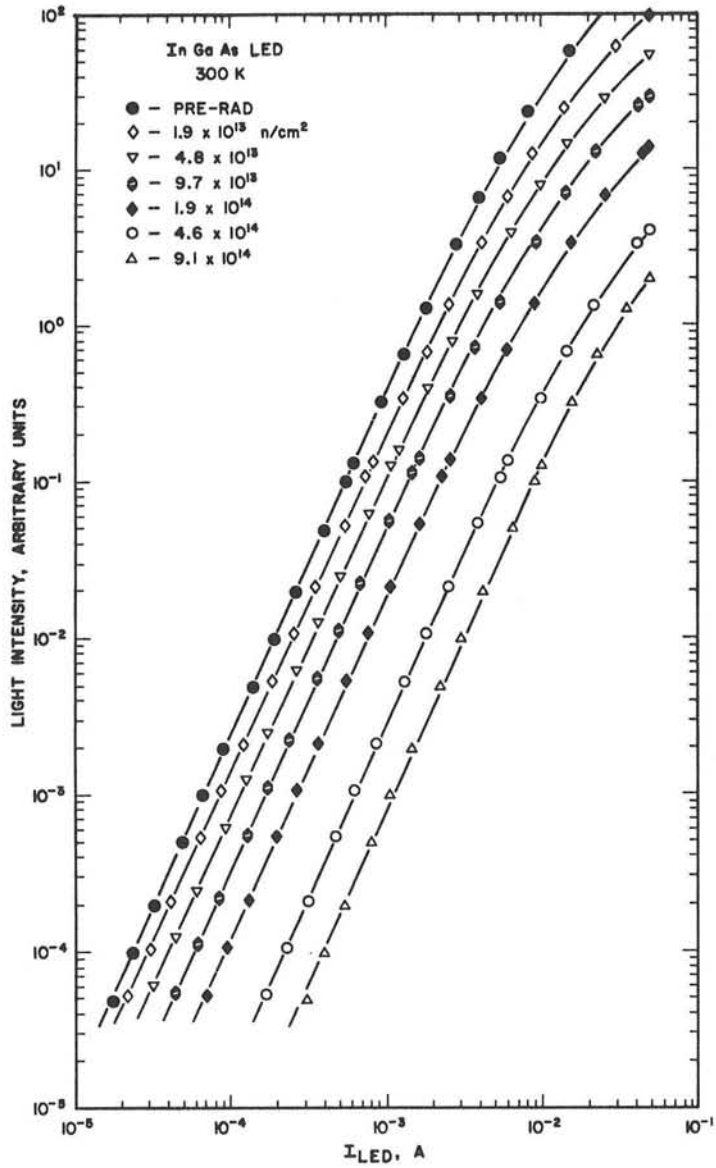

Fig. 1.27 Total light output at room temperature from a typical InGaAs LED as a function of LED current prior to and following successive neutron irradiations. Note that the curves remain parallel with a slope near 2 as irradiation proceeds.

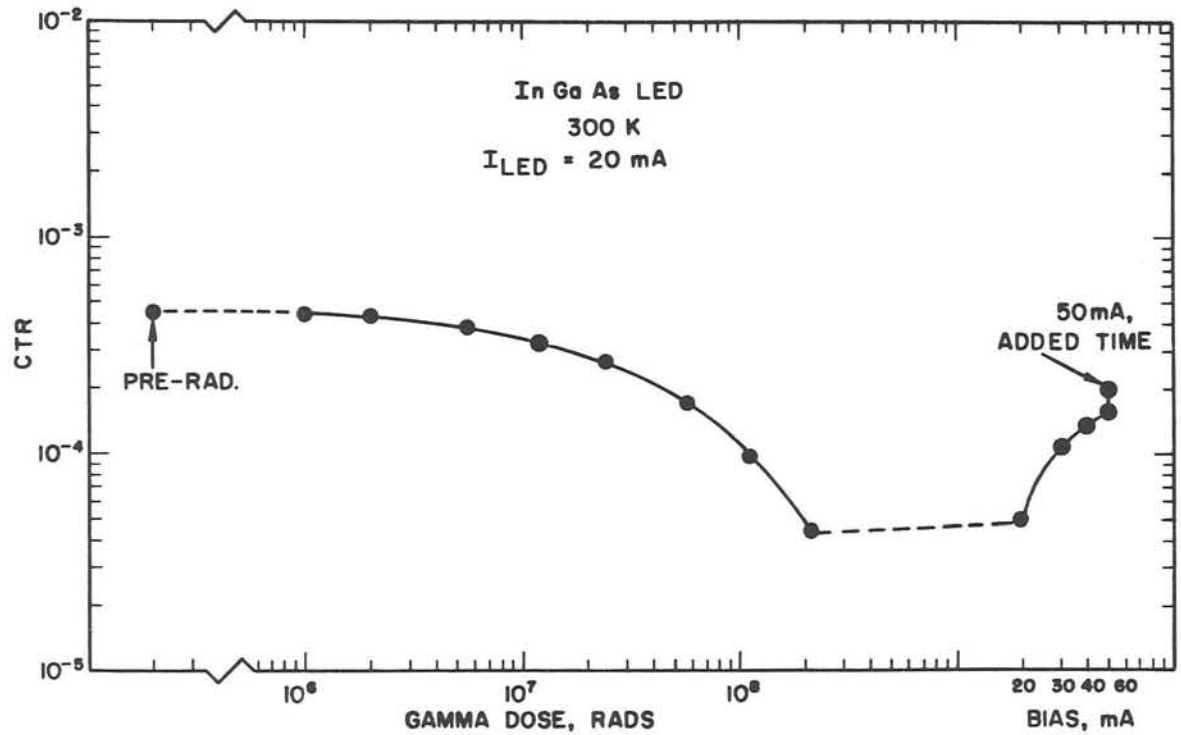

Fig. 1.28 Current-transfer ratio at I_{LED}=20 mA as a function of γ dose for an isolator containing an irradiated InGaAs LED. Shown at the right are the effects of bias annealing. Forward currents were applied for 15-min periods with a second 50-mA bias of 30 min.

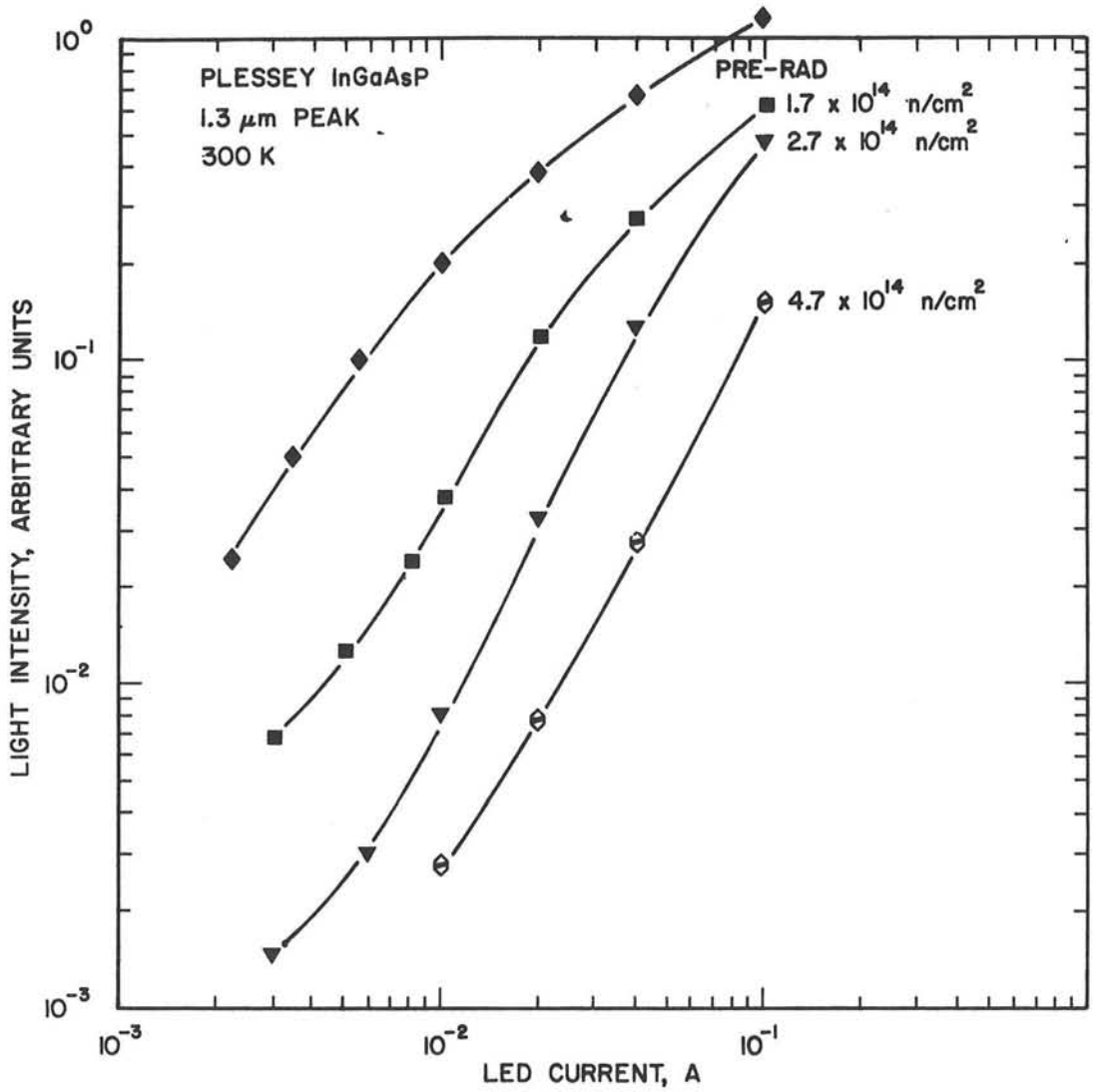

Fig. 1.29 Light intensity-LED current characteristics as a function of neutron fluence for Plessey high radiance InGaAsP LEDs emitting at 1.3 μm. Note that the degradation rate is less at higher currents.

insensitive to neutron irradiation. The authors found no degradation in power output up to fluences of 1×10^{14} n/cm^2.

The data on the InGaAs and InGaAsP LEDs indicate that these devices are relatively insensitive to irradiation. Consequently, long wavelength fiber optic link operation in a radiation environment should not be limited by radiation sensitivity of the light sources.

3. TRANSIENT RADIATION EFFECTS

Essentially no work on transient radiation effects in LEDs has been reported in the literature. Fortunately, work in our laboratory (Ref. 74) indicates that transient effects should not pose a severe problem for LED applications. In a study of the sensitivity of LEDs to x-ray pulses a variety of LEDs were exposed to 50 ns wide x-ray pulses from a Febetron x-ray machine in the dose rate range, 10^7 to 10^{10} rads/s. Light from the LEDs was detected by passing it through a shielded fiber to a Si PIN photodiode with a response time of a few ns. The LEDs were exposed in the passive state, and while being operated either in the DC mode or in the pulse mode with a pulse width large compared to the x-ray pulse. The results of these measurements indicated that the only transient effect of the x-rays was a simple superposition of a volume photoluminescence effect. In small area, thin LEDs no x-ray generated light output was observed because of the small volume of semiconductor material in the LED. In addition, when the x-ray pulse arrived during LED operation, either DC or long pulse, no effects on LED output were observed.

For large area, thick LEDs a light pulse from the LED was detected during the x-ray pulse due to simple excess carrier generation by the x-rays with subsequent radiative recombination. An example of an x-ray induced light pulse from a large area device is shown in the oscilliscope traces in Figure 1.30 for a Monsanto ME-5 GaAs LED. This emitter has an area of 2.3×10^{-2} cm^2 (60 x 60 mils) which is roughly a factor of 10 greater than other typical GaAs LEDs mentioned in this report (TIL-26, TIXL-36). The middle trace is the photodiode response to a 1.8 μs wide LED current pulse of 40 mA. Although nearly all the fiber was shielded, some fiber luminescence was detected as shown by the bottom trace taken at a higher dose rate of approximately 10^9 rads/s. Clearly, however, there is very little fiber luminescence contributing to the light pulses shown in the upper trace for a lower dose rate of 5.7×10^8 rads/s. Thus, this x-ray generated light pulse whose shape is the same as the x-ray pulse, is due to radiative recombination in the GaAs. The shape and magnitude of the x-ray generated light pulse were independent of the LED operating characteristics present at the time of the pulse. For example, the light pulse shown in Figure 1.30 was the same size whether or not the LED was receiving current. In addition, no long tails were observed following the x-ray generated light pulse.

The small tail on the x-ray generated light pulse shown in Figure 1.30 was believed to be associated with circuit time constants (note the tail on the 1.8 μs wide light pulse) due to the fact that the photodiode load resistor was placed some distance away from the detector itself. Here, it is important to note that

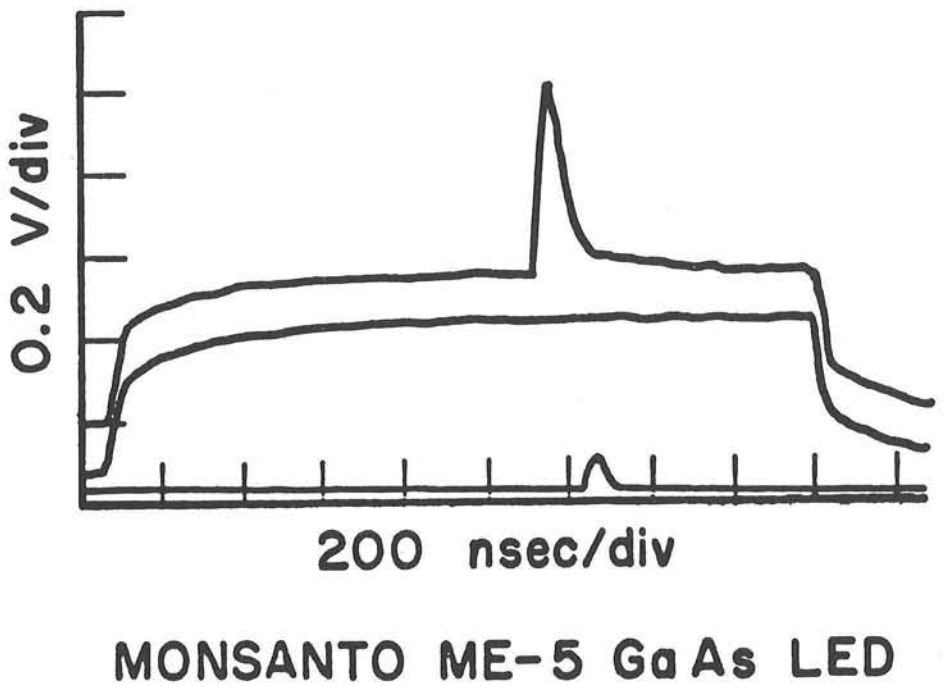

Fig. 1.30 Febetron x-ray-induced light emission from a large volume GaAs LED. Top trace: LED and fiber exposed to a 30 nsec wide x-ray pulse at a dose rate of 5.7×10^8 Rads/sec. Middle trace: Light output of LED with no x-ray pulse. Bottom trace: LED blocked with a dose rate of approximately 1×10^9 Rads/sec.

amphoterically Si doped LEDs were included in this study. One might expect the x-ray-generated light pulse to last roughly as long as the radiative decay time in these LEDs; that is, a few tenths of a μs. Lastly, even for dose rates approaching 10^{10} rads/s the magnitude of the x-ray-generated light pulse in typical, smaller volume LEDs was negligible compared to the light output at typical operating currents. We, therefore, conclude that ionization induced effects are unimportant in most LEDs, especially when compared to possible problems associated with exposure of fibers and detectors to transient ionizing radiation.

More recently (Ref. 74), we have examined the effects of pulsed neutron exposure on two relatively sensitive LEDS: an amphoterically Si doped GaAs device (TIL-26) and an amphoterically Si doped AlGaAs LED from Bell Labs. In addition, two relatively resistant LEDs were exposed: a Zn diffused, dome shaped GaAs LED (TIXL-35) and the Plessey AlGaAs LEDs (like P65B-13) referred to earlier as part of the Avionics study. The LEDs were placed near the SPR II reactor and shielded fibers were used to transfer the light signal to a Si APD in a nearby instrument building. Just prior to the neutron pulse the LED was turned on at a typical operating current level and then the LED current pulse was terminated well after the neutron pulse was over. Some difficulty was encountered with spurious pulses at the APD during the neutron pulse. Repeated experiments indicated that these pulses were not due to direct interaction between the neutrons and the LED. Rather, they were the result of electrical noise (pulses

were sometimes seen on the LED current monitoring trace), fiber luminescence, and interaction of gamma rays directly with the APD (pulse size was reduced by lead shielding around the APD).

Typical results for the two sensitive LED types and also the TIXL-35 are shown in Figure 1.31. Figure 1.31a graphically demonstrates the radiation sensitivity of the TIL-26 when exposed to a neutron pulse for which $\phi = 5 \times 10^{12}$ n/cm^2. Note that the light output near the end of the current pulse is nearly zero in contrast with the pre-shot signal of approximately 40 mV. Similar data are shown in Figure 1.31b for the Bell Labs AlGaAs LED which is also quite sensitive. This is not the case, however, for the relatively radiation hard TIXL-35 GaAs LED shown in Figure 1.31c. Note that a pulse fluence of 4.4×10^{13} n/cm^2 is required to produce a 60% reduction in output, a fluence value nearly ten times that for the TIL-26.

Additional results of pulsed neutron measurements are shown in Figure 1.32 for the bare Plessey AlGaAs LED P65B-13 and a Plessey pigtailed AlGaAs device. In both cases the decrease in output after the pulse is relatively small. As one might expect there is a positive signal due to luminescence in the fiber pigtail.

All of the pulsed neutron results have two features in common. First, there are no transient effects occurring within the LED during and immediately after the neutron pulse. The LEDs operate in normal fashion through the pulse and there is no increase in output immediately after the pulse which would be characteristic of transient damage recovery. Second, measurements several minutes after the pulse indicate that there is also no slow component of recovery.

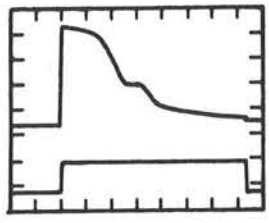

a) TIL-26 exposed to neutron pulse of $5x10^{12}n/cm^2$. Vertical deflection is 10mV/div. on upper trace and 2V/div. on lower trace. LED current = 100mA.

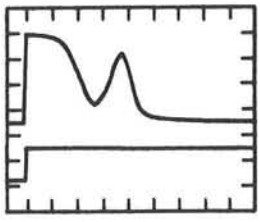

b) Bell Labs GaAℓAs: Si LED exposed to $4.3x10^{13}n/cm^2$. Vertical deflection is 5mV/div. on upper trace and 2V/div. on lower trace. LED current = 50mA.

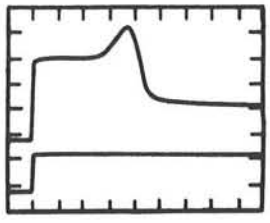

c) TIXL-35 GaAs: Zn with a neutron burst of $4.4x10^{13}n/cm^2$. Vertical deflection is 5mV/div. on upper trace and 5V/div. on lower trace. LED current = 150mA.

Fig. 1.31 Neutron pulse exposure of three different LEDs: TIL26 is a highly sensitive amphoterically Si doped GaAs device; the GaAlAs LED in the center is also amphoterically Si doped and very sensitive. In the bottom picture, the TIXL-35 is a Zn diffused, dome shaped GaAs emitter whose hardness is relatively good. The peaks in the pictures are artifacts due to electrical noise and gamma rays. The upper trace is the light signal while the lower trace is the LED current. Sweep time for all three pictures is 50μs per division.

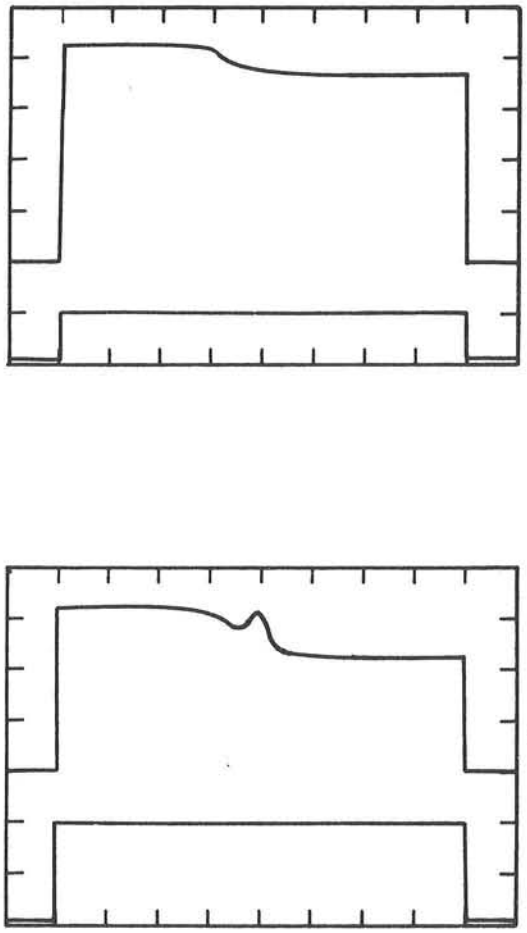

a) Plessey bare GaAℓAs LED exposed to $\phi = 6.5 \times 10^{12} n/cm^2$.

b) Plessey pigtailed GaAℓAs LED exposed to $\phi = 5.1 \times 10^{13} n/cm^2$.

Figure 1.32 Neutron pulse exposure of two Plessey LEDs: a bare GaAlAs LED (P65B) and a pigtailed GaAlAs device (C45) from the most recent group. Special care was taken in these later measurements to eliminate the extraneous effects of noise and gamma ray interaction with the detector. Therefore, the peak in the lower picture is due to fiber luminescence as one would expect since the pigtail is also exposed. The upper trace is the light signal (10mV/division) and the lower trace is the LED current through a 25 Ω resistor (1V/division). Sweep time is 50μs/division.

4. PROTON IRRADIATION EFFECTS

In our laboratory, we recently investigated the effects of 16 meV proton bombardment on several commercially available LEDs (Ref. 90). Irradiations were performed at room temperature at the Los Alamos Tandem Van de Graaf Accelerator Facility.

The LEDs used in the investigation were: an amphoterically Si-doped GaAs LED (Texas Instruments TIL-26), a dome-shaped GaAs LED (Texas Instruments TIXL-35), a high radiance, etched well AlGaAs LED (Laser Diode Laboratories IRE-160), a side emitting AlGaAs LED (Laser Diode Laboratories IRE-150), and two long wavelength (1.30 μm emitting InGaAsP LEDs (Varian VLED-127 and Plessey CXL011).

The proton-induced changes in current voltage characteristics shown in Figure 1.33 for the TIXL-35 are typical of large area, planar LEDs. As we have seen for neutron irradiation there is considerable proton-added current over most of the voltage range. The dashed curve, which is the difference between pre and post irradiation I-V characteristics demonstrates that the proton-induced excess current is an SCR current. Recall that a major advantage of high radiance/high current density LEDs is that they show minimal radiation-induced excess currents in their practical operating ranges. The data in Figure 1.34 illustrate that this is also true for proton bombardment. Of the six LED types investigated three are high radiance LEDs and it is these three types in Figure 1.34 which show a minimal increase in total current with increasing proton fluence.

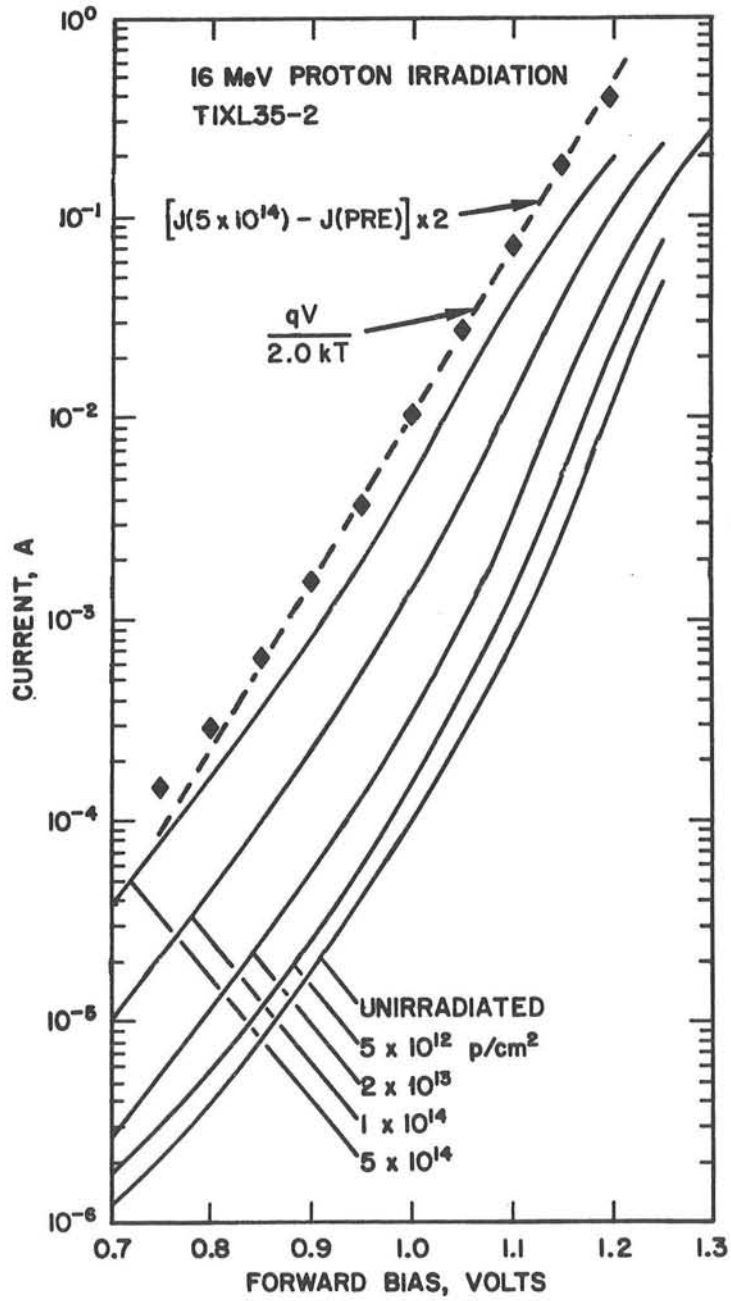

Fig. 1.33 Current-voltage characteristics prior to and following 16-MeV proton irradiation of a Zn-diffused, dome-shaped GaAs LED. The solid diamond symbols represent the difference between the current after the final irradiation (5×10^{14} p/cm^2) and the pre-irradiation current. These data have been displaced upward by a factor of 2 for clarity. The slope of the dashed line through these points indicates that the proton-added current is due to space-charge recombination.

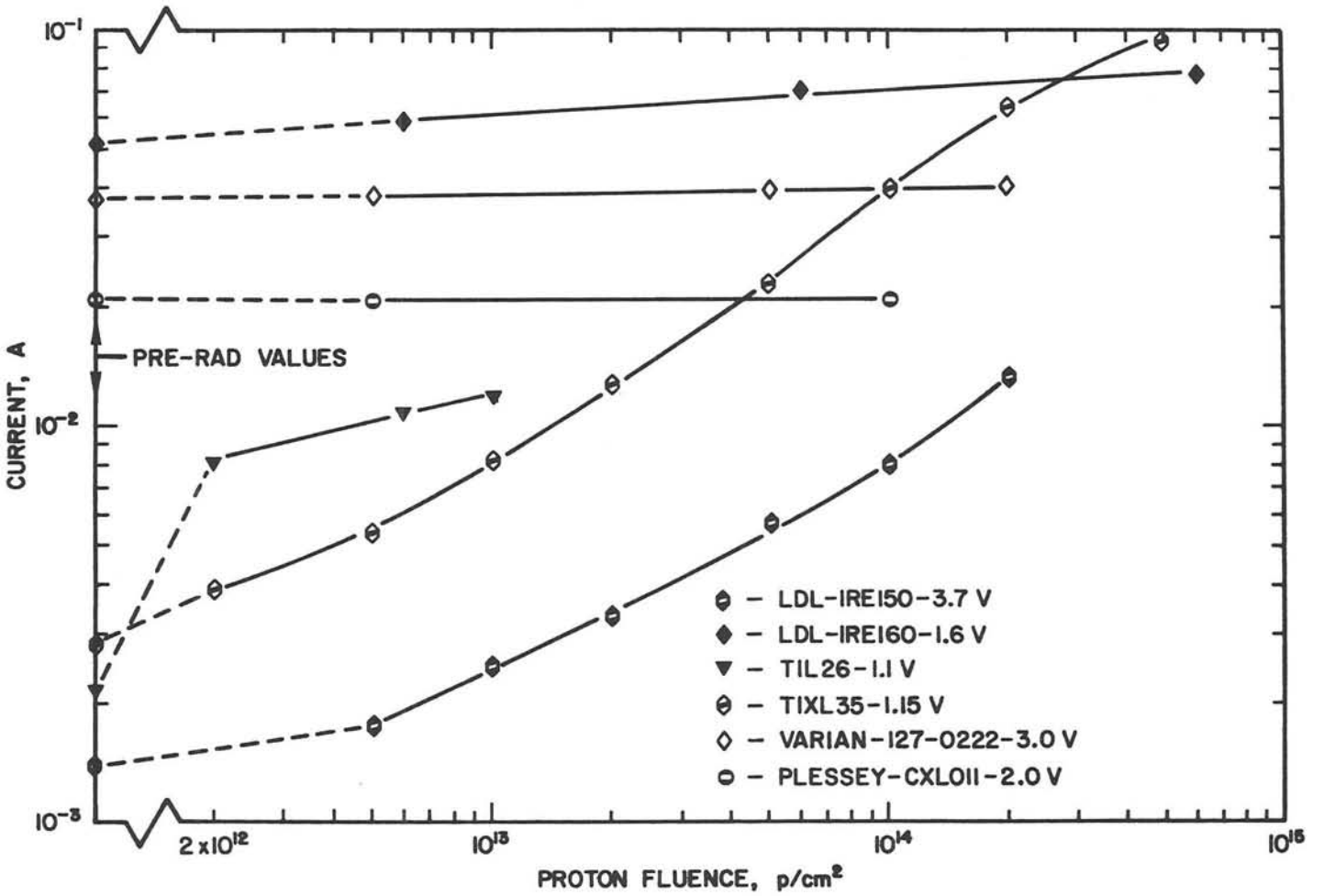

Fig. 1.34 LED current vs 16-MeV proton fluence at selected large voltages for the six LED types examined in this study. Note the minimal increase in LED current for the three high radiance LEDs shown in the upper portion of this figure.

The degradation of the light intensity-voltage characteristic for the TIXL-35 is shown in Figure 1.35. Note that while the total current is dominated by SCR over much of the voltage range (see Figure 1.33), the light intensity is diffusion controlled (diode factor ≈ 1.0). Light intensity-current curves as a function of proton fluence are shown in Figure 1.36. Using these data, $\tau_o K_p$ was calculated to be 3.8×10^{-13} cm^2/p for constant current operation.

The normalized constant current light output degradation data for all six LED types is summarized in Figure 1.37. Also shown for comparison are neutron-induced degradation curves for three of the six LED types, the IRE-160 (AlGaAs), the TIXL-35 (GaAs) and the TIL-26 (GaAs). In all three cases, the neutron-induced light output degradation rates are significantly less per unit fluence than the proton degradation rates.

Although there is considerable variation in the amount of degradation at a given fluence experienced by the LEDs in Figure 1.37, it is significant that for $L/L_o << 1$, the curves all have approximately the same slope. In this range of L/L_o values, Equation 1.23 has the form,

$$\left(\frac{L_o}{L}\right)^{\frac{2}{n+2}} \approx \tau_o K_{p'n} \Phi . \qquad (1.36)$$

Taking the log of each side one obtains

$$\log \frac{L_o}{L} \approx \frac{n+2}{2} \log \tau_o K_{p'n} + \frac{n+2}{2} \log \phi \qquad (1.37)$$

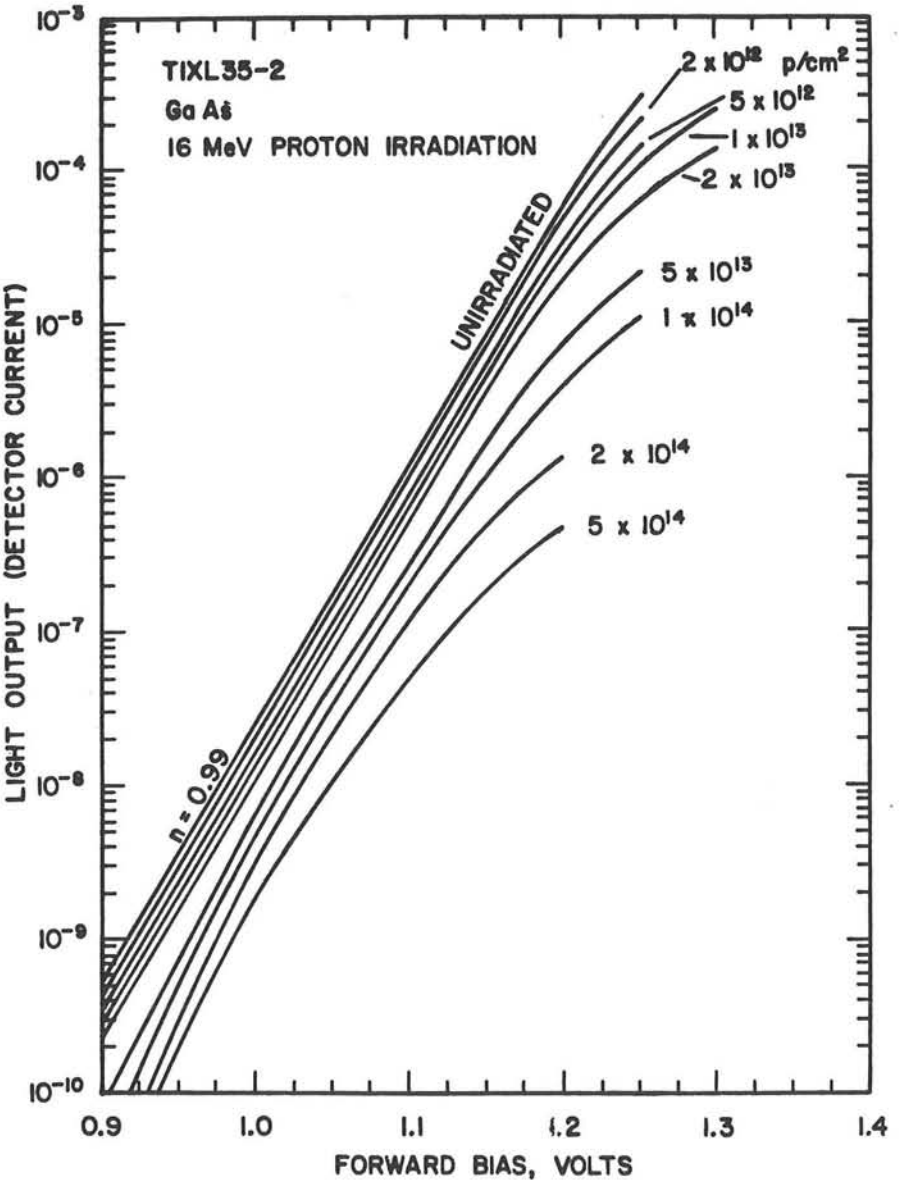

Fig. 1.35 Total LED light output vs forward bias for a Zn-diffused, dome-shaped GaAs LED emitting at .90 μm. The diode factor of n=0.99 taken from the slope indicates that the light output is diffusion controlled.

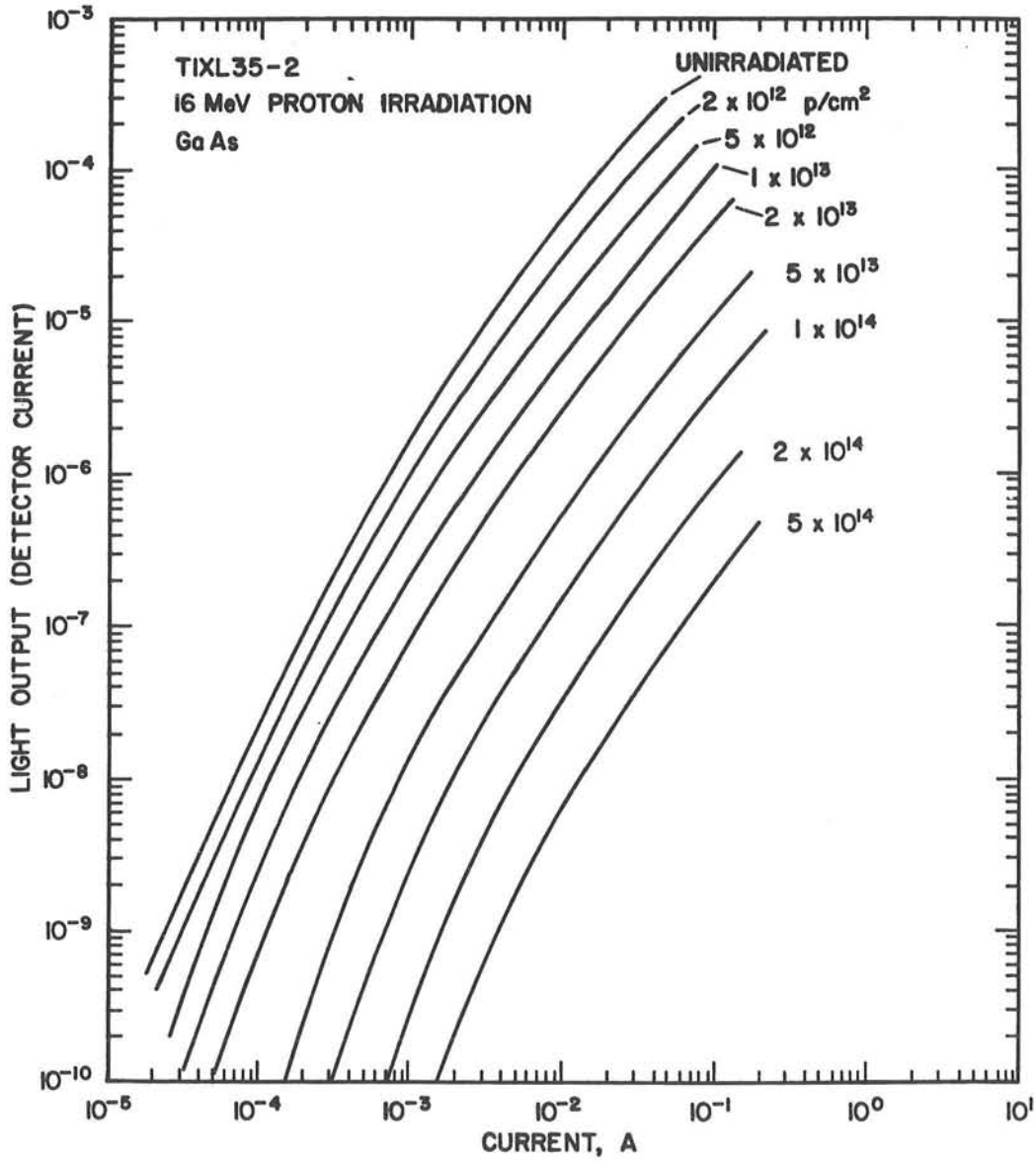

Fig. 1.36 Total light output vs LED current before and after a sequence of 16-MeV proton irradiations of a Zn-diffused, dome-shaped GaAs LED emitting at .90 μm.

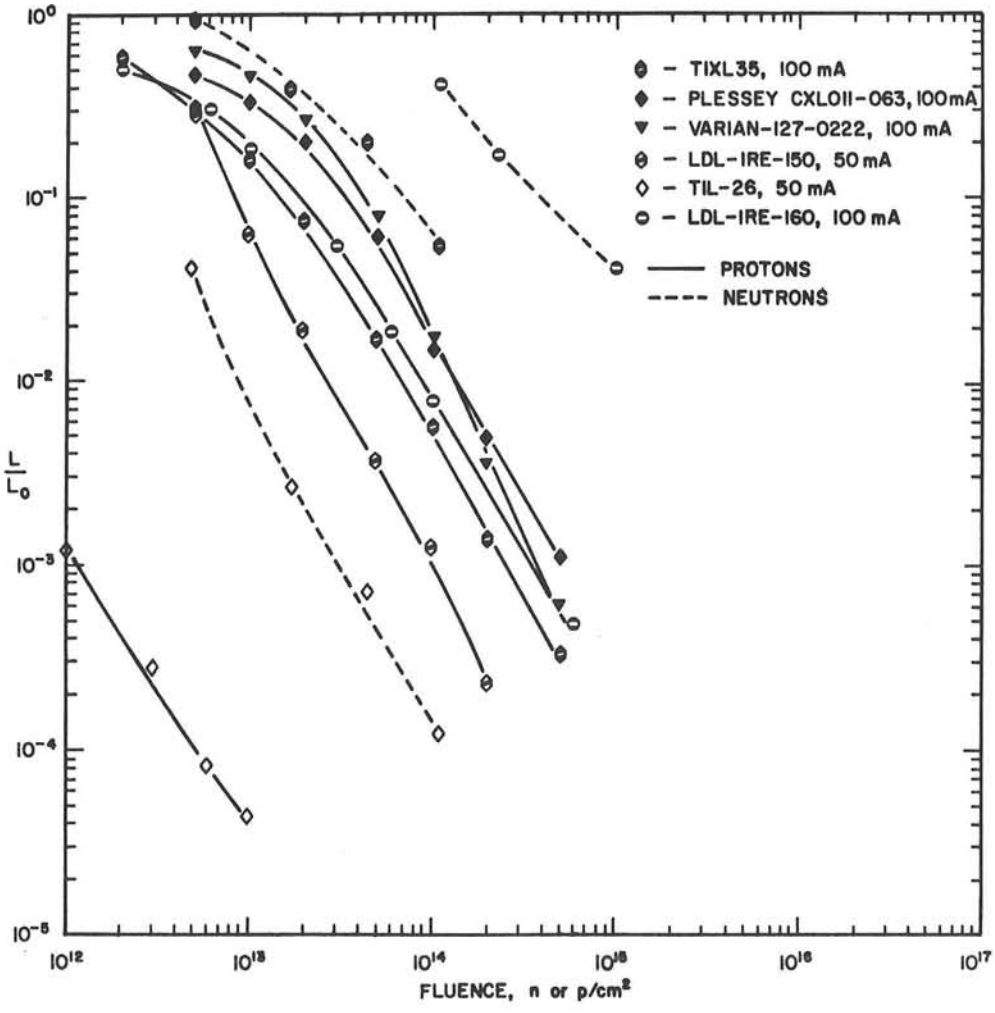

Fig. 1.37 Normalized constant current light output degradation for six LED types as a function of proton or neutron fluence. Note that for the three cases for which neutron data are shown, the proton-induced degradation is significantly larger than the neutron-induced degradation.

so that if n is the same for all the LEDs, the slopes will be the same and the variation in the curves in Figure 1.37 is essentially determined by changes in the intercept, that is $\tau_o K_{p,n}$. Consequently, the values of $\tau_o K_{pn}$ provide a valid basis for comparing the relative radiation hardness of the LEDs. The values of $\tau_o K_p$ for all the LEDs are given in Table II.

Comparisons of our results with the previous work of Hum and Barry (Ref. 91) and Hardwick and Kalma (Ref. 92) are complicated by the fact that the proton energy is different in each of the three studies. While we employed 16-MeV protons, Hum and Barry (Ref. 91) used an energy of 100 MeV and Hardwick and Kalma (Ref. 92) bombarded their LEDs with 30-MeV protons. Data from the 100-MeV irradiations revealed a $\tau_o K_p$ value of 1×10^{-12} cm^2/p, approximately 100 times smaller than the $\tau_o K_p$ value found for the TIL-26 in this study. This difference is too large to be accounted for by the change in proton energy. The degradation rates found by Hardwick and Kalma (Ref. 92) using 30-MeV protons varied considerably from one LED to another. However, the devices typically degraded by 50% after 2×10^{11} p/cm^2. This corresponds to a $\tau_o K_p$ of 2.9×10^{-12} cm^2/p which falls within the range of our values.

Our investigation (Ref. 90) of proton damage in LEDs emitting from .82 μm to 1.3 μm has shown that the effects of proton irradiation are similar to those of other types of irradiation. The amphoterically Si-doped GaAs LED, TIL-26, with its relatively long pre-irradiation minority carrier lifetime is very sensitive to protons as it is to neutron and gamma irradiations. The value of the lifetime-damage constant product, $\tau_o K_p = 1.1 \times 10^{-10}$ cm^2/p, is

nearly 1000 times larger than that for the most radiation hard LED, the Varian-127-0222 InGaAsP high-radiance LED which emits at 1.27 μm. As in the case of Si devices, the proton-induced degradation rates of LED light output are significantly larger than for neutron irradiation. Because of the inverse dependence of the Rutherford scattering cross section on proton energy, the degradation rates also vary inversely with proton energy so that one can expect larger $\tau_o K_p$ values at energies below 16 MeV until, of course, the proton energy is too low to penetrate the LED or displace lattice atoms. The damage constant K_p will also increase with the mass of the material exposed to proton bombardment, again through the scattering cross section. Consequently, one can expect somewhat greater degradation rates in LEDs made up of heavier elements, i.e., GaAs versus AlGaAs.

There are two proton-induced degradation components inherent in the constant current operation of LEDs. First, the introduction of defect-related, nonradiative recombination centers degrades the lifetime and the light output through the increased competition for excess carriers. This effect can be minimized by using an LED with low preirradiation minority carrier lifetime, such as the Zn-diffused, dome-shaped TIXL-35 GaAs emitter, or an LED such as the Plessey AlGaAs device discussed in an earlier section which has a very heavily doped active region. Second, as in the case of neutron irradiation, proton irradiation can cause a significant increase in LED current. This excess current is due to additional recombination at defects in the space-charge layer. However, in

the case of high-radiance LEDs which operate at very high current density, this effect is minimal. Therefore, the combination of low preirradiation lifetime and high current density operation leads to small value of $\tau_o K_p$. The two long wavelength emitters examined in this study, both high radiance devices, also show minimal degradation at constant voltage, an indication of low preirradiation lifetime. Consequently, these devices exhibit excellent radiation hardness which favorably enhances the prospects of using long wavelength fiber optic communication links in radiation environments.

5. SUMMARY

The review of radiation effects in LEDs is summarized by presenting Figure 1.38 and Tables I through V which give lifetime-damage constant products for gamma irradiated GaAs LEDs (Table I), gamma irradiated LEDs other than GaAs (Table II), neutron irradiated GaAs LEDs (Table III), neutron irradiated LEDs other than GaAs (Table IV), and proton irradiated LEDs (Table V). Comments and conclusions based on these Tables and Figure 1.38 will be accompanied by recommendations for radiation hardening. We emphasize that our recommendations are made from the point of view of radiation damage in LEDs. Obviously, the realistic selection of an LED for a system exposed to a radiation environment must be based, in part, on considerations of the radiation sensitivity of other components of the optical data link: fibers, detectors, preamplifiers, etc. In addition, for those applications where the expected radiation exposure is minimal, such as certain

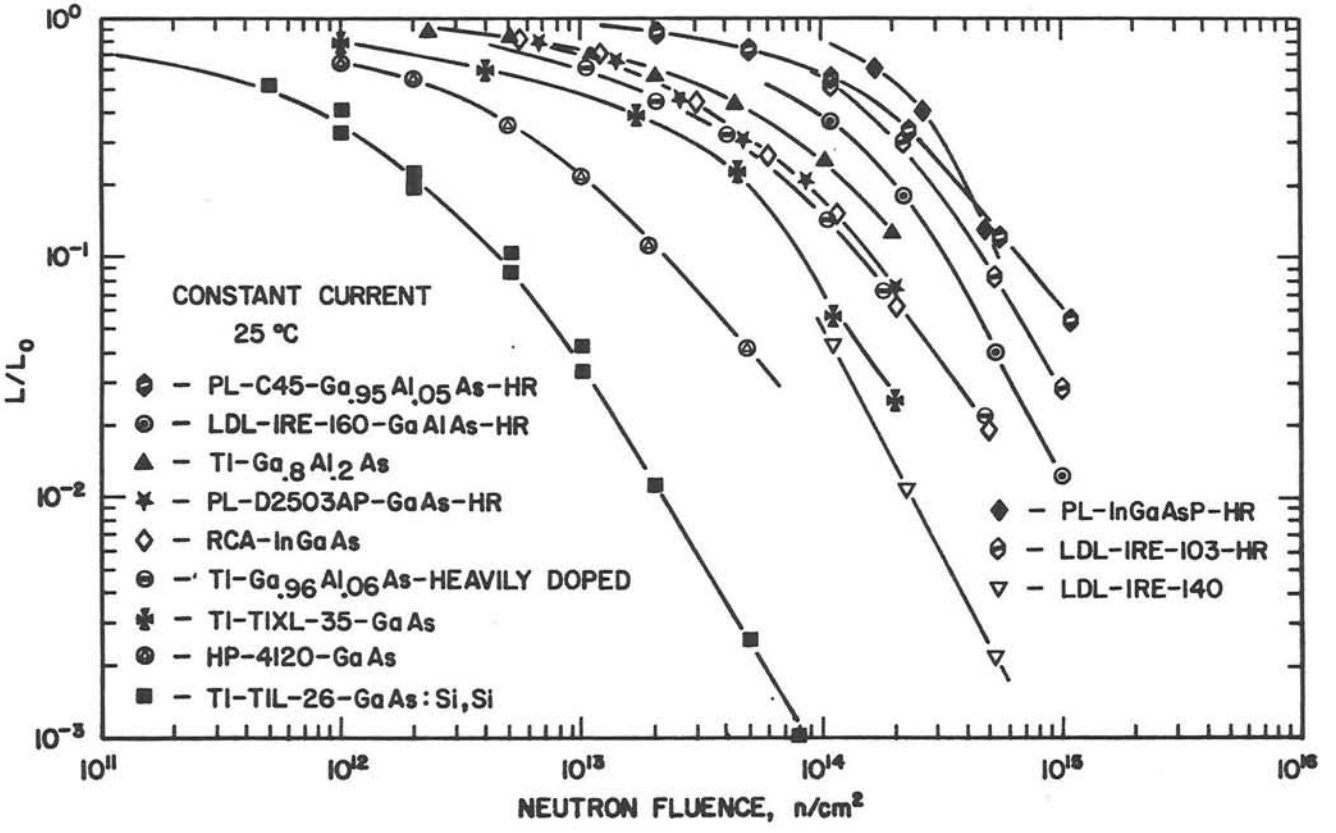

Fig. 1.38 Normalized constant current light output degradation due to neutron irradiation in a wide variety of LEDs investigated at Sandia National Labs. Note that high radiance (HR) LEDs are generally less sensitive to irradiation.

Table I

Lifetime - Damage Constant Products for Gamma and Electron Irradiated GaAs LEDs

LED Characteristics	τ_o	K_{γ,e^-}	$\tau_o K_{\gamma,e^-}$ *	Comments	Reference
Zn diffused junction			$2\times10^{-15}cm^2/e^-(L)$	Electron Irrad.	60
Zn diffused junction, n-type: $5\times10^{16}Te/cm^3$	-	-	$1\times10^{-13}cm^2/e^-(L)$	Electron Irrad. } Note Inverse	8
Zn diffused junction, n-type: $2\times10^{17}Te/cm^3$	-	-	$3.8\times10^{-14}cm^2/e^-(L)$	Electron Irrad. } Variation of $\tau_o K_{e^-}$	8
Zn diffused junction, n-type: $2\times10^{18}Te/cm^3$	-	-	$3.9\times10^{-15}cm^2/e^-(L)$	Electron Irrad. } with Te Conc.	8
Epi Laser Diode, p: $3.7\times10^{19}Zn/cm^3$, n: $3.4\times10^{18}Si/cm^3$	1.0×10^{-8}sec	3.3 $Rads^{-1}sec^{-1}$	$3.3\times10^{-8}Rads^{-1}(L)$	Sub-threshold Operation	7
Zn diffused into Si doped ($1.5\times10^{18}cm^{-3}$)Boat Grown	2.1×10^{-8}sec	2.1 $Rads^{-1}sec^{-1}$	$9.0\times10^{-8}Rads^{-1}(\eta)$	Closely compensated p-region, η_o = 1%	64
Zn diffused junction	-	-	$9.0\times10^{-8}Rads^{-1}(L)$		67
Zn diffused into Te doped n-type	9.0×10^{-9}sec	50 $Rads^{-1}sec^{-1}$	$4.5\times10^{-7}Rads^{-1}(\eta)$	η_o = 1.2%	66
Vary n-Substrate Dopant Type Concentration: $1\times10^{17}cm^{-3}$ to $2\times10^{18}cm^{-3}$ — Se	-	-	$1.5\times10^{-7}Rads^{-1}(\eta)$	Se shows greatest	58
Sn	-	-	$2.3\times10^{-7}Rads^{-1}(\eta)$	annealing recovery	58
Si	-	-	$4.6\times10^{-7}Rads^{-1}(\eta)$		58
Te	-	-	$5.2\times10^{-7}Rads^{-1}(\eta)$		58
Ge	-	-	$8.0\times10^{-7}Rads^{-1}(\eta)$		58
Si(Amphoteric)	-	-	$8.4\times10^{-7}Rads^{-1}(\eta)$		58
Amphoterically Si doped, n: $1.5\times10^{18}Si/cm^3$, LPE Grown	2.7×10^{-7}sec	3.1 $Rads^{-1}sec^{-1}$	$8.4\times10^{-7}Rads^{-1}(\eta)$	η_o = 11%	64
Large Area, high power, Amphoterically Si doped	2.7×10^{-7}sec	3.1 $Rads^{-1}sec^{-1}$	$8.4\times10^{-7}Rads^{-1}(\eta)$	Texas Instr. TIXL-16	75
Large Area, high power, Amphoterically Si doped	2.7×10^{-7}sec	4.3 $Rads^{-1}sec^{-1}$	$1.2\times10^{-6}Rads^{-1}(\tau)$	158 mW @ 1 Amp	75
Amphoterically Si doped	1.4×10^{-7}sec	4.4 $Rads^{-1}sec^{-1}$	$6.1\times10^{-7}Rads^{-1}(L)$	Texas Instr. TIXL-13	76
Amphoterically Si doped	5.0×10^{-7}	1.5 $Rads^{-1}sec^{-1}$	$7.5\times10^{-7}Rads^{-1}(L)$	Texas Instr. TIL-26	67
Amphoterically Si doped	-	-	$8.3\times10^{-7}Rads^{-1}(L_{SCLC})$	Texas Instr. TIL-26	86
High radiance, etched well, Ge doped			$<<1\times10^{-8}Rads^{-1}(L)$	Plessey LED. No measurable effect at 10^6 Rads	74
Planar Ge doped			$2.5\times10^{-8}Rads^{-1}(L)$	Texas Instruments LED	

*Symbol in parentheses denotes parameter used to determine $\tau_o K_{\gamma,e^-}$

Table II

Lifetime-Damage Constant Products for Gamma Irradiated LEDs Other Than GaAs

LED Characteristics	τ_o	K_γ	$\tau_o K_\gamma$*	Comments	Reference
GaP, Diffuse Zn into Te ($1\times10^{18}cm^{-3}$) doped	4.5×10^{-9}sec	4.4 $Rads^{-1}sec^{-1}$	2.0×10^{-8} $Rads^{-1}$(τ)		42
GaP:N, Diffuse Zn into VPE ($3\times10^{16}Te/cm^3$)	2.0×10^{-7}sec	0.20$Rads^{-1}sec^{-1}$	4.0×10^{-8} $Rads^{-1}$(η)	Green emitting η_o = .012%	50
GaP:N, LPE Grown	-	-	1.1×10^{-7} $Rads^{-1}$(L)	Green emitting	87
GaP:Zn, O, LPE Grown, p: $2\times10^{17}Zn/cm^3$, n: $7\times10^{17}Te/cm^3$	-	-	3.6×10^{-8} $Rads^{-1}$(L)	Recomb. @ Zn-O center	87
$GaAs_{0.8}P_{0.2}$	-	1.0 $Rads^{-1}sec^{-1}$	- (η)		58
$GaAs_{0.1}P_{0.9}$	7.0×10^{-8}sec	0.43$Rads^{-1}sec^{-1}$	3×10^{-8} $Rads^{-1}$(η)	Commercial Yellow Emitting η_o = .014%	50
$Ga_{.99}Al_{.01}As$ — LPE Layers on GaAs, p: $2\times10^{18}Zn/cm^3$, n: $2\times10^{18}Te/cm^3$	3.0×10^{-9}sec	2.4 $Rads^{-1}sec^{-1}$	7.2×10^{-9} $Rads^{-1}$(η)	Note Variation with Alloy Composition η_o = 0.39%	66
$Ga_{.89}Al_{.11}As$	1.0×10^{-8}sec	2.0 $Rads^{-1}sec^{-1}$	2.0×10^{-8} $Rads^{-1}$(η)	η_o = 0.77%	66
$Ga_{.66}Al_{.34}As$	5.0×10^{-9}sec	1.7 $Rads^{-1}sec^{-1}$	8.5×10^{-9} $Rads^{-1}$(η)	η_o = 0.17%	66
$Ga_{.85}Al_{.15}As$	-	2.0 $Rads^{-1}sec^{-1}$	- (η)		58
Planar, Ge doped — $Ga_{.98}Al_{.02}As$			1.7×10^{-8} $Rads^{-1}$ (L)		
$Ga_{.94}Al_{.06}As$			3.9×10^{-9} $Rads^{-1}$ (L)		
$Ga_{.94}Al_{.06}As$ - heavily doped			2.6×10^{-9} $Rads^{-1}$ (L)		
$Ga_{.88}Al_{.12}As$			3.9×10^{-9} $Rads^{-1}$ (L)		
$Ga_{.80}Al_{.20}As$			2.1×10^{-9} $Rads^{-1}$ (L)		
[illegible]	-	-	[illegible]		88

*Symbol in parentheses denotes parameter used to determine $\tau_o K_\gamma$.

Table III

Lifetime-Damage Constant Products for Neutron Irradiated GaAs LEDs

LED Characteristics	τ_o	K_n	$\tau_o K_n$*	Comments	Reference
Zn Diffused Laser Diode	-	-	3.2×10^{-15} cm^2/n(L)	Sub-Threshold Operation	69
Epi Laser Diode, p: 3.7×10^{19} Zn/cm^3, n: 3.4×10^{18} Si/cm^3	7.1×10^{-10} sec	1.8×10^{-6} cm^2/n.sec	1.3×10^{-15} cm^2/n(J_{SCR})	Sub-Threshold Operation	70
	3.9×10^{-9} sec	1.8×10^{-6} cm^2/n.sec	7.1×10^{-15} cm^2/n(L)		70
	-	-	1.1×10^{-14} cm^2/n(J_{th})	Variation of Threshold Current	70
Zn Diffused into Si Doped (1.8×10^{18} cm^{-3}) Boat Grown	1.9×10^{-8} sec	2.5×10^{-6} cm^2/n.sec	4.7×10^{-14} cm^2/n(τ)		52
Zn Diffused into Si Doped (1.5×10^{18} cm^{-3}) Boat Grown	2.1×10^{-8} sec	1.2×10^{-5} cm^2/n.sec	2.5×10^{-13} cm^2/n(η)	Closely Compensated p-region, η_o = 1%	64
Zn Diffused into Te Doped n-Type	8.0×10^{-9} sec	5.0×10^{-5} cm^2/n.sec	4.0×10^{-13} cm^2/n(η)	η_o = 1.1%	66
Amphoterically Si Doped, n: 1.5×10^{18} cm^{-3}, LPE Grown	3.5×10^{-7} sec	1.0×10^{-6} cm^2/n.sec	3.5×10^{-13} cm^2/n(η)	η_o = 11%	64
Amphoterically Si Doped	$1.8\pm.4\times10^{-7}$ sec	2.0×10^{-6} cm^2/n.sec	$3.6\pm.8\times10^{-13}$ cm^2/n(L)	Texas Instr. TIXL-13	76
Large Area, High Power, Amphoterically Si Doped	3.5×10^{-7} sec	1.0×10^{-6} cm^2/n.sec	3.5×10^{-13} cm^2/n(η)	Texas Instr. TIXL-16	75
Large Area, High Power, Amphoterically Si Doped	3.5×10^{-7} sec	3.0×10^{-6} cm^2/n.sec	1.1×10^{-12} cm^2/n(τ)	165 mW @ 1 Amp.	75
Amphoterically Si Doped	-	-	3.8×10^{-13} cm^2/n(L, const. J_{SCR})	Note Dependence	87
Texas Instr. TIL-26	-	-	9.1×10^{-13} cm^2/n(L, const. J_{Diff})	on Method of	87
	-	-	1.6×10^{-12} cm^2/n(L, const. J_{SCLC})	Determination	87
Zn diffused into Te doped (3×10^{18} cm^{-3}) planar epitaxial	2×10^{18} Zn/cm^3	2.8×10^{-7} sec	1.9×10^{-6} cm^2/n.sec	5.2×10^{-13} cm^2/n(L)		71
	7×10^{18} Zn/cm^3	2.2×10^{-8} sec	3.5×10^{-6} cm^2/n.sec	7.8×10^{-14} cm^2/n(L)	Note decreased $\tau_o K_n$	71
	2×10^{19} Zn/cm^3	1.7×10^{-8} sec	1.9×10^{-6} cm^2/n.sec	3.3×10^{-14} cm^2/n(L)	at high doping	71
Plessey High Radiance, Ge doped, etched well			5.3×10^{-14} cm^2/n(L)	Current = 10 mA	74
			2.3×10^{-14} cm^2/n(L)	Current = 100 mA	74
Texas Instr. planar, Ge doped			1.9×10^{-13} cm^2/n(L)	Current = 50 mA	73

*Symbol in parenthesis denotes parameter used to determine $\tau_o K_n$.

Table IV

Lifetime-Damage Constant Products for Neutron Irradiated LEDs Other Than GaAs

LED Characteristics		τ_o	K_n	$\tau_o K_n$*	Comments	Reference
GaP: Zn, O, LPE Grown, p: 2×10^{17} Zn/cm^3, n: 7×10^{17} Te/cm^3		-	-	2.2×10^{-14} cm^2/n(J_{SCR})		53
		-	-	2.7×10^{-14} cm^2/n(L)		53
		-	-	2.0×10^{-14} cm^2/n(η_{max})	Recomb. @ Zn-O Center	53
GaP: N, Zn Diffused into VPE (2.2×10^{16} Te/cm^3)		2.9×10^{-8} sec	1.6×10^{-6} cm^2/n-sec	4.7×10^{-14} cm^2/n(τ)		52
$GaAs_{.35}P_{.65}$	Zn Diffused into VPE	1.2×10^{-8} sec	4.3×10^{-6} cm^2/n-sec	5.1×10^{-14} cm^2/n(τ)	Note Variation with	52
$GaAs_{.65}P_{.35}$	Se: 5.0×10^{16} cm^{-3} to 2.0×10^{17} cm^{-3}	5.5×10^{-9} sec	9.1×10^{-6} cm^2/n-sec	5.0×10^{-14} cm^2/n(τ)	Alloy Composition	52
Monsanto LEDs	$GaAs_{.13}P_{.87}$, yellow			1.4×10^{-12} cm^2/n(L)		59
	$GaAs_{.35}P_{.65}$, orange			7.4×10^{-13} cm^2/n(L)		59
	GaP, green			4.8×10^{-13} cm^2/n(L)		59
	$GaAs_{.61}P_{.39}$, red			1.8×10^{-13} cm^2/n(L)		59
SiC				8.0×10^{-15} cm^2/n(L)		38
$Ga_{.99}Al_{.01}As$	LPE Layers on GaAs	2×10^{-9} sec	5.0×10^{-5} cm^2/n-sec	1.0×10^{-13} cm^2/n(η)	Note Variation η_o = .54%	66
$Ga_{.82}Al_{.18}As$	p: 2×10^{18} Zn/cm^3	5×10^{-9} sec	2.7×10^{-5} cm^2/n-sec	1.4×10^{-13} cm^2/n(η)	with Alloy η_o = .70%	66
$Ga_{.66}Al_{.34}As$	n: 2×10^{18} Te/cm^3	8×10^{-9} sec	8.6×10^{-6} cm^2/n-sec	6.9×10^{-14} cm^2/n(η)	Composition η_o = .16%	66
$Ga_{.94}Al_{.06}As$, $Ga_{.88}Al_{.12}As$	Planar Texas			1.9×10^{-13} cm^2/n(L)		73
$Ga_{.94}Al_{.06}As$, heavy doping	Instruments Ge			6.7×10^{-14} cm^2/n(L)	Current = 50 mA	73
$Ga_{.80}Al_{.20}As$	doped			3.3×10^{-14} cm^2/n(L)		73
				2.4×10^{-14} cm^2/n(L)	Current = 0.54 mA	74
Plessey high radiance, etched well $Ga_{.95}Al_{.05}As$				8.1×10^{-15} cm^2/n(L)	Current = 150 mA	74
Plessey high radiance, etched well $Ga_{.95}Al_{.05}As$, heavy doping				5.4×10^{-15} cm^2/n(L)	Current = 100 mA	74
Laser Diode Labs IRE-103, GaAlAs high radiance edge emitter				7.8×10^{-15} cm^2/n(L)		
Laser Diode Labs IRE-160, GaAlAs high radiance etched well				1.1×10^{-14} cm^2/n(L)		
RCA InGaAs - C30116/F - 1.06 μm				1.0×10^{-14} cm^2/n(L)		88
Plessey high radiance InGaAsP - 1.3 μm				6.7×10^{-15} cm^2/n(L)		

*Symbol in parenthesis denotes parameter used to determine $\tau_o K_n$.

Table V

Lifetime-Damage Constant Products for Proton Bombarded LEDs

LED Characteristics	τ_o	K_p	$\tau_o K_p$*	Comments	Reference
Dome shaped, Zn diffused GaAs-TIXL-35-.90 μm			$3.8 \times 10^{-13} cm^2/p(L)$	16 MeV Protons	90
Amphoterically Si doped GaAs-TIL-26-.94 μm			$1.1 \times 10^{-10} cm^2/p(L)$		
Amphoterically Si Doped	2.2×10^{-7} sec	$5.5 \times 10^{-6} cm^2/p.sec$	$1.2 \times 10^{-12} cm^2/p(L)$	100 MeV Protons	91
Laser Diode Labs - IRE - 160, GaAlAs high radiance etched well - .82 μm			$3.4 \times 10^{-13} cm^2/p(L)$		90
Laser Diode Labs - IRE - 150, GaAlAs edge emitter - .82 μm			$6.4 \times 10^{-13} cm^2/p(L)$	16 MeV Protons	90
Varian - 127 - 0222 InGaAsP - 1.27 μm high radiance			$1.5 \times 10^{-13} cm^2/p(L)$		90
Plessey - CXL001 - InGaAsP - 1.3 μm			$3.0 \times 10^{-13} cm^2/p(L)$		90

*Symbol in parenthesis denotes parameter used to determing $\tau_o K_p$

tactical systems, optoelectronic components selection may be based on criteria other than radiation sensitivity.

Based on Tables I-V, Figure 1.38, and the preceding text, we give the following conclusions and recommendations:

1. As discussed early in this Section, the damage constant K is determined primarily by the nuclear interaction with the semiconductor atoms, and by the effectiveness of the specific defects as recombination centers. Both of these characteristics are dependent essentially only on the semiconductor material and the type of radiation. The data in Tables I-IV tend to confirm this statement because in Tables I and III which are restricted to GaAs, there is a remarkable similarity in K values. However, in Tables II and IV which are for a variety of materials, there is a significantly wider variation in K values.

2. Comparison of the $\tau_0 K$ values in Tables I and III indicates that the method of determination of this product can have some bearing on the value (see, for example, the three entries in Table III, Ref. 87). Recall that $\tau_0 K$ values based on efficiency and constant current measurements are influenced by the effect of the irradiation on the total current. If irradiation induces a change in the total current flow mechanism, the equation used to analyze efficiency or constant current light output degradation will change in form as shown by a comparison of Equations 1.20 and 1.23. Therefore, care must be exercised in this type of analysis, and we conclude that constant voltage determinations of $\tau_0 K$ values are more reliable, although constant current (efficiency) methods are more practical since LEDs are usually operated at constant current.

3. Tables I, III, V and Figure 1.38 clearly show that amphoterically Si doped GaAs LEDs possess the greatest radiation sensitivity and the largest $\tau_0 K$ values for both gamma and neutron irradiation. The high degree of radiation sensitivity is due to the long preirradiation lifetime and the presence of radiative space-charge limited current (SCLC) flow at practical operating current levels. The effect of a long initial lifetime is especially obvious in this case because as we have noted above, the damage constants are approximately the same for all the GaAs entries independent of the details of crystal growth and LED manufacturing. Therefore, since K is relatively constant, large τ_0 values are not conducive to radiation hardening.

4. In this report we have drawn several distinctions between amphoterically Si doped GaAs LEDs and those fabricated using other dopants. Therefore, it is important to be able to distinguish the two types of devices merely on the basis of LED catalogue information which does not usually contain descriptions of dopants or growth methods. To illustrate how to do this, we reproduce in Table VI a portion of the array of LEDs offered by Spectronics, Inc., according to one of their catalogues. The two important parameters we wish to focus attention on are the radiative rise time, t_r, and the peak wavelength λ_p. In our previous discussion of amphoterically Si doped GaAs LEDs, it was pointed out that the lifetimes and the peak emission wavelengths of these devices are long. With this in mind, note the comparison of the two parameters of interest between the SE6451, SE6452 devices and the remainder of the LEDs. This comparison indicates that

Table V I

Typical commercial specifications of GaAs LED characteristics [from a recent Spectronics, Inc. Optoelectronic Components Catalogue].

PARAMETER	OPTICAL POWER			BEAM ANGLE	FORWARD DROP			REVERSE BREAKDOWN		RADIATION RISE TIME	PEAK WAVELENGTH	FORWARD CURRENT CONTINUOUS		MAXIMUM TEMPERATURE	
TEST CONDITION	@ I_F (mA)			Note 1	@ I_F (mA)			$I_R = 10\mu A$			$I_F = 100mA$	25°C Ambient	25°C Case		
SYMBOL	P_o			θ	V_F			BV_R		tr	λP				
UNIT	mW			degrees	VOLTS			VOLTS		µsec	nm	mA		°C	
	MIN	TYP	I_F	TYP	TYP	MAX	I_F	MIN	TYP	TYP	TYP	MAX		Operating	Storage
SE-3451-1	1.0		100	90		2.0	100	2		0.7	935	100	750	−65 to + 100	−65 to + 100
SE-3451-2	2.0	3.0	100	90	1.3	1.7	100	6		0.7	935	100	750	−65 to + 100	−65 to + 100
SE-3451-3	4.0	6.0	100	90	1.3	1.7	100	6		0.7	935	100	750	−65 to + 100	−65 to + 100
SE-5450-1	0.5		100	12		2.0	200	2		0.7	935	100	750	−65 to + 100	−65 to + 100
SE-5450-2	1.0	1.5	100	12	1.3	1.7	100	6		0.7	935	100	750	−65 to + 100	−65 to + 100
SE-5450-3	2.2		100	12	1.3	1.7	100	6		0.7	935	100	750	−65 to + 100	−65 to + 100
SE-5451-1	1.0		100	16		2.0	100	2		0.7	935	100	750	−65 to + 100	−65 to + 100
SE-5451-2	2.0		100	16	1.3	1.7	100	6		0.7	935	100	750	−65 to + 100	−65 to + 100
SE-5451-3	3.5		100	16	1.3	1.7	100	6		0.7	935	100	750	−65 to + 100	−65 to + 100
SE-6450-2**	10	15	300	135	1.8	2.0	300	2		0.7	935	100	300*	0 to 70	−50 to 90
SE-6450-3**	15	25	300	135	1.8	2.0	300	2		0.7	935	200	300*	0 to 70	−50 to 90
SE-6451-1**	0.4		300	120	1.6	2.0	300	6		.02	910	160	500*	−65 to + 100	−65 to + 100
SE-6451-2**	1.0		300	120	1.6	2.0	300	6		.02	910	160	500*	−65 to + 100	−65 to + 100
SE-6451-3**	2.0		300	120	1.6	2.0	300	6		.02	910	160	500*	−65 to + 100	−65 to + 100
SE-6452-1**	1.3		1000	120	1.6	2.0	1000	6		.02	910	200	2000*	ALL	ALL
SE-6452-2**	3.4		1000	120	1.6	2.0	1000	6		.02	910	200	2000*		
SE-6452-3**	6.8		1000	120	1.6	2.0	1000	6		.02	910	200	2000*		
SE-6474-020	20		300	150	1.6	2.0	300	3.0		0.7	935	160	500*		
SE-6474-030	30		300	150	1.6	2.0	300	3.0		0.7	935	160	500*		
SE-6474-040	40		300	150	1.6	2.0	300	3.0		0.7	935	160	500*		
SE-6477-030	30		1000	150	1.6	2.0	1000	2.0		0.7	935	160	2000*		
SE-6477-040	40		1000	150	1.6	2.0	1000	2.0		0.7	935	160	2000*		
SE-6477-060	60		1000	150	1.6	2.0	1000	2.0		0.7	935	160	2000*		
SE-6478-2**	300		3000	180	2.2	3.0	3000	2.0		0.7	935	200	3000*		

all of the LEDs except the SE6451 and SE6452 emitters are amphoterically Si doped. The distinction between the two device types for peak wavelength and radiative rise or fall times is then as follows: λp = .90 to .91 μm for the SE6451, SE6452 while λ_p = .93 to .95 μm for GaAs:Si; t_r = 20 to 30ns for the SE6451, SE6452, while t_r = 300 to 700 ns for GaAs:Si. As expected expected, the optical power output of the SE6451 and SE6452 devices is low relative to the GaAs:Si LEDs. In addition, as indicated in Table VI and in other LED catalogues, most of the very high power output GaAs LEDs available today are amphoterically Si doped devices.

5. The practical possibilities of removing defects through thermal annealing of LEDs are remote because very little recovery is observed below 200°C, especially for neutron irradiated devices. On the other hand, it may be practical in certain cases to reduce the net degradation in gamma or electron irradiated LEDs and neutron irradiated high radiance LEDs through the athermal defect annealing produced by forward biasing the device near room temperature. This process is significant in GaAs and GaP although our review indicates the observation of this effect is somewhat erratic. For example, Figsures 1.17 and 1.28 show that bias annealing is effective in GaAs:Zn and InGaAs LEDs, but not in GaAs:Si devices. These results provide yet another reason for not using GaAs:Si devices in radiation environments.

6. The presence of radiative SCLC flow, as encountered in closely compensated p-regions such as the amphoterically Si doped GaAs LED, should be avoided because it is highly sensitive

to degradation as a comparison of Equation 1.30 with Equation 1.14 indicates. In addition, radiative SCLC will lead to light emission over the entire p-region resulting in increased self-absorption for devices mounted n-side up.

7. It is desirable to have the light output due to radiative space charge recombination (SCR) because this mode of current flow is insensitive to irradiation when the device is operated at constant voltage. However, this is difficult to achieve at room temperature with high efficiency. Most commercially available LEDs show radiative SCR only at low temperatures.

8. Of the various type of LEDs reviewed in this work, one of the most radiation tolerant is the SiC device (see Figures 1.2 and 1.3). Not only does radiative SCR persist at room temperature, but there is also considerable evidence that radiation-induced defects act as radiative recombination centers. Unfortunately, these devices are not commercially available at the present time.

9. The collection of constant current normalized light output degradation curves in Figure 1.38 clearly indicates that high radiance LEDs degrade less than others. Note that this is a relatively general conclusion which does not depend on LED material type. It has been shown that there is minimal neutron-induced excess current at high current densities. In addition, at very high current densities in the bimolecular recombination range, one can reduce the lifetime by increasing the current density (see Equation 1.5).

10. Our more recent work on AℓGaAs LEDs from Texas Instruments and Plessey has firmly established the fact that heavy doping of the active region minimizes radiation sensitivity. In most LEDs the radiative recombination is band-to-band or near band-to-band so that, as suggested by Equation 1.1, the radiative recombination rate can be increased by increased doping which leads to a corresponding decrease in radiative lifetime. The $\tau_0 K$ entries in Tables II, III, and IV clearly demonstrate this effect. Fortunately for commercial development of radiation hardened LEDs, heavy doping also leads to high speed which is usually a desirable characteristic irrespective of radiation considerations.

11. Our proton irradiation study (Ref. 90) (see Table V) has shown that sensitivity to this type of irradiation follows the same trends as for gamma and neutron irradiation. That is, amphoterically Si doped GaAs LEDs are very sensitive, while high radiance, heavily doped devices perform quite well. As for Si devices, proton irradiation is more damaging per unit fluence than is neutron irradiation. Note that the $\tau_0 K$ values in Table V are greater than the $\tau_0 K$ values in Tables III and IV.

12. Investigations of transient x-ray bombardment and transient neutron irradiation effects in LEDs have shown that there are no unique or severe effects of pulsed irradiation. Active measurements of LED behavior prior to, during, and following pulsed neutron irradiation demonstrate that the LED behaves as if it were exposed to a low flux, steady state irradiation. Ionization effects in the form of photoluminescence are observed in large volume LEDs at dose rates of the order of 10^{10} rads/s.

As the dose rate is increased, one might expect to see the same effect in smaller volume LEDs. While these effects appear to be minimal it is noted that our measurements above 10^{10} rads/s have been performed only on one type of AℓGaAs LED. It is conceivable that very high dose rates ($\gtrsim 10^{12}$ rads/s) may cause new effects such as catastrophic failure.

13. Although the investigations of long wavelength (>1.0 μm) emitting LEDs have been somewhat limited, results thus far are promising in that the LEDs studied (InGaAs, InGaAsP) appear to be quite insensitive to irradiation (see Tables II, IV, and V and Figure 1.38.

14. A comparison of Table I with Table II and of Table III with Table IV shows that the $\tau_0 K$ values for non-GaAs LEDs are significantly lower than for GaAs LEDs, with the exception of the laser diodes, for all types of irradiation. This can be attributed primarily to the shorter lifetimes in these other LED materials. However, it is interesting to note that, on the average, the $K\gamma$ values are also less for the non-GaAs LEDs than for the GaAs devices. In contrast, the K_n values appear to be actually somewhat larger for the non-GaAs devices. Although K_n and $K\gamma$ both decrease with increasing Al content in $Al_xGa_{1-x}As$ LEDs, as shown by the Ref. 66 entries in Tables II and IV, the value of $K_n = 8.6 \times 10^{-6}$ cm^2/n.s at 34% Aℓ is still larger than all the K_n values in Table III for GaAs with the exception of two values. Sorting out the physical reasons for these various differences will require additional experimental investigation. One might expect, however, that the

K_n values would be more independent of the material than the $K\gamma$ values. In contrast with neutron-induced cluster damage, the point defects created during γ irradiation are often mobile at typical irradiation temperatures and can interact with residual impurities resulting in a greater variety of irradiation-induced defects.

15. While the lifetime-damage constant products for non-GaAs LEDs are generally smaller than those for GaAs LEDs, it does not necessarily follow that the non-GaAs devices are always the best choice for applications in a radiation environment. As we have indicated earlier, one must also consider the initial power output of the LED. In addition to low $\tau_0 K$ values, the non-GaAs LEDs are often characterized by low output powers relative to the GaAs devices. Consequently, for those applications requiring high output power in the presence of low radiation fluences, a GaAs LED may well be the better choice. The preceding statements suggest that the $\tau_0 K$ value, which we have termed an "inverse" figure of merit, does not adequately decribe the suitability of a particular LED for radiation applications. To take into account the intial power output we propose using the quantity, $F \equiv P_0/JV\tau_0 K$ as a figure of merit for the usefulness of LEDs in a radiation environment. Here, P_0 is the initial power output, while J and V are the current and voltage, respectively, at which P_0 is observed. Therefore, this quantity is the ratio of the power efficiency, η_p to the lifetime damage constant product: $F = \eta_p/\tau_0 K$. The quantity F also serves to emphasize the importance of efforts to minimize τ_0 by increased doping without

significant sacrifice in η_p. To compare one LED against another, values of $F = \eta_p/\tau_o K$ can be calculated using information from catalogues for power output and Tables I-V for $\tau_o K$. If the minimum acceptable power output and the radiation tolerance levels are known, one can also calculate the expected degradation for the maximum dose or fluence, Φ, to see if it matches the permissible difference between initial output and minimum acceptable output. Using a value of $\tau_o K$ appropriate for the LED, one multiplies by Φ and adds 1.0 to obtain $(1 + \tau_o K\Phi)$. This number can be used to estimate the degradation of the appropriate quantity as follows:

$$\frac{P_o}{P} \text{ or } \frac{L_o}{L} = 1 + \tau_o K\Phi \quad \text{, constant voltage operation} \quad , \tag{1.38}$$

and

$$\frac{P_o}{P} \text{ or } \frac{L_o}{L} \text{ or } \frac{\eta_o}{\eta} = (1 + \tau_o K\Phi)^{3/2} \quad \text{, constant current operation} \quad . \tag{1.39}$$

As we have seen, these equations can take several forms depending on the radiative center profile and the current flow mechanisms. Here we have assumed the most commonly observed case; that is, a linearly graded profile and, for constant current, a diffusion-limited total current flow which is appropriate for calculations at large operating currents.

Sample calculations using the above equations are shown in Tables VII and VIII for a variety of LEDs that are now commercially available. The information in the first six columns of Tables VII and VIII is taken from manufacturer's specifications. Note that for most of the entries in Table VII the $\tau_o K_\gamma$ values are determined in two ways as indicated in note 2. The agreement between these two methods demonstrates that manufacturer specified rise or fall times are adequate for calculating $\tau_o K$ values. In the case of neutron irradiation, $\tau_o K_n$ values are taken from Tables III and IV. The figures of merit for gamma irradiation, F_γ, and for neutron irradiation, F_n, are shown in column eight of both Tables. In spite of the fact that the GaAs:Si devices have high power efficiencies their extreme radiation sensitivity results in nearly the smallest F_γ and F_n values. Clearly, for low to moderate power requirements the GaAs:Zn LED (TIXL-36) with its large F_γ and F_n values is the preferred emitter for GaAs devices. With regard to the non-GaAs emitters, the high radiance AlGaAs LEDs and the 1.3 μm InGaAsP LED have large $F\gamma$'s and F_n's making them attractive candidates for radiation environment applications. In Table VII columns 9 and 10 provide sample calculations of expected degradation in power output for a gamma dose of 10^7 rads. In Table VIII we show expected power outputs for 10^{12} n/cm^2 and 10^{14} n/cm^2. Once again, the strong degradation of the GaAs:Si devices contrasts sharply with the other entries in the Tables.

For the LEDs that are least sensitive to irradiation, a comparison of the power degradation values in Tables VII and VIII

TABLE VII

Sample calculations of the figure of merit, F, and power output degradation for a variety of commercially available LEDs.

LED Type	Manufacturer - Device No.	Peak Wavelength	Power Output, P_o	Current at P_o	Voltage at P_o	$\tau_o K_\gamma$ (note 2)	$F_\gamma = \eta P_o / \tau_o K_\gamma$	$P = P_o(1+\tau_o K_\gamma \Phi)^{-\frac{3}{2}}$, $\Phi = 1 \times 10^7$ Rads: P	P/P_o
GaP	Hewlett-Packard, 5082-4958	565 nm(green)	0.08[1] mW	20 mA	2.4 V	4.0×10^{-8} 7.0×10^{-8} Rads^{-1}	3.0×10^4 Rads	0.041 mW	0.52
GaAsP	Hewlett-Packard, 5082-4558	583 (yellow)	0.11[1]	10	2.2	3.9×10^{-8} 3.5×10^{-8}	1.4×10^5	0.069	0.52
GaAsP	Hewlett-Packard, 5082-4658	635 (red)	0.56[1]	10	2.2	6.3×10^{-8} 3.0×10^{-8}	5.4×10^5	0.31	0.56
GaAℓAs	RCA, C30123	830	1.0	200	2.0	1.7×10^{-8} 2.0×10^{-8}	1.3×10^5	0.77	0.77
GaAℓAs	RCA, C30119	850	0.50	200	1.5	6.3×10^{-8} 2.0×10^{-8}	7.9×10^4	0.38	0.75
GaAs:Zn	Texas Instr., TIXL 36	910	1.2	50	1.5	3.0×10^{-8} 1.0×10^{-7}	2.5×10^5	0.57	0.47
GaAs:Si	Texas Instr., TIL26	940	1.0	35	1.2	5.3×10^{-7} 7.9×10^{-7}	3.6×10^4	0.048	0.048
GaAs:Si	Texas Instr., TIXL16C	940	400	3000	1.8	8.4×10^{-7}	8.8×10^4	13.9	0.035
InGaAs	RCA, C30116	1060	0.2	50	3.0	1.6×10^{-8}	8.3×10^4	0.16	0.80

1. A small uncertainty exists in these values because of the necessity of converting from photometric to radiometric units.
2. The upper $\tau_o K_\gamma$ value is the product of the K_γ value from Tables I-IV and the manufacturer-specified rise or fall time. Lower values are taken directly from Tables I-IV.

TABLE VIII

Sample calculations of the figure of merit, F, and power output degradation for a variety of commercially available LEDs.

LED Type	Manufacturer - Device No.	Peak Wavelength	Power Output, P_o	Current at P_o	Voltage at P_o	$\tau_o K_n$	$F_n = \eta_{P_o}/\tau_o K_n$	$P = P_o(1+\tau_o K_n \phi)^{-\frac{3}{2}}$ @$\phi = 1 \times 10^{12}$ n/cm^2	@$\phi = 1 \times 10^{14}$ n/cm^2
GaAsP	Monsanto, MV5053	0.67 μm	60 μW	20 mA	1.7 V	1.8×10^{-13} cm^2/n	9.8×10^{9} n/cm^2	47 μW	0.72 μW
GaAs:Si, Si	Texas Instr., TIL-26	0.94 μm	1.0 mW	35 mA	1.2 V	9.1×10^{-13} cm^2/n	2.6×10^{10} n/cm^2	.38 mW	1.1 μW
GaAs:Si, Si	Texas Instr., TIXL-16C	0.94 μm	400 mW	3.0 A	1.8 V	7×10^{-13} cm^2/n	1.1×10^{11} n/cm^2	180 mW	0.7 mW
GaAs:Zn	Texas Instr., TIXL-36	0.90 μm	1.2 mW	50 mA	1.5 V	5.0×10^{-14} cm^2/n	3.2×10^{11} n/cm^2	1.1 mW	0.08 mW
GaAs, high radiance, etched well, pigtailed	Plessey, HR-950	0.90 μm	0.6 mW (out of pigtail)	300 mA	1.6 V	2.3×10^{-14} cm^2/n	5.4×10^{10} n/cm^2	0.6 mW	0.1 mW
GaAℓAs, high radiance, edge emitter	Laser Diode Labs, IRE-103	0.82 μm	1.0 mW	300 mA	1.8 V	7.8×10^{-15} cm^2/n	2.4×10^{11} n/cm^2	1.0 mW	0.42 mW
GaAℓAs, high radiance, etched well	Laser Diode Labs, IRE-160	0.82 μm	0.30 mW	100 mA	2.0 V	1.1×10^{-14} cm^2/n	1.4×10^{11} n/cm^2	0.30 mW	0.10 mW
InGaAs	RCA, C30116/F	1.06 μm	0.2 mW	50 mA	3.0 V	1.0×10^{-14} cm^2/n	1.3×10^{11} n/cm^2	0.2 mW	0.07 mW
InGaAsP	Plessey, CXL011	1.3 μm	~ 0.4 mW	150 mA	3.0 V	6.7×10^{-15} cm^2/n	1.3×10^{11} n/cm^2	0.4 mW	0.2 mW

with typical military radiation tolerance requirements indicates that total dose due to gamma irradiation is not a particularly important problem. Consequently, the critical consideration for most LEDs will be sensitivity to neutron damage.

16. As a concluding statement to our summary we describe the optimum LED for radiation exposure. This device should be a high radiance LED which operates at high current densities in its normal range. The active region of the LED should be heavily doped to enhance the speed of the device and also the radiative recombination rate. When this rate is high the minority carrier lifetime for radiative recombination is small making the total lifetime less sensitive to irradiation. If only one side of the LED, say the p-region, is active, then the possible doping level increase may be limited because the injection efficiency must be maintained high by keeping the non-active side of the junction even more heavily doped.

The LED material should be either ternary or quaternary since these materials are somewhat less sensitive than binary material LEDs when other characteristics are equal. With regard to the choice of a specific material, and hence a particular wavelength, the above criteria do not restrict the choice to one LED material. This is fortuitous in that it allows operating wavelength selection to be determined by possibly more restrictive characteristics such as fiber radiation sensitivity, fiber bandwidth, and detector response to ionizing radiation. Considering present commercial availability of LEDs, AlGaAs devices in the .82 μm to .85 μm range, and InGaAsP LEDs in the 1.2 μm to 1.6 μm range should be equally good. from the point of view of radiation hardness.

6. REFERENCES

1. P. J. Dean, "Junction Electroluminescence," in Applied Solid State Science, edited by R. Wolfe (Academic Press, NY, 1969), Vol. 1, p. 1.
2. J. I. Pankove, Optical Processes in Semiconductors (Prentice-Hall, Inc., NJ, 1971).
3. P. R. Thornton, The Physics of Electroluminescent Devices (Spon, London, 1967).
4. C. E. Barnes, "Radiation Effects in Electroluminescent Diodes," IEEE Trans. Nuc. Sci. NS-18, No. 6, 322 (1971).
5. V. C. Burkig, J. L. McNichols, and W. S. Ginell, "Infrared Absorption in Neutron Irradiated GaAs," J. Applied Physics 40, 3268 (1969).
6. See, for example, p. 48 in Physics of Semiconductors, S. M. Sze, (Wiley Interscience, NY, 1969).
7. C. E. Barnes, "Effects of Co-60 Gamma Irradiation on Epitaxial GaAs Laser Diodes," Phys. Rev. B1, 4735 (1970).
8. L. W. Aukerman, M. F. Millea, and M. McColl, "Effects of Radiation Damage on the Behavior of GaAs p-n Junctions," IEEE Trans. Nucl. Sci. NS-13, 174 (1966).
9. See, for example, p. 99 in reference 6.
10. C. T. Sah, R. N. Noyce, and W. Shockley, "Carrier Generation and Recombination in p-n Junctions and p-n Junction Characteristics," Proc. IRE 45, 1228 (1957).
11. See, for example, p. 104 in reference 6.
12. See, for example, p. 99 in reference 6.

13. M. Gershenzon, R. A. Logan, and D. F. Nelson, "Electrical and Electroluminescent Properties of Gallium Phosphide Diffused p-n Junctions," Phys. Rev. 149, 580 (1966).

14. D. F. Nelson, "Recombination Kinetics and Electroluminescence from Deep Levels in the Carrier Diffusion Region of a p-n Junction," Phys. Rev. 149, 574 (1966).

15. D. J. Dumin and G. L. Pearson, "Properties of Gallium Arsenide Diodes between 4.2 and 300K," J. Appl. Phys. 36, 3418 (1965).

16. J. I. Pankove, "Tunneling-Assisted Photon Emission in Gallium Arsenide p-n Junctions," Phys. Rev. Lett. 9, 283 (1962).

17. D. F. Nelson, M. Gershenzon, A. Askhin, L. A. D'Asaro, and J. C. Sarace, "Band-Filling Model for GaAs Injection Luminescence," Appl. Phys. Lett. 2, 182 (1963).

18. R. J. Archer, R. C. C. Leite, A. Yariv, S. P. S. Porto, and J. M. Whelan, "Electron-Hole and Electron-Impurity Band Tunneling in GaAs Luminescent Junctions," Phys. Rev. Lett. 10, 483 (1963).

19. R. C. C. Leite, J. C. Sarace, D. H. Olson, B. G. Cohen, J. M. Whelan, and A. Yariv, "Injection Mechanisms in GaAs Diffused Electroluminescent Junctions," Phys. Rev. 137, A1583 (1965).

20. H. C. Casey, Jr. and D. J. Silversmith, "Radiative Tunneling in GaAs Abrupt Asymmetrical Junctions," J. Appl. Phys. 40, 241 (1969).

21. K. L. Ashley and A. G. Milnes, "Double Injection in Deep-Lying Impurity Semiconductors," J. Appl. Phys. 35, 369 (1964).

22. M. A. Lampert, "Double Injection in Insulators," Phys. Rev. 125, 126 (1962).

23. N. E. Byer, "Electroluminescence in Amphoteric Silicon-Doped GaAs Diodes. I. Steady State Response," J. Appl. Phys. 41, 1597 (1970).

24. K. L. Ashley, "Radiation from Double Injection Devices," Solid-State Elect. 16, 641 (1973).

25. K. L. Ashley, R. L. Bailey, and J. K. Butler, "GaAs:Mn Double-Injection Devices," Solid-State Elect. 16, 1125 (1973).

26. R. J. Chaffin, Microwave Semiconductor Devices: Fundamentals of Radiation Effects (Wiley, New York, 1973), pp. 96-98.

27. J. E. Crawford, Jr. and L. M. Slifkin, Point Defects in Solids, Vol. 2. Semiconductors and Molecular Crystals, (Plenum, New York, 1975, p. 76).

28. A. G. Stanley, "Comparison of Light-Emitting Diodes in a Space Radiation Environment," IEEE Trans. Nucl. Sci. NS-17, 239 (1970).

29. See, for example, W. J. Choyke, D. W. Feldman, and Lyle Patrick, "Donor Acceptor Pair Spectrum in Cubic SiC," p. 632 in Tenth Intl. Conf. on the Physics of Semiconductors (MIT Press, Cambridge, 1970).

30. V. V. Makarov and N. N. Petrov, "Cathodoluminescence Spectra of Silicon Carbide Crystals Irradiated by Fast Electrons," Sov. Phys. - Solid State 8, 2714 (1967).

31. P. J. Dean, D. Bimberg, and W. J. Choyke, Defects and Radiation Effects in Semiconductors, 1978, p. 447 in Inst. Phys. Conf. Ser. No. 46, Great Britain (1979).

32. V. V. Makarov, "Cathodoluminescence of SiC Crystals of Various Modifications Containing Radiation Defects," Sov. Phys. - Solid State 9, 457 (1967).

33. R. W. Brander and M. P. Calaghan, "Cathodoluminescence of Ion-Implanted SiC," Phys. Status Solidi (a) 3, K143 (1970).

34. I. I. Geitsi, A. A. Nesterov, and L. S. Smirnov, "Fine Structure of the "Red" Cathodoluminescence Band of β-SiC Irradiated with Fast Electrons," Sov. Phys. Semicond. 4, 744 (1970).

35. R. W. Brander, M. P. Callaghan, and A. Todkill, Ion Implantation (Peter Peregrinus Ltd., Stevenage, Eng., 1970), p. 135.

36. I. P. Akimcheuko, U. S. Vavilov, V. V. Krasnopevtsev, Yu. V. Milyutin, and Chan KimLoi, "Photoluminescence of βSiC Synthesized by the Ion Implantation Method," Sov. Phys. Semicond. 1, 659 (1973).

37. A. Addamiano, G. W. Anderson, J. Comas, H. L. Hughes, and W. Lucke, "Ion Implantation Effects of Nitrogen, Boron, and Aluminum in Hexagonal Silicon Carbide," Electrochem. Soc. J. 119, 1355 (1972).

38. C. E. Barnes, "Neutron Damage in SiC Light Emitting Diodes," Appl. Phys. Lett. 20, 86 (1972).

39. C. E. Barnes, "Tunneling in SiC Electroluminescent Diodes," J. Appl. Phys. 45, 193 (1974).

40. R. M. Potter, J. M. Blank, and A. Addaminao, "Silicon Carbide Light Emitting Diodes," J. Appl. Phys. 40, 2253 (1969).

41. G. Gramberg and M. Konigen, "Preparation and Properties of Vapour Phase Epitaxial Silicon Carbide Diodes," Solid-State Elect. 15, 285 (1972).

42. R. A. Logan, H. G. White, and R. M. Mikulyak, "Effects of Gamma Irradiation upon Lifetime and Luminescence of GaP Diodes," Appl. Phys. Lett. 5, 41 (1964).

43. D. V. Lang and L. C. Kimerling, "Observation of Athermal Defect Annealing in GaP," Appl. Phys. Lett. 28, 248 (1976).

44. D. V. Lang and L. C. Kimerling, "Observation of Recombination-Enhanced Defect Reactions in Semiconductors," Phys. Rev. Lett. 33, 489 (1974).

45. C. E. Barnes, "A Comparison of Gamma-Induced Degradation and Forward Bias-Induced Degradation in GaP:Zn,O LEDs," J. Elect. Mat. 7, 589 (1978).

46. C. E. Barnes, "The Effect of Gamma Irradiation and Forward Bias on the 76K Electroluminescence Spectrum of GaP:Zn,O," J. Elect. Mat. 8, 377 (1979).

47. P. J. Dean, M. Gershenzon, and G. Kaminsky, "Green Electroluminescence from Gallium Phosphide Diodes Near Room Temperature," J. Appl. Phys. 38, 5332 (1967).

48. P. J. Dean and M. Ilegems, "The Optical Properties of Be, Mg, and Zn-Diffused Gallium Phosphide," J. Lum. 4, 201 (1971).

49. P. J. Dean, private communication.

50. A. S. Epstein, S. Share, R. A. Polimadei, and A. H. Herzog, "Gamma Irradiation and Annealing Effects in Nitrogen-Doped GaAsP Green and Yellow Light-Emitting Diodes," IEEE Trans. Nuc. Sci. NS-19, No. 6, 386 (1972).

51. C. E. Barnes, "Neutron Damage in GaP Light Emitting Diodes," Appl. Phys. Lett. 20, 110 (1972).

52. A. S. Epstein, S. Share, R. A. Polimadei, and A. H. Herzog, "Effect of Neutron Irradiation in GaAsP Electroluminescent Diodes," Appl. Phys. Lett. 23, 472 (1973).

53. C. E. Barnes, "Neutron Damage in GaP:Zn,O Light Emitting Diodes," J. Appl. Phys. 48, 1921 (1977).

54. We are indebted to R. W. Dixon and O. G. Lorimor of Bell Labs, Murray Hill, NJ for the contribution of GaP LEDs.

55. W. Rosenzweig, W. H. Hackett, Jr., and J. S. Jayson, "Kinetics of Red Luminescence in GaP," J. Appl. Phys. 40, 4477 (1969).

56. C. J. Nuese, H. Schade, and D. Herrick, "Efficiency Degradation of GaAsP Electroluminescent Diodes Due to High Energy Electron Irradiation," Met. Trans. 1, 587 (1970).

57. H. Schade, C. J. Nuese, and D. Herrick, "Defect Centers in GaAsP Electroluminescent Diodes Due to High-Energy Electron Irradiation," J. Appl. Phys. 41, 3783 (1970).

58. A. S. Epstein, S. Share, R. A. Polimadei, and A. H. Herzog, "Dopant and Alloying Effects in Gamma Irradiated GaAs Light Emitters," Trans. Nuc. Sci. NS-23, 1654 (1976).

59. J. M. Lambert, P. A. Treado, R. G. Allas, and L. Leopold, "Temperature Dependence of Neutron Damage to Commercial GaAsP LED Devices," p. 191 in Proc. of the Fiber Optics in the Nuclear Environment Symposium, Vol. II, R. C. Webb (Ed.), (DNA 5308P-2, 1980).

60. M. F. Millea and L. W. Aukerman, "The Role of Diffusion Current in the Electroluminescence of GaAs Diodes," Appl. Phys. Lett. 5, 168 (1964).

61. L. W. Aukerman and M. F. Millea, "Band-Filling Current in Heavily Doped GaAs Diodes," J. Appl. Phys. 36, 2585 (1965).

62. M. F. Millea and L. W. Aukerman, "The 1.0- and 1.28-eV Emission from GaAs Diodes," J. Appl. Phys. 37, 1788 (1966).

63. A. S. Epstein and P. A. Trimmer, "Radiation Damage and Annealing Effects in Photon Coupled Isolators," IEEE Trans. Nuc. Sci. NS-19, No. 6, 391 (1972).

64. S. Share, A. S. Epstein, and R. A. Polimadei, "Radiation Damage and Hardening Effects on Compensated GaAs Light Emitting Diodes," IEEE Trans. Nuc. Sci. NS-20, No. 6, 256 (1973).

65. S. Share, A. S. Epstein, R. A. Polimadei, "Properties of Compensated GaAs Light-Emitting Diodes Following Co-60 Irradiation," Solid-State Elect. 18, 471 (1975).

66. R. A. Polimadei, S. Share, A. S. Epstein, R. J. Lynch, and D. Sullivan, "Performance of GaAℓAs Light Emitting Diodes in Radiation Environments," IEEE Trans. Nuc. Sci. NS-21, No. 6, 96 (1974).

67. K. J. Soda, C. E. Barnes, and R. A. Kiehl, "The Effect of Gamma Irradiation on Optical Isolators," IEEE Trans. Nuc. Sci. NS-22, 2475 (1975).

68. M. C. Petree, "Degradation of Luminescence in Neutron-Irradiated GaAs Diodes," Appl. Phys. Lett. 3, 67 (1963).

69. B. W. Noel, C. E. Barnes, and H. D. Southward, "Neutron Irradiation Effects on Diffused GaAs Laser Diodes," IEEE Trans. Nuc. Sci. NS-18, No. 6, 378 (1971).

70. C. E. Barnes, "Neutron Damage in Epitaxial GaAs Laser Diodes," J. Appl. Phys. 42, 1941 (1971).

71. C. E. Barnes, "Development of Efficient, Radiation-Insensitive GaAs:Zn LEDs," IEEE Trans. Nuc. Sci. NS-24, 2309 (1977).

72. H. C. Casey, Jr., B. I. Miller, and E. Pinkas, "Variation of Minority Carrier Diffusion Length With Carrier Concentration in GaAs Liquid-Phase Epitaxial Layers," J. Appl. Phys. 44, 1281 (1973).

73. C. E. Barnes, "Neutron Damage Effects in AℓGaAs LEDs," p. 189 in reference 59.

74. C. E. Barnes, Radiation Effects in Pigtailed GaAs and GaAlAs LEDs, Air Force Wright Aeronautical Laboratories Report No. AFWAL-TR-81-1086 (Wright Patterson AFB, Ohio, 1981).

75. R. A. Polimadei, S. Share, A. S. Epstein, and G. E. Gowins, "Radiation Susceptibility of High Power (>200mW) Spontaneous Infrared Emitters," Report No. HDL-TR-1650, available from National Tech. Information Service, U.S. Dept. of Commerce, Springfield, VA, 22151.

76. R. H. Hum and A. L. Barry, "Radiation Damage Constants of Light Emitting Diodes by a Low-Current Evaluation Method," IEEE Trans. Nuc. Sci. NS-22, 2482 (1975).

77. H. Kressel, J. U. Dunse, H. Nelson, and F. Z. Hawrylo, "Luminescence in Silicon-Doped GaAs Grown by Liquid Phase Epitaxy," J. Appl. Phys. 39, 2006 (1968).

78. H. Kressel and H. Nelson, "Electrical and Optical Properties of n-Type Si-Compensated GaAs Prepared by Liquid Phase Epitaxy," J. Appl. Phys. 40, 3720 (1969).

79. J. A. Rossi, N. Holonyak, Jr., P. D. Dapkus, R. D. Burnham, and F. V. Williams, "Laser Transitions in p-Type GaAs:Si," J. Appl. Phys. 40, 3289 (1969).

80. D. Redfield, J. P. Wittke, and J. I. Pankove, "Luminescent Properties of Energy-Band Tail States in GaAs:Si," Phys. Rev. B2, 1830 (1970).

81. I. Ladany, "Electroluminescence Characteristics and Efficiency of GaAs:Si Diodes," J. Appl. Phys. 42, 654 (1971).

82. N. E. Byer, "Electroluminescence in Amphoteric Silicon-Doped GaAs Diodes. II. Transient Response," J. Appl. Phys. 41, 1602 (1970).

83. H. Rupprecht, J. M. Woodall, K. Konnerth, and D. G. Pettit, "Efficient Electroluminescence from GaAs Diodes at 300K," Appl. Phys. Lett. 9, 221 (1966).

84. T. Moriizumi and K. Takahashi, "Si- and Ge-Doped GaAs p-n Junctions," Jap. J. Appl. Phys. 8, 348 (1969).

85. C. E. Barnes, "The Effect of Gamma Irradiation on the Low Temperature Properties of Amphoterically Si-Doped GaAs LEDs," J. Electrochem. Soc. 124, 1901 (1977).

86. C. E. Barnes and K. J. Soda, "Application of Damage Constants in Gamma Irradiated Amphoterically Si-Doped GaAs LEDs," IEEE Trans. Nuc. Sci NS-23, 1664 (1976).

87. C. E. Barnes, "A Comparison of Gamma-Irradiation-Induced Degradation in Amphoterically Si-Doped GaAs LEDs and Zn-Diffused GaAs LEDs," IEEE Trans. Elect. Dev. ED-26, 739 (1979).

88. C. E. Barnes, "Radiation Effects in 1.06-μm InGaAs LEDs and Si Photodiodes," J. Appl. Phys. 50, 5242 (1979).

89. I. Arimura and R. S. Caldwell, "Radiation Degradation and Recovery in Long Fiber-Optics Data Links," p. 175 in reference 59.

90. B. H. Rose and C. E. Barnes, "Proton Damage Effects on Light-Emitting Diodes," J. Appl. Phys. 53, 1772 (1982).

91. W. H. Hardwick and A. H. Kalma, "Effects of Low-Dose-Rate Radiation on Opto-Electronic Components and the Consequences Upon Fiber Optic Data Link Performance," IEEE Trans. Nuc. Sci. NS-26, 4808 (1979).

II. SEMICONDUCTOR LASER DIODES

During the last several years, laser diodes have progressed from the simple GaAs p-n junction device which had a very high threshold current density, J_T, to more sophisticated double heterostructure stripe geometry lasers which are capable of room temperature CW operation (Ref.1). More recent efforts have concentrated on a reduction of the magnitude and temperature dependence of J_T (Ref.2), and on mode stabilization to facilitate single mode operation (Ref.3). Once this has been achieved, high density optical communication links will become a reality. Therefore, it is appropriate to assume that laser diodes will also play a role in high data rate transmission links which will be exposed to a radiation environment. In addition to this motivation for studying radiation damage in laser diodes, it will be shown, as in the case of LEDs, that the introduction of defects in a controlled manner can provide information about the pre-irradiation properties of laser diodes.

1. RELEVANT PRE-IRRADIATION PROPERTIES

The method of construction of a simple injection laser diode is illustrated in Figure 2.1. The size of the diode itself is usually kept small because of heat dissipation requirements and the large current densities which are required to produce laser action. The laser diode is mounted on a heat sink whose dimensions are large compared to the diode's dimensions. In order to achieve

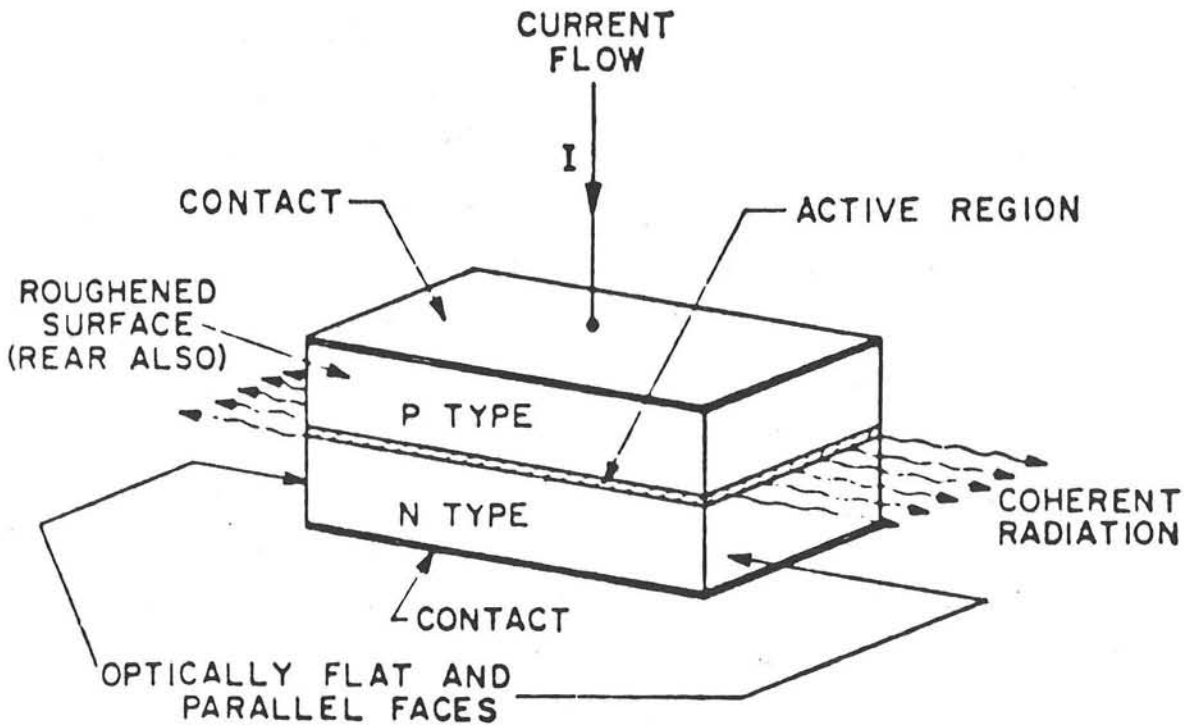

Fig. 2.1 Basic structure of a junction laser in the form of a Fabry-Perot cavity, i.e., a pair of parallel planes are cleaved or polished and the two remaining sides roughened [from S. M. Sze, Physics of Semiconductor Devices (Wiley-Interscience, N.Y., 1969)].

laser action the device must also be formed into an optical cavity. This is most easily done by forming a Fabry-Perot cavity as shown in Figure 2.1. As indicated, the sides of the device are roughened to eliminate reflection. The ends are cleaved or polished parallel to each other to achieve high internal reflection. Sometimes a special reflecting coating is also put on the ends. Typical dimensions are 100 μm to 200 μm for the cavity length and 10 μm to 30 μm for the width. For increased output power the diodes can be stacked in arrays. Unfortunately, the simple homojunction laser structure shown in Figure 2.1 has quite high threshold currents because of poor carrier confinement and high cavity losses due to relatively poor waveguiding. These problems can be alleviated to a large extent by fabricating a double heterostructure (DH) laser in which the active region is sandwiched between layers of a larger band gap material, i.e. a GaAs active region between AlGaAs layers. This greatly improves both carrier confinement and waveguiding within the active region. In the typical commercial DH laser, the active region is restricted to a narrow stripe through proton bombardment or oxide isolation. Even greater complexities have been introduced in recent years using alternative fabrication techniques and sophisticated geometries in order to improve a variety of laser performance properties, such as mode stability or the amount of power coupled into a fiber. The end result is an extensive and rather bewildering array of laser types (Ref.4).

Commercially available laser diodes are restricted to fewer semiconductor materials than are LEDs. This is primarily because

laser action is much easier to achieve in a semiconductor with a direct energy gap. In such a material, the band-to-band optical transition is a first-order process so that the optical gain is high. However, the same transition in an indirect gap semiconductor is a second-order process because it involves the emission or absorption of phonons. Dumke (Ref.5) has shown that free carrier absorption can be a significant irreducible loss mechanism in laser diodes. At the very high injection levels required for laser action, absorption of emitted light by free carriers becomes important. This is also a second-order process of the same magnitude as emission in an indirect gap material. Consequently, the achievement of laser action in an indirect gap material is very difficult.

With the aid of Figure 2.2, we wish to consider three basic transition processes occurring in a direct-gap material that play a major role in semiconductor laser action (Ref.4). Figure 2.2a depicts the usual absorption process in which an atom in the ground state, E_1, absorbs a photon of energy $h\nu_{12} = E_2-E_1$ and is transferred into the excited state, E_2. After a short time, corresponding to the spontaneous lifetime of the excited state, the excited atom will decay to the ground state without any outside disturbance with the emission of a photon of energy $h\nu_{12}$ (Figure 2.2b). In the case of stimulated emission shown in Figure 2.2c the excited atom interacts with the electro-magnetic field associated with the $h\nu_{12}$ photon and immediately decays to the ground state with the emission of a photon of energy $h\nu_{12}$ which is in phase with the stimulating incident photon. In order for the

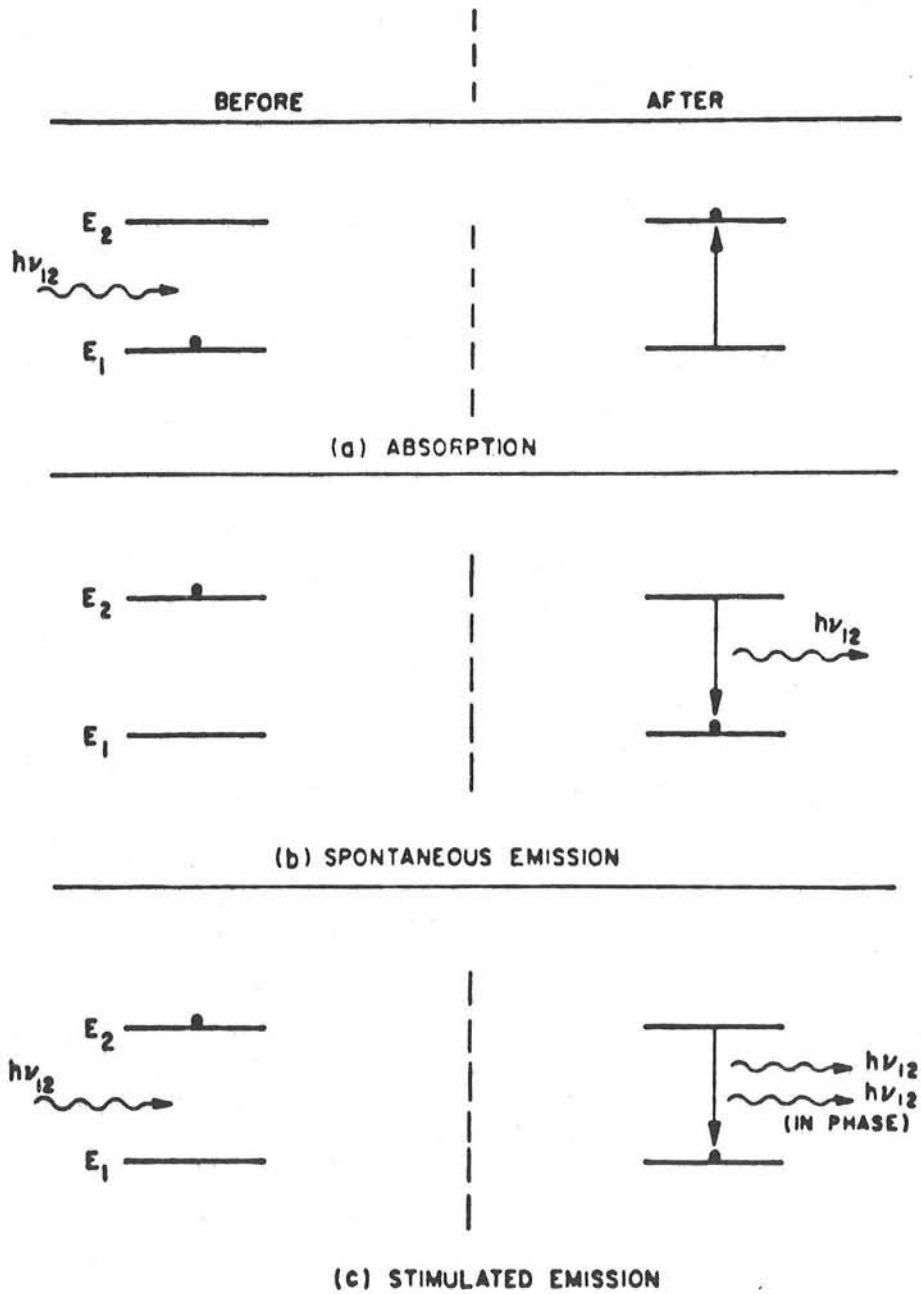

Fig. 2.2 The three basic transition processes between two energy levels E_1 and E_2. The black dots indicate the state of the atom. The initial state is at the left; the final state, after the process has occurred, is at the right [from S. M. Sze, Physics of Semiconductor Devices (Wiley-Interscience, N.Y., 1969)].

stimulated emission rate to exceed the absorption rate, a population inversion must exist in the crystal corresponding to a larger number of atoms in the excited state than in the ground state. This situation is illustrated in Figure 2.3 where enough carriers have been excited into the conduction band tail to cause inversion. This condition can be achieved in an injection laser by degenerately doping the p-side, and preferably also the n-side, and then injecting a large number of electrons into the conduction band tail on the p-side. The region where laser action occurs, called the active region (see Figure 2.1), is in or near the junction; this is a heavily compensated region where the n-type and p-type doping is degenerate resulting in the band tails shown in Figure 2.3.

The condition of population inversion necessary to give greater emission than absorption can be derived in a more quantitative fashion as follows (Ref.4). The emission rate for transitions from filled states near energy, E, in the conduction band to empty states at $E - h\nu$ in the valence band is given by the product of the number of occupied states, $n_c(E)F_c(E)$, and the number of unoccupied valence band states, $n_v(E - h\nu)[1 - F_v(E - h\nu)]$. Here, $n_c(E)$ and $n_v(E)$ are the densities of states in the conduction band and valence band, respectively, and $F_c(E)$ and $F_v(E)$ are the occupation probabilities given by the Fermi-Dirac distribution for states in the conduction and valence bands, respectively:

$$F_c(E) = \frac{1}{1 + \exp\left(\frac{E - E_{FC}}{kT}\right)} \qquad (2.1)$$

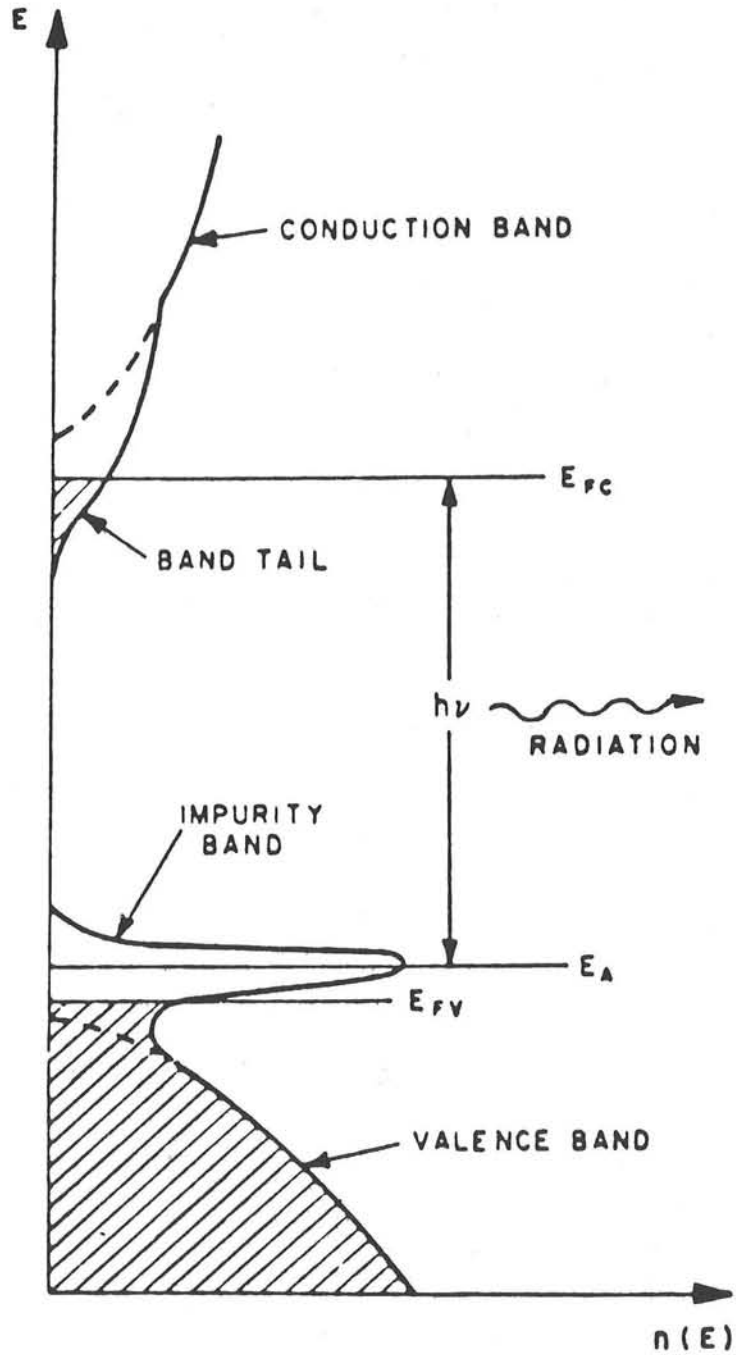

Fig. 2.3 A special distribution of density of states where the conduction band has a band tail and the valence band has a high density of impurity states which merges with the main valence band [from S. M. Sze, Physics of Semiconductor Devices (Wiley-Interscience, N. Y., 1969)].

where E_{FC} is the quasi-Fermi level for electrons. The total emission rate, W_e, is found by integrating the desired product over energy.

$$W_e = B\int n_c(E)F_c(E)n_v(E - h\nu)[1 - F_v(E - h\nu)]\, dE,\ cm^{-3}\ sec^{-1} \quad (2.2)$$

where B is a constant containing various material parameters. The product for the absorption rate is formed and integrated in a similar, but opposite, manner so that the total absorption rate, W_a, is

$$W_a = B\int n_v(E - h\nu)F_v(E - h\nu)n_c(E)[1 - F_c(E)]\, dE,\ cm^{-3}\ sec^{-1} \quad (2.3)$$

Substituting Equation 2.1 into Equations 2.2 and 2.3, and integrating one finds that the condition for achieving gain or amplification, that is, for $W_e > W_a$ is given by

$$E_{FC} - E_{FV} > h\nu,\ eV \quad (2.4)$$

This condition is shown in the energy band diagram of Figure 2.3.

Recall that the usual injection laser diode is constructed as shown in Figure 2.1 with cleaved or polished ends of reflectivity, R. This forms a Fabry-Perot cavity of length, ℓ_c. In order to find the relationship between the threshold gain and the losses, we need to consider the change in intensity dL, caused in an increment of length, dx, along ℓ_c by the gains and losses. Assuming that the condition given by Equation 2.4 holds, the gain per unit length, g, will be positive (emission > absorption) and the increase in L in dx is (gdx)L. The internal

loss per unit length, α, which is primarily due to free carrier absorption and scattering out of the active region, causes a decrease in L in dx of $(\alpha dx)L$. The net change in L is

$$dL = (g - \alpha)Ldx \quad , \text{ arbitrary units} \tag{2.5}$$

One then integrates Equation 2.5 over a complete traversal of the light path, that is, down to one end of the cavity and back again. At each end the light leakage out the end (end losses) is determined by R. The result is

$$L = L_i R^2 e^{2(g-\alpha)\ell c} \quad , \text{ arbitrary units} \tag{2.6}$$

where L_i is the initial intensity. The threshold for light oscillation in the cavity is reached when the light wave suffers no attenuation in traversing the complete path $2\ell_c$. Setting $L = L_i$ one obtains

$$Re^{(g-\alpha)\ell_c} = 1 \tag{2.7}$$

or

$$g\ell_c = \alpha\ell_c + \ln \frac{1}{R} \tag{2.8}$$

with the total gain on the left side of Equation 2.8 and the internal plus end losses given by the right side. The threshold current density, J_T, can be related phenomenologically to the gain, g, by defining a gain factor, β, as $g \equiv \beta J_T$. For this definition of β,

$$J_T = \frac{1}{\beta}\left[\alpha + \frac{1}{\ell_c}\ln\left(\frac{1}{R}\right)\right] \quad , \text{ A/cm}^2 \tag{2.9}$$

More detailed derivations of threshold current based on an analysis of stimulated and spontaneous emission and also absorption are given in several references (Refs.1,4,6,7). These considerations show that β is given by

$$\beta = \frac{\eta_i c^2}{8\pi q n_r^2 \nu^2 \Delta\nu d} \quad , \text{cm/A} \tag{2.10}$$

where η_i is the internal quantum efficiency, n_r is the refractive index, ν and $\Delta\nu$ are the frequency and line width of the laser line, respectively, and d is the active region width.

With regard to radiation damage effects, it is important to note that the quantum efficiency, η , in Equation 2.10 which determines β is characteristic of near-threshold operation. The quantity η_i can be written as

$$\eta_i = \frac{1/\tau_r}{1/\tau_r + 1/\tau_{nr}} = \frac{\tau}{\tau_r} \tag{2.11}$$

where τ_r and τ_{nr} are the radiative and non-radiative recombination lifetimes, and τ is the total measured lifetime. Just below threshold, τ_r is the spontaneous radiative lifetime characteristic of LED operation which is of the order of a few ns. However, well above J_T, τ_r is the stimulated radiative lifetime which is approximately 10^{-11} s (Ref.8). Consequently, under intense lasing conditions τ is determined by τ_r and $\eta_i \approx 1.0$. Therefore, many more irradiation induced non-radiative recombination centers would have to be introduced to affect η_i well above J_T. However, J_T itself will be sensitive to irradiation to about the same degree as the LED output of the laser when operated below threshold.

2. RADIATION DAMAGE IN LASER DIODES

In the previous Section our review of radiation effects in laser diodes was restricted to sub-threshold operation where the laser is essentially an LED. In this Section, attention is focused on the effects of irradiation on laser diode operation at and above the threshold current.

In an early study, Saji and Inuishi (Ref.9) studied the effect of Co-60 gamma irradiation on GaAs lasers and found that the threshold current and laser peak energy increased with gamma dose. Recovery of the threshold current was observed following thermal anneals between 120°C and 240°C. However, the peak energy shift did not recover with annealing. It is interesting to compare these results with our study (Ref.10) of gamma irradiation of GaAs laser diodes below the threshold. Recall that a major portion of the damage could be removed by forward biasing the diodes. One might then expect that Saji and Inuishi (Ref.9) would have observed very little damage by examining their diodes above threshold. The fact that they did observe significant damage can probably be attributed to the way in which the experiment was conducted. They operated their diodes at 77°K with current pulses 1 μs wide at a pulse rate of 5 Hz. The low temperature and low duty cycle were probably responsible for the lack of significant injection annealing.

Compton and Cesena (Ref.11) studied the effects of electrons and gamma rays on GaAs laser diodes and found that the radiation

induced increase in threshold current observed in their experiments and shown in Figure 2.4 could be attributed to a decrease in radiative efficiency, η_i, which occurs in the gain factor (see Equation 2.10). Although no thermal annealing was observed by Compton and Cesena (Ref.11) principally due to the low maximum annealing temperature of 100°C imposed by package limitations, they did observe considerable room temperature forward bias-induced recovery of the threshold current. Compton and Cesena (Ref.11) also observed changes in the mode structure of the laser spectrum following irradiation. Two groups of modes were observed after irradiation separated by about 6 Å. The individual modes were not as sharp as in the preirradiation case probably because of the increased heating during a pulse.

In our study (Ref.12) of neutron damage in laser diodes above and below threshold, the effect of neutron irradiation on the threshold current density, J_T, was examined over the temperature range, 76 K to 300 K. As irradiation proceeded, J_T was observed to increase uniformly over the entire temperature range. As in the case of Compton and Cesena's (Ref.11) work, it was assumed that the neutron induced increase in J_T was due primarily to a decrease in η_i because of the presence of neutron-induced non-radiative recombination centers. With this assumption, Equation 2.9 was modified to include the effects of irradiation, and it was shown that the increase in threshold current, $J_T - J_{To}$, where J_{To} is the pre-irradiation value, was proportional to $\tau_o K_n \Phi$.

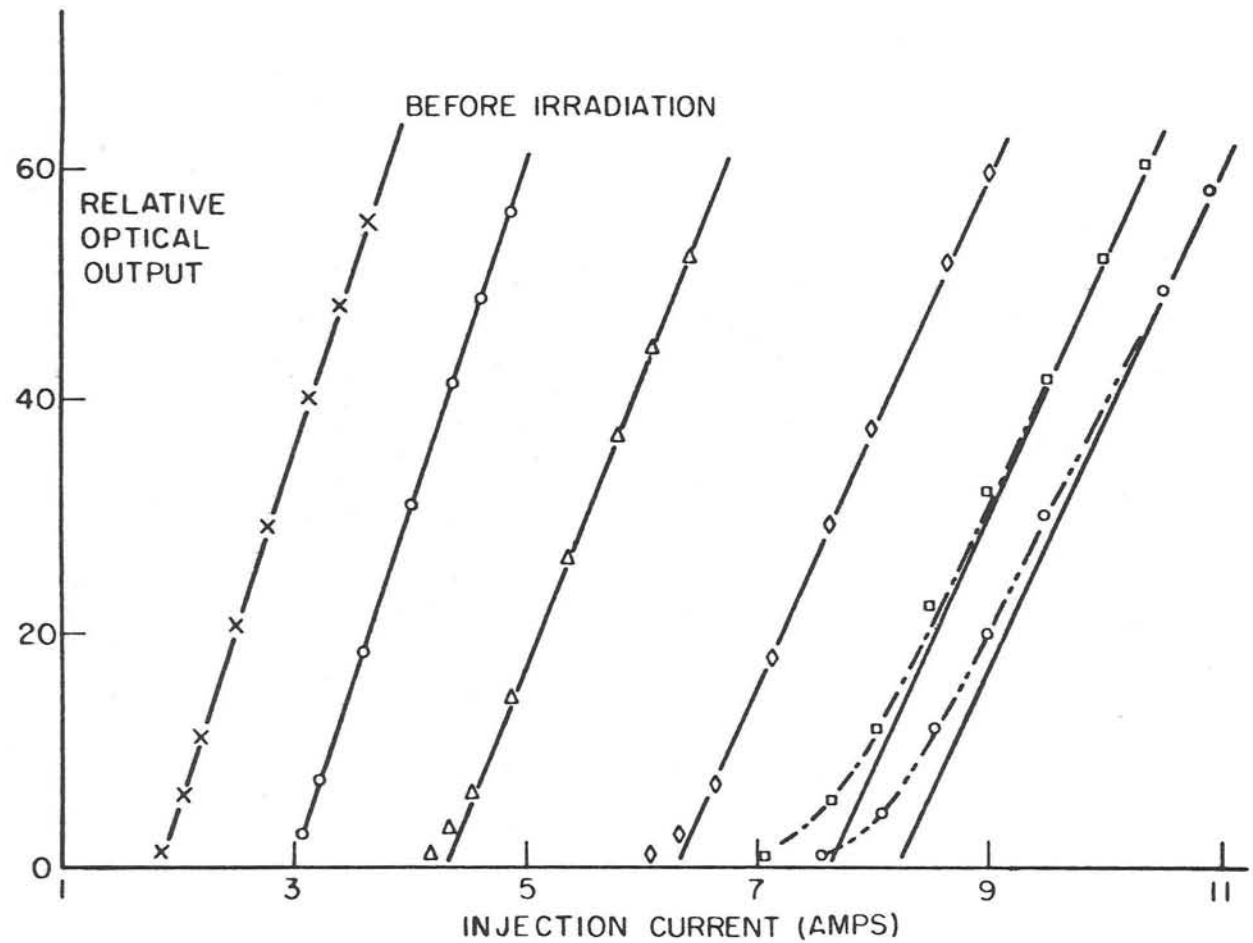

Fig. 2.4 The effect of electron irradiation on the output of a GaAs laser diode operated in the pulsed mode at 77K. The curves move to the right with increasing electron fluences. The intercept with the abscissa is the threshold current [from D. M. J. Compton and R. A. Cesena, IEEE Trans. Nucl. Sci. NS-14, No. 6, 55 (1967)].

The resulting equation for $J_T - J_{To}$ provided a satisfactory fit to the plot of $(J_T - J_{To})$ versus Φ over the temperature range, 76 K to 265 K, allowing the determination of $\tau_o K_n = 1.1 \times 10^{-14} cm^2$ a value fairly close to that of 7.1×10^{-15} determined from the degradation of subthreshold light intensity with neutron fluence (see Table III). As suggested earlier, these results provide confirming evidence that J_T increases at approximately the same rate with irradiation as the LED light output decreases with fluence. This follows from the fact that the gain factor, β, is controlled by the ratio of the total lifetime to the spontaneous radiative lifetime.

Results of a later study (Ref.13) in our laboratory provided further confirmation that the primary damage effect was a reduction in η_i. This experiment was based on the form of Equation 2.9 which indicates that if one plots J_T versus $(1/\ell_c)\ \ell n\ (1/R)$ for a set of lasers with varying cavity lengths ℓ_c, the slope of such a curve is $1/\beta$ and the intercept is α/β. Consequently, the manner in which the slope and intercept change with neutron irradiation should reveal whether J_T decreases because of an increase in α or a decrease in β. Neutron irradiation of a set of laser diodes with different ℓ_c values, obtained from RCA, showed that β decreased while α remained essentially constant following a cumulative fluence of 8.4×10^{13} n/cm^2. In addition, calculation of the expected decrease in β using the $\tau_o K_n$ value determined in the previous study (Ref.12) (1.1×10^{-14} cm^2) agreed with the observed decrease in β.

In addition to an examination of lasers of varying lengths, the effects of neutron irradiation on the spatial distribution of laser output were also studied (Ref.13). Room temperature near-field patterns of standard-length laser diodes were obtained by taking infrared photomicrographs at currents above J_T. In contrast with electron irradiation which introduces macroscopic (20 - 30 μm) non-lasing regions (Ref.14) neutron irradiation did not change the nearfield pattern which was usually non-uniform in unirradiated diodes. This difference was attributed to the possible presence of mobile point defects which migrate either during electron irradiation or laser operation, to form large agglomerations of defects resulting in large non-lasing regions. In contrast, one does not expect neutron damage to produce mobile point defects.

In a third study (Ref.15) in our laboratory, the laser diodes examined in previous studies (Refs.12 and 13) were subjected to neutron irradiation and their total light output was examined from low sub-threshold currents to the maximum permissible current above J_T. Room temperature results of these measurements are shown in Figure 2.5. In the sub-threshold region, designated as region 1 in Figure 2.5, the laser is essentially an LED and exhibits the expected degradation of light output with increasing Φ. Because the light output increases very rapidly just above J_T as lasing begins, and because J_T is sensitive to irradiation, neutron irradiation causes drastic decreases in light output for constant currents near J_T (region 2 in Figure 2.5). In marked contrast with this sensitivity, at currents well above J_T (region 3) the light output is insensitive to neutron irradiation.

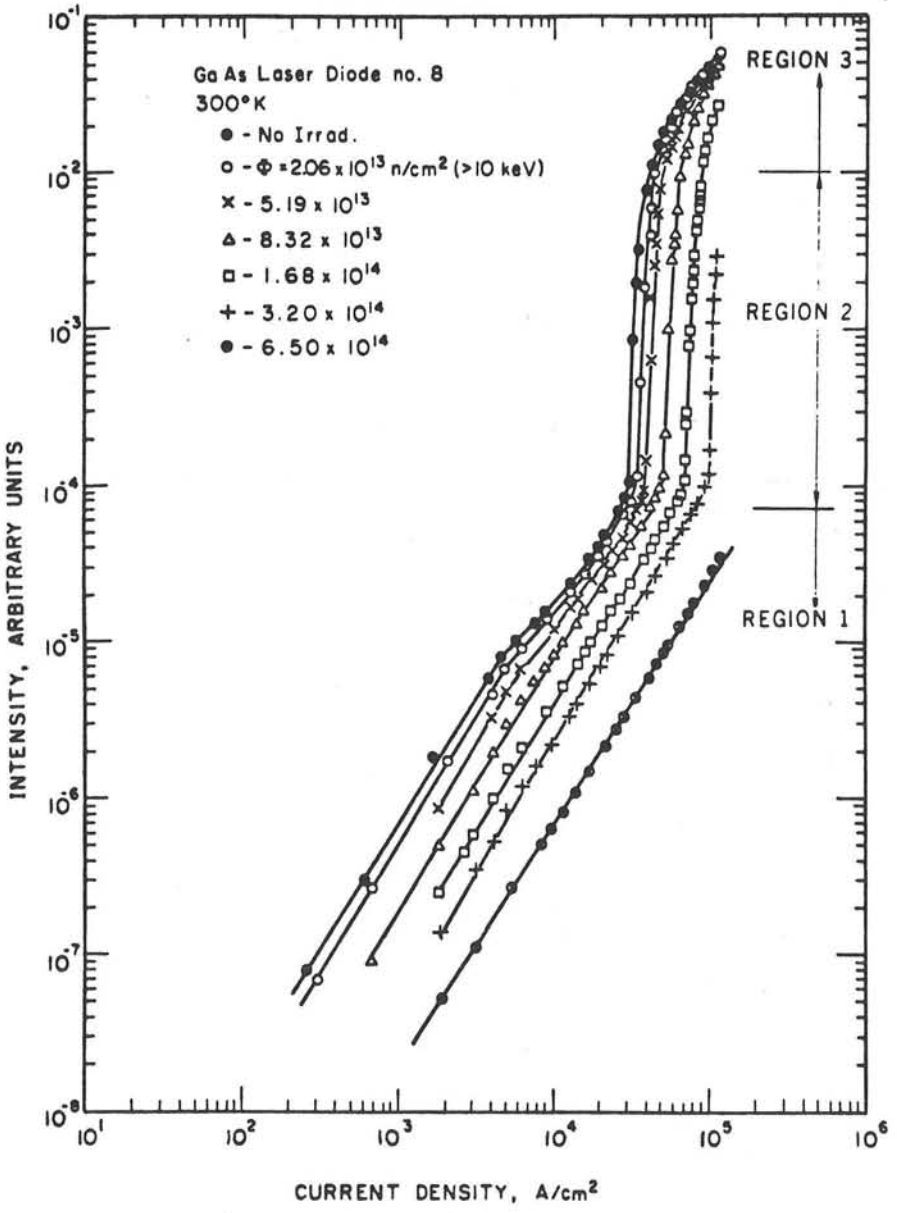

Fig. 2.5 Total light output of a GaAs laser diode at 300°K as a function of diode current density before and after successive neutron irradiations. The figure has been divided into three regions for purposes of discussion in the text [from C. E. Barnes, J. Appl. Phys. 45, 3485 (1974)].

This result is even more dramatic at low temperatures where, for some laser diodes, the light output increases following irradiation. The insensitivity to irradiation at high currents was attributed to the very short radiative lifetimes, of the order of 10^{-11} (Ref.8) characteristic of intense laser operation. These results are important from a practical point of view because they show that laser diodes are insensitive to irradiation at high currents. Since this radiation hardness is due to the fact that the minority carrier lifetime is controlled by the very short stimulated radiative lifetime, which is characteristic of all laser diodes, we expect this result to be applicable to laser diodes in general.

This general result was further confirmed by a more recent study (Ref.16) in our laboratory of a variety of sophisticated state-ofthe art laser diodes. These included AlGaAs CW stripe geometry DH lasers and both pulsed and CW InGaAsP long wavelength (1200 nm to 1.3 nm) emitting lasers. The results in Figure 2.6 for an RCA InGaAsP laser are typical of the devices examined in this study. As for the earlier lasers, the light output is insensitive to irradiation well above J_T. Also note that J_T is more sensitive to irradiation at higher temperatures.

The normalized increases in threshold currents for most of the laser types investigated in this study (Ref.16) are shown in Figure 2.7 at room temperature and 218 K. Note that the most sensitive device is a relatively simple, high J_T GaAs laser similar to those investigated previously (Refs.12,13,15). The results in Figure 2.7 indicate that for those lasers with a minimal increase in J_T with temperature, the radiation sensitivity and its

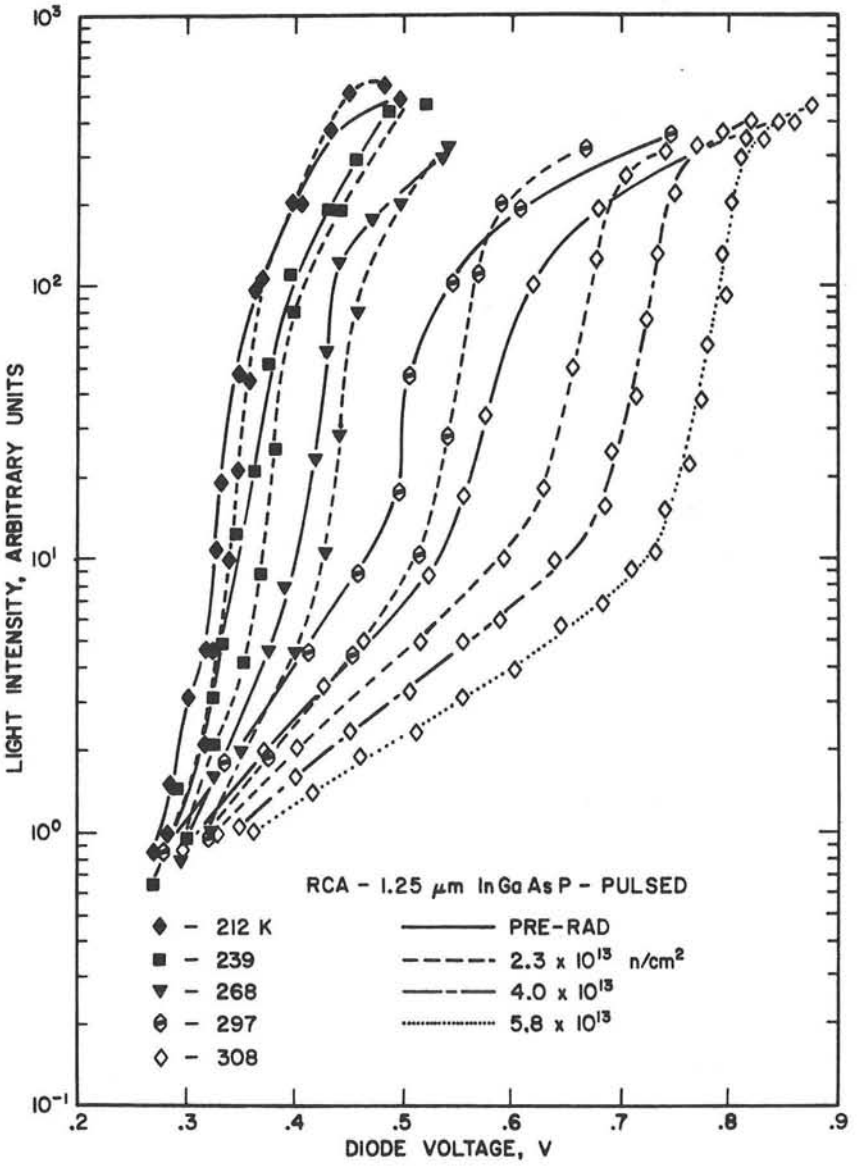

Fig. 2.6 Light output from below threshold to well above threshold as a function of laser forward voltage at four temperatures prior to and following neutron irradiation of a typical RCA long wavelength emitting pulsed laser diode (from C. E. Barnes, p. 88 in Laser and Laser Systems Reliability, G. A. Evans, Ed., Proc. SPIE 328, Jan. 28, 1982, Los Angeles, CA).

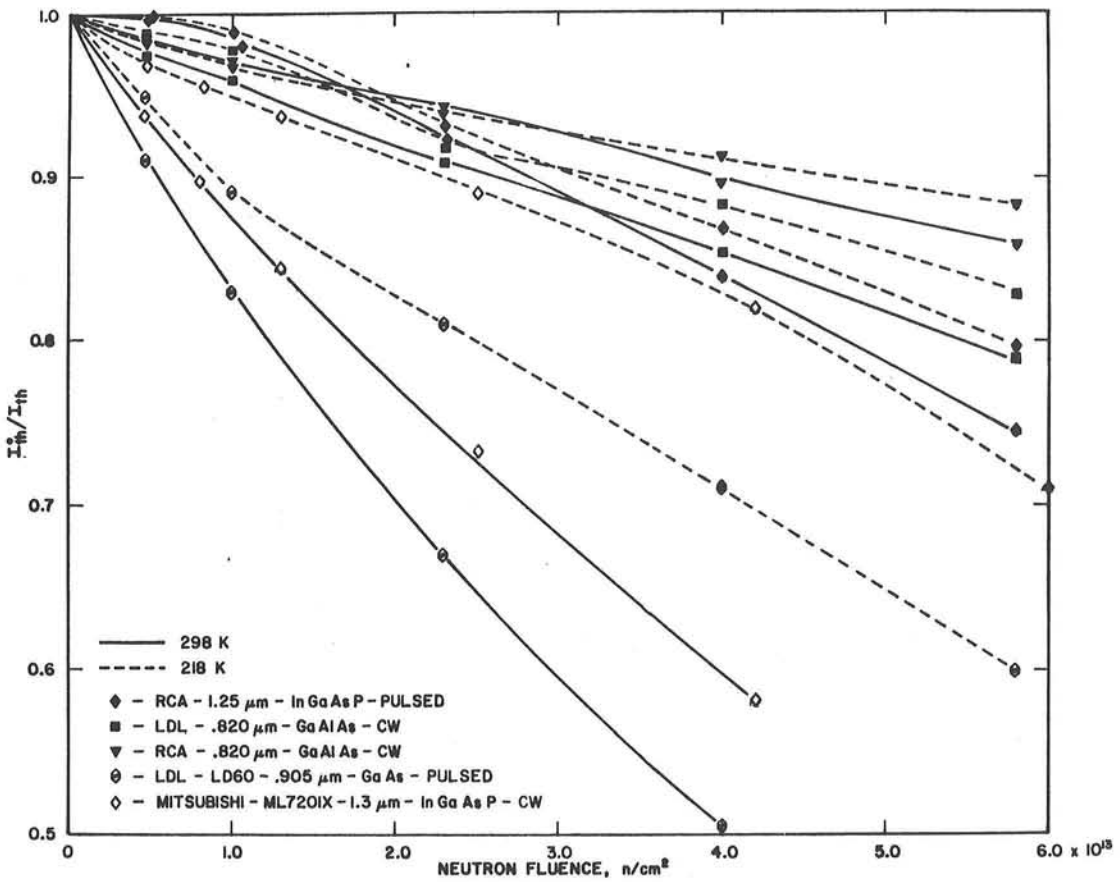

Fig. 2.7 Normalized increase in threshold current at two temperatures as a function of neutron fluence for a variety of laser diodes. Note that for most of the devices the increase in I_{th} is less than 10% at 2.3×10^{13} n/cm^2 (from C. E. Barnes, p. 88 in Laser and Laser Systems Reliability, G. A. Evans, Ed., Proc. SPIE 328, Jan. 28, 1982, Los Angeles, CA).

temperature dependence are also both minimal. This is an encouraging result since there is considerable motivation to reduce the temperature dependence of J_T irrespective of any consideration of radiation sensitivity.

For one of the long wavelength emitting devices, neutron-enhanced operational degradation was observed (Ref.16). Intuitively, one would expect similarities and possible interactions between radiation induced defects and slow, operational bulk degradation in lasers. Recent work (Refs.17 and 18) has shown that defects of various types can be present in lasers as fabricated, and that these defects can move and agglomerate during operation resulting in output degradation. Consequently, if additional defects are added through irradiation, the potential for greater operational degradation should be present. An example of such behavior (Ref.16) is shown in Figure 2.8 for an InGaAsP pulsed laser. The sequence of operations represented by the data in this Figure was as follows. Prior to irradiation, the laser was operated for one hour at room temperature at maximum allowable pulse current, pulse width, and duty cycle. As shown in Figure 2.8 this did not degrade the output. The laser was then irradiated to a neutron fluence in excess of 10^{13} n/cm^2 which also did not degrade the performance. However, when the laser was again operated for one hour under maximum conditions, severe degradation was observed as shown in Figure 2.8. Thus, it appears that the neutron induced defects caused severe device degradation through operationally-induced re-orientation of the defect structure and distribution.

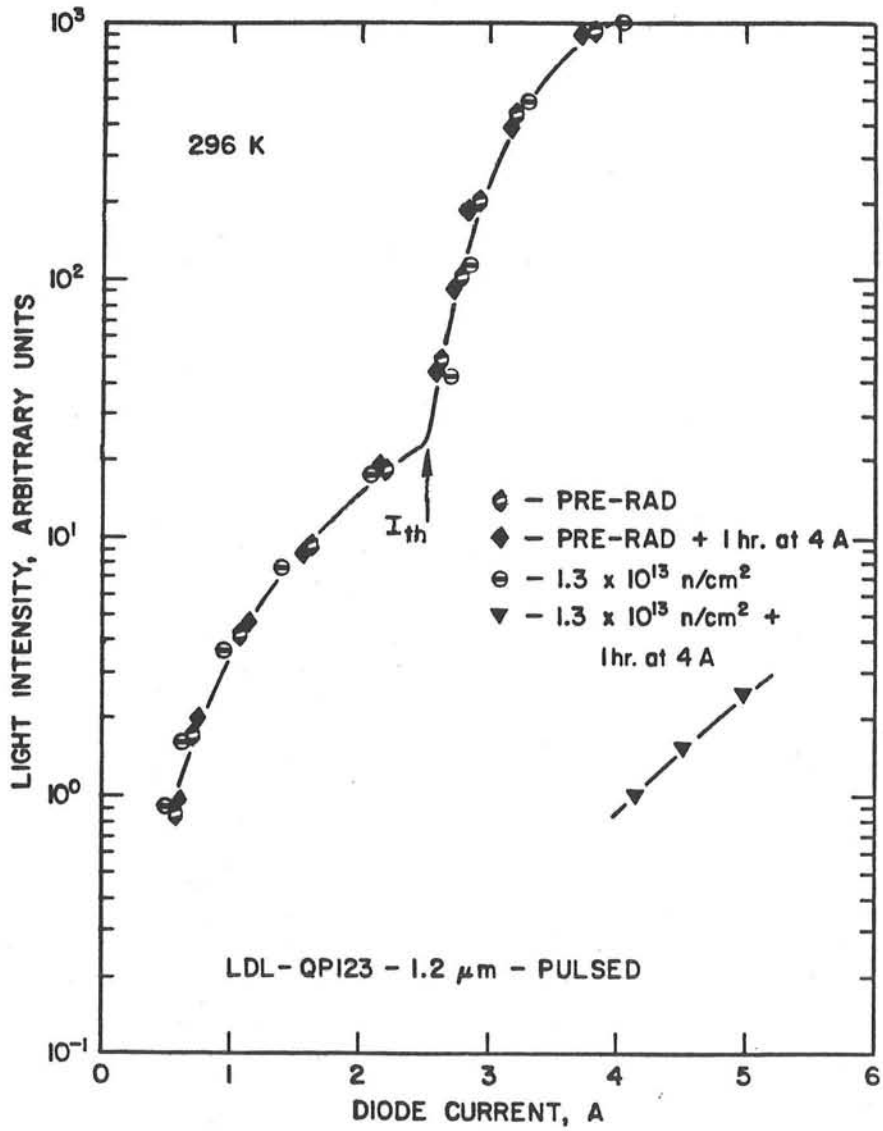

Fig. 2.8 Light output as a function of laser diode current for a Laser Diode Laboratories long wavelength emitting pulsed laser diode following a sequence of operations to demonstrate neutron enhanced operational degradation (from C. E. Barnes, p. 88 in Laser and Laser Systems Reliability, G. A. Evans, Ed., Proc. SPIE 328, Jan. 28, 1982, Los Angeles, CA).

In another recent study, Ackerman and Walsh (Ref.19) examined the effects of neutrons and Co-60 gamma rays on commercially available CW AlGaAs laser diodes from two suppliers. These devices were the same as those investigated in our recent study (Ref. 16). Degradation rates found by these authors were very similar to those observed in our previous studies (Refs. 10,12,15,16) resulting in similar lifetime-damage constant products as pointed out in a review of such work by Aukerman et. al. (Ref.20). There was, however, an important exception for the RCA AlGaAs laser (C 30127) when exposed to gamma rays. This device was found to be extremely sensitive: 1×10^4 Rads reduced the output by a factor of 2. This rather anomalous result could be an ionization-induced surface effect and further investigation is required.

Another laser diode property which may be susceptible to radiation is the time required for the laser to turn on after application of a current pulse. Pulsed operation of injection laser diodes near room temperature has shown, in some cases (Refs.21-23), that there is a delay in laser turn-on after application of the driving current pulse. This delay is greatest for currents near J_T and can reach values as high as a few hundred nanoseconds. The time delay has been explained using a double acceptor trapping model in which the empty second charged state of the trap causes strong optical absorption at the laser wavelength (Ref.23). Once this charged state is filled, the absorption decreases and the laser turns on. Since the model is based on the existence of nonradiative traps, it is possible that similar centers introduced by irradiation could induce the time

delay. This effect has been studied by Schroeder, et. al. (Ref.24) in neutron irradiated GaAs laser diodes. A neutron induced time delay was found which increased with fluence. The effect was most pronounced at currents well above J_T where the time delay prior to irradiation was quite short. In addition, it was determined that laser operation at a current about 20 percent above J_T minimized the damage-induced time delay in laser turn-on.

Thus far, we have discussed the effects of neutrons, gamma rays, and electrons on laser diodes. The results of a recent study by Minden (Ref.25) on proton bombardment of laser diodes are interesting because they differ with our earlier neutron damage studies. (Refs.12 and 13). Following 2 MeV proton bombardment, the threshold current increased. This was accompanied by majority carrier removal in the active p-type GaAs region. However, no increase in total current at low voltages was observed following bombardment. This latter result led to the conclusion that the proton-induced defects acted primarily as hole traps rather than as recombination centers. Further, it was concluded that the trapped holes were responsible for increased optical absorption in the active region leading to an increase in α. Consequently, in contrast with neutron irradiation, proton bombardment increases α but does not have a significant affect on the gain factor, β.

A more recent study (Ref.26) of proton damage in GaAs lasers has shown that the damage can be highly orientation dependent. In agreement with Minden (Ref.25) irradiation with 1.5 MeV protons perpendicular to the junction plane, that is, parallel to current flow, did not result in a significant change in current voltage

characteristic. However, irradiation parallel to the junction plane into one facet resulted in significant increases in diode current even though the protons penetrated only a fraction of the distance into the cavity (~ 20 μm into a > 500 μm cavity). Such an irradiation may have created a current shunt path along the near-surface region. This result is reminiscent of Ackerman and Walsh's (Ref.19) observation of the sensitivity of the RCA laser to Co-60 irradiation. Irradiation parallel to the junction also resulted in a light output degradation rate several times greater than that observed for perpendicular irradiation. While this result may be attributed in part to the current increase, it may also be due to a proton-induced change in the reflecting properties of the facet.

Lastly, we wish to mention other studies (Refs. 20,27,28) which discuss laser radiation damage within the context of fiber optic systems applications in radiation environments. While there appears to be some question about reliability and aging characteristics, irrespective of radiation effects, Aukerman, et. al. (Ref.20) and Evans and Leary (Ref.28) conclude that laser diodes are insensitive enough to irradiation to be employed in fiber optic links for radiation environments. Greenwell (Ref.27) in his analysis of fiber optic links for the Ground Launched Cruise Missile (GLCM) concludes that LED's are preferable to laser diodes at the present time primarily because this system does not require very high data rates, and also because of the greater reliability and simplicity of use of LED's.

Note that this choice was not based primarily on radiation sensitivity. Thus, we see that in the case of systems considerations, parameters other than radiation sensitivity may play a greater role in component selection.

3. SUMMARY

Studies of radiation damage in laser diodes have shown that injection laser operation is quite radiation insensitive because of the very short pre-irradiation lifetimes characteristic of intense laser operation. Therefore, these devices should perform quite well in those optoelectronic applications requiring exposure to a radiation environment. Care should be taken, however, to select a laser diode with low threshold current and high maximum allowable operating current. One should also be sure that the maximum expected radiation fluence will not cause an increase in J_T which results in laser shut-down at the operating current. The radiation-induced increase in J_T can be calculated using subthreshold $\tau_o K$ values for lasers and LEDs in a manner similar to that used to calculate light output degradation for LEDs in the previous Section. The effect of irradiation on J_T can be minimized by selecting lasers whose sub-threshold operation is similar to that of radiation-insensitive LEDs as described in the previous Section.

4. REFERENCES

1. For a thorough discussion of semiconductor lasers, see H. Kressel and J. K. Butler, Semiconductor Lasers and Heterojunction LEDs, (Academic Press, New York, 1977).
2. D. Botez, J. C. Connolly, and D. B. Gilbert, "High-Temperature CW and Pulsed Operation in Constricted Double-Heterojunction AℓGaAs Diode Lasers," Appl. Phys. Lett. 39, 3 (1981).
3. K. J. Ebeling, L. A. Coldren, B. I. Miller, and J. A. Rentschler, "Single-Mode Operation of Coupled-Cavity GaInAsP/InP Semiconductor Lasers," Appl. Phys. Lett. 42, 6 (1983).
4. S. M. Sze, Physics of Semiconductor Devices, 2nd edition (Wiley-Interscience, New York, 1981) p.
5. W. P. Dumke, "Interband Transitions and Laser Action," Phys. Rev. 127, 1559 (1962).
6. M. H. Pilkuhn, "The Injection Laser," Phys. Status Solidi. 25, 9 (1968).
7. J. I. Pankove, Optical Processes in Semiconductors (Prentice-Hall, New Jersey, 1971) p. 218.
8. N. G. Basov, "Effect of Injection Current on the Time Dependence of the Emission from GaAs Lasers," Sov. Phys. - Solid State 8, 2254 (1967).
9. M. Saji and Y. Inuishi, "Radiation Damage and Annealing of GaAs Lasers," Japan J. Appl. Phys. 4, 830 (1965).
10. C. E. Barnes, "Effects of Co-Go Gamma Irradiation on Epitaxial GaAs Laser Diodes," Phys. Rev. B1, 4735 (1970).

11. D. M. J. Compton and R. A. Cesena, "Mechanisms of Radiation Effects on Lasers," IEEE Trans. Nucl. Sci. NS-14, No. 6, 15 (1967).

12. C. E. Barnes, "Neutron Damage in Epitaxial GaAs Laser Diodes," J. Appl. Phys. 42, 1941 (1971).

13. C. E. Barnes, "Neutron Damage in GaAs Laser Diodes: At and Above Laser Theshold," IEEE Trans. Nucl Sci. NS-19, No. 6, 382 (1972).

14. H. Kressel and N. E. Byer, "Physical Basis of Noncatastrophic Degradation in GaAs Injection Lasers," IEEE Proc. 57, 25 (1969).

15. C. E. Barnes, "Increased Radiation Hardnes of GaAs Laser Diodes at High Current Densities," J. Appl. Phys. 45, 3485 (1974).

16. C. E. Barnes, "Neutron Damage Effects in Laser Diodes," in Laser and Laser Systems Reliability, Proc. of SPIE, Vol. 328, edited by G. A. Evans (SPIE, Bellingham, WA, 1982) p. 88.

17. T. Uji, T. Suzuki, and Kamejima, "Deep-Level Changes in (AℓGa)As Double-Heterostructure Lasers Degraded During Accelerated Aging at High Temperatures," Appl. Phys. Lett. 36, 655 (1980).

18. M. Ettenberg and H. Kressel, "The Reliability of (Aℓ Ga)As CW Laser Diodes," IEEE J. Quantum Elect. QE-16, 186 (1980).

19. H. Ackerman and T. E. Walsh, Sr., Air Force Weapons Laboratory Report No. AFWL-TR-79-43 (AFWL, Kirtland AFB, NM, 1980).

20. L. W. Aukerman, Y. Soug, F. L. Vernon, Jr, G. A. Evans, and J. Z. Wilcox, "Radiation Effects on Semiconductor Optical Devices for Space Communications," in Laser and Laser Systems Reliability, Proc. of SPIE, Vol. 328, edited by G. A. Evans (SPIE, Bellingham, WA, 1982) p. 56.

21. C. D. Dobson, J. Franks, and F. S. Keeble, "Characteristics of GaAs Lasers Near Room Temperature," IEEE J. Quantum Electronics QE-4, 151 (1968).

22. J. C. Dyment and J. E. Ripper, "Temperature Behavior of Stimulated Emission Delays in GaAs Diodes and a Proposed Trapping Model," IEEE J. Quantum Electronics, QE-4, 155 (1968).

23. J. E. Ripper, "Time Delays and Q Switching in Junction Lasers: I - Theory," IEEE J. Quantum Electronics QE-5, 391 (1969).

24. J. O. Schroeder, B. W. Noel, and H. D. Southward, "Radiation Damage-Induced Time Delay in GaAs Lasers," IEEE Trans. Nucl. Sci. NS-20, No. 6, 261 (1973).

25. H. J. Minden, "Effects of Proton Bombardment on the Properties of GaAs Laser Diodes," J. Appl. Phys. 47, 1090 (1976).

26. I. Arimura and C. E. Barnes, "Proton Damage in Laser Diodes and Light Emitting Diodes (LEDs)," in Laser and Laser Systems Reliability, Proc. of SPIE, Vol. 328, edited by G. A. Evans (SPIE, Bellingham, WA, 1982) p. 83.

27. R. A. Greenwell, "Tradeoff Between Laser Diodes and Light Emitting Diodes (LEDs) for the Common Weapon Control System," Ibid, p. 66.

28. G. Evans and J. Leary, "Application of Semiconductor Lasers in Space Communications," Optical Eng. 22, 247 (1983).

III. OPTICAL FIBERS

One can envisage many optoelectronic applications in which transmission of signals over finite distances is required and, hence, an optical fiber must be interposed between the emitter and detector. If such a data transmission link will be exposed to a radiation environment, an awareness of radiation effects in fibers can assist the designer in choosing those emitters and detectors which will minimize the effects of damage in the transmission link as a whole. The principal variable that must be chosen in this case is the wavelength of the light which will carry the signal. We have seen that a variety of LEDs and lasers are available which emit at several different peak wavelengths. In addition, various detectors are available which cover broad wavelength ranges. Consequently, there is enough flexibility in the choice of wavelength for emitters and detectors to allow consideration of those wavelengths at which radiation damage effects, either permanent or transient, are minimal in the optical fiber. In this section, we consider the work on radiation effects in fibers essentially from this point of view; that is, what restrictions does it place on the choice of emitters and detectors.

1. RELEVANT PRE-IRRADIATION PROPERTIES

Prior to a review of radiation damage effects, we briefly discuss the properties of optical fibers relevant to this report. More detailed presentations can be found elsewhere, (Refs.1-4)

including several books, (Refs.5-8) and articles in trade magazines (Refs.9 and 10) and Scientific American (Refs.11 and 12).

a. Operating characteristics - During recent years several types of fibers have been developed including step-index fibers, graded-index fibers, loose clad fibers (Ref.13), hollow core fibers (Ref.14) and liquid core fibers (Ref.15). The latter three types are rather exotic and do not enjoy wide usage. The operation of step index fibers is based on a difference in refractive indices between that for the core of the fiber, n_{co}, and that for the cladding surrounding the core, $n_{c\ell}$. Light entering the fiber core at an angle, θ_o, with the fiber axis will be refracted by the core material to an angle θ. The light ray will experience total internal reflection at the core-cladding interface and propagate down the fiber as long as θ is less than the critical angle, $\theta_c = \text{arc cos}\,(n_{c\ell}/n_{co})$. The magnitude of the total acceptance angle for light entering the fiber is usually expressed by the numerical aperture, N.A., which is given by

$$\text{N.A.} = n_{co} \sin \theta_c = [n_{co}^2 - n_{c\ell}^2]^{1/2}. \qquad (3.1)$$

Typically, $n_{co} - n_{c\ell} \approx .01$ to $.04$, N.A. ≈ 0.1 to 0.3, and $\theta_c \approx 10°$ to $15°$. As one would expect, the larger the N.A., the easier it is to couple an LED to the fiber. It has been shown (Ref.16) that the coupling efficiency for butt-end coupling of an LED to a step index fiber is proportional to $(\text{N.A.})^2$ when the LED emitting area is less than or equal to the size of the fiber core.

Unlike the step index fiber which depends on total internal reflection for confinement, n_{co} of the graded index fiber decreases from the center of the core to the cladding edge which results in confinement by continuous refraction of the light waves. This continuous bending of the light ray results in a near-sinusoidal ray pattern in contrast with the segmented straight-line ray reflection pattern in the step index fiber. As we will see shortly, the confinement method of the graded index fiber is highly advantageous compared to that of the step index fiber.

A light pulse of a certain shape and magnitude will, upon entering and traveling a significant distance through a real, non-ideal fiber, experience a reduction in magnitude and a temporal spreading of the pulse shape. The first effect is due to attenuation in the fiber, while the latter is due to dispersion. The attempt to minimize both of these deleterious effects has been the driving force behind continued modification and improvement of optical fibers. The operating wavelength chosen for a fiber optic link is also often determined by the need to avoid these effects. Hence, they can dictate the choice of source and detector. Therefore, it is pertinent to briefly discuss attenuation and dispersion in fibers.

b. <u>Fiber dispersion</u> - The three types of dispersion which cause degradation of the pulse shape and, hence, limit the fiber bandwidth are:

1) modal dispersion
2) material dispersion
3) waveguide dispersion

In the case of step index fibers, we have noted that the coupling efficiency can increase as $(N.A.)^2$. Unfortunately, modal dispersion effects also increase as $(N.A.)^2$ in the step index fiber. Because of the different angles at which light rays can enter the fiber and the consequent differing path lengths traveled by these rays, several modes of electromagnetic propagation are set up within the fiber with differing group velocities for each of the modes. It has been shown (Ref.17) that the number of modes, N_m, that can be supported by the fiber is proportional to the square of the core radius, r_c^2, and $(N.A.)^2$:

$$N_m \approx 0.5\left(\frac{\pi r_c \ N.A.}{\lambda}\right)^2 \tag{3.2}$$

where λ is the wavelength of the light. The various group velocities associated with these modes lead to dispersion or pulse broadening which limits the information bandwidth of multi-mode step-index fibers. The maximum difference in arrival time at the end of a fiber of given length is also proportional to $(N.A.)^2$ and is typically 20 ns to 50 ns/km.[2,3,5-8] Consequently, one is forced to make a compromise between efficient coupling of the LED to the step-index fiber, and the maximum bandwidth of the fiber. In spite of this, multi-mode step index fibers are attractive and useful, especially for moderate length and bandwidth applications that require transmission of considerable power. Fortunately, the observed mode dispersion is not as severe as expected for two reasons. First, higher order modes are severely attenuated. Second, there is coupling between modes caused by

longitudinal geometric and index of refraction variations along the fiber (Ref.18). If the mode mixing is sufficient the differences in group velocities will average out and the dispersion will be minimized.

The primary reason for the development of the graded index fiber was to minimize modal dispersion without sacrificing the coupling efficiency advantages of a relatively large N.A. fiber. When the index of refraction is smaller away from the core center line, those rays which enter the core at a large angle and, hence, have a longer path length, travel much of their path length in the lower index outer regions of the core where the velocity is higher than at the center of the core. When the index distribution is parabolic, the axial rays which travel a shorter distance, but at a slower speed, arrive at the fiber end at nearly the same time as the rays entering at a large angle. The net result is a reduction in multi-mode broadening to about 1 ns/km (Ref.6).

An alternate method of avoiding multi-mode dispersion is to eliminate all modes but the axial mode by reducing the core radius to a point where it will only support the axial mode as suggested by Equation 3.2.However, single mode fibers are restricted to a maximum radius of only a few microns which imposes two difficulties. First, it is difficult to manufacture long, uniform fibers at these radii and also maintain a close tolerance on the refractive index difference. Second, the only way to efficiently couple light into a small diameter fiber core is to use an injection laser. However, a great deal of progress has been made recently

in the manufacture of single mode fibers (Ref.19) and in the development of reliable laser diodes (Ref.20). Therefore in spite of these difficulties, single mode telephone systems have been deployed (Ref.21) and a single mode link operating at 5 GHz has been demonstrated (Ref.22).

Material dispersion and waveguide dispersion are both chromatic effects, that is, they depend on the presence of light of more than a single wavelength. Waveguide or intermodal dispersion arises because the group velocity of a given guided mode in a fiber depends on the wavelength. This type of dispersion is usually negligible unless both material and modal dispersion have been eliminated. Material or intramodal dispersion is present because the refractive index of the fiber material varies with wavelength in such a way that $d^2n_{co}/d\lambda^2$ is non-zero. Thus, the pulse broadening in time, Δt, in a fiber of length, L, is

$$\frac{\Delta t}{L} = \frac{\lambda^2}{c} \cdot \frac{\Delta\lambda}{\lambda} \cdot \frac{d^2n}{d\lambda^2}, \quad \text{ns/km} \tag{3.3}$$

where c is the speed of light and $\Delta\lambda$ is the source bandwidth. Fortunately, glasses have a wavelength value at which material dispersion is zero. For pure silica this occurs at $\lambda = 1.27$ μm (Ref.23). This zero dispersion wavelength can shift within the range 1.2 μm to 1.5 μm depending on the glass type and the dopants in the glass. For example, the addition of significant amounts of Ge to silica shifts the zero point from 1.27 μm to longer wavelengths (Ref.5) The existence of zero dispersion points at wavelengths in excess of 1.0 μm has provided considerable

motivation for developing sources and detectors in this wavelength range so that very high data rate, low loss systems can be constructed. At shorter wavelengths, a viable alternative is to substitute a laser for an LED to minimize material dispersion. For example, at 0.85 μm a typical AlGaAs LED will have a $\Delta\lambda$ of a few hundred angstroms resulting in a broadening of a few ns/km while the use of an AlGaAs laser at the same wavelength will reduce pulse broadening by a factor of about 30 to 100 (Refs.5 and 6). These results, and other aspects of dispersion-induced broadening are summarized in Figure 3.1 from Reference 24. Note that the pulse broadening can vary by more than a factor of 1000 depending on the type of fiber and the source spectral width.

c. Fiber attenuation - There are two mechanisms responsible for the attenuation which reduces the magnitude of the light signal as it travels down a fiber. The first is due to a variety of scattering mechanisms such as Raman or Brillouin scattering, scattering off imperfections, and Rayleigh scattering. In a normal, high quality fiber the only type of scattering which is significant is Rayleigh scattering (Refs.6 and 25). This type arises because of refractive index fluctuations in the glass due primarily to fluctuations in the atomic density of the basic material, and also to variations in the density of intentionally added impurities. It is important to note that this is essentially an intrinsic effect and represents the lower attenuation limit attainable for glass fibers. The Rayleigh scattering loss, α_r, is given approximately by $\alpha_r = A_s \lambda^4$, and therefore has a very strong dependence on wavelength. Recent measurements

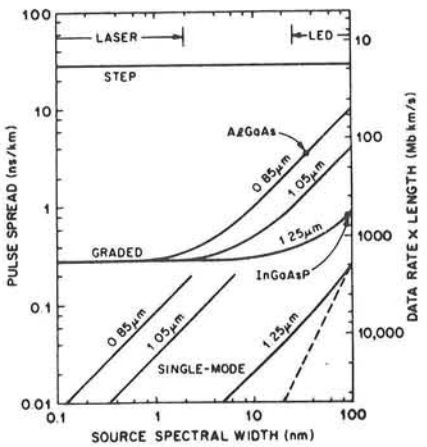

Fig. 3.1 Signal dispersion and bandwidth plotted versus the spectral width of the light source for three different types of fibers: step index, graded index and single mode. The dashed line corresponds to the fundamental limit for dispersion in silica fibers (from T. Li, IEEE Trans. Commun., COM-26, 946 (1978)).

(Ref.25) indicate that the scattering coefficient, A_s, is between 0.5 and 1.5 dB $\cdot$ km^{-1} $\cdot$ μm^4. In recent years many fibers have been fabricated which possess total attenuation figures near the Rayleigh scattering limit at wavelengths of interest.

The second and far more important attenuation mechanism from our point of view, is absorption of light within the fiber. Since the most important effect of radiation is a significant increase in absorption, we will be primarily concerned with this type of attenuation throughout the remainder of this Section. In addition to radiation-induced absorption centers (color centers), absorption in the fiber prior to any irradiation can also be significant. These attenuation effects are due to either intrinsic absorption, such as electron transitions and Si-O bond-induced absorption, or to impurities, such as dopants, OH-radicals, or transition metals, which may or may not be intentionally added to the fiber. Because of the nature of fibers, absorption is expressed in dB/km of fiber length rather than as cm^{-1} as is usually the case for absorption coefficients. The two units are related as follows,

$$\text{attenuation in } \frac{\text{dB}}{\text{km}} = 4.34 \times 10^5 \text{ (absorption coeff. in cm}^{-1}\text{)} \quad (3.4)$$

so that an attenuation of 10 dB/km, suitable for a practical fiber of significant length is equal to 2.3×10^{-5} cm^{-1}, an exceedingly small absorption coefficient.

The spectral behavior of various attenuation mechanisms is summarized in the composite graph shown in Figure 3.2 (Ref.6).

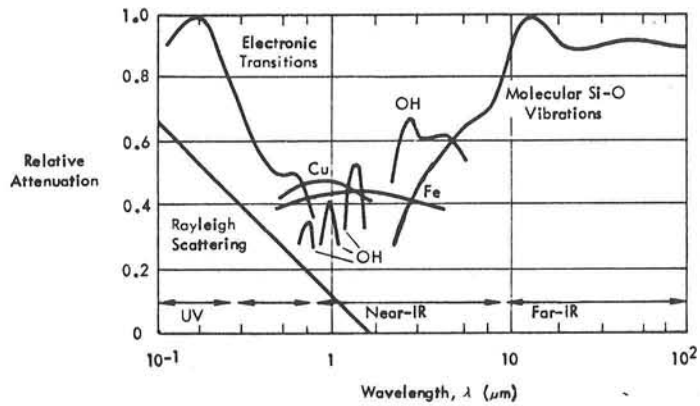

Fig. 3.2 Major contributions to the attenuation of light propagating in glass fibers. Note that the wavelength range is very broad and that the region of practical interest is between 0.8 μm and 1.6 μm (from H. F. Wolf, Ed., Handbook of Fiber Optics: Theory and Applications (Garland STPM Press, New York, 1979) p. 45).

Herein, relative attenuation rather than dB/km is plotted over a very broad wavelength range. Note that at the present time the range of practical interest is approximately 0.8 μm to 1.6 μm. All of the curves are absorption spectra with the exception of the Rayleigh scattering curve which, as we have already indicated, decreases rapidly with λ.

The various absorption phenomena can be classed as either intrinsic or extrinsic. The intrinsic absorption curves in Figure 3.2 are due to electronic transitions and Si-O bond vibrations. Because they are associated with the basic fiber material, these intrinsic mechanisms cannot be reduced significantly for a given type of glass. The electronic transition spectrum is due to electron-hole transitions near the band edge which have been broadened by local variations in the electric field (Ref.6). Fortunately, the broadening is usually not strong enough to cause strong absorption in the near IR region of practical interest. It is also fortunate that the UV attenuating mechanisms (Rayleigh scattering and electronic transitions) in combination with the strong far-IR absorption due to molecular Si-O bond vibrations, form a window between about 0.7 μm and 2 μm which corresponds with the wavelength region of available efficient sources and detectors. It should be noted that the IR side of this window can vary significantly from one glass to another and with various dopants added to the glass (Refs.26 and 27).

As shown in Figure 3.2, the attenuation in the window region is dominated by impurity absorption due to such species as OH and transition metals. Consequently considerable effort has been

expended to eliminate unwanted impurities through glass purification, and to find index-modifying dopants which do not strongly absorb in this region. Since the data in Figure 3.2 are given in relative units, we should note that an attenuation of about 1dB/km is expected for transition metal ion concentrations of one ppb, while the same loss is produced by OH concentrations of about one ppm (Ref.8). Progress in fiber fabrication techniques has essentially eliminated problems due to metals (Refs.28 and 29) but OH-induced absorption is somewhat more troublesome because it can come from several sources such as water absorption in starting materials, dissolution of starting materials, and contamination from nearby atmospheres (Ref.6).

Actual attenuation spectra for three typical low-loss silica fibers are shown in Figure 3.3 for the near IR. The absorption bands due to OH, centered at 0.95 μm and 0.725 μm, are superimposed on a continuously increasing attenuation with decreasing λ. As indicated by curve C, if the fiber is manufactured from "water-free" high purity fused silica, the OH band is significantly reduced. Spectra of fibers made by a variety of techniques from doped and high purity silicas are of this general appearance (Refs.3,5-8) as are the spectra for the better low-loss fibers made from compound glasses such as Selfoc (Refs.3 and 30). Recent reports of low loss fibers (Refs.29 and 31) also show the inverse dependence of attenuation on wavelength as the Rayleigh scattering limit is approached for the wavelength range below about 1.3 μm. An example of a state-of-the-art fiber with very low losses is shown in Figure 3.4 from the work of Miya,

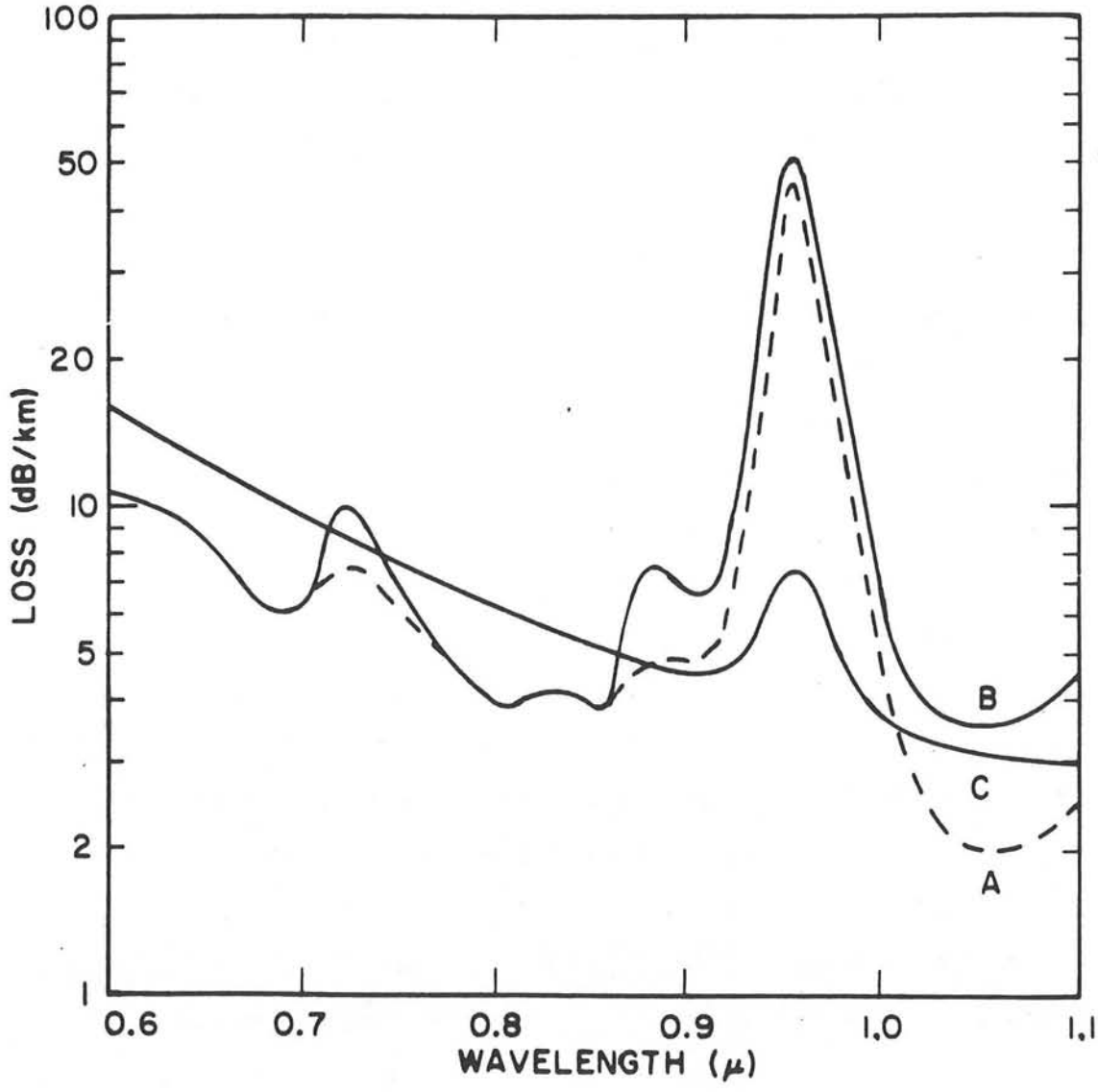

Fig. 3.3 Loss spectrum of three low-loss fibers. A and B-multimode fibers of doped-silica core and silica cladding drawn from flame-deposited preforms. C-single-material fiber drawn from Spectrosil WF (adapted from T. Li, p. 97 in Symposium on Optical and Acoustical Micro-Electronics (1974)).

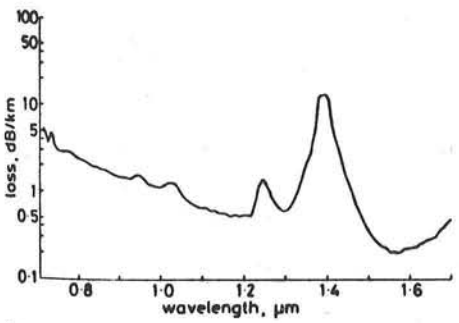

Fig. 3.4 The attenuation spectrum of a state-of-the-art single mode Ge doped silica core fiber. Core diameter is 9.4 μm and the refractive index difference is 0.0028 (from T. Miya, Y. Terunuma, T. Hosaka, and T. Miyashita, Electronics Lett. 15, 107 (1979)).

et. al. (Ref.29). This fiber is composed of a Ge doped silica core and a pure silica cladding. The index difference (0.0028) and the core diameter (9.8 μm) are both quite small as appropriate for a single mode fiber. The bands at 1.24 μm and 1.39 μm are due to residual OH. Note that near 1.3 μm and 1.6 μm the attenuation is below 1 dB/km. In fact, the value of 0.20 dB/km at 1.55 μm is very close to the Rayleigh scattering limit of 0.18 dB/km at this wavelength. These results also demonstrate that dopants, in this case Ge, can be added to the fiber core without sacrificing low attenuation characteristics.

Although the high purity doped and undoped silica core fibers possess low losses, they are relatively expensive, especially single mode fibers. Unfortunately, the less expensive, common compound glasses such as Pb flint, Zn crown, and Ba-La crown glasses contain relatively large impurity concentrations and therefore exhibit strong attenuation in the near IR and visible. Near $\lambda = 1.0$ μm, Pb flint and Zn crown glasses possess intrinsic losses of 10^3 to 10^4 dB/km (Ref.32). It has been argued (Ref.32), however, that these losses can be reduced to acceptable levels for short fiber runs. Recent work (Ref.33) in which losses as low as 20 dB/km were reported for Pb flint fibers, indicates that this approach may hold promise for the future.

Another important class of fibers are the plastic fibers such as polystyrene and polymethylmethacrylate (PMMA) which possess somewhat differernt absorption spectra compared to the high silica glasses. While they exhibit an absorption edge which increases with decreasing wavelength as one proceeds from the near IR into

the visible and ultra-violet, they also possess several intrinsic absorption bands for wavelengths greater than 0.80 μm which cause prohibitively high losses in this region (Refs.34 and 35). Consequently, visible emitting LEDs discussed earlier such as GaP and GaAsP, are more appropriate purely from the point of view of intrinsic loss. Since the plastics also show absorption edges increasing toward shorter wavelength, the optimum wavelength range would correspond to the visible red, such as 0.65 μm (Refs.34 and 35), which is above the absorption edge but also below the intrinsic absorption bands. The GaP:Zn, O LED and GaAsP LEDs are most appropriate for this range. Therefore, plastic fiber-visible LED combinations are appropriate for very short length data links and visible display applications.

d. Mechanical properties - Recent studies (Refs.6,36-40) have shown that fiber attenuation properties are susceptible to mechanical stress. This is an important consideration for certain applications which employ very rapid and rather exotic fiber pay-out techniques. In addition, although little work has been done in the area, there is some evidence in the literature and from work in our laboratory that there are strong synergistic effects of stress and radiation.

Increased losses due to mechanical loading fall into two classes. First, are so-called bending losses which increase the attenuation because the radius of curvature of the fiber is too small. The critical radius below which significant loss occurs is inversely proportional to N.A. (Ref.6). Even in a straight

length of fiber, bending losses can occur through so-called "microbending" in which a small particle or mechanical defect in the cladding or jacket causes a bump to occur in the fiber.

The second class of mechanical distortion has to do with actual mechanical stress applied to the fiber through such processes as winding, payout, jacketing, and rigid fastening to a supporting substrate. These processes include both dynamic strength and static strength loading. Catastrophic failures due to limitations of dynamic strength are important but a more insidious effect, and one that is most important for long term storage and usage, is static fatigue. This type of failure begins at a flaw in the fiber, such as a crack or hackle or dust particle within the glass (Refs.6,37 and 38). In addition to the presence of stress, moisture also considerably enhances the propagation of a flaw which leads to increasing attenuation and static failure. An additional complication with regard to failure testing is that static failure coefficients or "constants" are not independent of fiber length (Refs.36 and 38) and must be used with care in extrapolating to long fiber lengths. Lastly, recent Raman studies (Ref.39) have shown that stress causes changes in Si-O bond lengths as well as changes in the glass network structure. Consequently, one might expect intrinsic losses in the IR to change markedly due to stress.

e. <u>LED and laser selection</u> - The introductory remarks to this section indicated that one of the more important parameters on which to base selection of LED-fiber combinations is the

wavelength of the signal-carrying light. The dispersion and attenuation data summarized above for various fibers represent examples of the type of information required for proceeding with this selection. While the relationships between intrinsic losses and radiation induced losses in fibers are often complex, it is natural to consider the intrinsic losses in fibers prior to any examination of radiation-induced effects. The general form of the attenuation spectra for low loss silica core fibers represented by the data in Figures 3.2, 3.3, and 3.4 suggests that the appropriate wavelength regions for minimum loss are the minima between the various OH bands; that is, .82 μm, 1.05 μm, 1.2 μm, 1.3 μm, and 1.55 μm. As indicated above, these minima can shift depending on the glass type and the dopants. Also recall that the longest wavelength, 1.55 μm, is limited on the high wavelength side by the instrinsic IR absorption. The wavelength region near 0.82 μm corresponds to the peak emission wavelength of $Ga_{1-x}Al_xAs$ LEDs and lasers, where larger x values give emission at shorter wavelengths. The technology of these devices is well established and high power, high reliability emitters are available from a variety of suppliers. These include optimized configurations, such as high radiance Burrus and edge emitting LEDS which can be efficiently coupled to fibers.

Recent interest and development has focused on the longer wavelengths, especially 1.3 μm and 1.5 μm. Indeed, since the original writing of this Report in 1976, one of the most rapidly advancing research and development areas has centered on fibers, sources and detectors for the wavelength range 1.2 μm to 1.6 μm.

Not only are the attenuation losses extremely low in this range (see Fig. 3.4), but also the material dispersion is near zero at wavelengths within this range. LEDs, lasers, and detectors fabricated from various materials are now commercially available for operation between 1.2 μm and 1.6 μm. As indicated in other Sections, the most important material system for these devices is the quaternary, InGaAsP.

In summary, then, one can list the following points with regard to wavelength selection based on intrinsic losses in fibers:

1. For very short length applications and visible display purposes, plastic fibers coupled to visible-emitting sources are appropriate.

2. Multimode, step-index fibers are appropriate for short length applications which require only low to moderate data rates but high power transmission. The wavelength of choice would be the 0.80 μm to 0.85 μm window.

3. At moderate lengths and bit rates a graded index fiber also operating near 0.82 μm is most desirable.

4. For very high data rate, long length applications, single mode fibers coupled to 0.82 μm laser diodes are appropriate. However, the very low attenuation values and the lack of material dispersion at long wavelengths suggest that the long wavelength region near 1.3 μm to 1.6 μm is ultimately the most desirable.

2. RADIATION DAMAGE EFFECTS

It has been well established that the operation of optical fibers can be severely impaired in radiation environments. In particular, false signals can be generated by luminescence and signal strengths can be lowered by radiation-induced absorption. These effects are illustrated in Figure 3.5 for a polystyrene fiber exposed to a 1 krad dose from a 50 ns wide x-ray pulse (Ref.35). During irradiation the signal level increases due to luminescence generated in the fiber. Immediately after the peak of the x-ray pulse the signal level decreases and becomes less than the preirradiation level due to radiation-induced absorption, and then recovers with time to some permanent value. Typically the absorption remaining 24 hours after irradiation is considered permanent, although in reality thermally-induced recovery processes continue indefinitely. Consequently, the demarcation between "transient" and "permanent" attenuation is somewhat arbitrary and often highly dependent on the ambient temperature. However, we will retain this distinction in our discussion of radiation effects in fibers. This will be followed by a review of photobleaching studies which is the area of research our laboratory has been currently investigating.

Since the original edition of this Report (1976), there has been intensive effort devoted to research on radiation effects in optical fibers. This is exemplified by three symposia at recent meetings (Refs.41-43) and several recent review articles (Refs. 8,44-51) on this subject. This Report will emphasize this more recent work including that in our laboratory. We begin with a

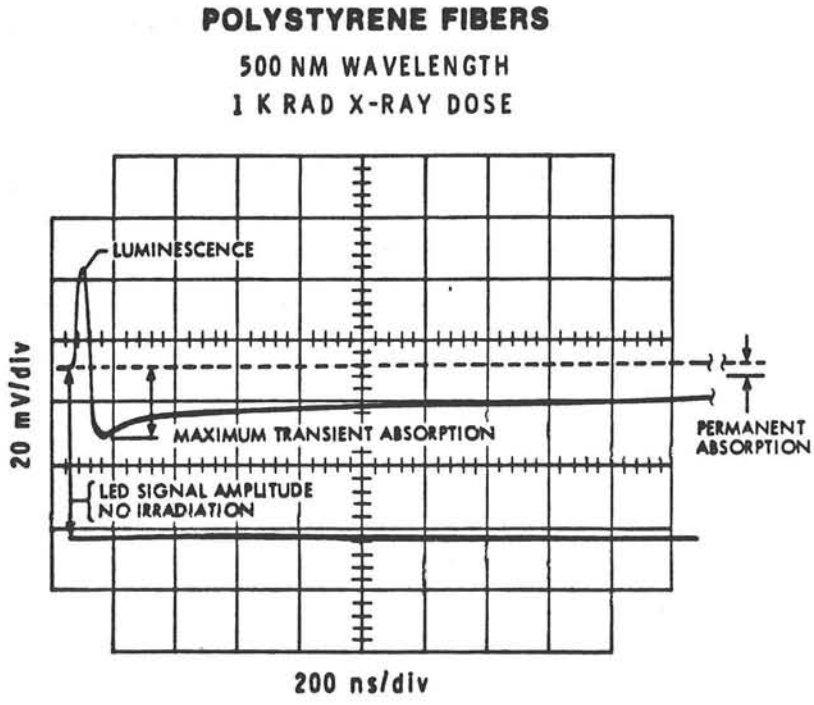

Fig. 3.5 An oscilloscope trace demonstrating radiation-induced luminescence and absorption in a polystyrene fiber bundle. The sharp increase in detected intensity, which peaks at 100 ns, is caused by luminescence in the fiber. A minimum in detected intensity is seen to occur near 170 ns, shortly after the termination of the irradiation, and indicates the maximum transient absorption (from P. L. Mattern, L. M. Watkins, C. D. Skoog, J. R. Brandon and E. H. Barsis, IEEE Trans. Nucl. Sci. NS-21, No. 6, 81 (1974)).

discussion of permanent damage effects in fibers and glasses.

a. Permanent damage effects - Permanent radiation-induced attenuation has been studied in a wide variety of glasses and optical fibers. An example of such work is shown in Figure 3.6 taken from Friebele et. al. (Ref.52) Attenuation in dB/km is plotted versus Co-60 gamma ray dose for several fibers. At this point, we will not discuss any of these results in detail, except to emphasize the wide variation in response of different fibers. First, we wish to make some background comments on radiation effects in bulk materials.

(1) Defects in glasses - Early work (Refs.53 and 54) established that irradiation of natural quartz and fused silica resulted in the growth of absorption bands associated with the creation of color centers as in the alkali halides. The most powerful tool for the microscopic identification of such centers is electron spin resonance (ESR). Once the structure of a color center is established by its characteristic ESR signature, correlations can be made between absorption bands and ESR signals through various parameters such as gamma-induced growth rates and isochronal annealing stages. In this way, one hopes to identify specific absorption bands with defects of known structure. Because of the nature of the ESR measurement, such identifications have usually been made in quartz and silica bulk material rather than in fibers. An excellent example of such a study is that by Griscom, et al (Ref. 54a) in which several correlations were made between ESR identified defects and optical absorption bands in P doped silica. Recent reviews of the microscopic nature of de-

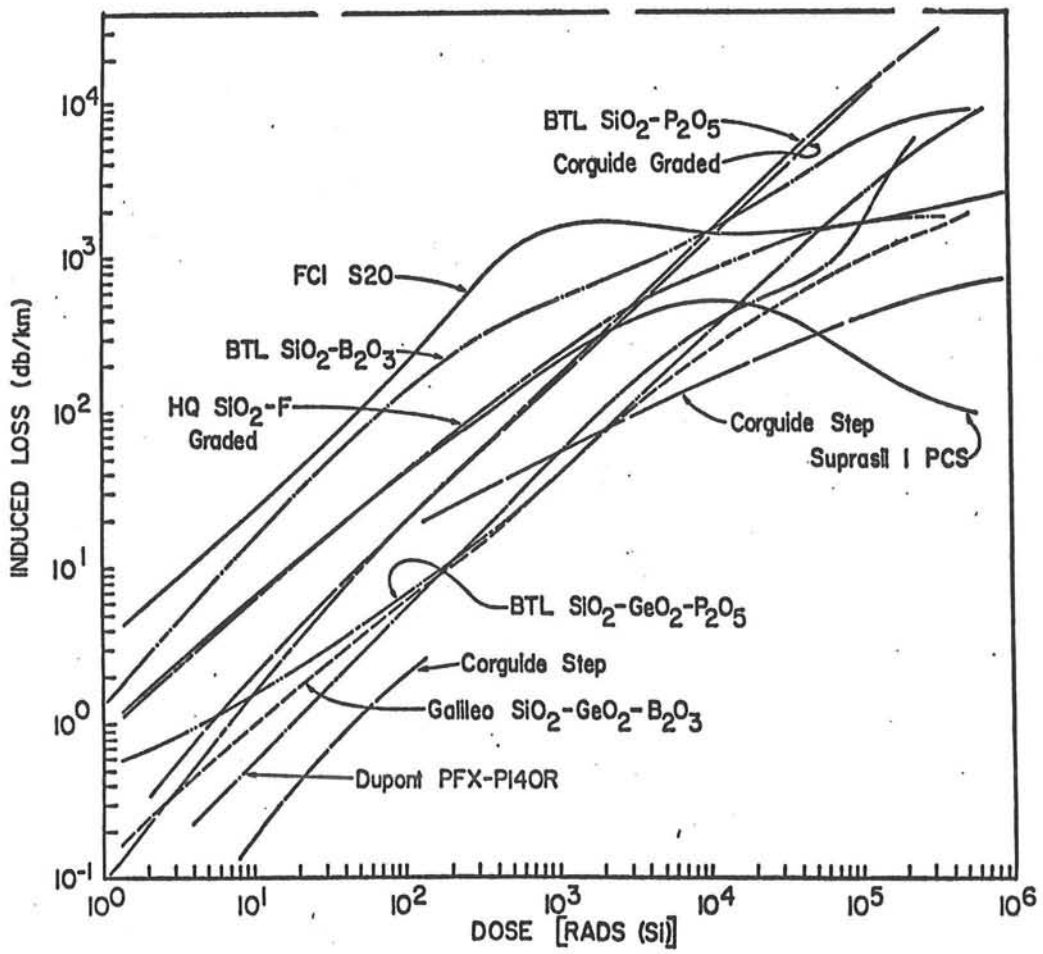

Fig. 3.6 Co-60 induced-attenuation growth curves for a variety of fibers at .820 μm. Dose rates were 25 rad/min for doses less than 100 rad and 1.8×10^4 rad/min for doses larger than 100 rad. Note that some of the curves are nearly linear while others show saturation effects (from E. J. Friebele, M. E. Gingerich, and G. H. Sigel, Jr., Appl. Phys. Lett. 32, 619 (1978)).

fects in quartz and silica have been provided by Griscom (Refs.54a and 55), and Friebele et. al. (Ref.56), Weil (Ref.57) and Greaves (Ref.58). We wish to merely indicate some of the most pertinent features of this large body of excellent work.

As schematically depicted in Figure 3.7, during exposure to irradiation, one can expect that a wide variety of defects will be created, and that the growth and anneal of these centers will proceed simultaneously in a complex fashion. The net result of this, as illustrated in Figure 3.8, is a wide variation in radiation sensitivity and in the resulting attenuation spectra for different glasses. This situation comes about because of the structure of quartz and silica in which both ionic and covalent bonding occur (Ref.53). In addition, as shown in Figure 3.7, a variety of impurities and defects such as dangling bonds, oxygen vacancies, and peroxy radicals, are often present even in high purity, quality materials, especially fibers. Color centers can be created in several ways in quartz and silica by both ionization and displacement. However, for those types of radiation which are strongly ionizing, direct displacement damage is believed to play a minor role in the build-up of color centers until very large doses are reached. This is primarily because large concentrations of trapping centers, often called precursors, are present prior to irradiation. The trapping of radiation-induced electrons and holes at these sites then constitutes the formation of color centers. Representative examples are given in Figure 3.7 and will be mentioned below.

An additional color center formation process, often referred

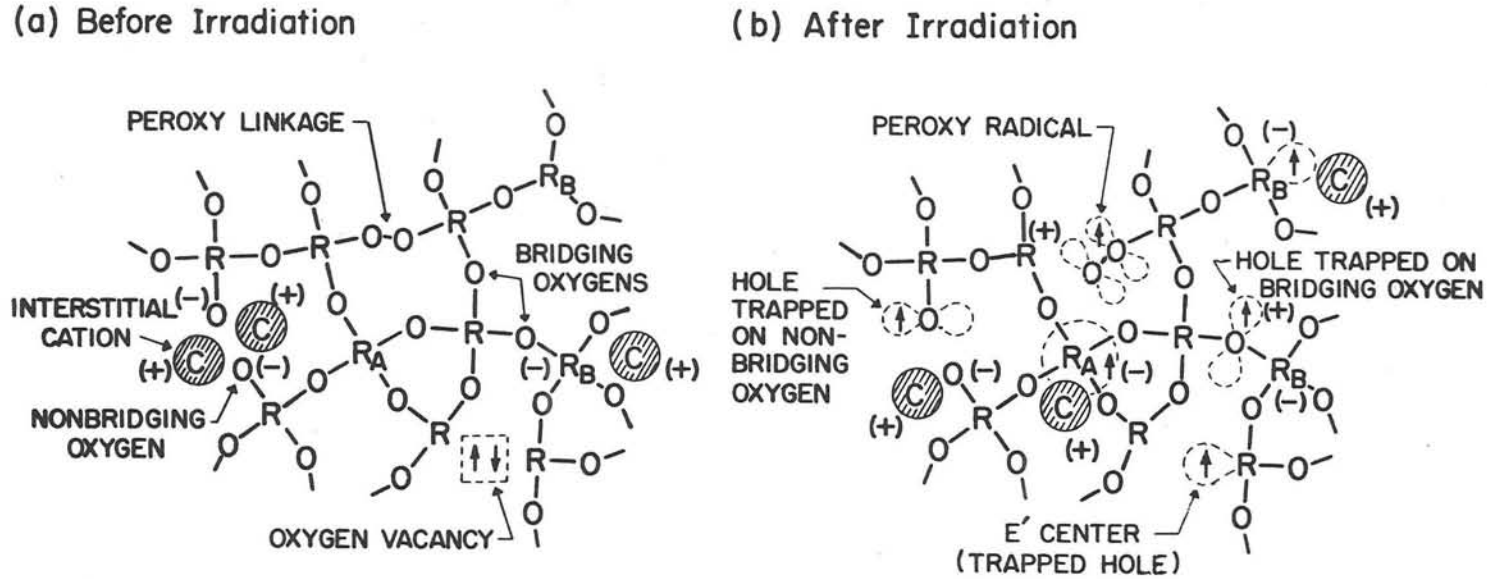

R, R_A, R_B = Network Formers = Si, B, P, Ge, Al, ...

C = Monovalent Network Modifying Cation = H, Li, Na, K, ...

Fig. 3.7 A schematic representation of a microscopic section of a silica glass before and after exposure to radiation. Several types of defects are shown both before and after irradiation. Note that alterations in charge compensation due to irradiation result in migration of certain species (from D. L. Griscom, E. J. Friebele, M. Stapelbroek, and G. H. Sigel, Jr., p. 11 in Proceedings of the Fiber Optics in the Nuclear Environment Symposium, R. C. Webb, Chairman, March 25-27, 1980, Harry Diamond Labs, ADelphi, MD, DNA Report No. DNA-5308 P-2).

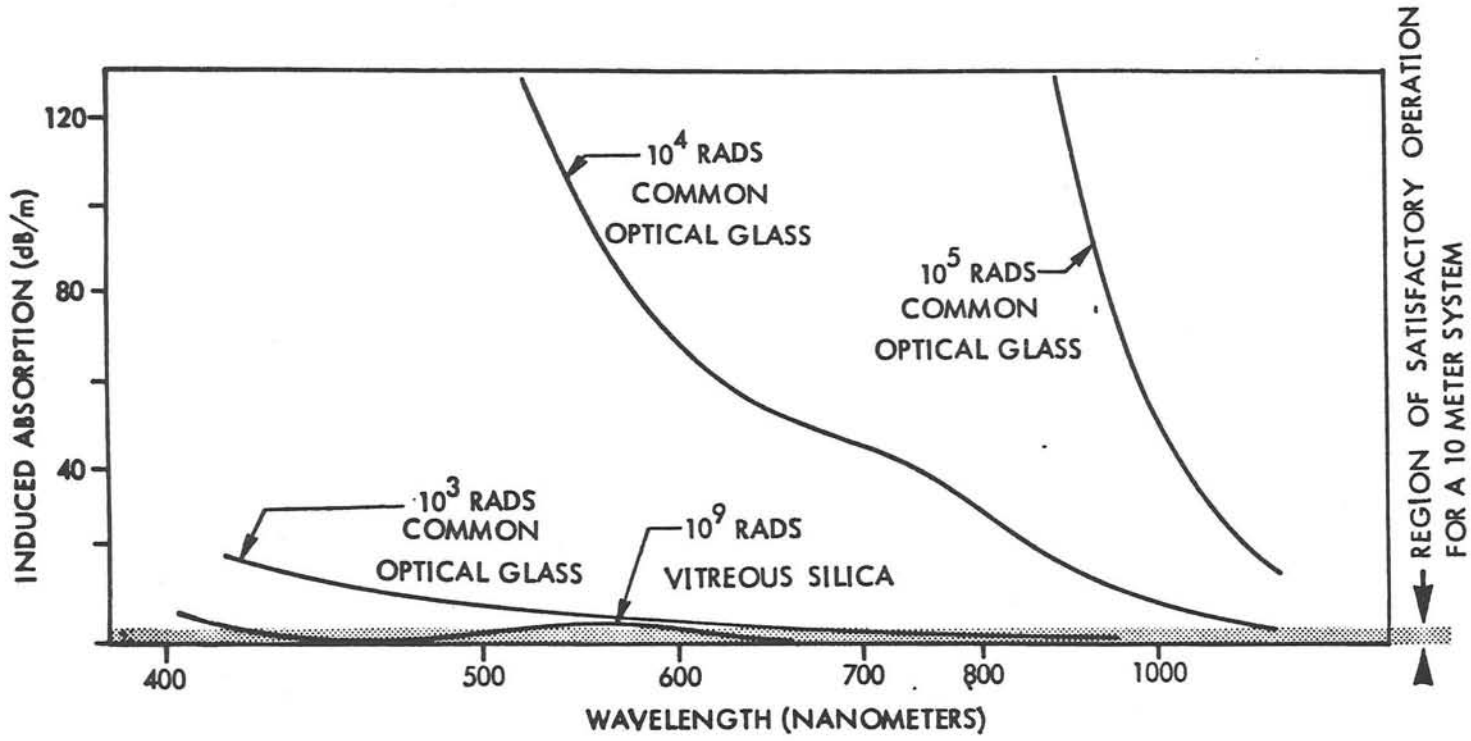

Fig. 3.8 Optical absorption spectra of common optical glass following Co-60 irradiations of 10^3, 10^4, and 10^5 rads, and of vitreous silica after 10^9 rads. The shaded region indicates the permissible range of induced absorption for a representative application employing a fiber length of 10 m (courtesy of E. H. Barsis, Sandia Laboratories).

to as radiolysis, is important and introduces a considerable amount of complexity. In radiolysis, after trapping an electron or hole, the trap becomes mobile, or if it is a complex center, breaks up and one or more of the components migrates away from the original site. As shown in Figure 3.7, an example of this process occurs in quartz which contains significant concentrations of Al, Ge, and an alkali (Refs.55 and 59). Prior to irradiation, many of the substitutional Al atoms are charge compensated by nearby alkali cations since Al normally has one less positive charge than the host Si atom. Upon irradiation, holes are trapped at the Al center and provide charge compensation which allows the alkali cation to migrate and, in turn, become part of a Ge center. It should be noted that hydrogen, an ubiquitous impurity in glasses, often plays the same role as the alkali atom. Such exchange reactions obviously complicate the color center formation and annealing processes which go on during irradiation. The kinetics of such processes are also influenced by the variation in concentrations of impurities and native defects. For example, for low concentrations of precursors, color center saturation can be observed. The above comments lead one to conclude that it is not surprising that many growth rate curves such as those in Figure 3.6 are not linear with dose.

One of the earliest and most widely studied (Ref.57) color centers in quartz is the so-called "Al center". The bare Al center, that is one that is not compensated by a nearby atom, consists of a hole trapped in a non-bonding 2 p orbital of an oxygen bonded to a substitutional Al and a neighboring Si atom. This center is

shown on the right side of Figure 3.7. As suggested in the previous paragraph, it is possible for an alkali or hydrogen atom to compensate the Al. In this case irradiation can produce different centers depending on the irradiation temperature which, in turn, governs the mobility of the migrating species (Ref.55). Although certain authors (Ref.60) are in disagreement, it is generally held that the bare Al center in quartz is associated with visible optical absorption bands at 2.0 eV and 2.6 eV (Ref.55).

With regard to most color centers, including the Al center, there are strong similarities between crystalline quartz and fused silica. This is not surprising since color center absorption processes depend on short range order rather than coupling to the lattice through phonon interactions. A greater variety of centers can be expected in silica, however, because many impurities, such as boron, which cannot be incorporated in crystalline quartz are easily added to silica glasses. In addition, silica will often tolerate greater concentrations of impurities. In the case of boron, an analogue to the Al center is found in borosilicate glasses. The ability to more easily incorporate impurities in silica can complicate the color center distribution and behavior, however. For example, Sigel (Ref.59) found that the visible absorption spectrum of silica was much more dramatically affected by irradiation when the glass contained both Al and alkali atoms as compared to silica containing either of these species by themselves.

The most important native defect center in quartz and fused silica is called the E′ center (Ref.55). In both materials, this center consists of an unpaired spin trapped at an oxygen vacancy

(see Figure 3.7). Whether the trapped spin is an electron or hole apparently depends on other characteristics (Ref.56). In high OH content silicas or those containing B or Al, the E′ center is believed to be an electron trap while in high purity, low-OH silicas it is a hole trap. There is also some question as to exactly what the E′ center precursor is in wet silicas (Ref.55). It has been been definitely established (Ref.61), however, that the E′ center is responsible for an absorption band in irradiated silica at 5.8 eV (0.215 μm). Based on several observations including the lack of photobleaching (Ref.59) and photoluminescence (Ref.59) for absorption in the 5.8 eV band, Griscom and Fowler (Ref.62) concluded that the energy transfer responsible for the 5.8 eV absorption consists of the electron hopping from one adjacent Si to the other. In this context, it should be noted that the formation of the E′ center is accompanied by highly asymmetric relaxation of the two Si atoms neighboring the oxygen vacancy (Ref.55).

Phosphorus is a particularly important impurity in silica fibers because it strongly alters the transient response of a fiber to pulsed irradiation (Refs.54a and.56). ESR studies (Refs. 54a and 56) of phosphorus doped silica glass have identified several phosphorus-asociated electron and hole traps, and correlated them with observed absorption bands. In particular, three of these defects, including a phosphorus-oxygen hole center, were associated with absorption bands in the UV, and a fourth center, the P_1 trap, was identified with an absorption band at 0.79 eV. These important correlations should be of value in sorting out the behavior of P-doped silica fibers.

With regard to Ge, irradiation does not produce unique Ge-associated color centers in silica as it does in crystalline quartz (Ref.56). An exception to this is that E′ centers do form in silica at oxygen vacancies where one of the nearest neighbors is a Ge atom.

Another important class of defects in irradiated silica, shown in Figure 3.7, is oxygen-associated hole centers (OHC's) (Ref.63). The precursors of these centers depend on whether the silica is "wet" (high OH) or "dry" (low OH). In high OH silica, there is an exchange of the hydrogen atom trapped at an oxygen with an ionization induced hole. Apparently, the liberated hydrogen atom travels at least several neighbors away from the remaining OHC (Ref.63). In low OH content silica, the precursor is either nonbridging (non-bonded) oxygen (NBO) or a peroxy linkage (an oxygen bonded to an oxygen) (Ref.56). Both of these defects are shown in Figure 3.7. The "dry" OHC formed by hole trapping at these precursors has been correlated with a UV absorption band at 7.6 eV (0.163 μm) (Ref.63).

In summary, we merely note that this very brief review of color centers in quartz and silica serves to emphasize the complexity associated with radiation damage in these materials. As we will see, this comment also applies to optical fibers.

(2) Pure silica core fibers - Inspection of Figure 3.7 suggests that if all the impurities could be eliminated from the silica structure, then the material would be less sensitive to radiation because of a lower concentration of color center precursors. This has been one of the motivating factors behind the development of the polymer clad silica (PCS) fiber. In this fiber, the core is drawn from very high purity synthetic silica

and clad with a polymer whose index of refraction is less than the silica. Such fibers are necessarily step-index fibers and, therefore have limited bandwidth. Coupling and splicing is also somewhat more difficult than with glass-on-glass fibers. In addition PCS fibers perform poorly below about -55° C due to the temperature dependence of the polymer properties. Although these detrimental properties are gradually being improved upon, alternative glass-on-glass structures have been developed which retain the pure silica core. Since the cladding must have a lower index of refraction than the core, the only dopants which can be used are those which lower the index of silica, namely boron and fluorine. Borosilicate and fluorosilicte clad pure silica core fibers are now available from suppliers. These fibers have low intrinsic losses and are a valuable complement to PCS fibers. All of the pure silica core fibers have one very important property in common, and that is, they are a very radiation resistant class of fibers. This general conclusion is the result of a wide variety of experimental studies (Refs.44,47,48,52,64-74).

The radiation insensitivity of pure silica core fibers can be attributed, in general, to their highly non-linear response of induced attenuation with dose. An example of this behavior is shown in Figure 3.6 for the Galileo PCS fiber. Note that the attenuation saturates, and that at higher doses radiation-induced recovery actually dominates. For low dose levels, the attenuation growth rate is often comparable to or greater than other types of fibers (Ref.66). However, the saturation behavior ultimately results in the PCS fibers being less sensitive. This behavior is generally characteristic of recent pure silica core fibers, either

characteristic of recent pure silica core fibers, either PCS or glass clad (Refs.67-69,74). Additional examples of this type of response are shown in Figure 3.9 from work in our laboratory (Ref. 74). In all, the response of five different PCS fibers and two fluoro-silicate clad fibers are shown in Figure 3.9 along with a standard Ge-doped silica core Corning fiber. Measurements were made using an AlGaAs laser operating at 0.82 μm. These data were taken at -55° C but room temperature behavior is similar (Refs.67 and 68).

Several features of Figure 3.9 are worth pointing out. First, as stated above, note that for irradiation times less than about 1 minute (dose ~ 4.1 krad), the initial, relatively rapid linear rise in attenuation is greater for some of these fibers than for the Ge-doped Corning SDF fiber. Second, all seven pure silica core fibers are either well into saturation or approaching it at doses of 8 krad to 20 krad for a dose rate of 4.1 krad/min. The similarities in response for all these fibers demonstrate that the cladding plays a minor role in the radiation response. This agrees with previous studies (Refs.66 and 67) of variations in cladding. In addition, it was found that the method of fiber drawing did not severely affect the fiber response (Refs.66 and 67).

Although the shapes of the curves in Figure 3.9 are all similar, except, of course, for the Corning SDF fiber, there are significant differences in the attenuation levels at which saturation occurs, and whether or not radiation-induced recovery is present. These differences can be attributed primarily to variations in the OH content of the fiber cores. Indeed, the water content of the fibers is the only important controllable parameter

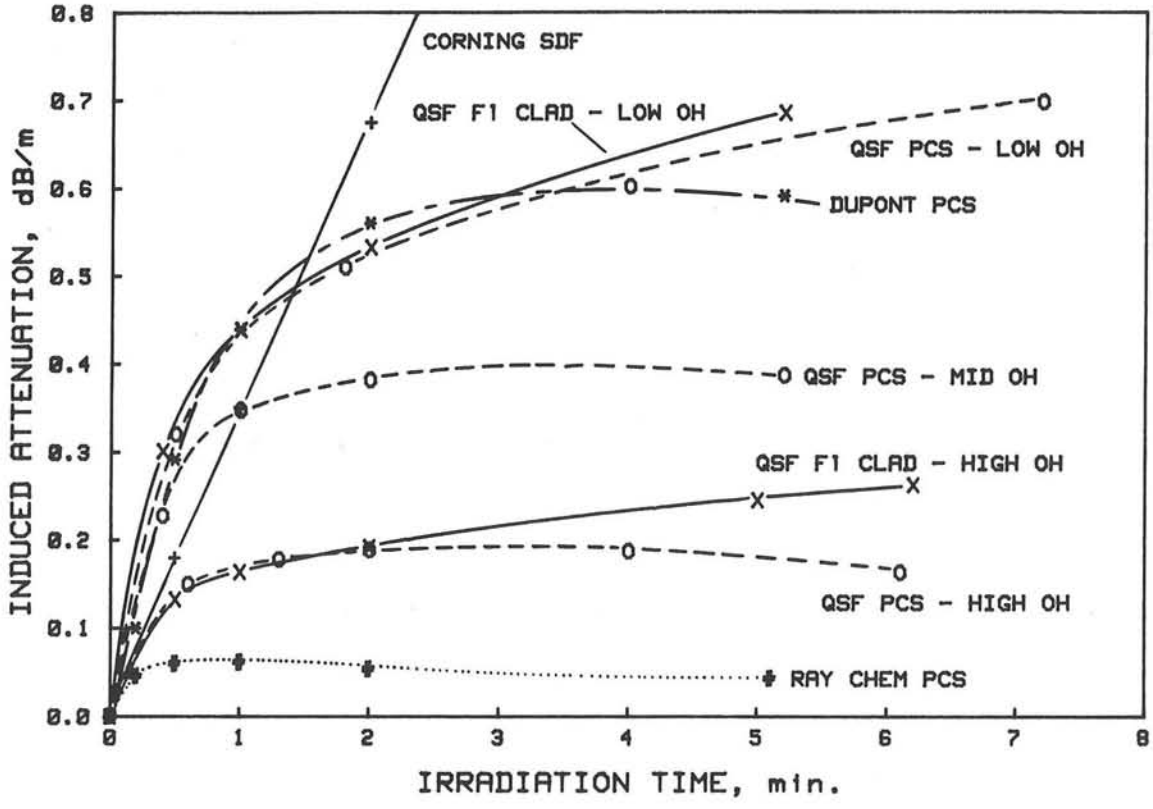

Fig. 3.9 Co-60 induced attenuation at -55°C and .820 μm in a variety of pure silica core fibers clad either with polymer (PCS) or fluorosilicate (F1) glass. A standard Corning fiber with Ge doped core is also shown. Dose rate for these irradiations was 4.1 krad/min (from C. E. Barnes, IEEE Trans. Nuc. Sci. NS-29, 1479 (1982)).

affecting radiation response of these fibers (Refs.47,67,68,71). Certainly, inadvertently added impurities such as transition metals affect the response but these are minimized by general purification techniques. In any case, several studies (Refs.44,47,48,52, 67,68,71) have shown that greater OH concentrations reduce the sensitivity of pure silica core fibers to irradiation and enhance the saturation effects. The results in Figure 3.9 at 0.82 μm illustrate this behavior. Of the three Quartz and Silice (QSF) PCS fibers shown, the dry, low OH (~ 10 ppm) fiber is the most sensitive, while the wet, high OH (~ 1200 ppm) fiber saturates quickly and exhibits recovery during irradiation. The third, moderate OH content (30-50 ppm) fiber is intermediate between these two. Similar results are shown for the fluorosilicate clad fibers.

Since higher OH content also leads to greater intrinsic attenuation at wavelengths corresponding to the OH absorption bands (see Figures 3.2, 3.3, 3.4) one must compromise between radiation sensitivity and intrinsic attenuation. An example of the wavelength dependence of the induced attenuation in a pure silica fiber is shown in Figure 3.10 for a PCS fiber with a high OH content Suprasil 2 core (Ref.71). At low doses the spectrum is dominated by broad featureless absorption, while at higher doses a band at 0.63 μm emerges with radiation-induced recovery occurring at longer wavelengths. At wavelengths between 1.0 and 1.6 μm the induced attenuation is even lower (Ref.71). Friebele and Gingerich (Ref.71) have summarized the near IR induced absorption in high OH silica fibers as consisting of a UV tail, featureless IR absorption, a band at 0.63 μm, and a

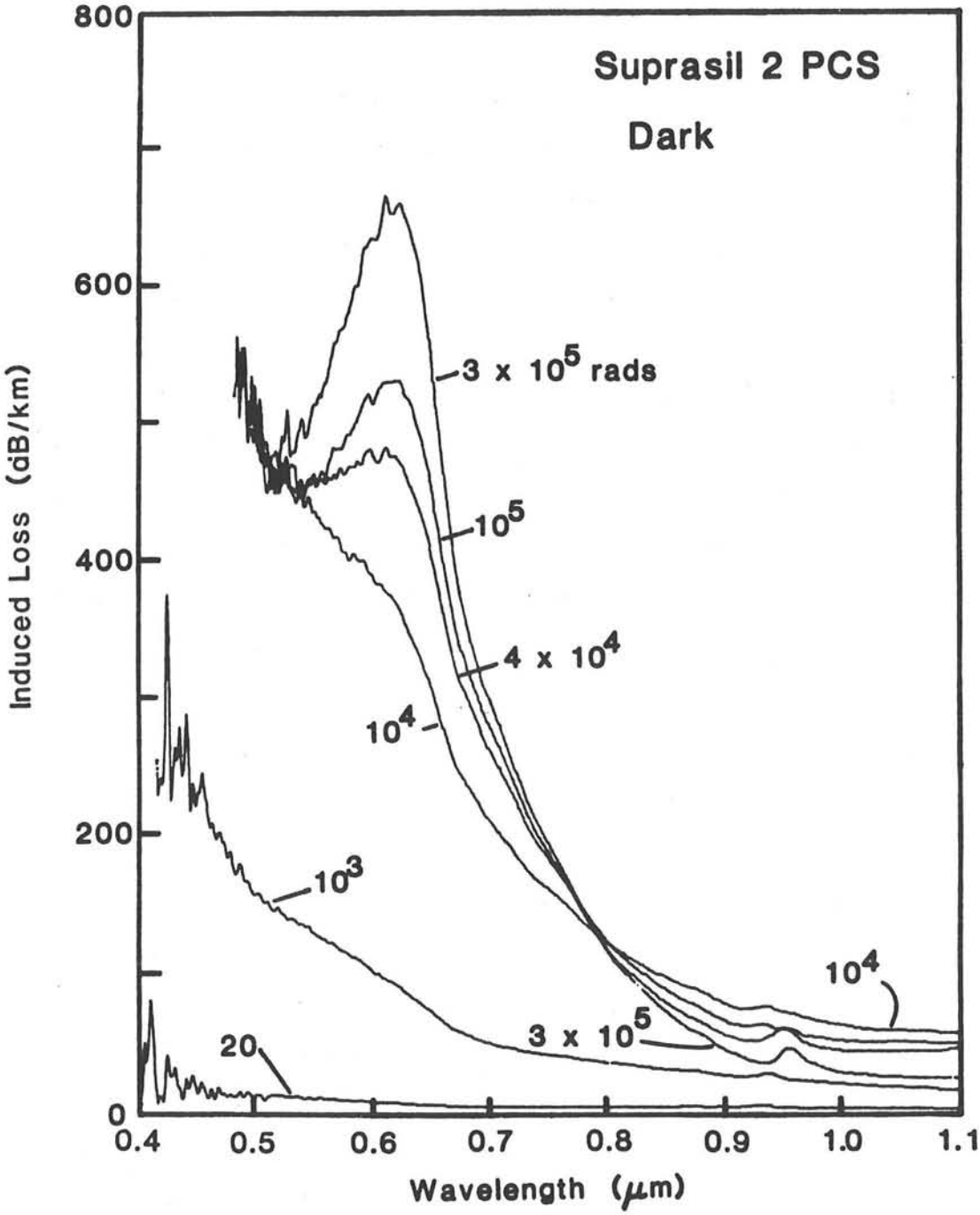

Fig. 3.10 Attenuation spectra at room temperature as a function of Co-60 dose for a PCS fiber with high OH content. Note the radiation-induced recovery above 0.80 μm (from E. J. Friebele and M. E. Gingerich, p. 37 in Proceedings of the Fiber Optics in the Nuclear Environment Symposium, R. C. Webb, Chairman, March 25-27, 1980, Harry Diamond Labs, Adelphi, MD, DNA Report No. DNA-5308 P-2).

band near 0.67 μm which can be photobleached. In dry fibers the photobleachable band is near 0.76 μm and is broader and relatively more intense so that it dominates the attenuation spectrum.

A definitive identification of the center responsible for the 0.63 μm band has not been achieved primarily because it has not been correlated with any ESR signals observed thus far (Ref.56). In alkali silicate glasses this band has been attributed to holes trapped at non-bridging oxygens (NBO's), that is, to oxygen hole centers (OHC's) (Ref.52). The fact that the growth of the 0.63 μm band does not saturate in irradiated high purity bulk silica agrees with its identification as a native defect (Ref.71). This band can also be induced in low OH content silica by the fiber drawing process (Ref.75). It has been suggested that the greater hardness of high OH fibers is due to fewer NBO's being available as hole traps because of the formation of OH bonds (Refs.52 and 67). This explanation assumes that it is the tail of the 0.63 μm band which is responsible for attenuation at longer wavelengths in the near IR. However, we have already noted that the OH bonds are precursors for OHC's in high OH content silica. In more recent work (Ref.72) this explanation has been modified in accordance with the spectra shown in Figure 3.10 which suggests that the absorption near 0.80 μm is due to a different center than the 0.63 μm band. Assuming that the IR absorption is due to metal impurity precursors, then the irradiation of high OH fibers, and also the drawing of low OH fibers, creates large numbers of traps (the 0.63 μm OHC centers) which compete with the IR absorbing centers for radiation-induced holes (Ref.71). We also note that if the fiber inadvertently

contains P, an absorption band at 0.79 μm can be expected (Ref.54a).

Share (Refs.70 and 72) has examined the temperature dependence of Co-60 induced-attenuation in a wide variety of fibers including some pure silica core fibers. As expected, losses were greater in low OH silica PCS and glass clad fibers than in high OH fibers over the temperature range investigated of -50°C to 70°C. For a given OH content, variations in response were observed for different fiber suppliers. This agrees with the above explanation that metal impurities are responsible for the near IR attenuation rather than the tail of the 0.63 μm band which is due to native OHC's. Share (Refs.70 and 72) observed that while the attenuation in pure silica core fibers was comparatively low, there were doped silica core fibers of similar and sometimes lower response. However, as noted by Share (Refs.70 and 72) near the maximum dose employed the upper dose limit of 5 krads was not sufficient to bring about strong saturation of the pure silica core fibers. In accordance with the data in Figure 3.9 one expects the pure silica fibers to perform better at higher doses.

(3) Complex glass and doped silica fibers - Early work (Refs.32-35, 64,65,76,77) on radiation effects in optical fibers and materials necessarily emphasized impure glasses and so-called complex glasses containing high percentages of dopants. One such example, the Galileo Pb silicate glass fiber, is shown in Figure 3.6. Note the greater radiation sensitivity of this fiber relative to the others in Figure 3.6. For a large variety of complex glass fibers, previous work (Refs.35 and 77) indicates that losses are in excess of 5 dB/km near 0.80 μm after 1 rad of Co-60

gamma ray dose. This loss figure exceeds those of modern-day low loss fibers especially at large doses where many of the recent fibers saturate.

In state-of-the-art fibers the most common index modifying dopants used in fiber cores are Ge, B, and P. The Ge doped fibers are currently very popular among commercial offerings. While we have noted that Ge doped fibers can have exceedingly low intrinsic losses (see Figure 3.4), unfortunately, Ge and the other common dopants usually increase the radiation sensitivity (Ref.68). This is primarily true at high doses because these fibers often do not saturate while high OH content pure silica core fibers do saturate, in some cases below 100 dB/km. This contrast is illustrated in Figures 3.6 and 3.9. It should be pointed out, however, that for certain Ge doped fibers some degree of saturation is observed (see Figure 3.6) and when combined with very low intrinsic losses, these fibers are more attractive at low doses than pure silica core fibers. Unlike the pure silica core fibers, the OH content up to 200 ppm has no effect on the radiation sensitivity of Ge doped fibers (Ref.71). The radiation response of these fibers also appears to be independent of the dopant in the glass cladding (Ref.68) although for some Ge doped core fibers mode stripping of the cladding does affect the measured radiation response (Ref.47).

The wavelength variation of the induced attenuation of Ge doped fibers and others is shown in Figure 3.11 for a dose of 10^5 rads. Note that representative spectra for pure silica core fibers (Suprasil, Suprasil W) are also given. Below about 1.4 μm,

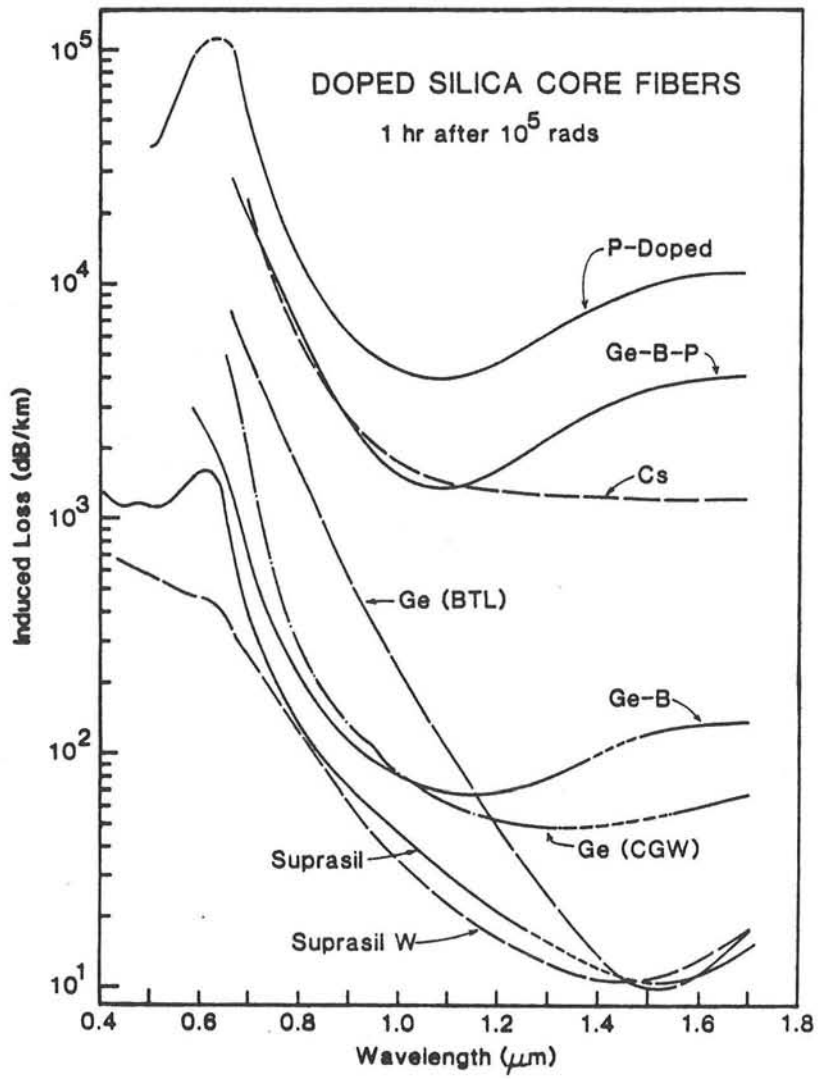

Fig. 3.11 Induced attenuation spectra for a variety of pure silica core and doped silica core fibers at room temperature one hour after a Co-60 irradiation of 10^5 rads. Note that both B and P doping strongly increase the IR attenuation (see Fig. 3-10 for reference).

the fibers doped only with Ge (BTL and CGW) show a featureless continuing increase of attenuation with decreasing wavelength. Recall that the E′ center earlier identified with an absorption band at 0.215 μm but which is shifted to 0.240 μm in Ge doped fibers (Ref.78), is one of the dominant color centers in Ge doped silica glass. Consequently, the continuum shown in Figure 3.11 may be the tail of this UV absorption. Note that for the Ge (BTL) fiber the losses are at or below 10 dB/km at 1.5 μm for this relatively large dose of 10^5 rads. Clearly this longer wavelength is a more desirable operating point as long as the OH concentration is minimized to reduce intrinsic attenuation.

The data in Figure 3.11 also show, however, that the various dopants added to the core can shift the wavelength of minimum attenuation. It has already been pointed out that B and P are also frequently used dopants. Phosphorus raises the refractive index at about the same rate per mole % as does Ge and it is significantly cheaper than Ge and forms high quality fiber cores readily (Ref.79). While the only effect of boron on the silica refractive index is to lower it slightly, it is an effective means of controlling the viscosity and, hence, the working temperature of the glass (Ref.5). We will see, however, that B has a detrimental effect on both the permanent and transient radiation response of fibers. As shown in Figure 3.11, the minimum attenuation increases significantly and the wavelength at the minimum moves to smaller values with the addition of B, possibly because of B-related color centers further in the IR (Ref.80). The differences shown between Ge (BTL) and Ge (CGW)

fibers were also attributed (Ref.71) to B because the cladding of the CGW fiber was B doped resulting in slight grading of the B into the core.

The addition of phosphorus to a silica fiber core causes dramatic changes in both the transient and permanent attenuation. As shown in Figure 3.11, the permanent attenuation is much greater over the entire wavelength range for P containing fibers. If boron is also added, the attenuation levels are between those of Ge doped and P doped fibers. As will be shown, however, the addition of P does have redeeming advantages with regard to the temperature dependence of the attenuation and, in particular, the transient attenuation following a radiation pulse.

In attempts to minimize the radiation sensitivity of doped silica core fibers, combinations of various dopants have been added to the core including several, such as Sb (Refs.68,81,82), Cs (Ref.83), Ce (Refs.36,76,77,81,84), Tl (Ref.83), Ta (Ref.68), and H (Refs.85 and 86) which are rather unusual. The elements Ta, Cs, and Tl appear to be ineffective in reducing attenuation. The same can be said for Sb (Ref.68), although it does seem to be effective as a co-dopant with P in minimizing the detrimental effects of P (Refs.81 and 82). It has been shown (Refs.85 and 86) that hydrogen dissolved in glass suppresses the formation of radiation-induced absorption centers. However, a practical scheme for retaining the necessary quantities of dissolved gas has not been demonstrated.

The results for Ce doping have been mixed. Wall et. al. (Ref.81) noticed a reduction in attenuation for certain co-dopants

and for some of the temperatures studied. A general improvement due to Ce was not observed, however. In other studies (Refs.32, 76,77, 84), Sigel, Friebele and co-workers have investigated the applicability of Ce-doping for the radiation protection of fibers made from lead flint, barium crown, soda lime silicate, and Zn crown glasses. The motivation for these studies is based on the lower cost of these glasses relative to low-loss silicas, and on the high N.A. values which are achievable with fibers made from these glasses. This work has shown that Ce doping is effective in reducing the radiation sensitivity of common glass fibers. For example, the induced attenuation rate at 0.80 μm measured 20 minutes after irradiation was reduced from about 9 dB/km-rad to 8 x 10^{-3} dB/km-rad when Pb flint glass was doped with 1% Ce. Unfortunately, this significant reduction in sensitivity is offset by a corresponding increase in the intrinsic attenuation so that the total attenuation, intrinsic plus induced, of these glasses is still markedly inferior to the low loss, high silica glasses.

The effect of various dopants on the temperature dependence of the induced attenuation in silica fibers has also been investigated (Refs.69,70,72,73,81,87-89). The results of Wall and co-workers (Refs.81 and 89) on fibers with Ge, P, B, Ce and Sb in different combinations seem to be rather unexpected in that greater attenuation was often observed at higher temperatures. In silica core fibers containing Ge and P, the 0.85 μm attenuation increased with increasing temperature over the range -55°C to +125°C (Ref.89). In the other study (Ref.81), the 0.905 μm

attenuation at +125 C was intermediate between the -55°C and +20°C values for various combinations of Ge, B, P, Ce and Sb except for a Ce, Ge, and P containing fiber for which there was almost no temperature dependence. The work of McAlarney et. al. (Ref.73) and Share and co-workers (Refs.70,72, 87,88) does not agree with this temperature dependence. With the exception of P containing fibers for which there was either no change with increasing temperature or a small increase, the attenuation always increased with decreasing temperature. Representative results at 0.80 μm are shown in Figure 3.12 from Ref. 70. Also included in these data are two fluorosilicate clad, undoped suprasil core fibers. Similar temperature dependences were obtained at a wavelength of 1.3 μm but the attenuation values were lower by factors of 5 to 10 as is generally the case in going to longer wavelengths. The striking feature of these results is the suppression of the temperature dependence brought about by P doping. We have noted earlier that the presence of P causes significantly greater attenuation at room temperature at all wavelengths (see Figure 3.11). However, the data in Figure 3.12 illustrate that because of the lack of temperature dependence, P containing fibers have lower attenuation than many others at temperatures near -30°C to -50°C. The lack of temperature dependence suggests that the P-associated traps are very deep and quite stable.

(4) Plastic fibers - Radiation effects in plastic fibers have received limited attention (Refs.35,64,83,90) especially in more recent years as practical interest has shifted to fiber

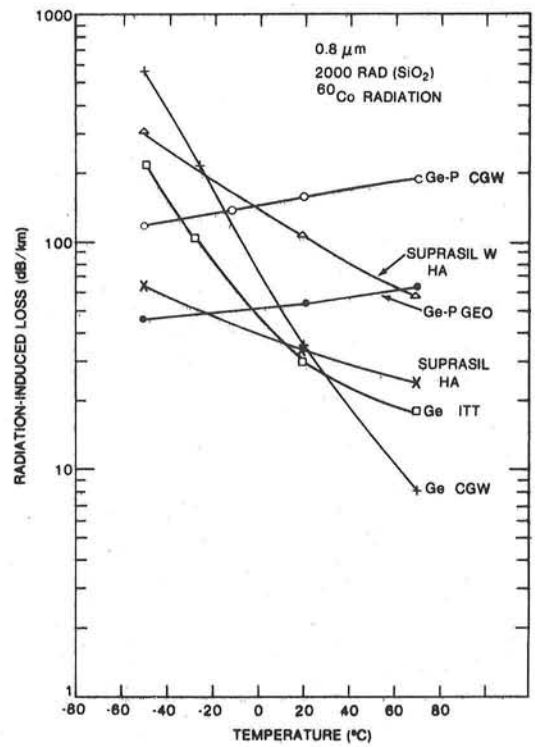

Fig. 3.12 Co-60 induced attenuation at 0.80 μm in a variety of fibers for a 2.0 krad irradiation at 95 rads/sec. Irradiations and measurements were performed as a function of temperature. Note the significant effect of P-doping on the temperature dependence (from S. Share, p. 51 in Fiber Optics in Adverse Environments, P. B. Lyons, Ed., Proc. of SPIE 296, Aug. 25-27, 1981, San Diego, CA).

optic links at longer wavelengths where the plastics are poor because of high intrinsic losses. It should be emphasized, however, that plastic fibers are relatively insensitive to radiation as demonstrated by the all plastic DuPont fiber shown in Figure 3.6. Generally, radiation affects these fibers in a manner similar to that for glass core fibers. That is, the induced attenuation increases with decreasing wavelength (Refs.35 and 64). It has been concluded that, within the wavelength range 0.65 μm to 0.80 μm, plastic fibers are appropriate for those applications requiring fiber lengths less than 30 to 40 m for maximum doses less than 10^6 rads (Ref.35).

b. Transient damage effects

(1) Luminescence - The transient radiation effects shown in Figure 3.5 consist of both luminescence and attenuation. The luminescence is undesirable in communications applications because of possible false signal generation. The induced luminescence occurs primarily during irradiation, while the transient attenuation can persist for long times after irradiation. For this reason, luminescence has been regarded as less of a problem, and thus has received somewhat less attention than the transient attenuation. This is not to say that luminescence poses no problems. For example, Mattern, et. al. (Ref.35) estimated that at a dose rate of 10^9 rads/s of 1 MeV photons into 10 m of a low loss fiber (which shows less luminescence than other fibers) one can expect a light output power of 1 mW during the pulse even when the light is filtered by a 0.10 μm wide band pass

filter centered at 0.90 μm. These authors (Refs. 35 and 65) also found that the light output after the radiation pulse was always less than 1% of the prompt luminescence signal for a variety of fibers.

Various studies (Refs.35,59,65,77,91) have found luminescence peaks at or below 0.45 μm in both silica and quartz exposed to different types of radiation. More recently (Ref.92), however, an additional luminescence band centered at 0.65 μm has been observed during x-ray irradiation of a high OH PCS fiber. This same band has also been detected as photoluminescence in both irradiated fibers and as-drawn low OH fibers (Ref.92). Fortunately, the spectral width of the 0.65 μm band is approximately 0.10 μm so that it should not pose a problem for fiber optic operation at wavelengths greater than 0.80 μm.

In a series of elegant experiments, P. B. Lyons and co-workers (Refs.91,93-97) at LANL have examined both transient radiation-induced luminescence and attenuation at times less than 1 μs after the radiation pulse. These studies have included exposures on underground nuclear tests. With regard to luminescence, the most important result of this work was the demonstration that the primary luminescence from fibers during an intense ionization pulse was of Cerenkov origin. This conclusion was based on the dependence of luminescence intensity on the angle between the fiber axis and the electron beam, and also on the value of this angle (45°) at which the light is most intense. Fortunately, for most fiber optic applications, although not for underground test diagnostics, the Cerenkov luminescence is prompt and is not

present after the radiation pulse has ceased.

(2) Transient attenuation in pure silica core fibers - For the majority of practical applications involving exposure to a radiation environment, the fiber optic data link must be operable a short time after a burst of ionizing radiation has occurred. When this requirement is imposed on the system, transient attenuation in the fiber becomes the most severe radiation effects problem, and, therefore, the limiting criterion one must use in selecting a fiber for a given set of conditions. As for the case of permanent damage, several studies (Refs.47,52,66,67,69, 91,95-100) have shown that the pure silica core fibers exhibit relatively low transient attenuation following a radiation pulse. Investigation (Refs.91,95-97) of transient attenuation in a variety of pure silica core fibers at early times after a radiation pulse, that is, from 1 ns to 100 ns, demonstraated that the decay of transient attenuation could be described by a geminate recombination model. Typical recovery transients at .85 μm are shown in Figure 3.13 from this work (Ref.97). Note that the best fiber, the ITT T303 PCS, is below 10^4 dB/km at 100 ns, an exceedingly low attenuation at this point in time after a pulse greater than a megarad. The geminate recombination model describes the recombination of correlated diffusing pairs. At these early times, apparently the transient attenuation follows the same behavior as the recombination of radiation-ionized lattice atoms with their electrons. An analysis (Ref.97) of the temperature dependence of the early time recovery revealed an activation energy for geminate recombination of 0.22 eV.

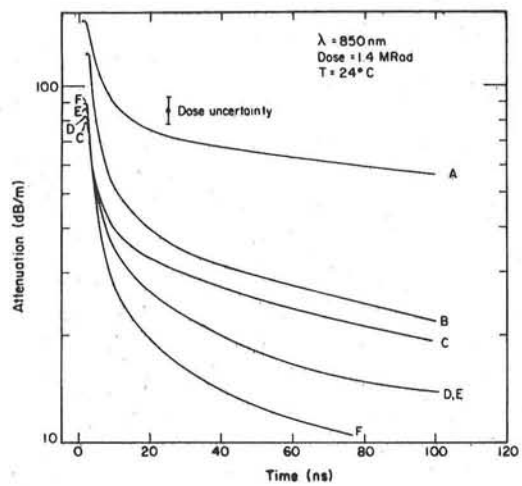

Fig. 3 .13 Transient attenuation at early times in a variey of pure silica core fibers following a radiation pulse of 1.4 Mrad. Fibers A, C, and D have doped glass cladding, while B, E, and F are PCS fibers. Fibers C and D are the same except D has higher OH content (from L. D. Looney, G. Turquet de Beauregard, P. B. Lyons, R. E. Kelly, p. 17 in Fiber Optics in Adverse Environments, P. B. Lyons, Ed., Proc. of SPIE 296, August 25-27, 1981, San Diego, CA).

Typical transient attenuation data at 0.82 μm in pure silica core fibers at later times after a 3.7 krad electron pulse are shown in Figure 3.14 from Ref. 47. As in the case of the early time behavior, an ITT fiber has the lowest attenuation in this group of fibers. Included in Figure 3.14 are two fluorosilicate clad fibers (C, D) with differing OH concentrations. Similar to permanent damage in pure silica fibers, a higher OH content also leads to less transient attenuation. Note that for some of these fibers there is a shoulder in the recovery curves at around 10^{-2} s. In other pure silica core fibers (Ref.66) this is a much more pronounced feature of the transient attenuation curves. Such structure in the recovery curves implies the existence of at least two recovery processes with significantly differing time constants.

The wavelength dependence of the transient attenuation is also similar to the permanent damage in that the transient effects are significantly lower at longer wavelengths. An example of real-time spectral measurements using a vidicon tube is shown in Figure 3.15 for a low OH PCS fiber exposed to a 14 krad electron pulse (Ref.45). Within 10's of μs of the pulse, the attenuation is centered near 0.50 μm. At later times, as the attenuation recovers the peak moves to longer wavelengths until at 30 s after the pulse, the absorption peaks near .70 μm. Recall that this latter wavelength is near the peak (.76 μm) of the photobleachable band seen in the "permanent" attenuation spectrum of low OH pure silica core fibers (Ref.71). From a qualitative point of view one might expect a center which is susceptible to bleaching to

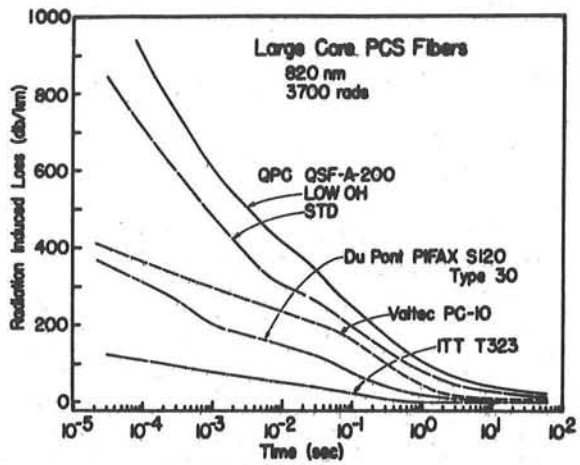

Fig. 3.14 Recovery of transient attenuation at room temperature and 0.82 μm in a variety of PCS fibers all with large diameter cores. The radiation pulse was a 3 nsec wide electron pulse from a Febetron 706 (from G. H. Sigel, Jr., E. J. Friebele, M. E. Gingerich, and L. M. Hayden, IEEE Trans. Nuc. Sci. NS-26, 4796 (1979)).

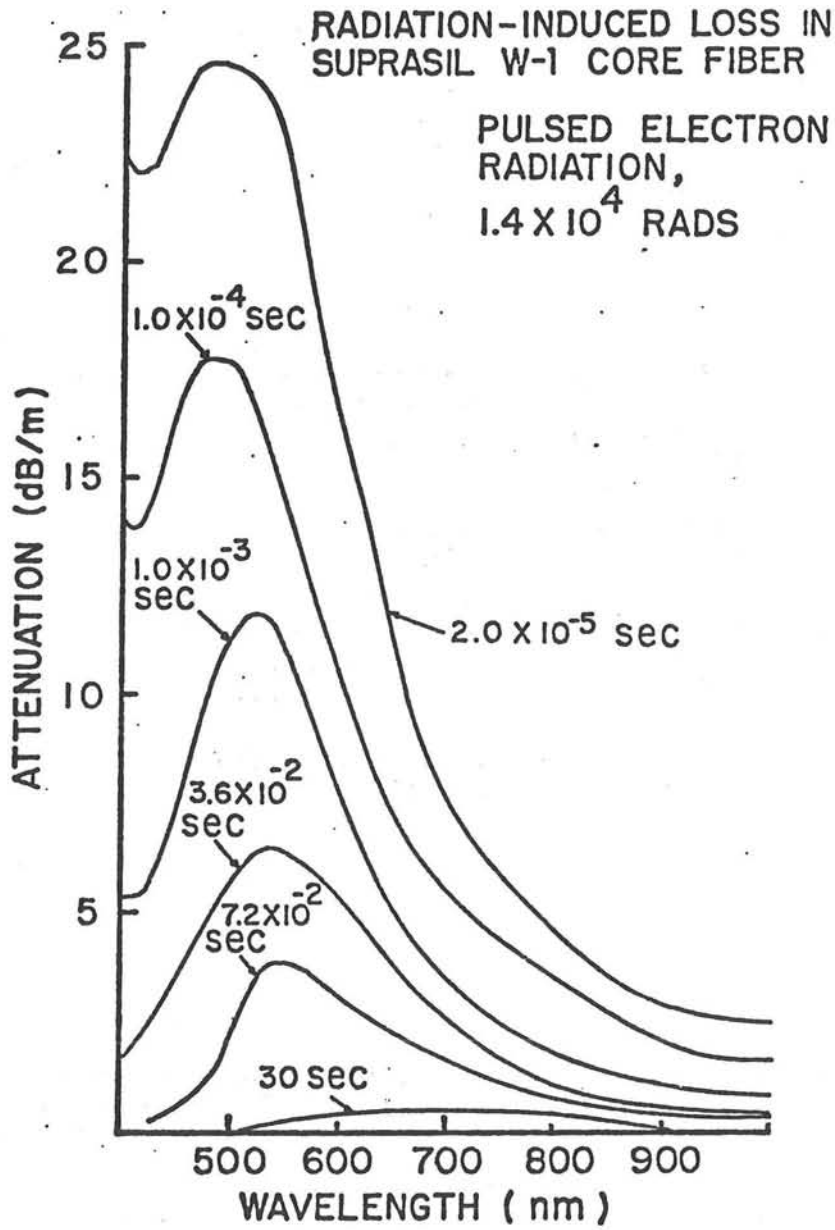

Fig. 3.15 Transient attenuation spectrum in a PCS fiber at different times following a 0.5 MeV electron pulse at room temperature. The suprasil W-1 core is a low OH material (from G. H. Sigel, Jr., presented at Recent Advances in Fiber Optics, University of Rhode Island, June 20, 1978).

be unstable enough to play a role in long time recovery of transient effects. Photobleaching effects will be discussed in more detail in a later section.

Indeed, an alternative method of examining transient attenuation is to slow the recovery down by cooling the fiber. One might expect for many fibers that "transient" attenuation will be "permanent" at low enough temperatures. Along with Looney, et. al. (Ref.97), the temperaature dependence of transient attenuation in pure silica core fibers has been examined by Taylor et. al. (Ref.69) and Barnes (Ref.74) and Barnes and Wiczer (Ref.100). These studies have shown that there is significant recovery in times of the order of a few minutes after Co-60 irradiation of pure silica fibers even at temperatures as low as -55°C. While the peak transient attenuation (PTA) following a 50 ns x-ray pulse between -45°C and 25°C in a group of PCS fibers was independent of cladding thickness and material type, it did depend on OH content, temperature, and wavelength as shown in Figure 3.16 (Ref.100). The significant increase in PTA with decreasing temperatures demonstrates that a significant portion of the recovery is thermally activated. These data also indicate that the wavelength dependence of PTA over the range .82 μm to 1.06 μm is much less for the dry fiber (A-SD-TC) containing ~ 10 ppm OH than it is for the standard fiber (A-TC) with about 30 ppm OH. The net result is that at .82 μm, the PTA is approximately the same in the two fibers, but at 1.06 μm the higher OH content fiber has a much smaller PTA. With regard to the recovery of transient attenuation, there was no dependence of the recovery

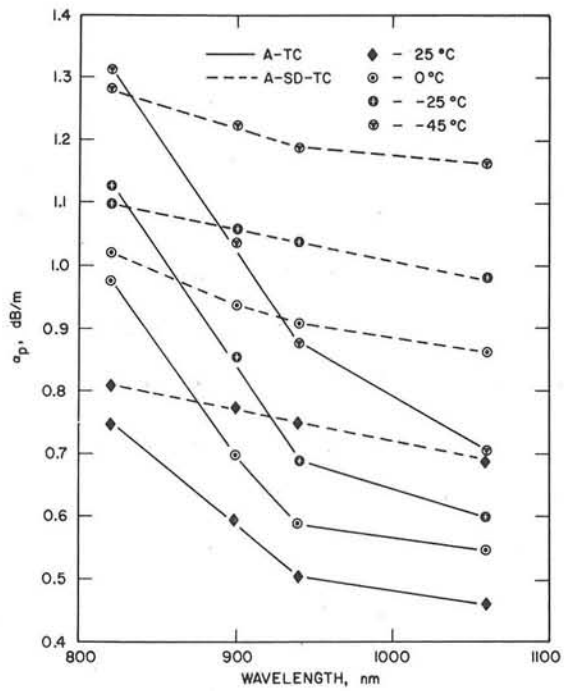

Fig. 3.16 Peak transient attenuation versus wavelength of transmitted light following pulsed x-ray bombardment of PCS fibers at various temperatures. The A-TC fiber is a thin clad fiber with normal water content (OH ≈ 30 ppm), while the A-SD-TC fiber is also thin clad but has very low water content (OH $\lesssim$ 10 ppm).

rate on cladding thickness or type, but the higher OH fiber did recover faster. Thus we see once again that in pure silica core fibers, higher OH content leads to less radiation sensitivity.

(3) Transient attenuation in doped silica core fibers - Early measurements (Refs.35,64,77) of transient attenuation in doped silica core and compound glass core fibers exposed to radiation pulses illustrated that the responses of such fibers can vary drastically. In general, transient attenuation in doped core fibers is significantly stronger than that in typical pure silica core fibers such as shown in Figure 3.14. Typical results for doped core fibers are shown in Figure 3.17 taken from the extensive body of work done by Friebele and co-workers at the Naval Research Laboratory (Refs.47,52,68,71,83,84,101,102). Several important points are illustrated by these data. First, comparing with Figure 3.14, we see that while all of the pure silica core fibers are below 1000 dB/km even at the shortest times, none of the Ge doped fibers in Figure 3.17 reach this level until at least 1 ms after the radiation pulse. Consequently, the presence of Ge results in very strong transient attenuation.

The top three curves in Figure 3.17 illustrate another important point: that is, unlike pure silica core fibers, the OH concentration does not have a significant impact on the radiation response, presumably because of the very strong effect of the Ge. In contrast, if the fiber core is co-doped with B the transient attenuation is enhanced still further. This result is demonstrated in Figure 3.17, where the lower most curve is for a

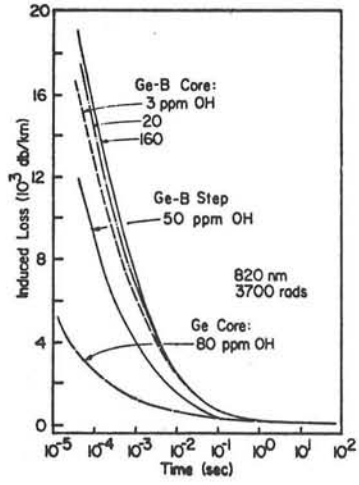

Fig. 3.17 Recovery of room temperature transient attenuation at 0.82 μm induced in Ge and B doped core fibers by a 3 nsec wide 3.7 krad electron pulse. Note that the OH content does not significantly influence the attenuation. (From E. J. Friebele, P. C. Schultz, and M. E. Gingerich, Appl. Optics 19, 2910 (1980)).

Ge doped core with no B, and the middle curve (Ge-B step) is for a fiber with lower B concentration in the outer portions of the core than that for the fiber of the uppermost set of curves (Ge-B core). Recall that doping with B also increased the permanent attenuation at long wavelengths (see Figure 3.11). Consequently, we see that the inclusion of B is generally detrimental to the fiber behavior in a radiation environment.

In earlier sections it was shown that when one co-dopes a fiber core with P, there is a significant effect on radiation response. Although the permanent damage is usually greater at room temperature for P-containing fibers (see Figure 3.11), the presence of phosphorus dramatically suppresses the transient attenuation as shown in Figure 3.18. Note that these data were taken at 1.3 μm and that the dose is approximately 100 times greater than that in Figure 3.17. The curves for fibers without P have the same general appearance and magnitude at 1.3 μm as those in Figure 3.17 for 0.82 μm. This is to be expected since at early times before slow recovery processes have an impact, the attenuation grows linearly with dose and the attenuation at 1.3 μm is usually about a factor of 100 below that at 0.82 μm for the same dose. At the longer wavelength of 1.3 μm, the data in Figure 3.18 demonstrate that it is possible to arrive at a relatively satisfactory compromise between the higher permanent attenuation due to P and the lower transient attenuation due to P. For a fiber containing 9% P the transient attenuation is suppressed but the permanent damage is large. However, if the P content is decreased to 2%, the transient attenuation is still insignificant at times greater than 10^{-4} s

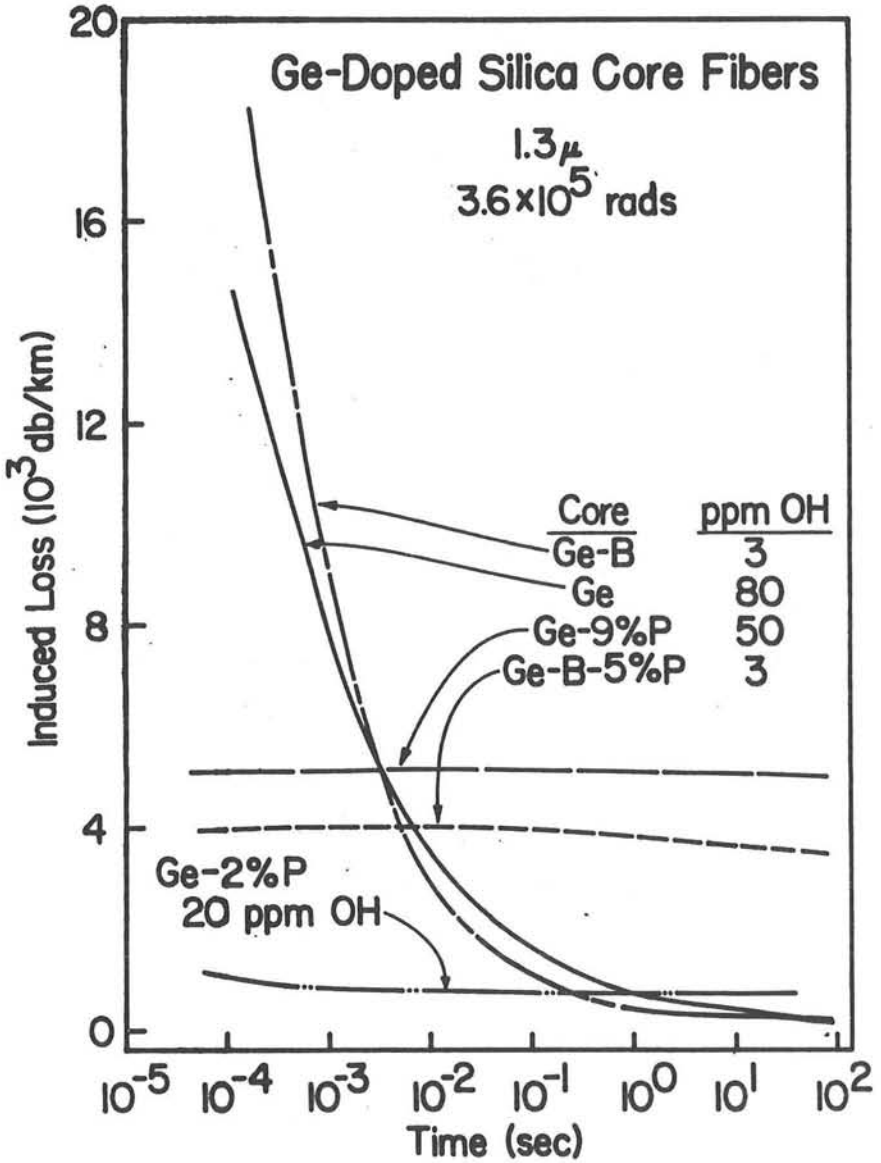

Fig. 3.18 Transient attenuation at 1.3 μm as a function of time after 360 krad electron pulse irradiations of fibers doped with Ge, B, and P. (From E. J. Friebele, P. C. Schultz, and M. E. Gingerich, Appl. Optics 19, 2910 (1980)).

and the permanent damage has decreased to a value much closer to that of the P-free fibers. The transient attenuation curves taken at 0.82 μm are not parallel as they are for different P concentrations at 1.3 μm. At short times ($t < 1$ s) the transient attenuation is higher for larger P concentrations. However, the magnitude is still relatively small: at 1 ms the loss is 400 dB/km in a 9% P fiber for a 3.7 krad dose. In any case, P doping can create the necessity for a compromise in many situations. Therefore, the fiber must be tailored to the radiation environment. For low dose rate, high dose applications P doping can be detrimental, but it is advantageous in high dose rate, low dose environments for systems which must turn-on within a short time after the radiation pulse.

Friebele, et al (Refs.52 and 102) have performed spectral measurements on doped core fibers as a function of time after a radiation pulse. As in the case of the pure silica core fibers (see Figure 3.15) the attenuation is most intense at the shortest wavelengths. Once again the very strong UV absorption in the Ge doped fibers due primarily to the creation of Ge-associated E′ centers, is strongly suppressed by adding P.

Transient attenuation in doped silica core fibers as a function of temperature has been examined by Share, et al (Refs.87 and 88) The trends observed with temperature are similar to those seen for permanent damage as shown in Figure 3.12. That is, in P-doped fibers the temperature dependence of the transient attenuation is suppressed so that at a given time after a radiation pulse, the attenuation is greater at high temperatures than in

non-P containing fibers, but less at low temperatures. An important result of Share, et. al's study (Refs.87 and 88) is that in P doped fibers the transient attenuation is large immediately after the radiation pulse at temperatures below -30°C. Also, over the time domain studied, there is significant recovery of this attenuation below -30°C. Consequently, while P doping strongly suppresses transient attenuation it is not absent. Rather, it would appear that at room temperature, whatever transient attenuation that is present is very fast in P doped fibers and appears as slower recovery at lower temperatures.

(4) Bleaching effects - By now we have seen that radiation-induced attenuation in fibers, whether transient or permanent, can be a severe problem. Consequently, any method of minimizing this effect should be pursued. It is therefore of interest to explore the various ways in which bleaching, that is, the disappearance of color-center induced attenuation, can be made to occur in fibers. From a practical point of view, it is usually not feasible to heat significant lengths of fiber in order to induce thermal bleaching. However, bleaching effects induced by light, termed photobleaching, may be achieved in practical situations. In particular, if the fiber optic link light source is strong enough, then photobleaching is practically possible. As a technique for minimizing attenuation, photobleaching is particularly important for low temperature fiber transmission in which case thermal recovery is very slow. Recent studies (Refs. 68,74,91,99,103-107) have shown that photobleaching effects

are significant in a variety of fibers, and that, indeed, the technique does hold promise for minimizing attenuation in fiber optic links.

While pure silica core fibers are the most sensitive to photobleaching, significant effects are also observed in Ge doped fibers as demonstrated by the data in Figure 3.19. In this Figure we show the growth of induced attenuation at -55°C for three fibers irradiated with and without an AlGaAs laser diode (.820 μm) on at full power (≈ 80 μW) during irradiation. As one might expect the phosphorus containing fiber shows little photobleaching, while the PCS fiber exhibits strong photobleaching. The ITT Ge-doped fiber is intermediate between these two fibers. There appears to be a wide variation in the sensitivity of doped core fibers to photobleaching. Even P doped fibers can be photobleached for high light input power and long time exposures to the photobleaching light beam (Refs.103 and 105).

The strong photobleaching effects which can occur in pure silica core fibers are typified by the data in Figure 3.20 which demonstrate that light power levels of the order of a tenth of a μW enhance the recovery at 0.85 μm and room temperature following a 3.7 krad irradiation. As the optical power is raised the rate of recovery increases rapidly.

As one might expect for a pure silica core fiber, the OH content of the core affects the photobleaching characteristics. This is demonstrated by the data in Figures 3.21 and 3.22 taken from

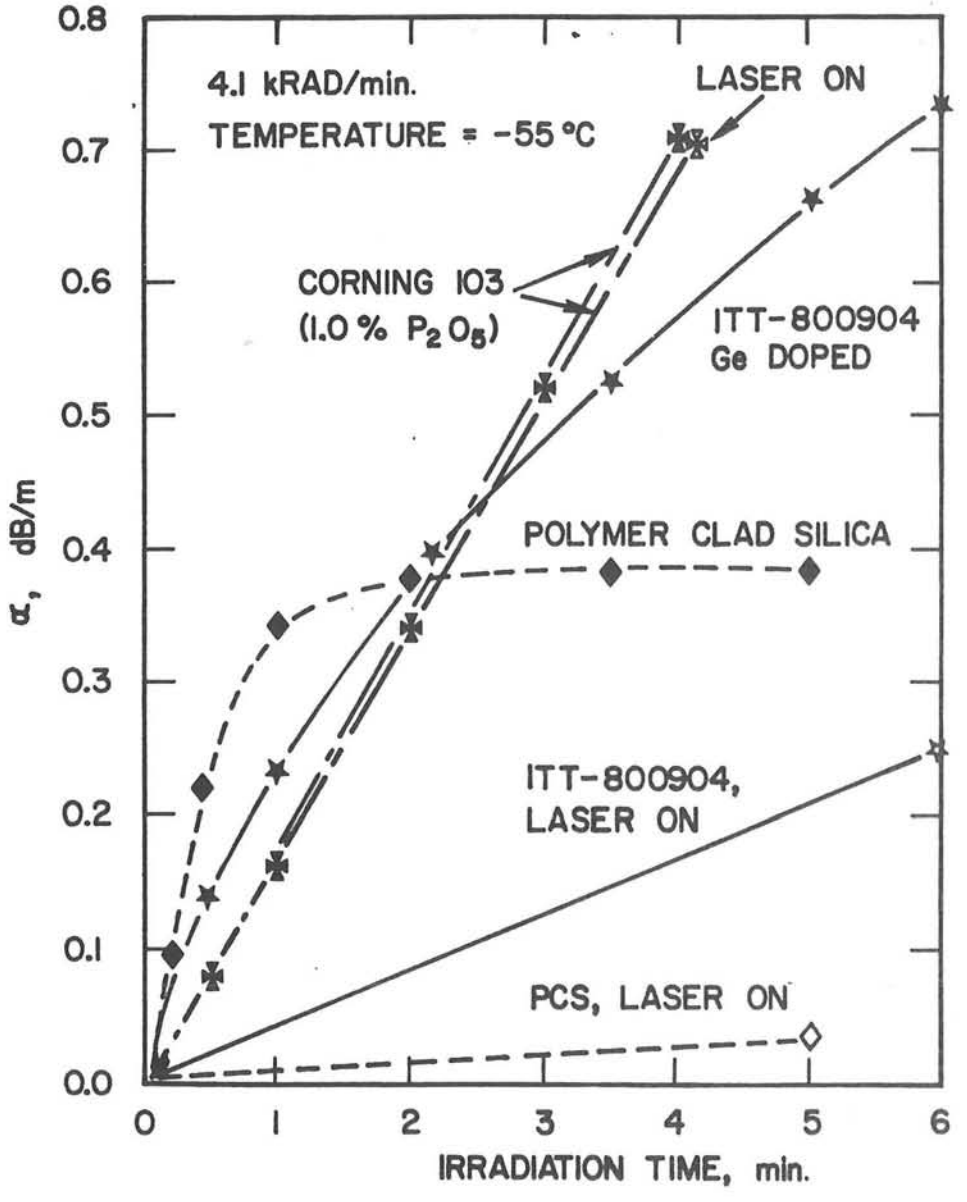

Fig. 3.19 Induced attenuation at -55°C in various fibers with and without AlGaAs laser diode 0.82 μm photobleaching light present during Co-60 irradiation.

our study of photobleaching in fibers Co-60 irradiated at -55°C. In these figures as in Figure 3.20, photobleaching and measurement were carried out with the .820 μm AlGaAs laser. For attenuation measurement, the laser was operated in the LED mode at a very low output level. A sequence of three irradiations are shown in Figure 3.21 for a low OH content (super dry) fiber and a standard OH content fiber. At the end of the first 5 min irradiation, the attenuation begins to decrease due to thermal recovery. As shown in the figure, when the laser is turned on, significant additional recovery occurs even though the thermal recovery has flattened out. Note that the attenuation is greater in the low OH fiber throughout this sequence, and that the laser-induced photobleaching removes nearly all the induced attenuation from the higher OH fiber. The second 5 min irradiation was then carried out with the laser on at full power during exposure. For both fibers the growth in attenuation is much less than that for the first irradiation. The initial sequence was then repeated for the third irradiation which resulted in a much higher level of attenuation (~ 0.4 dB/m) in the dry fiber. It is interesting to compare the first and third irradiations for the dry fiber. While all of the attenuation induced by the third irradiation was removed by bleaching, only 2/3 of that induced during the first irradiation was removed. Similar results have been observed for other pure silica core fibers. This comparison suggests that a saturable, but non-bleachable color center is contributing to the attenuation in these fibers.

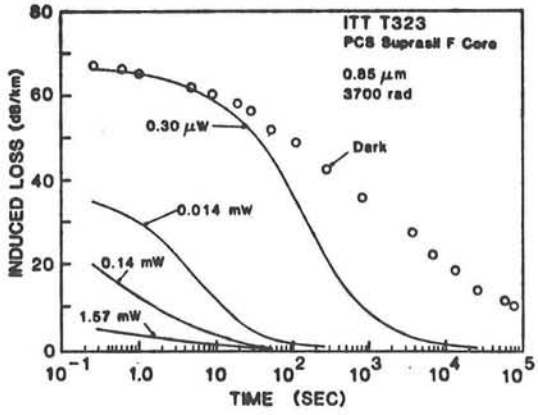

Fig. 3.20 Recovery of induced attenuation in the dark and at various power levels of 0.85 μm bleaching light in a high OH content PCS fiber. (From E. J. Friebele and M. E. Gingerich, Appl. Optics 20, 3448 (1981)).

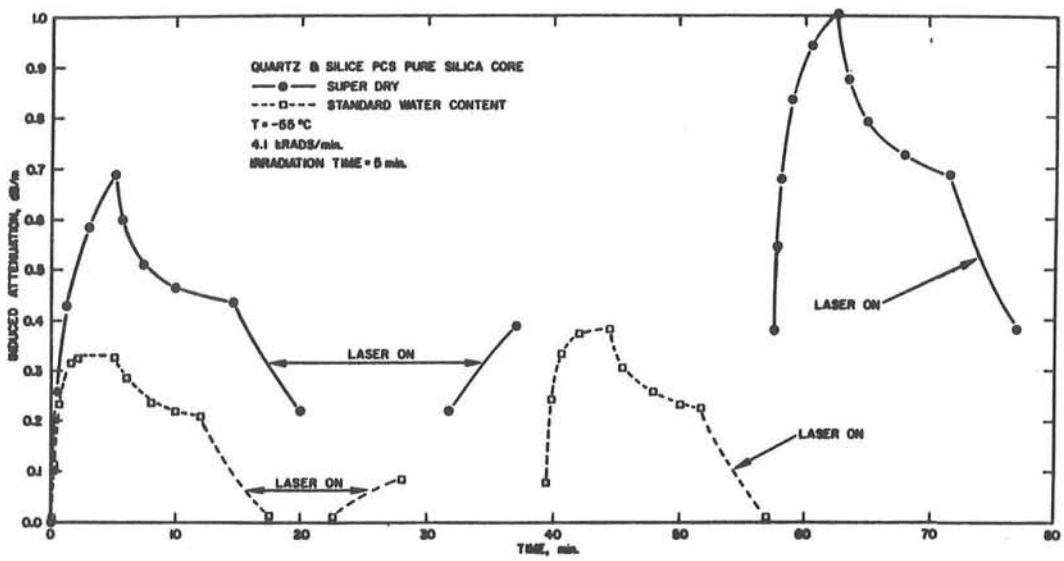

Fig. 3.21 A sequence of irradiations and photobleaching steps at -55°C for two PCS fibers with differing OH content. Measurement and bleaching were accomplished with 0.82 μm AlGaAs laser light.

The data in Figure 3.22 also illustrate that high OH containing fibers are less susceptible to irradiation both with and without photobleaching light present during irradiation. Included in this Figure in addition to PCS fibers, are two fluorosilicate clad fibers. Note that the attenuation growth is not sensitive to cladding type, but that in both fiber types the dry fibers are much more sensitive to irradiation. The lower set of four curves for irradiation with the laser on clearly show that photobleaching is effective in all of these fibers at -55° C.

Having established that steady state exposure of irradiated fibers to light can result in significant photobleaching, one can then ask if photobleaching can be achieved using short pulses of light. Arimura and Caldwell (Ref.99) and Sigel et al (Ref.105) have shown that ruby and YAG:Nd laser pulses can cause significant recovery. However, such sources may not be practically feasible. Work in our laboratory has shown that an 80 μW, 1 s wide pulse from an .820 μm AlGaAs laser diode induces a recovery of about 50% at 0.85 μm. Higher peak power levels would undoubtedly achieve the same recovery with shorter pulses.

Measurements of the effect of photobleaching on attenuation spectra have revealed several interesting results and helped to identify those absorption bands which can be bleached. For example, Friebele and Gingerich (Ref.103) found bleachable bands near 0.7 μm in PCS fibers. In high OH content PCS fibers the band is centered at 0.67 μm (see Figure 3.10), while in low OH content fibers it is broader and peaks at 0.76 μm. The bleaching of an

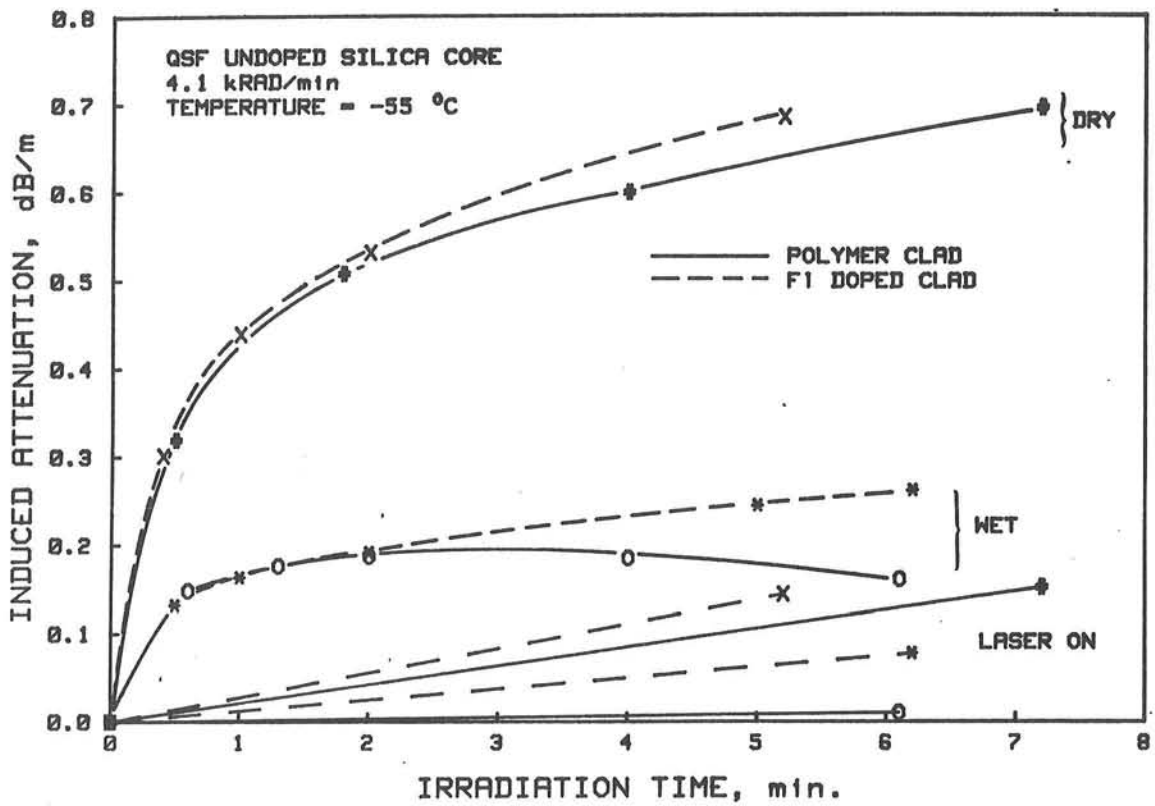

Fig. 3.22 Comparisons of low temperature irradiations with the 0.82 μm AlGaAs laser on and off for undoped silica core fibers with either polymer cladding or fluorosilicate cladding, and with two different OH concentrations.

absorption band in this range in a fluorosilicate clad, pure silica core fiber is shown in Figure 3.23 taken from spectral measurements in our laboratory at -55° C. These data have several interesting features. After irradiation to 120 krad the attenuation is strongest in the UV with an indication of a peak near .67 μm. The fiber was then allowed to thermally recover in the dark for 30 min resulting in fairly uniform recovery over the wavelength range of .45 μm to .85 μm. After this 30 min period, added thermal recovery was minimal and the .82 μm laser was turned on for 5 min. The attenuation spectrum following photobleaching is given by the lowest solid curve in Figure 3.23. The corresponding dashed curve is the difference between the attenuation curve after thermal anneal and the post-laser curve, that is, the attenuation removed by the laser. In agreement with Friebele and Gingerich (Ref.103), the 0.67 μm band is photobleached and, in addition, there is significant recovery at the UV end of the spectrum. This latter effect is particularly interesting since it demonstrates that the 0.82 μm laser light causes photobleaching at much higher photon energies. We have observed similar effects in other pure silica core fibers independent of cladding type and OH content. Gilbert (Ref.104) has also observed photobleaching at high energies above the photobleach photon energy. It is important to note that this is a significant effect: in Figure 3.23 for wavelengths greater than about .475 μm, at least half of the attenuation remaining after thermal anneal is removed by 80 μW of laser light at .82 μm for a laser exposure time of 5 min.

In an attempt to find out if photobleaching at .82 μm was due

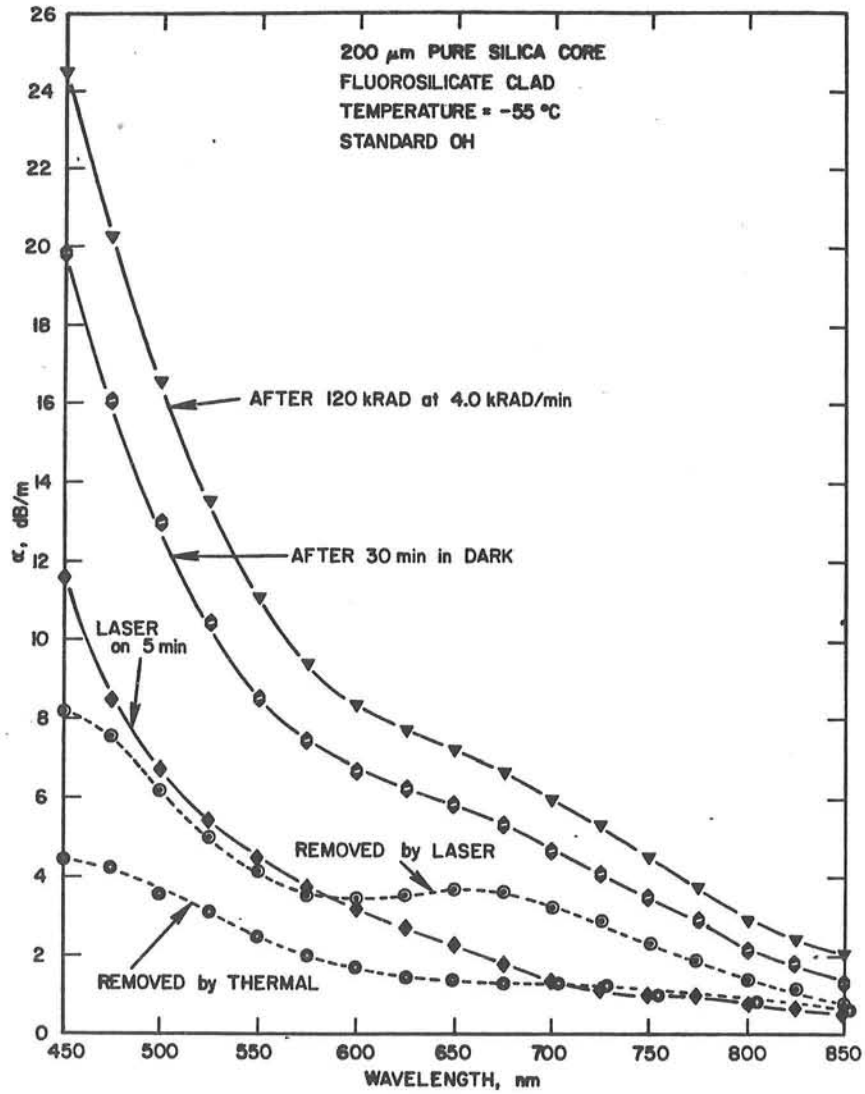

Fig. 3.23 Induced-attenuation spectra for a pure silica core fiber Co-60 irradiated at -55°C. Changes in the spectrum caused by thermal recovery in the dark and by 0.82 μm AlGaAs laser bleaching light are also shown. Dashed curves are the corresponding amounts removed by each operation.

to absorption into a relatively narrow band, the photobleaching effect was examined as a function of photobleaching wavelength. The relative amount of attenuation that was bleached did not significantly depend on bleaching wavelength. For example, the degree of photobleaching at measurement wavelengths above the photobleach wavelength was no greater than that below the photobleach wavelength. These results indicate that photobleaching by absorption into one or more narrow bands is not occurring.

Simultaneous measurements by Sigel et al (Ref.105) of photobleaching and photoluminescence generated by a pulsed ruby laser (0.69 μm) have provided additional information about the photobleaching process. In pure silica core fibers, the photoluminescence was centered at 0.65 μm, and was relatively independent of excitation wavelength. This result suggests that the photoluminescence is not due to an internal transition. Rather, there appears to be transfer of electrons via the conduction band from the absorbing center to the radiative recombination center. These authors also found that for pulsed ruby excitation, the photobleaching followed the laser pulse while the photoluminescence lasted significantly longer than the laser pulse. This seems to suggest that photobleaching is associated with the excitation process and not the final radiative recombination step. There may also be an intermediate trapping and release of carriers prior to radiative recombination.

Additional information concerning the photobleaching process induced at -55° C in pure silica core fibers by .820 μm laser light is revealed by the time dependence of the photobleaching.

These data are shown in Figure 3.24 for a fluorosilicate clad fiber irradiated to a dose of 354 krads. The normalized reduction in attenuation at each of the four measurement wavelengths shown is given as a function of the cumulative time the fiber is exposed to the 0.82 μm laser at full power (≈ 80 μW). Note that photobleaching is much more rapid at longer wavelengths. The solid lines in Figure 3.24 are theoretical curves generated by the geminate recombination model, the equation for which is given in the Figure. This model appears to fit the data in Fig. 3-24 quite well. The parameter β is a recombination rate constant which is proportional to the diffusion coefficient of the recombining pairs. In the geminate recombination model the recombining species are inhomogeneously distributed and are correlated with each other so that the rate does not depend on the concentration of pairs. This model has been used successfully to describe attenuation recovery in glasses (Refs.108,109,110) and fibers (Refs.64,95,97) over quite wide ranges in time. The agreement with the data in Figure 3.24 suggests that the 0.82 μm laser light activates the recombination of correlated ion pairs with those species responsible for attenuation at short wavelengths recombining at a slower rate. At this point in time, we do not have a detailed physical explanation for this recovery process. The reasons for the magnitude of β and its variation with wavelength are not known as yet.

This brief review of photobleaching has shown that, like the color center creation process, photobleaching in a given fiber

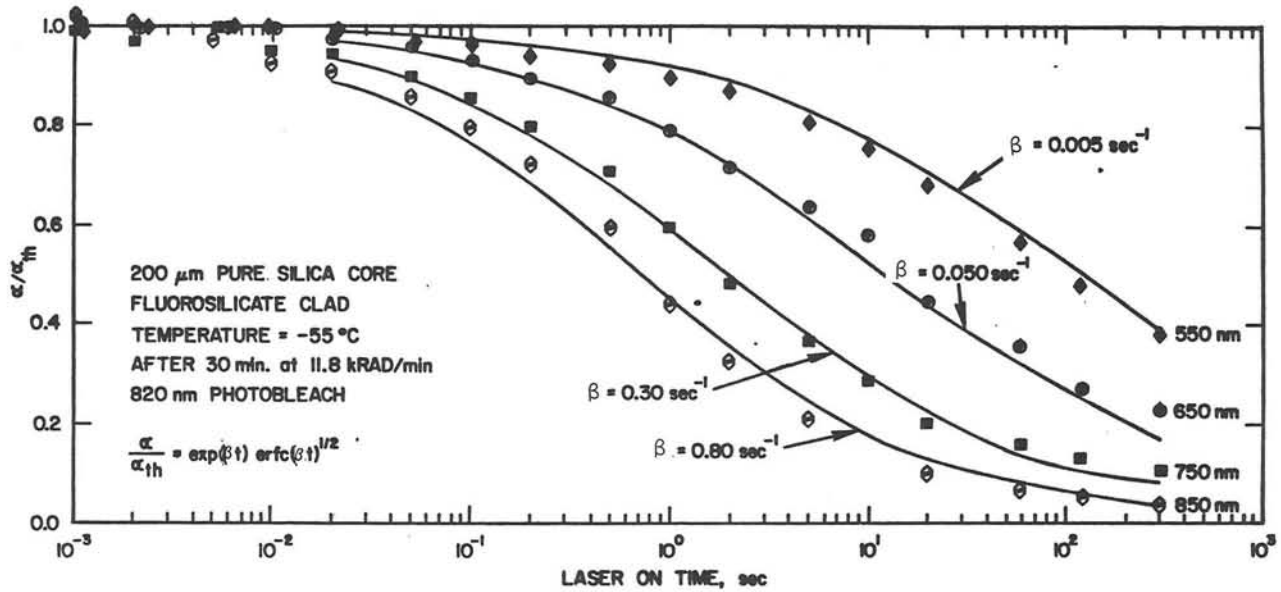

Fig. 3.24 AlGaAs 0.82 μm laser-induced bleaching at -55°C of the normalized attenuation in a fluorosilicate clad, pure silica core fiber as a function of cumulative laser-on time. Measurement wavelengths are shown at the right. The solid curves are a fit to the data using the geminate recombination with the rate constants (β) shown.

is a subtle and complex process which is difficult to unravel. It is clear, however, that in many fibers, especially pure silica core fibers, significant photobleaching occurs at light levels characteristic of operational levels in fiber optic links. Therefore, photobleaching is a practically relevant technique for minimizing attenuation. A word of caution is in order, however, for long links. As pointed out by other authors (Refs.99 and 103) the photobleaching process is a "bootstrap" process in which bleaching must occur before significant light levels can penetrate to long path lengths in the irradiated fiber. Therefore the effectiveness of this technique may be limited in very long fibers.

3. SUMMARY

Perhaps the most important conclusion one can reach based on radiation studies of fibers is that, at this point in time, there is not a single, particular fiber which best satisfies all operational requirements in a radiation environment. Therefore, before selecting a fiber, the pre-irradiation operating characteristics of the link must be well-defined as well as the specifics of the anticipated radiation exposure. A variety of recent applications which do not involve radiation are centered near the wavelengths of 0.82 μm and 1.3 μm so that commercial offerings of optoelectronic devices and fibers are emphasizing these wavelengths. Consequently, it would be to the advantage of the system designer concerned with radiation environments if these operating wavelengths could also be used. It is important to note that with

regard to fibers there are almost no disadvantages in selecting a longer wavelength over 0.82 μm as an operating point. Nearly all fibers have lower dispersion and less intrinsic absorption near 1.3 μm. In addition, the permanent and transient radiation-induced attenuation is generally less at longer wavelengths as shown by the data in Figures 3.11, 3.17 and 3.18. However, as indicated in Figure 3.11, care must be taken in selecting the wavelength if the fiber contains B or P. From the point of view of radiation induced attenuation B is to be avoided. In addition, if P is added to minimize transient attenuation then a wavelength shorter than 1.3 μm may have to be employed.

Clearly, the decision whether or not to use a P doped core fiber depends on dose rate versus total dose, and on the required turn-on time after a radiation pulse. For high dose rates and minimum turn-on times but moderate to low doses, such as one might have for flash x-ray machine diagnostic links, phosphorus as a co-dopant with Ge is appropriate. For the opposite case, relatively large doses but low dose rates, as one might have in a long-term space application, P doping is to be avoided. Either a Ge doped core fiber or a pure silica core fiber would be desirable. Generally the pure silica core fiber is less sensitive. However, one should note, as shown in Figure 3.19, that initially the attenuation growth rate is often larger in pure silica core fibers than in Ge doped core fibers. Consequently, for low total dose applications the Ge doped core fiber may be preferable.

For very stringent applications where the dose rate and dose are both large, or where the fiber must essentially function during

a radiation pulse, pure silica core fibers are most advantageous. For example, in an underground testing application the fiber optic link must function within ns of the pulse. Under these conditions, Lyons and co-workers at LANL have found pure silica core fibers to be the best. The use of PCS fibers can be detrimental in other ways, however. Because of the polymer cladding, the low temperature properties are poor as are the mechanical and splicing/connectorizing properties. Fortunately, with the recent emergence of fluorosilicate clad, pure silica core fibers in the commercial market, one is not restricted to PCS fibers for pure silica cores. Our measurements (see Figure 3.9) and those of others indicate that fluorosilicate clad fibers are just about as radiation resistant as PCS fibers. Lastly, an additional attractive feature of pure silica core fibers is their sensitivity to link light source-induced photobleaching.

4. REFERENCES

1. T. A. Giallorenzi and J. F. Weller, "Integrated and Fiber Optical Devices and Systems," IEEE Trans. Nucl. Sci. NS-22, 2440 (1975).
2. T. Li, "Advances in Optical-Fiber Transmission Research," p. 97 in Symposium on Optical and Acoustical Micro-Electronics, 1974.
3. W. G. French, J. B. MacChesney, and A. D. Pearson, "Glass Fibers for Optical Communications," p. 373 in 1975 Annual Review of Materials Science, 5, R. A. Huggins (Ed.) (Palo Alto, CA, Annual Reviews, 1975).
4. R. D. Maurer, "Glass Fibers for Optical Communications," IEEE Proc. 61, 452 (1973).
5. S. E. Miller and A. G. Chynoweth, Eds., Optical Fiber Telecommunications (Academic Press, New York, 1979).
6. H. F. Wolf, Ed., Handbook of Fiber Optics: Theory and Applications (Garland STPM Press, New York, 1979).
7. C. P. Sandbank, Ed., Optical Fibre Communication Systems (John Wiley, Chichester, 1980).
8. Technical Staff of CSELT, Optical Fibre Communication (McGraw-Hill, New York, 1981).
9. J. P. Wittke, "Designer's Guide to: Optical-fiber Communications Systems," EDN, May 20, 1975.
10. R. T. Blanks, "It's a Testing Time for Fiber Research," Optical Spectra 10, 30, (October, 1976).
11. N. S. Kapany, "Fiber Optics," Scientific American 203, No. 5, 72 (1960).

12. J. S. Cook, "Communication by Optical Fiber," Scientific American 229, No. 5, 30 (1973).

13. D. A. Pinnow, A. L. Gentile, A. G. Staudlee, A. J. Timper, and L. M. Hobrock, "Polycrystalline Fiber Optical Waveguides for Infrared Transmission," Appl. Phys. Lett. 33, 28 (1978).

14. T. Hidaka, T. Morikawa, and J. Shimada, "Hollow-core Oxide-glass Cladding Optical Fibers for Middle-Infrared Region," J. Appl. Phys. 52, 4467 (1981).

15. J. Stone, "Optical Transmission in Liquid-Core Quartz Fibers," Appl. Phys. Lett. 20, 239 (1972).

16. D. C. Johnson and B. S. Kawasaki, "The Coupling of Light Emitting Diodes to Bulb-Ended Optical Fibers," p. 95 in Proc. of the Tech. Program, 1974 Inter. Electro-Optics Conf., Brighton, England (Kiver Communications, Surrey, England, 1974).

17. D. Gloge, "Dispersion in Weakly Guiding Fibers," Appl. Opt. 10, 2442 (1971).

18. S. D. Personick, "Time Dispersion in Dielectric Waveguides," Bell System Tech. Jour. 50, 843 (1971).

19. P. C. Schultz, "Progress in Optical Waveguide Process and Materials," Appl. Optics 18, 3684 (1979).

20. D. Botez and G. J. Herskowitz, "Components for Optical Communications Systems: A Review," Proc. IEEE 68, 689 (1980).

21. I. Jacobs, "Lightwave Communications in the Bell System: 1982 and Beyond," presented at the Sixth Topical Meeting on Optical Fiber Communication, New Orleans, Louisiana, Feb. 28-March 2, 1983.

22. J. J. Pan, "5 GHz Wideband Fiber-Optic Link," Ibid.

23. J. W. Fleming, "Material Dispersion in Lightguide Glasses," Electronic Lett. 14, 326 (1978).

24. T. Li, "Optical Fiber Communication - The State of the Art," IEEE Trans. Commun., COM-26, 946 (1978).

25. K. Yoshida, Y. Furui, S. Sentsui, and T. Kuroha, "Loss Factors in Optical Fibers," Optical and Quantum Elect. 13, 85 (1981).

26. S. Kobayashi, N. Shibata, S. Shibata, and T. Izawa, Rev. Elect. Commun. Lab. 26, 453 (1978).

27. H. Osanai, T. Shioda, T. Moriyama, S. Araki, M. Horiguchi, T. Izawa, and H. Takata, "Effect of Dopants on Transmission Loss of Low-OH-Content Optical Fibres," Electronics Lett. 12, 549 (1976).

28. J. Conradi, F. P. Kapron, and J. C. Dyment, "Fiber-Optical Transmission Between 0.8 and 1.4 μm," IEEE J. Solid-State Circuits SC-13, 106 (1978).

29. T. Miya, Y. Terunuma, T. Hosaka, and T. Mryashita, "Ultimate Low-Loss Single-Mode Fibre at 1:55 μm," Elect. Lett. 15, 106 (1979).

30. K. Koizumi, Y. Ikeda, I. Kitano, M. Furnkawa, and T. Sumimoto, "New Light Focusing Fibers Made by a Continuous Process," Appl. Opt. 13, 255 (1974).

31. R. G. Sommer, R. D. Deluca, G. E. Burke, "New Glass System for Low-Loss Optical Waveguides," Electronic Letters 12, 408 (1976).

32. B. D. Evans and G. H. Sigel, Jr., "Radiation Resistant Fiber Optic Materials and Waveguides," IEEE Trans. Nucl. Sci. NS-22, 2462 (1975).

33. G. R. Newns, "Materials Systems and Fibre Fabrication Processes in the UK," Tech. Digest of Topical Meeting on Optical Fiber Transmission, Paper TuB1. Williamsburg, Va., Jan. 7-9, Optical Soc. of America (1975).

34. P. L. Mattern, "A Summary of Preliminary Studies on the Effects of Co-60 Gamma-Ray Irradiation of Fiber Optic Materials," Sandia Tech. Report SLL-73-0287 (October 1973).

35. P. L. Mattern, L. M. Watkins, C. D. Skoog, J. R. Brandon, E. H. Barsis, "The Effects of Radiation on the Absorption and Luminescence of Fiber Optic Waveguides and Materials," IEEE Trans. Nucl. Sci., NS-21, No. 6, 81 (1974).

36. C. R. Kurkjian, R. V. Albarino, J. T. Krause, H. N. Vazivani, F. V. DiMarcello, S. Torza, and H. Schonhorn, "Strength of 0.04-50-m Lengths of Coated Fused Silica Fibers," Appl. Phys. Lett. 28, 588 (1976).

37. J. J. Mecholsky, S. W. Freiman, and S. M. Morey, "Fractographic Analysis of Optical Fibers," Amer. Ceramic Soc. Bull. 56, 1016 (1977).

38. B. Justice, "Strength Considerations of Optical Waveguide Fibers," Fiber and Integrated Optics 1, 115 (1978).

39. G. E. Walrafen, P. N. Krishnan, and S. W. Feiman, "Raman Investigation of Optical Fibers Under High Tensile Stress," J. Appl. Phys. 52, 2832 (1981).

40. Y. Katsuyama, Y. Mitsunaga, H. Kobayshi, and Y. Ishida, "Dynamic Fatigue of Optical Fiber Under Repeated Stress," J. Appl. Phys. 53, 318 (1982).

41. Proceedings of the Fiber Optics in the Nuclear Environment Symposium, R. C. Webb, Chairman, held March 25-27, 1980 at Harry Diamond Laboratories, Adelphi, MD, DNA Report No. DNA-5308 P-2.

42. Fiber Optics in Adverse Environments, P. B. Lyons, Ed., Proc. of SPIE 296, August 25-27, 1981, San Diego, CA.

43. Tri Service Workshop on Fiber Optic Sensors and Guided Wave Technology, Fort Eustis, Virginia, Oct. 5-8, 1982.

44. E. J. Friebele, G. H. Sigel, Jr., M. E. Gingerich, "Nuclear-Radiation Effects on Fibers," Laser Focus, p. 50, September, 1978.

45. G. H. Sigel, Jr., "Radiation Effects in Optical Fibers," presented at Recent Advances in Fiber Optics, Univ. of Rhode Island, June 20, 1978.

46. R. C. Webb, L. Isaacson, and E. P. Marram, "Response of Fiber Optic Waveguides to Ionizing Radiation," Optical Eng. 18, 568 (1979).

47. E. J. Friebele, "Optical Fiber Waveguides in Radiation Environ-Ments," Optical Eng. 18, 552 (1979).

48. G. H. Sigel, Jr., "Fiber Transmission Losses in High-Radiation Fields," Proc. IEEE 68, 1236 (1980).

49. R. A. Greenwell, G. H. Baker, and W. H. Hardwick, "Fiber Optics in the Nuclear Environment," Inter. Fiber Optics and Communications, p. 19, September, 1981.

50. G. A. Taylor and J. C. Thacker, "Fibre Optics Systems for Space Applications," Optics and Laser Tech., p. 93, April, 1982.

51. A. N. Paolantonio, "Military Fiber-Optic Links: Can They Take the Heat?" Microwaves, p. 104, January, 1982.

52. E. J. Friebele, G. H. Sigel, Jr., and M. E. Gingerich, "Radiation Response of Fiber Optic Waveguides in the 0.4 to 1.7 μm Region," IEEE Trans. Nuc. Sci. NS-25, 1261 (1978).

53. G. J. Dienes, "Introduction - Defects in Silicas," J. Phys. Chem. Solids 13, 272 (1960).

54. P. W. Levy, "Reactor and Gamma-Ray Induced Coloring of Corning Fused Silica," J. Phys. Chem. Solids 13, 287 (1960).

54a. D. L. Griscom, E. J. Friebele, K. J. Long, and J. W. Fleming, "Fundamental Defect Centers in Glass: Electron Spin Resonance and Optical Absorption Studies of Irradiated Phosphorus-Doped Silica Glass and Optical Fibers," J. Appl. Phys. 54, 3743 (1983).

55. D. L. Griscom, "Defects and Impurities in α-Quartz and Fused Silica," in The Physics of SiO_2 and Its Interfaces, S. T. Pantelides, Ed. (Pergamon Press, New York, 1978) p. 232.

56. D. L. Griscom, E. J. Friebele, M. Stapelbroek, and G. H. Sigel, Jr., "Radiation-Induced Defect Centers in Fiber Optic Glasses," p. 11 in Ref. 41.

57. J. A. Weil, "The Aluminum Center in αQuartz," Rad. Effects 26, 261 (1975).

58. G. N. Greaves, "Colour Centres in Vitreous Silica," Phil. Mag. B 37, 447 (1978).

59. G. H. Sigel, Jr., "Ultraviolet Spectra of Silicate Glasses: A Review of Some Experimental Evidence," J. Non-Crystalline Solids 13, 372 (1974).

60. R. A. Weeks, "Paramagnetic Resonance and Optical Absorption in Gamma-Ray Irradiated Alpha Quartz: The "Al" Center," J. Am. Ceramic Soc. 53, 176 (1970).

61. R. A. Weeks and E. Souder, "The Relation Between the Magnetic Susceptibility, Electron Spin Resonance, and the Optical Absorption of the E1 Center in Fused Silica," in Symposium on Paramagnetic Resonance, Vol. 2, W. Low, Ed. (Academic Press, New York, 1963) p. 869.

62. D. L. Griscom and W. B. Fowler, "Electron-Transfer Model for E'-Center Optical Absorption in SiO_2," in The Physics of MOS Insulators, G. Lucovsky, S. T. Pantelides, F. L. Galeener, Eds., (Pergamon Press, New York, 1980) p. 97.

63. M. Stapelbroek and D. L. Griscom, "Oxygen-Associated Trapped-Hole Centers in High-Purity Fused Silica," in The Physics of SiO_2 and Its Interfaces, S. T. Pantelides, Ed. (Pergamon Press, New York, 1978) p. 263.

64. P. L. Mattern, L. M. Watkins, C. D. Skoog, and E. H. Barsis, "Absorption Induced in Optical Waveguides by Pulsed Electrons as a Function of Temperature, Low Dose Rate Gamma and Beta Rays, and 14 MeV Neutrons," IEEE Trans. Nucl. Sci. NS-22, 2468 (1975).

65. C. D. Skoog, "A Summary of Radiation Induced Transient Absorption and Recovery in Fiber Optic Waveguides," Sandia Tech. Report SAND76-8056, (November 1976).

66. E. J. Friebele, R. E. Jaeger, G. H. Sigel, Jr., and M. E. Gingerich, "Effect of Ionizing Radiation on the Optical Attenuation in Polymer-Clad Silica Fiber-Optic Waveguides," Appl. Phys. Lett. 32, 95 (1978).

67. G. H. Sigel, Jr., E. J. Friebele, M. E. Gingerich, and L. M. Hayden, "Radiation Response of Large Core Polymer Clad Silica Optical Fibers," IEEE Trans. Nuc. Sci. NS-26, 4796 (1979).

68. G. H. Sigel, Jr., E. J. Friebele, and M. E. Gingerich, "Recent Progress in the Investigation of Radiation Resistant Optical Fibers," p. 2 in ref. 42.

69. E. W. Taylor, J. M. Emines, W. R. Ayres, J. D. Wiltse, and J. M. Maier, "Response of Irradiated Opitcal Waveguides at Low Temperatures," p. 40 in ref. 42.

70. S. Share, "Effect of Ionizing Radiation on Fiber-Optic Waveguides," p. 51 in ref. 42.

71. E. J. Friebele and M. E. Gingerich, "Radiation Damage of Optical Fiber Waveguides at Long Wavelengths," p. 37 in ref. 41.

72. S. Share, "Temperature Dependence of Radiation Darkening in Optical Waveguides," p. 49 in ref. 41.

73. J. J. McAlarney, X. G. Glavas, R. A. Greenwell, and S. Share, "Lessons Learned in the Manufacturing of Radiation Resistant Optical Fiber," IEEE Trans. Nuc. Sci. NS-28, 4125 (1981).

74. C. E. Barnes, "Laser Diode-Induced Photobleaching at Low Temperatures," IEEE Trans. Nuc. Sci. NS-29, 1479 (1982).

75. P. Kaiser, "Drawing-induced Coloration in Vitreous Silica Fibers," J. Opt. Soc. Am. 64, 475 (1974).

76. G. H. Sigel, Jr. and B. D. Evans, "Effects of Ionizing Radiation on Transmission of Optical Fibers," Appl. Phys. Lett. 24, 410 (1974).

77. B. D. Evans and G. H. Sigel, Jr., "Permanent and Transient Radiation Induced Losses in Optical Fibers," IEEE Trans. Nucl. Sci. NS-21, No. 6, 113 (1974).

78. E. J. Friebele, D. L. Griscom, and G. H. Sigel, Jr., "Defect Centers in a Germanium-Doped Silica-Core Optical Fiber," J. Appl. Phys. 45, 3424 (1974).

79. D. N. Payne and W. A. Gambling, "New Silica-Based Low Loss Optical Fibre," Electronics Lett. 10, 289 (1974).

80. E. J. Friebele, G. H. Sigel, Jr., and M. E. Gingerich, in Fiber Optics: Advances in Research and Development, B. Beadow and S. S. Matea, Eds. (Plenum Press, New York, 1979) p. 355.

81. J. A. Wall, T. J. Loretz, and J. E. Mattison, "Optical Fiber Composition and Radiation Hardness," p. 35 in ref. 42.

82. J. A. Wall, H. Posen, and R. Jaeger, "The Role of the Multi-dopants Sb/P in Radiation Hardening of Optical Fibers," p. 31 in ref. 41.

83. E. J. Friebele, M. E. Gingerich, and G. H. Sigel, Jr., "Effect of Ionizing Radiation on the Optical Attenuation in Doped Silica and Plastic Fiber-Optic Waveguides," Appl. Phys. Lett. 32, 619 (1978).

84. E. J. Friebele, "Radiation Protection of Fiber Optic Materials: Effect of Cerium Doping on the Radiation-Induced Absorption," Appl. Phys. Lett. 27, 210 (1975).

85. S. P. Faile, J. J. Schmidt, and D. M. Roy, "Irradiation Effects in Glasses: Suppression by Synthesis Under High-Pressue Hydrogen," Science 156, 1593 (1967).

86. T. Nishimura, H. Aritome, K. Masuda, and S. Namba, "A Loss Mechanism in Optical Waveguides Fabricated by Ion Implantation in Fused Quartz," Jap J. Appl. Phys. 15, 1167 (1976).

87. S. Share, R. M. McCracken, and I. Aggarwal, "The Effect of Temperature on the Response of Glass-Clad Optical Waveguides to Ionizing Radiation," IEEE Trans. Nuc. Sci. NS-25, 1288 (1978).

88. S. Share and J. Wasilik, "Radiation Effects in Doped Silica Optical Waveguides," IEEE Trans. Nuc. Sci. NS-26, 4802 (1979).

89. J. A. Wall, H. Posen, and R. Jaeger, "Radiation Performance of Germanium Phosphosilicate Optical Fibers as a Function of Temperature," p. 57 in ref. 41.

90. L. M. Watkins and E. H. Barsis, "Absorption Induced in Glass and Plastic Fibers by 14 MEV Neutrons," Sandia Tech. Report SAND 75-8714, (June, 1976).

91. J. E. Golob, P. Lyons, and L. D. Looney, "Transient Radiation Effects in Low Loss Optical Waveguides," IEEE Trans. Nuc. Sci. NS-24, 2164 (1977).

92. M. J. Marrone, "Radiation-Induced Luminescence in Silica Core Optical Fibers," Appl. Phys. Lett. 38, 115, (1981).

93. P. B. Lyons, L. D. Looney, J. E. Golob, R. Robichand, R. Seno, J. Madrid, L. Hocker, and M. Nelson, "Neutron-and Gamma-Induced Transient Effects in Optical Fibers," Proc. of 1978 Conf. on Physics of Fiber Optics, (Plenum, New York, 1978) p. 379.

94. P. B. Lyons, J. E. Golob, and R. E. Kelly, presented at OSA Meeting on Optical Fiber Communication, March, 1979, Wash., D. C.

95. P. B. Lyons, R. E. Kelly, and L. D. Looney, "Short-Term Radiation Effects in Optical Fibers," p. 83 in ref. 41.

96. P. Zagarino, C. H. Lin, M. A. Nelson, T. J. Davies, N. J. Norris, and J. W. Ogle, "Radiation Response Measurement of Fibers in the Picosecond Region," p. 117 in ref. 41.

97. L. D. Looney, G. Turquet de Beauregard, P. B. Lyons, R. E. Kelly, "Radiation-induced Transient Absorption in Optical Fibers," p. 17 in ref. 42.

98. R. M. Gilbert, R. C. Webb, and T. R. Oldham, "Transient Response of Optical Fibers Exposed to Pulsed Radiations," IEEE Trans. Nuc. Sci. NS-27, 1864 (1980).

99. I. Arimura and R. S. Caldwell, "Radiation Degradation and Recovery in Long Fiber-Optics Data Links," p. 175 in ref. 41.

100. C. E. Barnes and J. J. Wiczer, "X-Ray Induced Transient Attenuation at Low Temperatures in PCS Fibers," p. 25 in ref. 42.

101. E. J. Friebele, P. C. Schultz, and M. E. Gingerich, "Compo sitional Effects on the Radiation Response of Ge-doped Silica-Core Optical Fiber Waveguides," Appl. Optics 19, 2910 (1980).

102. E. J. Friebele and M. E. Gingerich, "Radiation Damage in Optical Fiber Waveguides at Long Wavelengths," Advances in Ceramics 2, Physics of Fiber Optics, 387 (1981).

103. E. J. Friebele and M. E. Gingerich, "Photobleaching Effects in Optical Fiber Waveguides," Appl. Optics 20, 3448 (1981).

104. R. M. Gilbert, "Photobleaching of Radiation-Induced Color Centers in a Germania-Doped Glass Fiber," IEEE Trans. Nuc. Sci. NS-29, 1484 (1982).

105. G. H. Sigel, Jr., E. J. Friebele, M. J. Marrone, and M. E. Gingerich, "An Analysis of Photobleaching Techniques for the Radiation Hardening of Fiber Optic Data Links," IEEE Trans. Nuc. Sci. NS-28, 4095 (1981).

106. R. H. West and A. P. Lenham, "Characteristics of Light Induced Annealing in Irradiated Optical Fibres," Electronics Lett. 18, 483 (1982).

107. J. G. Titchmarsh, "Signal-Level Dependence in the Recovery Rate of Irradiated Plastic-Clad Silica Fibre," Electronics Lett. 15, 111 (1979).

108. A. Barkatt, M. Ottolenghi, and J. Rabani, "Spur Recombination and Diffusion Processes in Pulse Irradiated Inorganic Glasses," J. Phys. Chem. 77, 2857 (1973).

109. A. Barkatt, C. A. Angell, and J. R. Miller, "Radiation Products and Tunneling Process in Ionic Glasses. 1. Radiation Products and Recombination in Undoped Nitrate and Acetate Glasses," J. Phys. Chem. 82, 2143 (1978).

110. E. J. Friebele and D. L. Griscom, "Radiation Effects in Glass," p. 257 in Treatise on Materials Science and Technology 17, Glass II, M. Tomozawa and R. H. Doremus, Eds., (Academic Press, New York, 1979).

IV. PHOTODETECTORS

Currently there are a large number of sensitive photodetectors available for use as optical to electrical transducer elements. Since a comprehensive review of all types of photodetectors would be unrealistic in this report, we restrict our discussion to those detectors most likely to be used with fiber optic systems or optoelectronic couplers. This limits the scope of our discussion to detectors sensitive to optical radiation in the .5 μm to 1.6 μm wavelength range. Further limitations are imposed by noting that we are primarily interested in high speed data links of rugged construction and compact size which can withstand some exposure to radiation environments. Using these conditions, our discussion can be confined to photovoltaic or photoconductive semiconductors containing one or more p-n junctions. Although special photomultiplier tubes and other types of detectors may satisfy the conditions outlined above, very few radiation damage studies have been made on these types of detectors.

1. TYPES OF PHOTODETECTORS

A brief overview of photodetector properties pertinent to optical fiber systems will be presented in this report. More complete discussions of the many types of photodetectors are easily accessible in the literature in the form of review papers (Refs. 1-5) and books (Refs. 6-10).

One of the simplest types of photodiode detectors currently used in applications requiring moderate to high response speed is

the p-n junction (Ref.6). This device is typically asymmetrically doped (e.g. n^+p) with the thin heavily doped layer situated on top, usually exposed to the incident light. Photogenerated carriers are created throughout the device at a rate $G_{op}(\lambda, x)$, where x is the distance into the device from the n^+ boundary and λ is the wavelength. The density of photogenerated carriers as a function of position is determined in part by the wavelength dependence of the optical absorption coefficient, α, of the semiconductor material. It can be shown (Ref.11) that the generation rate in a small thickness dx about the x position can be given by

$$G_{op}(\lambda,x) = N_{ph}(\lambda)\ \alpha\ (\lambda)e^{-\alpha(\lambda)x},\ cm^{-3}\ sec^{-1} \qquad (4.1)$$

where $N_{ph}(\lambda)$ is the incident photon flux as a function of wavelength. Since the p-region is lightly doped, the space charge (depletion) region will extend well into this region. Collection of photogenerated carriers will be significant throughout the entire space charge (depletion) region and approximately one minority carrier diffusion length into the undepleted p region. Due to the effects of surface recombination and the short hole (minority carrier) diffusion length in the thin n^+ region, it is usually assumed that the thin n^+ region on top will not make a significant contribution to the photocurrent. For the normal operating conditions of reverse bias, the total current is the sum of the space charge region drift current, J_{sc}, and the diffusion current, J_d (Ref.11),

$$J_{sc} = -q\ N_{ph}\int_0^W \alpha\ e^{-\alpha x}\ dx = q\ N_{ph}\ (1 - e^{-\alpha w}),\ A/cm^2 \qquad (4.2)$$

$$J_d = q\, N_{ph} \left[1 - \frac{e^{-\alpha w}}{(1 + \alpha L_e)} \right] + q\, n_{po} \frac{D_e}{L_e},\ A/cm^2 \qquad (4.3)$$

where w is the width of the space charge region and L_e, as defined earlier, is the electron diffusion length. In the interest of clarifying these equations, monochromatic incident light has been assumed to be the illumination source for minority carrier generation; this removes the λ dependence in the equations. The derivation of Equation 4.2 assumes thermal generation currents are negligible, which is normally a valid assumption for moderate illumination intensities. However, as exposure to radiation fluences increases the number of recombination-generation defect sites within the space charge region, this assumption may no longer be valid. To correct Equation 4.2, the thermal generation current component J_{gen} (Ref.12) is added to the space charge drift current component J_{sc}:

$$J_{sc} + J_{gen} = q\, N_{ph}(1 - e^{-\alpha w}) + \frac{q n_i w}{\tau_{SCR}}\ ,\ A/cm^2. \qquad (4.4)$$

This current, J_{gen}, is then a leakage current or dark current which generally increases with irradiation since $1/\tau_{scr}$ is proportional to the density of recombination centers in the space charge region (see Section I).

The fraction of the total photocurrent which is due to J_{sc} will depend on the doping level in the p-region, the applied voltage, the value of L_e, and the absorption coefficient at the wavelength of the incident light. While the collection of carriers contributing to J_{sc} occurs very rapidly under saturated drift conditions, the collection of carriers contributing to J_d occurs much

more slowly due to the diffusion mechanism; this is especially important for materials with large L_e (and long minority carrier lifetimes). Furthermore, one should note that the photocurrent portion of J_d (see Equation 4.3) depends on L_e but J_{sc} does not. Therefore, J_d is more likely to decrease from the effects of radiation through radiation induced degradation of L_e than is J_{sc}. Consequently, to build a fast radiation-insensitive detector, the contribution of J_d to the overall photocurrent should be made small and the contribution of J_{sc} should be made as large as possible.

Another problem with photodiodes characterized by large diffusion current components is the electrical series resistance (Ref.1). Since minority carriers in these devices must diffuse through a relatively thick region on either or both sides of the space charge region, the effective series resistance of the photodiode can be relatively large and cause problems in systems requiring large bandwidths and low input impedances. For the case of our typical n^+p simple photodiode structure, series resistance due to carriers diffusing through the p region might be reduced by increasing the doping of the p-region (i.e. lowering the p-region resistivity). Unfortunately, increases in the doping of the p-region generally cause decreases in the minority carrier diffusion length (Ref.9), L_e, which ultimately reduces the photocurrent. However, since the space charge region is fully depleted, photocurrent generation in this region does not contribute to series resistance effects.

To minimize the disadvantages of the simple p-n junction photodiode, a p-i-n (sometimes PIN) photodiode structure can be created which tends to greatly increase the J_{sc} component of

photocurrent and reduce the J_d component (Refs. 13 and 14). In such a device, an intrinsic (i.e. undoped semiconductor material characterized by high resistivity) region indicated by either an "i" or an "I", is sandwiched between the thin, heavily doped n and p regions of the photodiode. When moderate reverse bias voltages (10-200 V) are applied to the photodiode, the intrinsic region becomes a fully depleted part of the junction space charge region. In fact, often the intrinsic region is not strictly intrinsic semiconductor material but very lightly doped n or p material. If the doping is light enough, the region will still become completely depleted at moderate reverse bias voltages.

The overall result is a photodiode with most of the optical photons absorbed in the space charge region, and therefore a photodiode with a relatively small series resistance, high speed response and some inherent immunity to radiation effects. The thickness of the intrinsic region can range from less than a micron to a few hundred microns depending on the semiconductor material type, the design wavelength for peak optical responsivity, and the speed requirements for the device. In fact, in order to better control the optical wavelength of peak detector sensitivity, the intrinsic region thickness is often selected to be equal to one optical absorption length at the selected wavelength. Although carrier transit time increases and hence device response time increases as the depletion region thickness increases, actual carrier transit time is small enough to have a minimal effect on device speed even for relatively thick i-regions. For example, Springings and McIntyre (Ref.15) have shown that the electron transit time

for a 0.5 mm thick i-region in a silicon photodiode is approximately 20 nsec with 100 volts reverse bias. Typically p-i-n devices are used in systems requiring optical detection bandwidths up to 100 MHz.

Another type of photodiode detector of considerable interest in the fiber optics community is the avalanche photodiode (APD) detector. As the name of this class of detectors implies, an avalanche multiplication process in the space charge (depletion) region provides internal gain to boost the magnitude of the photocurrent signal (Refs. 16 and 17). This type of device is important in maximizing the signal to noise ratio in detection schemes involving very weak optical signals (Refs. 18-20). In general, the use of an APD with its characteristic internal gain results in a larger overall system's signal to noise ratio than the use of a p-i-n photodiode in a similar system with greater external gain.

An avalanche photodiode makes use of the impact ionization process to multiply the number of photo-induced minority carriers as they pass through the space charge region. One difference between a conventional p-i-n photodiode and an APD is the strength of the electric field in the space charge region. For the p-i-n photodiode, the electric field need only be strong enough to drive all photogenerated carriers to the opposite side of the depletion region. In the APD device, the internal electric fields in the space charge region must be large enough to significantly accelerate the carriers traveling through the depletion region. An accelerated carrier creates additional mobile carriers by impact

ionization during collision processes as the carrier travels through the depletion region, resulting in an internal signal multiplication process. In commercially available APDs, the internal gain can range from a factor of 10 to several hundred depending on the device material, design and applied bias voltage. Substantial improvements (Refs. 16-23) have been made in the quality and variety of commercially available APDs; however, use of avalanche photodiodes is still somewhat limited due to their temperature dependent operation (Ref.24), large required bias, and radiation sensitivity. With the inherent internal gain of APDs and the resulting larger gain-bandwidth product, APDs can be used in systems requiring bandwidths in the 500-1000 MHz range (Refs.10,16,17).

One of the main difficulties experienced with many APD devices during early development was non-uniformity in the avalanche multiplication effect across the light sensitive area. Local regions often exist near the edge of the active area where the breakdown voltage is lower than in the rest of the device resulting in microplasmas or hot spots which can ultimately lead to the destruction of the device. These problems have been minimized with guard ring structures to isolate the electrically active region from the physical edge of the semiconductor die (Refs.16,17,25).

APDs are also found to exhibit fairly high noise levels, in part, because the avalanche multiplication process contains inherent statistical fluctuations. This excess noise factor associated with APDs is found to be strongly linked to the device material type and in particular the ratio of holes to electrons created in the avalanche process. As this ratio approaches 1,

the noise factor increases. Although APDs have an excess noise factor, detailed systems calculations of signal to noise ratios for these devices and p-i-n devices indicate that APDs are a better selection in systems characterized by low power optical signals and large bandwidth requirements (which often necessitate a low value of load resistance) (Refs. 18-20, 25).

Another disadvantage of APDs, especially with regard to radiation damage is that they are operated at a reverse bias voltage very near to their breakdown voltage and hence APDs routinely function in a metastable state. Small fluctuations in environmental or electrical operating condition can lead to large fluctuations in device behavior and possible self-destructive reverse currents. This concern has caused some commercial APD manufacturers to include temperature compensating circuitry in the same physical package with the APD to prevent temperature induced catastrophic failure (Refs. 21 and 24).

The last type of photosensitive device to be considered here is the phototransistor (see for example Refs. 1, 4, or 9). A phototransistor can be considered as a conventional transistor connected to a photodiode across the collector-base junction so that the transistor base drive current can be supplied by the optically generated photodiode current. The phototransistor, usually an n-p-n device, is operated with an open base and a positive bias voltage applied to the n-type collector with respect to the emitter. Physically, the photodiode and transistor are merged into the same semiconductor device and operate similar to a conventional bipolar transistor with the base minority carriers

generated by incident light instead of being injected into the base by the emitter due to applied bias voltage. For the case of an n-p-n phototransistor with electron-hole pairs optically created in the base and collector regions, excess photogenerated electrons (minority carriers) are collected by the reverse biased collector-base junction leaving the photogenerated holes in the base region. The charge imbalance created by the excess holes causes increased injection of electrons from the n-type emitter region which then traverse the base region and are collected at the collector base junction. This results in the current through the transistor being controlled by the light incident on the base region.

To achieve good gain in a phototransistor, a long diffusion length is required for minority carriers in the base region; this dependence is explicitly stated in the equations which describe phototransistor action (e.g., see Ref. 9, p. 784). In general, a strong dependence on diffusion processes implies a susceptibility to radiation damage and a relatively slow response time. Typical silicon phototransistors provide a gain (signal current electrons/ incident optical photons) of approximately 200 with a response time on the order of microseconds. This moderate speed is often sufficient for many commercial applications such as optoelectronic isolators/couplers and discrete detectors. Their sensitivity to radiation limits their usefulness in hostile environments.

Phototransistors physically differ from conventional bipolar transistors in their relatively large area base-collector junction which is required to efficiently collect light and their mechanical package which requires a window to couple light into the

semiconductor die. These devices are readily available commercially in silicon material and available on a research basis in certain compound semiconductor materials.

2. SILICON DETECTORS

Presently, silicon based photodetectors are the most widely used commercial photodetectors on the market. This is due in part to the extensive research on silicon materials for use in transistor and integrated circuit technologies. The optical detector area has benefited from these development efforts by the availability of numerous high quality, low cost silicon based photodetectors - many including sophisticated integrated electronic amplifiers in the same package (Ref.21). Currently all types of detectors discussed above (p-n, p-i-n, APD, phototransistors) are commercially available in silicon material.

However, silicon based detectors have some important intrinsic limitations which reduce the usefulness of these detectors in many applications. The most important limitation of silicon based detectors is the restriction of their range of spectral sensitivity to optical wavelengths between .3 μm and 1.1 μm. This limits the usefulness of silicon based detectors in many long wavelength applications; this is of particular concern for new optical fiber systems due to the use of longer operating wavelengths. As noted in Section III, wavelengths in the 1.1 μm to 1.6 μm range are currently being considered to more fully exploit the potential low attenuation and large bandwidth of recent optical fiber materials. Despite these limitations there are

still many important applications for silicon detectors in glass fiber optic systems operating at .82 μm - .9 μm, in plastic fiber optic systems operating at .6 μm - .7 μm, and in optoelectronic isolators (Refs.2,3,10,19,20).

As noted earlier in this report, one of the most important parameters involved in the selection of ionizing-radiation insensitive optoelectronic components is the wavelength of the signal carrying light beam. Therefore, it is important to examine the spectral response of silicon detectors in some detail. Although it may appear that the response of a silicon photodetector is solely determined by the bandgap of the material, E_g = 1.12 eV (1.107 μm) at 300 K, actually the spectral response of a photodetector is subject to other important factors including the antireflection coating, device structure, layer thickness, and applied bias voltage. The spectral response curves shown in Figure 4.1 indicate a considerable variation in the spectral response of several different silicon detectors. In this Figure, quantum efficiency is defined as the number of electron-hole-pairs contributing to photocurrent per incident optical photon and is plotted versus wavelength. Also shown on this plot is the absolute responsivity in milliamps of signal current per milliwatt of incident optical power at the wavelength indicated on the horizontal axis.

In general for silicon material, the optical absorption coefficient, α, is small for optical wavelengths corresponding to photon energies only slightly greater than the bandgap and therefore, light in this range penetrates relatively deeply below the

device surface before it is absorbed. This wavelength range is of interest because of the use of InGaAs emitters and the use of neodymium yttrium aluminum garnate (Nd-YAG) lasers at 1.06 μm for certain fiber optic systems. Many silica optical fibers have a window of low attenuation at this wavelength (Refs.3 and 10). As shown in Figure 4.1, the responsivity in the range 1.00 to 1.10 μm can be considerably enhanced by making the i-region in a p-i-n photodiode thicker and by using the appropriate antireflection coating on the surface of the device. The data in Figure 4.1 also indicate that the spectral response for the p-i-n photodiode can be shifted to the shorter wavelengths by using a thin i-region and selecting an antireflection coating suitable for shorter wavelengths. The result is an ultrafast photodiode maximized for response at the 0.6328 μm wavelength.

The spectral response of another type of silicon photodetector, a Schottky barrier photodiode is also shown in Figure 4.1. Note that the Schottky barrier Au-i-n^+ device has a considerably enhanced short wavelength response. In this device a very thin layer of gold (Au) is deposited on an intrinsic layer which is grown on a low resistivity n^+ substrate. The junction is formed at the Au-i interface allowing depletion of the i-region with reverse bias. Under these conditions, the operation of the device is similar to a reverse biased p-i-n photodiode and the photocurrent is given by an expression similar to Equation 4.2 (Ref.16). Since this device has no heavily doped "photoactively dead" region at the top of the device (as in p-n and p-i-n photodiodes),

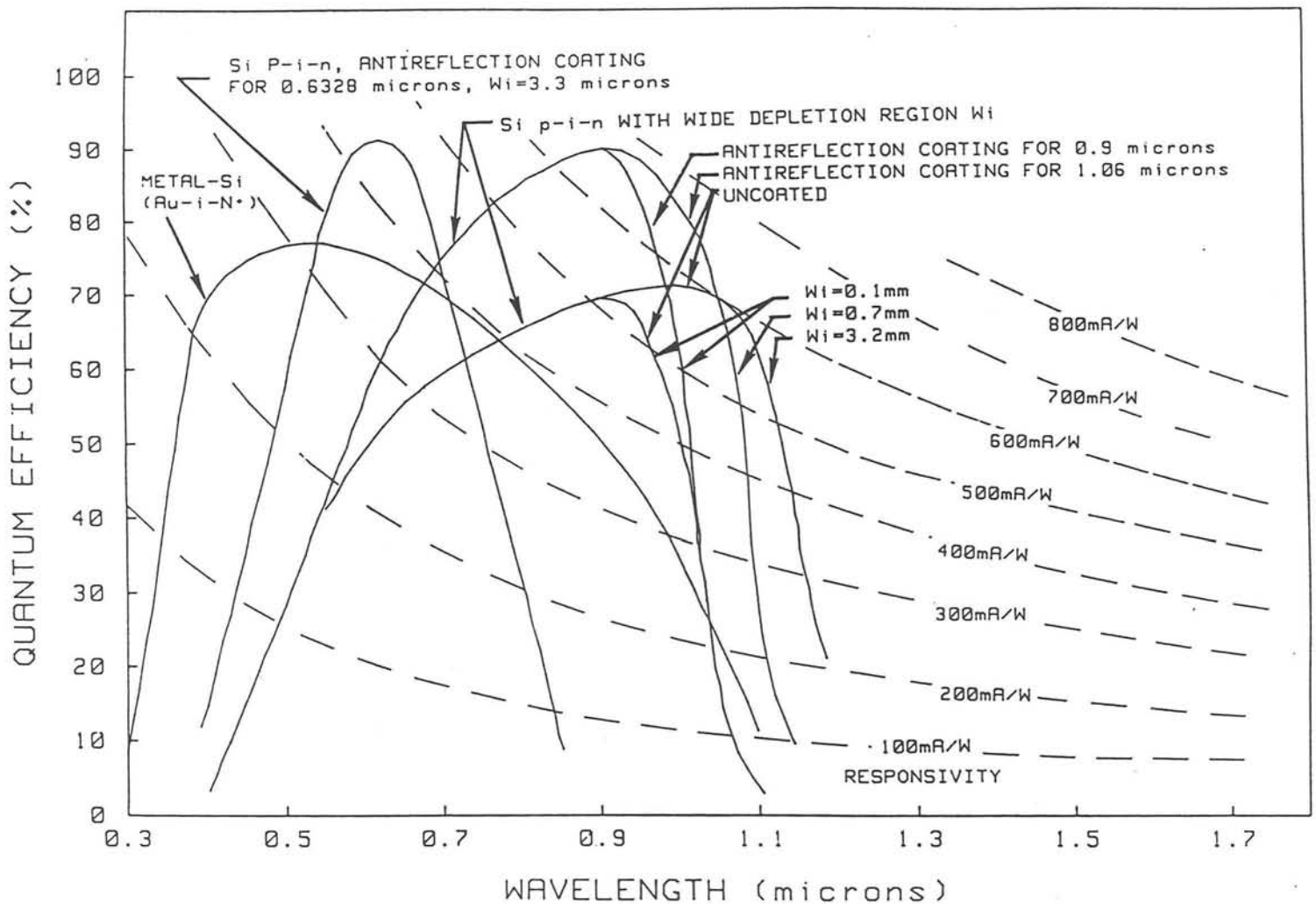

Figure 4.1 Quantum efficiency and responsivity data for several silicon photodiode detectors (from H. Melchior-Reference 16).

short wavelength light, which is absorbed near the optically illuminated surface, can contribute to the photocurrent. Schottky barrier photodiodes usually exhibit large leakage currents due to edge effects and so guard rings are usually employed to minimize the effects of these currents on overall performance.

The data for silicon photodetectors presented in Figure 4.1 clearly indicates that silicon materials can be used to detect light in the 0.50 μm to 1.10 μm range - an important spectral region, but somewhat limited for all fiber optics applications.

3. GERMANIUM DETECTORS

Germanium is used in the fabrication of some commercially available p-n junction photodiodes and avalanche photodiodes (Refs. 26 and 27) because the smaller bandgap (Eg - 0.66 eV @ 300 K) associated with Ge relative to Si makes these detectors sensitive to optical wavelengths in the infrared part of the spectrum to 1.9 μm - significantly beyond the range of silicon based detectors. Due to the smaller bandgap, germanium photodiodes are characterized by a larger thermally generated leakage current and greater noise equivalent power than silicon detectors. As shown in Figure 4.2, germanium detectors are sensitive from .5 μm to beyond 1.9 μm although due to their noise characteristics they are rarely used for optical detection at wavelengths below 1.0 μm (since silicon detectors are still responsive and have lower noise levels). Germanium detectors can be cooled to improve their noise characteristics.

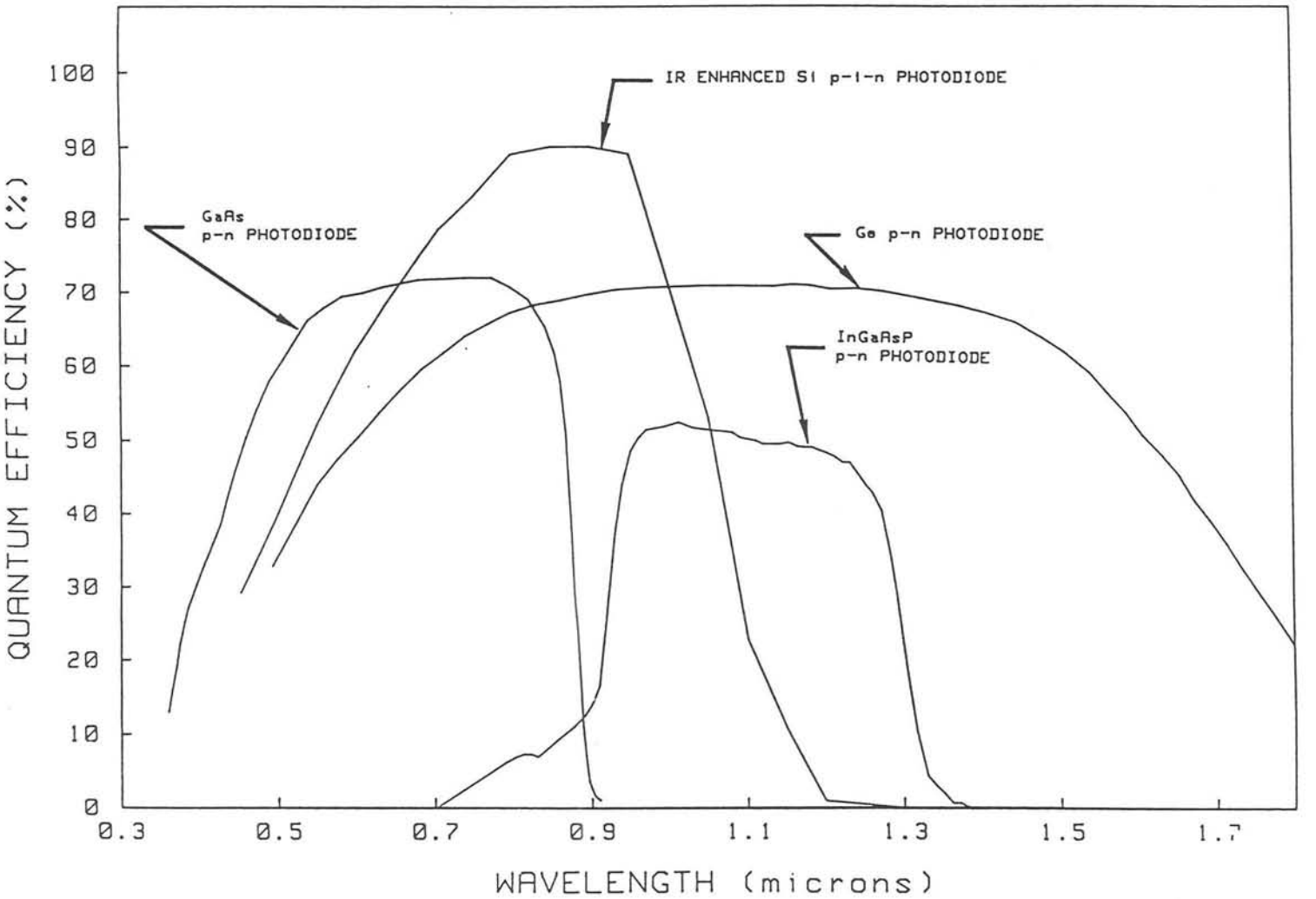

Figure 4.2 Quantum efficiency data for selected Si, Ge, GaAs, and InGaAsP photodiode detectors.

4. III-V COMPOUND SEMICONDUCTOR DETECTORS

In recent years, there has been increased interest in the infrared part of the optical spectrum between 1.1 μm - 1.6 μm. As discussed in the previous Section, in this range optical fibers have both low attenuation and dispersion so this region is appropriate for long distance, high data rate, communication systems. Since this part of the spectrum is beyond the range of sensitivity for silicon detectors, there has been renewed interest in fabricating high speed, high responsivity, low noise photodetectors from III-V semiconductor materials including binary, ternary and quaternary compounds of GaAs, InP, AlGaAs, InGaAs, GaAsSb, AlGaSb, GaAsP, AlGaAsSb, and InGaAsP. The term III-V is used to describe semiconductor materials composed of two or more elements with at least one element from the III column (Al, Ga, In) and one from the V column (P, As, Sb) of the periodic table of elements. Although the fabrication and growth technology associated with many III-V compounds is still in an early stage of development, some III-V detectors are currently commercially available.

Detectors fabricated from III-V materials have several advantages over silicon and germanium detectors. First, the bandgap (and thus the range of optical sensitivity) of ternary and quaternary III-V semiconductor materials can be varied by altering the alloy composition (Ref.28). In fact, the range of optical sensitivity can be selected to satisfy application requirements for wavelengths from .4 μm to over 9.0 μm.

With the appropriate selection of materials and alloy composition, III-V compound semiconductors can often be made to be

direct bandgap materials. The relatively large optical absorption coefficients characteristic of direct bandgap semiconductor materials is useful in the fabrication of efficient photodetectors with a small active region volume. The active region volume of a photodetector is a key parameter in designing radiation hardened photodetectors - generally smaller active region photodiodes are less sensitive to ionizing-radiation.

In addition to the qualities listed above, photodiodes fabricated from III-V compound semiconductors often are faster in response than similar structures in silicon or germanium devices due to shorter minority carrier lifetimes and larger carrier velocity. Finally, III-V devices (GaAs, AlGaAs, AlGaSb, InGaAsP and others) usually require a lower voltage bias supply for operation than silicon and many germanium devices. This is an important advantage in many applications where voltage supplies are limited to integrated circuit logic levels. In fact, some AlGaAs/GaAs photodiodes can operate with full optical responsivity and subnanosecond response time with 0 volts of applied bias (Ref.29).

Space limitations in this text prevent a complete discussion of all detectors fabricated with III-V materials; however, Figures 4.2 and 4.3 illustrate some typical quantum efficiency curves for photodiode detectors fabricated from GaAs, AlGaSb, GaAlAsSb, GaInAs, and InGaAsP. Also included in Figure 4.2 are quantum efficiency curves for silicon and germanium detectors for ease of comparison. Since the sensitivity of III-V detectors is strongly dependent on alloy composition, the curves presented in Figures 4.2

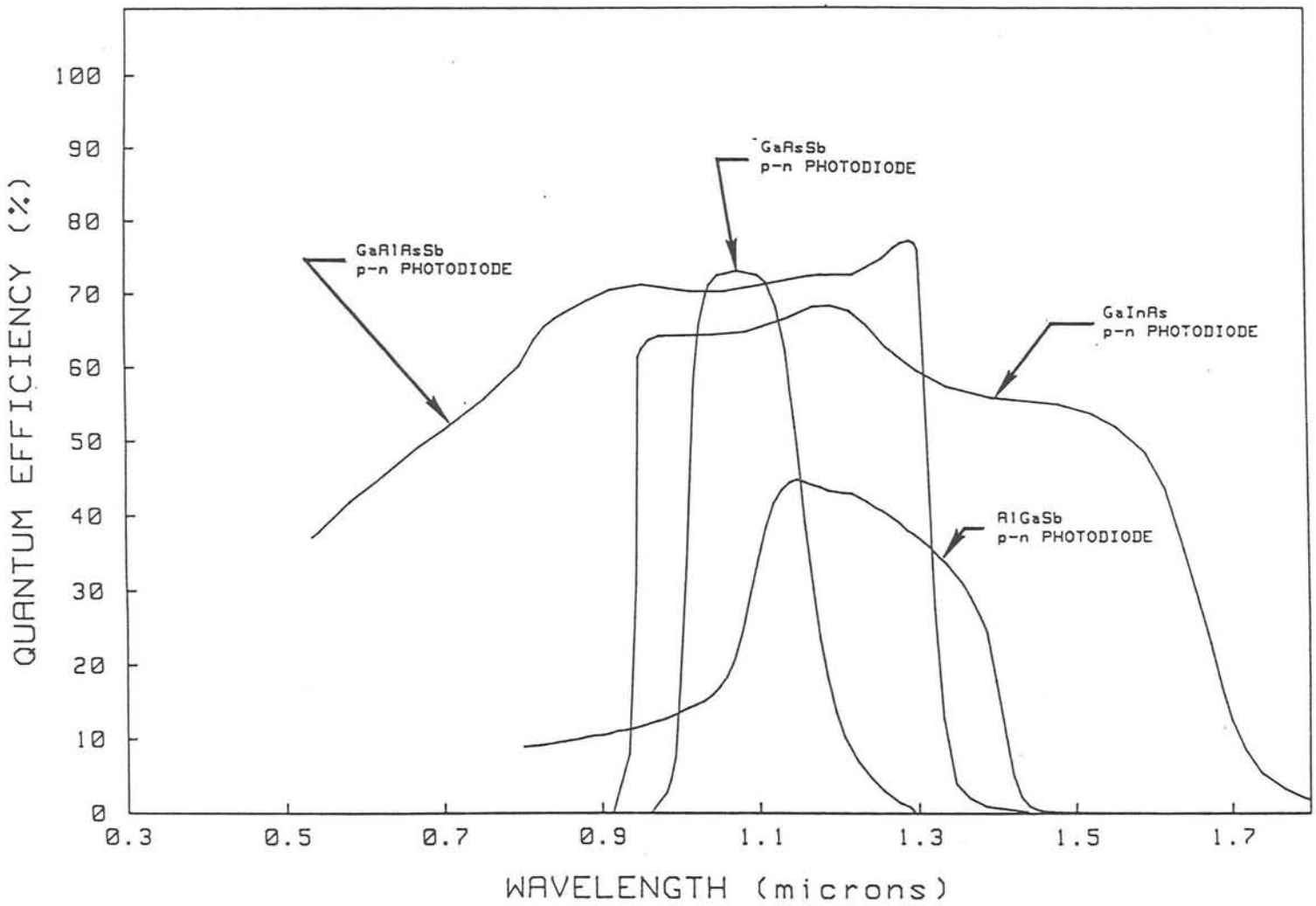

Figure 4.3 Quantum efficiency data for selected III-V compound semiconductor photodiodes including devices fabricated from GaAlAsSb, GaAsSb, GaInAs, AlGaSb.

and 4.3 are intended to be only representative of detector sensitivities that can be achieved in these material systems (Refs.29-33). A more complete discussion of these types of detectors can be found in several references (Refs. 30-37).

5. RADIATION EFFECTS

Certain military and civilian applications require the continuous operation of optoelectronic information transfer systems during and immediately after exposure to radiation. In this type of environment, the photodetector element can be the element which limits system operation; this is most common in relatively short distance links. Since semiconductor photodetectors generally respond to electromagnetic radiation with photon energy greater than the semiconductor bandgap, photodetectors generate electrical current due to incident ionizing-radiation (e.g. x-rays, gamma rays) as well as incident optical photons. In addition, some crystalline properties of semiconductor materials are often altered as a result of exposure to radiation. For photodetectors, the minority carrier diffusion length and the number of radiation induced defect sites in the crystal lattice are important factors in determining device degradation after exposure to radiation.

The effects of radiation on photodiode structures have been studied by several researchers during the past 10 years including Mitchell (Refs.38 and 39); Kalma and Hardwick (Refs.40-42); Loo, Kamath, and Knechtli (Refs.43-45); Wiczer, Barnes, Dawson, and Osbourn (Refs. 46-49); and others (Refs. 50-52). Much of the

information about radiation effects in photodetectors was derived from the relatively large body of data on radiation effects in bulk semiconductors and other semiconductor devices (Refs. 53-58) including signal diodes, signal transistors, and microwave devices.

In general, it would be expected that semiconductor devices not dependent on minority carrier diffusion lengths for optical sensitivity would be inherently insensitive to the permanent damage effects of radiation. For example, typical transit times in fully depleted p-i-n detectors are 1-10 nanoseconds for relatively thick i (intrinsic) regions (Ref.15). Before there is a significant probability of the minority carrier recombining as it crosses the i region, the lifetime must be reduced by radiation damage to a time comparable to the transit time. This will require a substantial radiation dose for high speed photodiodes. In fact, we will show that increases in photodiode leakage currents induced by large densities of deep trapping centers may become more of a problem in certain applications than a slight degradation of the photoresponse.

a. Permanent damage effects - For detectors in which the photocurrent is due to minority carrier generation in a depleted region, there is little dependence on radiation-induced minority carrier lifetime degradation. These detectors, which include p-i-n photodiodes, avalanche photodiodes, Schottky barrier photodiodes and certain heterostructure III-V photodiodes depend on internal electric fields to collect minority carriers. In these devices,

theory (Refs. 45 and 59) and experiments (Refs. 40 and 49) have shown that the most important permanent damage effect with regard to proper device operation is increased leakage current. In most cases, radiation damage also results in a decrease in optical responsivity which can result in greater than a 50% loss of signal after a 10^8 rad (Si) total dose exposure (Refs. 40 and 49). However, from a functional viewpoint, most optoelectronic systems will continue to properly operate with a factor of two decrease in signal current since generally optoelectronic systems must have a significantly greater signal margin to compensate for additional optical losses due to degradation in the other optical components (e.g. fiber optic connector excess loss, increased fiber loss due to microbending during installation, lens degradation due to environmental factors or misalignment, laser diode or LED degradation, etc.). A 10 to 10,000 factor increase in detector leakage current (Refs. 40 and 49) as a result of 10^8 rad (Si) total dose exposure will have significant effects on most optoelectronic systems. In fact, few systems will be able to continue to operate after a 100 fold increase in photodiode leakage current. In many optoelectronic systems, the minimum optical signal required for proper system operation is determined by the noise in the detection components. The photodiode noise current is approximately proportional to the square root of the leakage current (Refs. 6,16,60,61). Therefore, when the leakage current increases due to irradiation, the system's minimum detectable signal also increases.

This effect can be considered in more detail by referring back to Equation 4.4 where the photodiode leakage current is

explicitly related to the density of recombination centers ($1/\tau_{scr}$). One effect of radiation damage in semiconductor materials is an increased number of recombination centers due to the presence of crystal defect sites. Biard (Ref.59) and Kiehl (Ref.62) have made theoretical predictions which suggest that a neutron fluence of 10^{15} neutrons/ cm^2 will induce a leakage current of 10 μA in a typical silicon p-i-n photodiode. Similar calculations by Kiehl can be summarized by the curves in Figure 4.4. These curves consider the case of an optoelectronic isolator characterized by a source (LED) drive current and a typical p-i-n photodiode detector current plotted as a function of the concentration of radiation-induced trapping centers, N_t. At the lowest trap density levels (10^{11} - $10^{12}/cm^3$), the dark current increase is negligible and the total diode current, J_D is proportional to the light output over most of the LED current range. However, as N_t increases, the dark current component increases much faster than the photocurrent decreases due to increased minority carrier recombination. According to calculations by Kiehl, trap densities greater than $10^{14}/cm^3$ must be created by radiation damage before a decrease in photodiode signal current becomes significant; this level of damage results in a 1000 fold increase in dark current.

Experimental investigations of permanent damage effects in Si p-i-n photodiodes (Refs. 40,63,64) and AlGaAs/GaAs photodiodes (Refs. 49,63,64) tend to confirm the above theoretical predictions. Braeunig et al (Ref.63) found significant increases in leakage current for silicon p-i-n photodiodes due to x-ray and electron

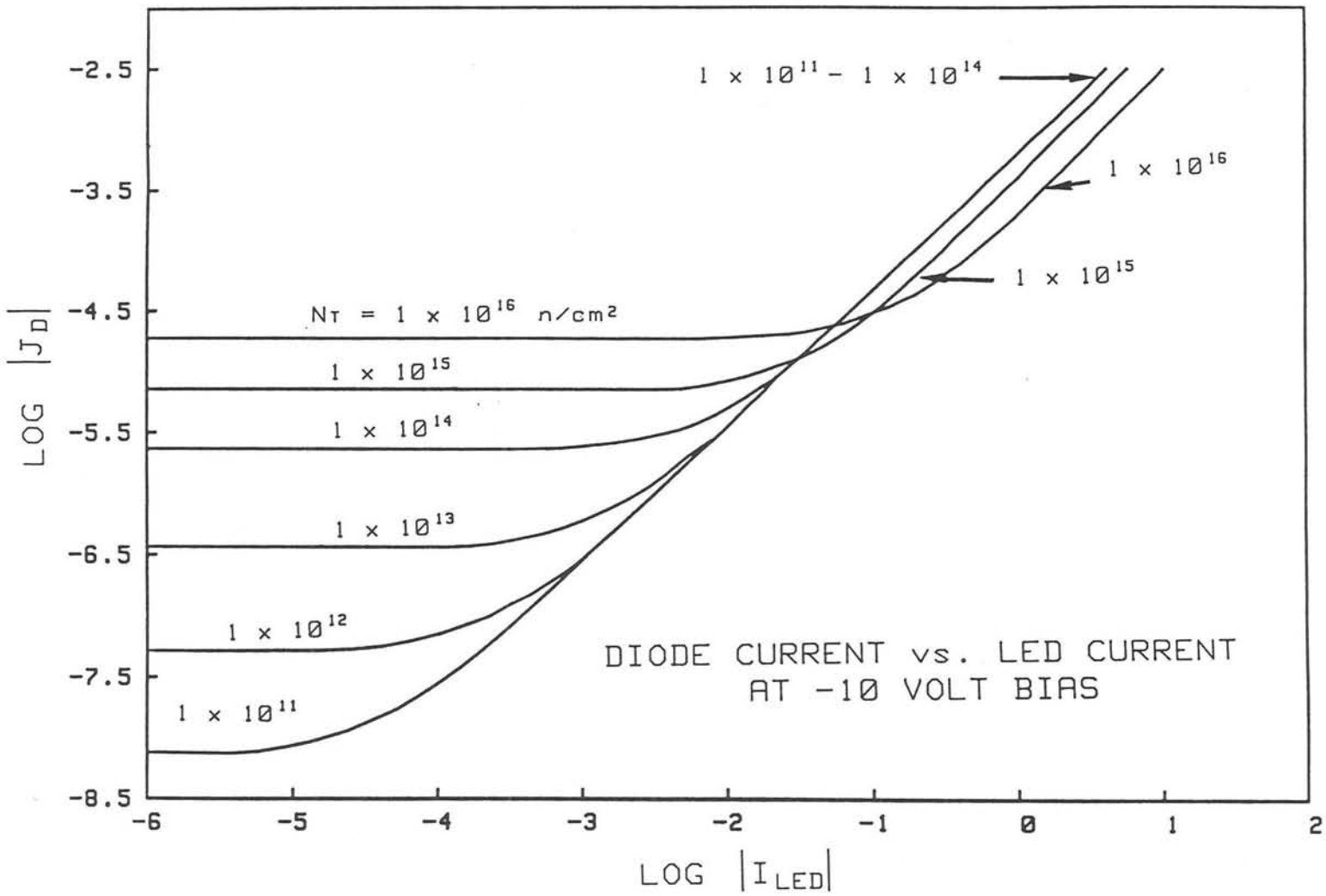

Figure 4.4 Calculated values for total p-i-n photodiode current (dark current plus signal current) as a function of LED source drive current after neutron irradiation. Each curve represents opto-isolator characteristics after exposure to indicated neutron fluence. Note that increases in dark current are more of a problem than recombination-induced decreases in photocurrent.

irradiation. Braeunig observed as large as a 1000 fold increase in noise equivalent power (NEP) due to a fluence of 10^{15}, 1.5 MeV electrons/cm^2. Kalma and Hardwick (Ref. 40) and Wiczer, Dawson, Barnes and Osbourn (Ref. 49) both observed significant increases in leakage current after 10^7 - 10^8 rads (Si) total dose exposure (gamma photons from cobalt-60) in silicon and AlGaAs/GaAs photodiodes. Leakage current increases from 10 to over 1000 times the pre-irradiation values were measured. The magnitude of the leakage current increase was found to be dependent on the overall device geometry (junction cross-sectional area, the presence of a guard ring), the semiconductor material used in the device, the details of the fabrication process (presence of a mesa structure to reduce excess leakage currents at the device edges) and the bias voltage used during operation. Kalma and Hardwick found that surface shunt paths were produced in all silicon p-i-n photodiodes tested but these surface shunts had a particularly detrimental effect on guard ring photodiodes making these devices effectively inoperative at gamma irradiation levels of 10^8 rad (Si) due to excessive leakage current at reverse bias. In fact, for some silicon guard ring p-i-n structures, Kalma and Hardwick (Ref. 40) observed a low impedance path on the order of 10^4 ohms between the guard ring and the photodiode cathode after exposure to 10^5 rad (Si) from a cobalt-60 source. Wiczer, et al. (Ref. 49) confirmed these observations. Another permanent damage effect noted was a decrease in device optical responsivity, particularly in the long wavelength end of the spectrum. In most semiconductor materials, the optical absorption coefficients decrease as the photon energy of the light approaches the bandgap energy - the long wavelength portion of the responsivity

spectrum. This results in long wavelength photons generating excess minority carriers a greater distance from the metallurgical junction region than shorter wavelength photons. Therefore, any minority carrier lifetime degradation due to radiation damage has a more pronounced effect on long wavelength optical responsivity.

Although these devices are not impervious to the effects of ionizing-radiation, a judiciously selected silicon p-i-n or AlGaAs/GaAs double heterostructure photodiode[49] can function after exposures to 10^8 rad (Si) gamma irradiation or a 10^{14} n/cm^2 neutron fluence. The optical responsivity will be degraded somewhat and the photodiode dark current will increase substantially, but with a proper circuit configuration, these devices should continue to operate. In certain applications where the speed of the detector response is in the 0.1-10.0 microsecond range, a photodiode may be operated in its photovoltaic (no reverse bias) mode. This effectively eliminates the device dark current and thus reduces the effects of dark current increase after irradiation. The AlGaAs/GaAs double heterostructure devices operate better than silicon devices in this mode since the minority carriers in these materials have shorter lifetimes so that the detectors respond with shorter rise and fall times.

Due to the lack of internal signal gain for p-i-n photodetectors, additional external signal gain is required for many applications. Some p-i-n photodiode structures are used in photodetector packages containing amplifying electronics, often fabricated in the same semiconductor wafer as the detector (e.g.

the photodiode photodarlington, the optical schmitt trigger Honeywell SD-3324, and others). In these devices, output degradation may be due to radiation effects in other components (e.g. transistor latch-up, transistor gain degradation) before significant degradation in the performance of the p-i-n photodiode can occur.

Avalanche photodiodes exhibit an insensitivity to permanent damage effects of radiation similar to p-i-n photodiodes. Studies on neutron damage effects in microwave IMPATT and TRAPATT avalanche diodes (similar to optical avalanche photodiodes) by Chaffin, et al. (Refs. 65 and 66) indicated that no permanent effects should occur below fluence levels of 10^{15} neutrons/cm^2. Although primary permanent damage effects in avalanche photodiodes due to incident radiation may be minimal at irradiation levels below 10^{15} neutrons/cm^2 and 10^8 rad (Si), the transient effects in avalanche photodiodes can be significant. In fact, because avalanche photodiodes are operated close to their breakdown voltage in a metastable state, permanent catastrophic damage may occur in the avalanche photodiode due to transient noise spikes in device current generated during a ionizing-radiation exposure burst. This problem can be alleviated with careful circuit design to limit peak current spikes in the APD. This effect will be discussed in greater detail in a later section.

In contrast to the radiation hardness of p-i-n and avalanche photodiodes, phototransistors are sensitive to irradiation because their internal gain is dependent on the minority carrier lifetime in the base region. Since the minority carrier life-

time in good quality p-type silicon material can be as large as a few milliseconds, the pre-irradiation lifetime-damage constant product, $\tau_o K$, can be quite large. Accordingly, relatively low radiation fluences can cause significant degradation in phototransistor output. Neutron irradiation studies on phototransistors and optoisolators containing phototransistors tend to confirm this sensitivity. Epstein and Trimmer (Ref. 67) found that the current transfer ratio (CTR) for phototransistor isolators decreased by a factor of 10^4 at an LED current of 10 mA after a neutron irradiation of 3.7×10^{13} n/cm^2. For an optoisolator containing a similar LED but a photodiode instead of a phototransistor, the neutron induced degradation was smaller by a factor of 10 at the same neutron fluence levels resulting in an overall 10^3 decrease in CTR. Measurements in our laboratory on neutron irradiated phototransistors reveal a degradation of 3 to 5 in the current transfer ratio at a constant phototransistor collector current following an irradiation of 1.5×10^{12} n/cm^2.

Surface effects caused by ionizing-radiation have also been shown to significantly affect phototransistors at relatively low dose rates (Refs. 62 and 67). Epstein and Trimmer (Ref. 67) observed current transfer ratio reductions in optoisolator phototransistors by a factor of 3 after receiving a dose of only 10^5 rad (Si). Similar results were found by Soda, et al. (Ref. 62) during their studies on the effects of gamma irradiation on phototransistor output as a function of phototransistor collector-emitter voltage (V_{ce}) and LED drive current. For typical operating values of V_{ce} and small LED current values, the surface effects were found to be most severe, causing reductions by factors of 3

to 5 in photocurrent after 10^5 rad (Si). Soda, et al attributed these effects to gamma induced spreading of the emitter-base depletion region along the surface of the base region adjacent to the SiO_2 passivation layer. Computer calculations on this model gave results in agreement with the main features of the observed experimental data.

The severity of irradiation-induced surface effects depend on the operating conditions during exposure. Epstein and Trimmer (Ref.67) found that for V_{ce} of 10 V applied during gamma irradiation, the degradation of the opto-isolator phototransistor was much smaller than with no bias applied. Experiments in our laboratory also demonstrate the dependence of gamma induced degradation in phototransistors on bias conditions. In agreement with previous measurements on transistor gain, we find that phototransistors degrade less when their junctions are forward biased during irradiation than similar devices in a reverse bias configuration.

With regard to permanent damage effects in photodetectors, some general statements can be made. Permanent damage effects in photodetectors due to radiation exposures can be grouped into two main categories: increases in photodetector dark current (leakage current) and decreases in photodetector optical responsivity. In APD and p-i-n photodiodes, total radiation dose exposures of 10^8 rad (Si) and neutron fluence levels of 10^{14} n/cm^2 result in only moderate degradation in optical responsivity (10%-50%), but significant increases in leakage currents. Leakage current increases are generally caused by increased numbers of

recombination-generation sites within the collection region (usually the depletion region) associated with radiation-induced defects in the crystal lattice; irradiation induced surface shunt paths also increase the dark current. Depending on the specific detector circuit configuration, continued normal operation can be achieved after these irradiation levels. Since many optical detection schemes are designed to operate with substantial margins (factors of 2-10) for miscellaneous optical signal losses, an irradiation induced 50% decrease in signal current may not be noticed in many opto-electronic systems. Leakage current increases often must be compensated for by special circuitry. In contrast to p-i-n photodiodes, phototransistors suffer from substantial decreases in optical responsivity and large increases in detector leakage current at similar levels of irradiation. In comparing permanent damage effects for similar device structures fabricated from different materials (silicon, III-V binary, III-V ternary, and III-V quaternary compounds), some additional studies are required for conclusive results. In general, III-V detectors can be made to be at least as insensitive to the permanent effects of radiation as silicon devices (Ref.49). Theoretical predictions suggest that some direct bandgap III-V alloys may be less sensitive to the permanent damage effects of radiation than silicon (Ref.48) due to the inherently shorter diffusion lengths and shorter lifetimes of minority carriers. Additional experiments and technology development may be required to confirm these suggestions. In certain applications where optical wavelengths greater than 1.1 microns must be detected, materials other than sili-

con must be used for detector fabrication and so any comparison of properties must be limited by the wavelength range being considered.

b. Transient effects - Photodetectors will experience severe effects when exposed to intense transient ionizing-radiation pulses, such as the conditions associated with a nuclear detonation. The same semiconductor processes which generate the desired signal current in a photodiode during normal device operation also generate current in the photodiode during exposures to ionizing-radiation. There are two possible approaches to this problem: assume the optoelectronic system is inoperable for the duration of the ionizing radiation pulse but will operate normally again after an appropriate delay, or design special photodiodes that will be insensitive to ionizing-radiation but will retain optical sensitivity. At our laboratory we have actively investigated both solutions to the problem.

In considering the optoelectronic system inoperative during exposure to ionizing-radiation environments two important aspects must be considered: can the intended application function normally with a "down time" during exposure and how long will the "down time" last? If the optoelectronic components are used in a critical timing-dependent application that cannot tolerate a one microsecond to 15 millisecond loss of operation then this approach to the transient ionizing-radiation problem is not viable. If short "down times" are acceptable, then silicon p-i-n or avalanche photodiodes may be acceptable in optoelectronic systems

that must operate after exposure to transient radiation pulses of 10^7 to 10^{10} rad/s. If the photodetector irradiation induced noise current lasts only as long as the ionizing-radiation pulse and short down times are acceptable, then considering the optoelectronic system off during exposure may be an acceptable solution to the ionizing-radiation problem. Unfortunately, some experimental and theoretical evidence tends to suggest that this may not always be the case; photodetectors may in fact be turned off for longer periods of time than the irradiation pulse duration. Computer modeling (Ref.68) of a reverse biased p-i-n detector exposed to an intense pulse of ionizing-radiation has demonstrated that long photocurrent tails can exist following termination of the radiation pulse. These long photocurrent tails are due to a phenomenon referred to as the "field collapse effect" which is briefly explained below. An intense ionizing-radiation pulse creates large densities of electrons and holes throughout the i-region of p-i-n photodiodes. Due to the influence of the electric field in the intrinsic region, the carriers drift toward the junctions, creating a depletion of holes near the n-i junction and a depletion of electrons near the p-i junction. The resultant nonuiniformities in carrier densities across the i-region lead to the formation of a space charge region which alters the electric field distribution across the i-region. In the center of the i-region, the field collapses to a small value but increases near each junction (p-i and n-i) to maintain the applied voltage. Consequently, the large densities of carriers remaining in the center of the i-region are collected slowly at low drift velocities

or diffusion limited velocities. This slow collection of carriers gives a long term photocurrent tail which could interfere with data link operation for significant times after the end of the ionizing-radiation pulse.

We have experimentally verified the field collapse effect by exposing p-i-n photodiodes to 30 ns wide x-ray pulses from a Febetron machine. Figure 4.5 shows a representation of the oscilloscope trace recorded during the x-ray pulse. For the lower dose rate of 7.7×10^8 rad/s (Si) illustrated in the upper curve of Figure 4.5, the induced current time signature is characteristic of the excitation x-ray pulse and in general at lower dose rates the induced current follows the irradiation pulse. However, at the higher dose rate of 8.7×10^9 rad/s (Si) illustrated in the lower curve of Figure 4.5, the irradiation-induced photo-current extends in time beyond the duration of the excitation x-ray pulse. By measuring the area under the irradiation-induced current versus time curves similar to Figure 4.5, the total charge collected as a function of total dose (where total dose is proportional to dose rate for fixed pulse durations as in this experiment) can be mathematically determined and is shown in Figure 4.6. As expected the charge collected is linearly related to the total dose; this is indicated by a unity slope for the total collected charge vs. dose curve illustrated with open circle data points on Figure 4.6. This linear variation shows that the long tail waveform of the irradiation-induced current is not due to some extraneous effect such as instrumentation amplifier saturation. If the waveform of the irradiation induced current was identical in shape to the x-ray pulse waveform,

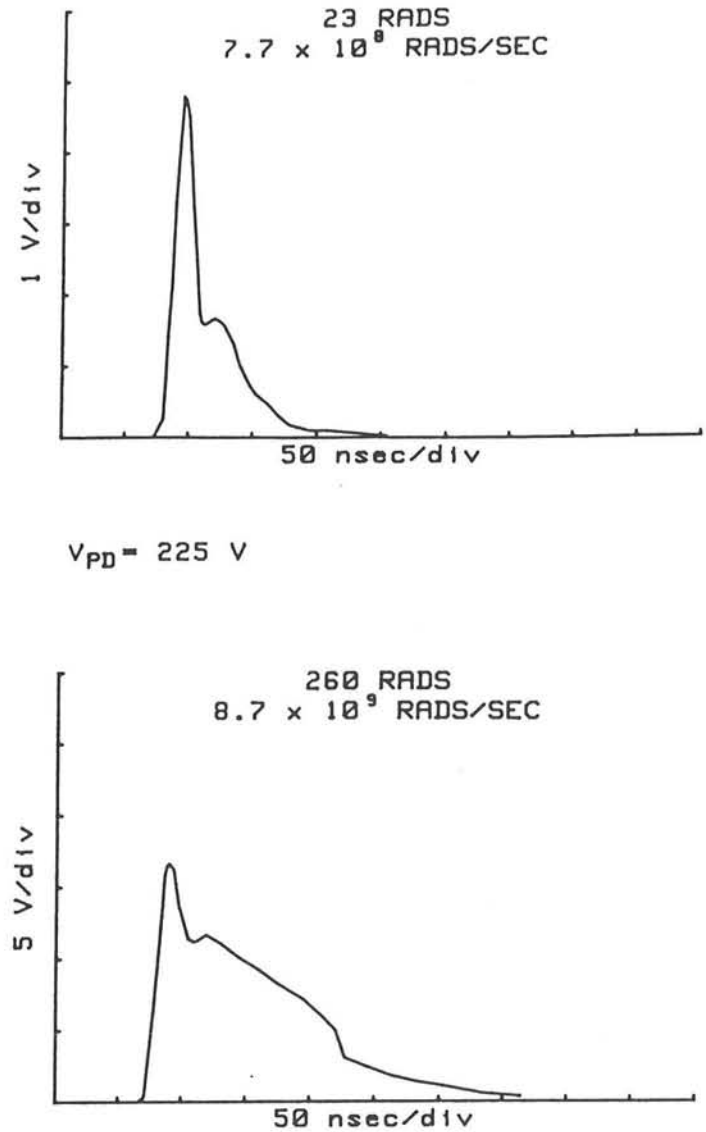

Figure 4.5 Oscilloscope traces of x-ray induced photocurrent in a typical silicon p-i-n photodiode. The top trace approximately follows the shape of the incident x-ray pulse. The lower trace shows the field collapse effect at higher incident dose rates.

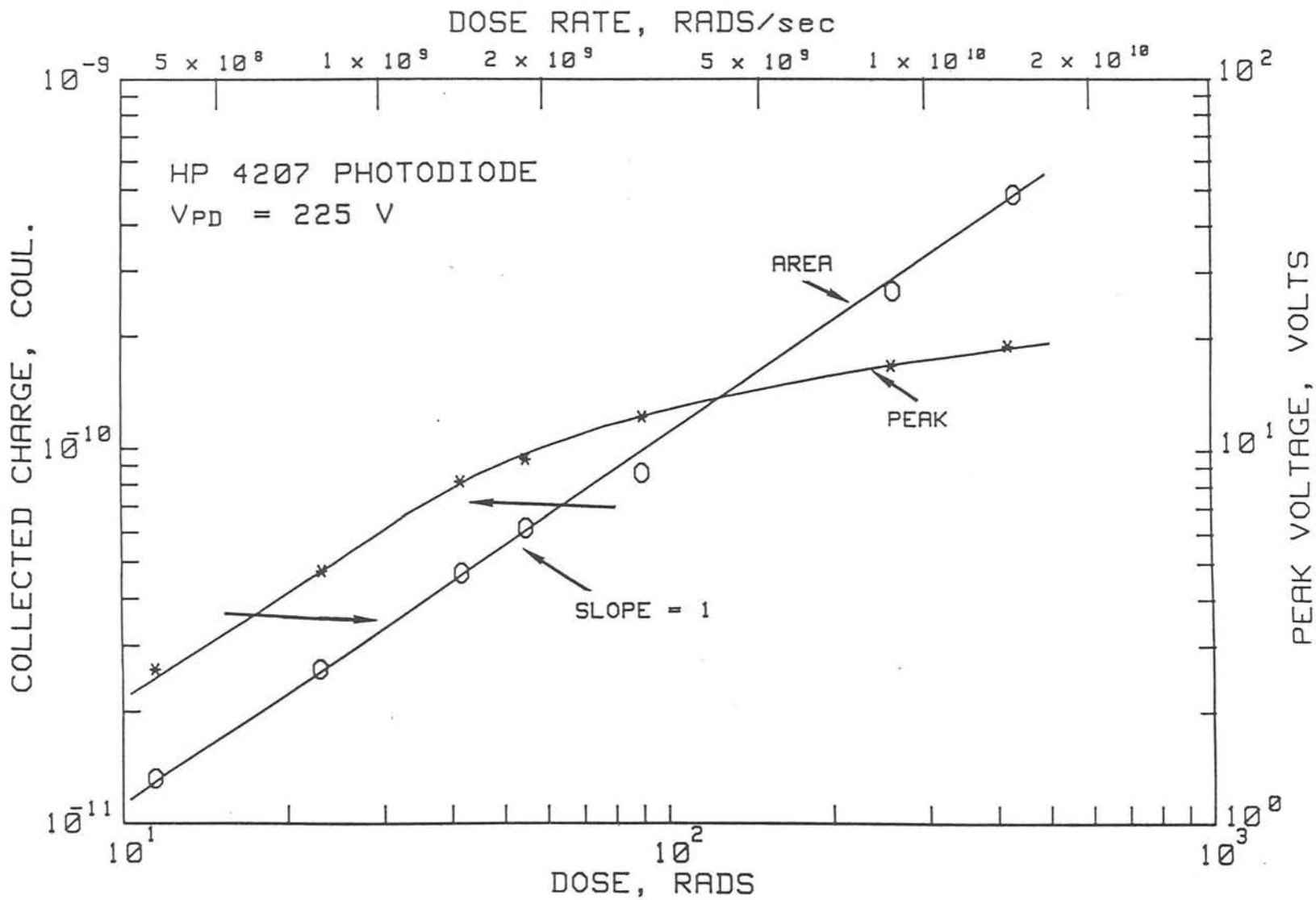

Figure 4.6 Collected charge (area under curve similar to Figure 4.5) in silicon p-i-n photodiode as a function of total dose due to 30 ns x-ray pulse is shown by curve with '0'. Note linear relationship between total dose and charge. Curve indicated by '*' plots the peak voltage observed by current viewing resistor during x-ray pulse. Non-linear relationship indicates field collapse effect at high dose rate x-ray irradiation.

then the peak voltage measured across the fixed load resistor (attached between the photodiode under test and the power supply) should vary linearly with dose. The curve denoted with asterisks in Figure 4.6 illustrates the nonlinear relationship between the measured peak voltage and the total dose for dose rates above 10^9 rad/s (Si). These observations agree with the delayed collection of a significant portion of the X-ray induced minority carriers as predicted by the field collapse theory. It can be concluded that the delayed collection effect due to the field collapse phenomenon can cause an optoelectronic data link to be "down" for several hundred nanoseconds after exposure to an intense pulse of ionizing-radiation. The length of time for recovery depends on the irradiation dose rate, the applied bias voltage, and the specifics of the device geometry.

Walters and Hall (Ref. 69) have found that pulsed neutron irradiation can produce similar long-term ionizing-radiation induced currents in avalanche photodiodes. Following a 50 microsecond neutron irradiation delivering 2.4×10^{12} neutrons/cm^2, 15 milliseconds of "down" time was required to allow irradiation induced photocurrents to decrease to near zero. These tests were performed at Sandia National Laboratories SPR-11A reactor facility which has a clean neutron spectrum free of significant gamma and beta doses. These results are interesting since the 15 millisecond recovery time is too long to be attributed to the field collapse effect described above. These longer times are characteristic of transient annealing of neutron damage in Si as observed in silicon solar cells after neutron irradiation (Ref. 57).

This relatively long recovery time has important implications on systems using these components and expected to operate shortly after a pulsed neutron exposure.

In addition to intense, short duration ionizing pulses, longer term, low dose rate environments can also affect photodetector performance. These include dose rates in the 10 rad/s to 10^6 rad/s range lasting for periods of milliseconds to steady state exposures. Lowery and Friddell (Ref.70) have made measurements of the magnitude of photocurrents generated in photodiodes from different irradiation sources. They normalized their results to generate an approximate value of the irradiation induced photocurrent for a dose rate of 1 rad/s, per cm^3 of detector volume. These approximations are for p-i-n detectors fabricated from silicon. Rough averages based on their results are as follows: 0.5 to 3 Megavolt (MeV) x-rays - 12 microamps; 10 to 20 MeV Bremmstrahlung - 5 microamps; cobalt-60 gamma rays - 10 microamps; and 10 MeV electrons - 8 microamps. These values are dependent on the specific device geometry but they give an approximate indication of the magnitudes of photodiode noise currents to be expected during an ionizing-radiation pulse. It should be noted that many optoelectronic systems normally operate with 1-10 microamps of signal current. A typical .25 cm^2 silicon p-i-n photodiode with an active volume of 6×10^{-3} cm^3 will generate about 60 microamps of gamma induced photocurrent when exposed to 10^3 rad/s from a cobalt-60 source. In many applications, this magnitude of photocurrent will overwhelm the signal current. Hardwick and Kalma (Ref.41) studied the effects of low dose rate irradiation on a complete optical fiber data link that

might be implemented in a space-borne application. In their study, they measured the increase in root mean square (rms) noise current for silicon p-i-n photodiodes that resulted from 1 MeV electron fluences of 10^9 to 10^{11} e/cm^2 and gamma irradiation dose rates of .1 to 10^4 rad/s from a cobalt-60 source. At 10^{11}, 1 MeV e/cm^2, Kalma and Hardwick measured an rms noise current of .1 microamps in a .01 cm^2 detector. In addition, Hardwick and Kalma studied the effects of random irradiation induced noise spikes in digital electronic detection systems. Finally they concluded that degradation in all aspects (photodetector, optical fiber, and optical source) of the link must be considered in evaluating the effects of low dose rate ionizing-radiation.

The other approach to the problem of transient irradiation effects in photodiodes is to construct special photodiodes that minimize these effects. These types of photodiodes have been investigated by our laboratory (Refs. 46-49,71) and by others (Refs.39 and 40) during the past 6 years. The goal of these efforts was to design a photodiode that minimizes the photocurrents generated by ionizing radiation without sacrificing sensitivity to optical radiation.

Kalma and Hardwick (Ref.40) studied a specially fabricated (Spectronics SPX-3290) small volume silicon p-i-n photodiode that had an active region thickness of only 20 microns. Although this device was demonstrated to be less sensitive to ionizing-radiation than many of the conventional silicon p-i-n photodiodes tested, it also was characterized by about half the optical responsivity of the other devices tested.

In our laboratory, we have designed, fabricated, and tested special direct bandgap, double heterostructure photodiodes that efficiently collect optically generated minority carriers but reject most of the ionizing-radiation generated minority carriers. The primary feature used here to improve the photodiode's ionizing-radiation immunity was the substitution of a direct bandgap semiconductor (i.e. AlGaAs, AlGaSb, and InGaAsP) for the indirect bandgap semiconductor (i.e. Si & Ge) currently used in most photodetectors. The relatively strong optical absorption effect in direct bandgap semiconductor materials makes possible relatively efficient photodiode structures with relatively thin active regions. In addition, these direct bandgap materials have significantly shorter minority carrier diffusion lengths than most indirect materials. This only allows the collection of excess minority carriers generated in the depletion region or within close proximity to the depletion region. Minority carriers created in other regions of the photodiode semiconductor die (e.g. substrate) are not collected at the junction and thus do not contribute to photodiode current. Since exposure to ionizing-radiation uniformly generates minority carriers throughout the semiconductor volume, the ionizing-radiation induced photocurrent in a photodiode is strongly related to the volume of the region in which excess minority carriers are collected. To further enhance the immunity of these structures to ionizing-radiation environments, an internal electric field was built into the device structure to prevent the junction region from collecting extraneous excess minority carriers generated in optically inactive regions of

the device. The built-in electric field, created by the heterostructure configuation, is a result of the energy bandgap mismatch between physically adjacent layers in the device's structure (Ref. 28). These structures have been grown in ternary and quaternary compound semiconductor materials by altering the alloy composition during the epitaxial growth process (Refs. 46-18,71, 72).

At our laboratory, these devices were fabricated in three material systems: AlGaAs, AlGASb, and InGaAsP. These materials were selected for their relatively large optical absorption coefficient in the optical wavelength range of interest (.7 um - 1.6 um), relatively short excess minority carrier diffusion lengths (approximately 1-2 microns), and the availability of a suitable materials processing technology - liquid phase epitaxy.

In designing and testing these devices, a relative gifure of merit for the radiation insensitivity of these devices was developed, A_{rr}:

$$A_{rr} = \frac{J_{opt}}{\phi} \quad \frac{\psi}{J_{rad}} \tag{4.5}$$

where J_{opt} is the optical current density induced by an incident flux ϕ and J_{rad} is the radiation induced current density resulting from a dose rate ψ. It should be noted that A_{rr} is also a function of the ionizing-radiation photon energy. Large values of A_{rr} correspond to less irradiation insensitivity and A_{rr}^2 is approximately proportional to the optical signal to radiation induced noise power ratio of the

detector. Extensive analysis of this problem by Osbourn (Ref.71) has shown the relationship between A_{rr} and quantum efficiency as a function of total active layer thickness. Figure 4.7 illustrates this relationship. For a given quantum efficiency design goal, different A_{rr} values can be achieved by judicious selection of layer thicknesses. Figure 4.8 shows the accuracy of Osbourn's model. For a range of device layer thicknesses, Osbourn calculated the expected quantum efficiency of the device and then we measured the actual quantum efficiency at the conditions of the calculation; agreement of theory and experiment was excellent.

Laboratory irradiation tests of these devices show that these direct bandgap, double heterostructure devices are significantly less sensitive to the effects of transient ionizing-radiation than the presently available commercial p-i-n photodiodes. Tests were performed at Sandia National Laboratories Relativistic Electron Beam Accelerator (REBA) operating in the pulsed x-ray (tantalum target) mode. The pulse was approximately 50 ns in duration with 95% of the emitted x-ray energy spectrum in the 1.5 to 2.5 MeV range. Dose rate variations were achieved by varying the distance of the darkened, electrostatically shielded test chamber from the x-ray source. Reversed bias photodiodes were connected to 50 ohm current viewing load resistors to measure x-ray induced photocurrents. A collection of commercially available photodiodes including germanium, silicon, and indium gallium arsenide phosphide devices and several specially designed double heterostructure photodiodes including devices fabriated from aluminum gallium arsenide, aluminum gallium antimonide, and indium

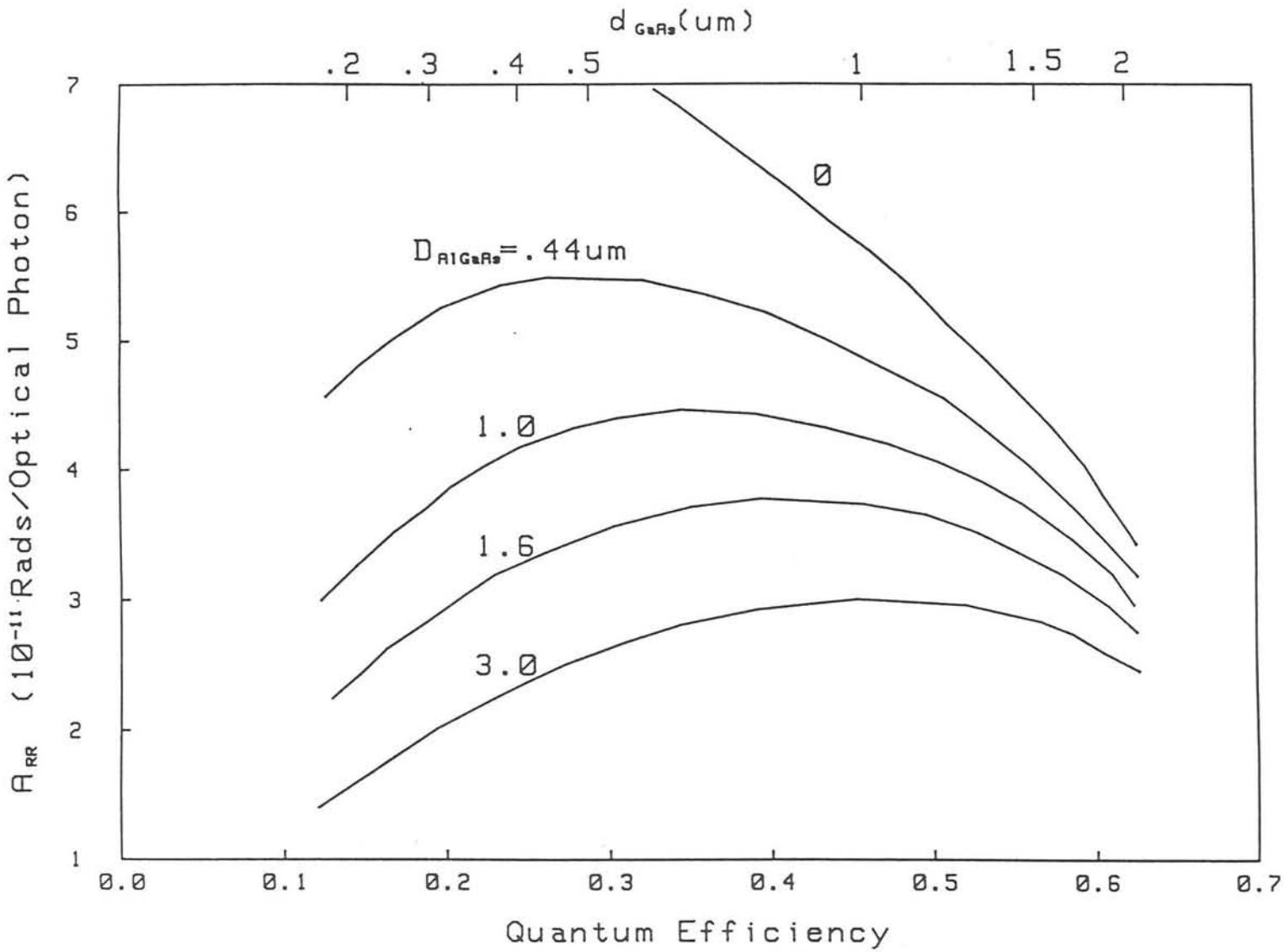

Figure 4.7 Calculated curves for quantum efficiency vs. figure of merit (A_{rr}) for immunity to transient ionizing-radiation in double heterostructure AlGaAs/GaAs photodiodes. Each curve represents a different set of device layer thicknesses.

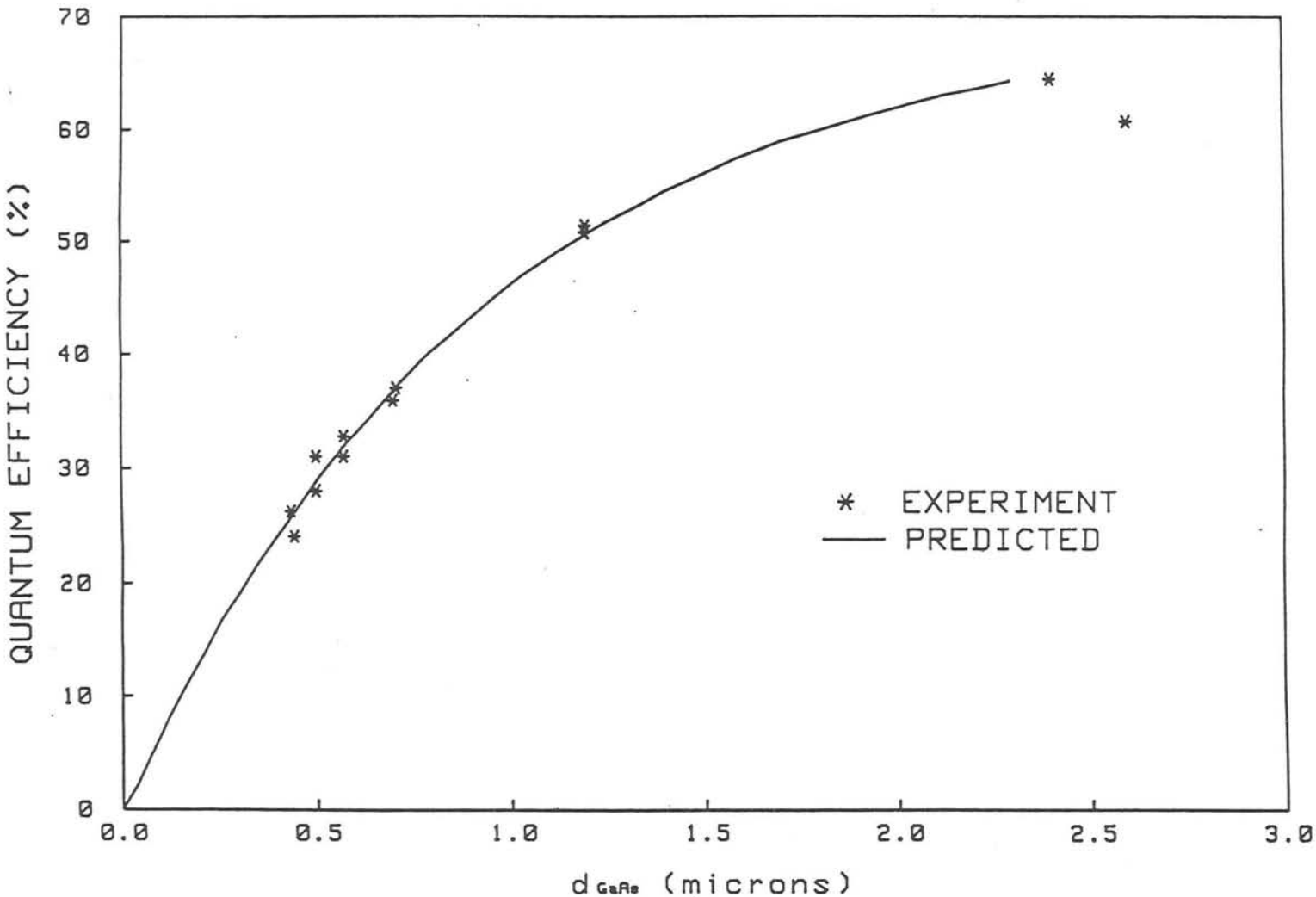

Figure 4.8 Calculated (solid line) and measured ('*') quantum efficiency data for AlGaAs/GaAs double heterostructure photodiodes as a function of active layer thicknesses.

gallium arsenide phosphide were studied. Our measurements indicate that our optimally designed AlGaAs double heterostructure photodiode had an A_{rr} value 25 times better than the best silicon or germanium device tested for .5 MeV to 2.0 MeV test spectrum. For the same material systems, our InGaAsP photodiode optimized for irradiation insensitivity had an A_{rr} 15 times greater than the commerical InGaAsP photodiode (presumably optimized for peak optical responsivity). For a system required to operate during exposure to a transient ionizing-radiation pulse, the effect of using one of these irradiation insensitive detectors would be to substantially reduce the system's initial optical signal power needs. In fact, to maintain the same signal to noise ratio during exposure to transient ionizing-radiation pulses, approximately 15 to 30 times more optical signal would be required if the best (greatest A_{rr}) commercial device were used instead of the optimally designed double heterostructure device. For these comparisons, signal to noise ratio is defined as the ratio of the desired optical signal induced photodiode current to the ionizing-radiation induced photodiode current.

6. SUMMARY

Carefully selected p-i-n and avalanche photodiodes can be relatively hard to the permanent damage effects of radiation. Phototransistors and certain integrated circuit combinations of detectors and amplifiers are somewhat sensitive to the permanent effects of radiation. Permanent damage effects in photodiodes often result in small decreases in optical responsivity and

large increases in device leakage current. Permanent damage in phototransistors often causes large decreases in optical sensitivity and large increases in transistor leakage currents.

Short, intense, ionizing-radiation pulses and long term, lower dose rate transient ionizing-radiation pulses cause significant and permanent increases in leakage (dark) current in most photodiodes. Specially designed photodiodes have been developed to reduce the effects of exposure to transient ionizing-radiation pulses. For some applications, systems that use optical detectors can be turned off or assumed inoperative during and shortly after exposure to an ionizing-radiation pulse. Care in applications circuit design must be used to prevent the large, irradiation induced currents from destroying the photodetector or sensitive amplifiers connected to the photodetector.

7. REFERENCES

1. L. K. Anderson and B. J. McMurtry, "High-Speed Photodetectors", Proc. IEEE. vol. 54, pp. 1335-1349, 1966.
2. H. Melchior, "Detectors for Lightwave Communications", Phys. Today, Nov. 1977, pp. 32-39.
3. D. Boetz and G. J. Herskowitz, "Components for Optical Communications Systems: A Review", Proc. IEEE, vol. 68, pp. 689-731, 1980.
4. J. S. Harris, ed. "Special Issue on Optoelectronic Devices", IEEE Trans. on Electron Devices, vol. ED-29, pp. 1353-1491, Sept. 1982.
5. G. E. Stillman, L. W. Cook, G. E. Bulman, N. Tabatabaie, R. Chin, and P. D. Dapkus, "Long-Wavelength (1.3- to 1.6- μm) Detectors for Fiber-Optical Communications", IEEE Trans. Electron Devices, vol. ED-29, pp. 1355-1371, 1982.
6. R. J. Keyes ed., Optical and Infrared Detectors-Topics in Applied Physics, vol. 19, Springer-Verlag, New York, 1980.
7. J. I. Pankove, Optical Processes in Semiconductors, Dover Press, New York, 1971.
8. W. G. Driscoll and W. Vaughan ed., Handbook of Optics, McGraw-Hill, New York, 1978.
9. S. M. Sze, Physics of Semiconductor Devices 2nd ed., Wiley, New York, 1981.
10. H. F. Wolf, Handbook of Fiber Optics: Theory and Applications, Garland STPM Press, New York, 1979.

11. See for example reference 9 pp. 755-758.

12. See for example reference 9 pp. 84-92.

13. W. W. Gartner, "Depletion-Layer Photoeffects in Semiconductors", Phys. Rev., vol. 116, pp. 84-87, Oct. 1959.

14. R. P. Riesz, "High Speed Semiconductor Photodiodes", Rev. Sci. Instr., vol. 33, pp. 994-998, Sept. 1962.

15. H. C. Springings and R. J. McIntyre, presented at the Int. Electron Devices Meeting, Washington, D.C., Oct. 1968.

16. H. Melchior, "Sensitive High Speed Photodetectors for the Demodulation of Visible and Near Infrared Light", J. Luminescence, vol. 7, pp. 390-414, 1973.

17. J. R. Grierson and S. O'Hara, "A Theoretical Assessment of Low and High Bandwidth Gallium Arsenide, Germanium, and Silicon Avalanche Photodiodes for Optical Communication Systems", Solid State Electronics, vol. 18, pp. 1003-1011, 1975.

18. S. D. Personick,."Statistics of a General Class of Avalanche Detectors with Applications to Optical Communications", Bell System Technical Journal, vol. 50, pp. 3075-3095, Dec. 1971.

19. J. E. Mazo and J. Salz, "On Optical Data Communication via Direct Detection of Light Pulses", Bell Systems Technical Journal, vol. 55, pp. 347-369, March 1976.

20. G. J. Foschini, R. D. Gitlin, and J. Salz, "Optimum Direct Detection for Digital Fiber-Optic Communications Systems", Bell System Technical Journal, vol. 54, pp. 1389-1430, 1975.

21. See for example product data sheets from RCA, Solid State Division, Electro Optics and Devices, Lancaster, Pa. 17604 or EG&G Inc, Electro-Optics Division, 35 Congress St., Salem, Ma. 01970

22. S. R. Forrest, R. C. Smith and O. K. Kim, "Performance of InGaAs/InP Avalanche Photodiodes", IEEE J. Quantum Electronics, vol. QE-18, pp. 2040-2048, Dec. 1982.

23. H. Ando, H. Kanbe, T. Kimura, T. Yamaoka, and T. Kaneda, "Characteristics of Germanium Avalanche Photodiodes in the Wavelength Region 1 - 1.6 um", IEEE J. Quantum Electronics, vol QE-14, pp. 804-809, Nov. 1978.

24. R. L. Bell and W. E. Spicer, "Temperature Dependence of Avalanche Photodiodes", Proc IEEE, vol. 58, p. 1738, 1970.

25. G. E. Stillman and C. M. Wolfe, "Avalanche Photodiodes", in Semiconductors and Semimetals vol. 12 : Infrared Detectors II , ed. R. K. Willardson and A. C. Beer, Academic Press, N.Y., 1977.

26. Germanium Photodiode #7460, Data Sheet by Rofin Optics & Electronics, Echo Bridge Office Park, 381 Elliot Street, Newton Upper Falls, Ma., 02164.

27. Germanium Avalanche Photodiode Detector #CG-4000, Macom Laser Diode, Inc., 1130 Somerset St., New Brunswick, N. J. 08901

28. See for example H. Kressel and J. K. Butler, Semiconductor Lasers and Heterojunction LEDs, Academic Press, New York, Ch. 11, 1977.

29. C. Y. Chen, A. Y. Cho, C. G. Bethea, and P. A. Garbinski, "Bias Free Selectively Doped AlGaAs-GaAs Picosecond Photodetectors", Appl. Phys. Lett., vol. 41, pp. 282-284, Aug. 1982.

30. T. P. Pearsall and M. Papuchon, "The GaInAs Homojunction Photodiode - A New Avalanche Photodetector in the Near Infrared between 1.0 and 1.6 um", Appl. Phys. Lett., vol. 33, pp 640-642, Oct. 1978.

31. R. Chin and C. M. Hill, "Low Dark Current GaAlAsSb Photodiodes", Appl. Phys. Lett., vol. 40, pp. 332-333, Feb. 1982.

32. G. E. Stillman, C. M. Wolfe, A. G. Foyt, and W. T. Lindley, "Schottky Barrier InGaAs Alloy Avalanche Photodiodes for 1.06 um", Appl. Phys. Lett., vol. 24, pp. 8-10, Jan. 1974.

33. H. D. Law, L. R. Tomasetta, and H. Nakano, "Ion Implanted InGaAsP Avalanche Photodiode", Appl. Phys. Lett., vol. 33, pp. 920-923, Dec. 1978.

34. R. Yeats and K. Von Dessonneck, "Detailed Performance Characteristics of Hybrid InP-InGaAsP APD's", IEEE Elect. Dev. Lett., vol. EDL-2, pp. 268-271, Oct. 1981.

35. L. R. Tomasetta, H. D. Law, R. C. Eden, I. Deyhimy, and K. Nakano, "High Sensitivity Optical Receivers for 1.0-1.4 um Fiber-Optic Systems", IEEE. J. Quantum Elect., vol. QE-14, pp. 800-804, Nov. 1978.

36. R. C. Eden, "Heterojunction III-V Alloy Photodetectors for High-Sensitivity 1.06-um Optical Receivers", Proc. IEEE., vol. 63, pp. 32-37, Jan. 1975.

37. see for example W. L. Wolfe and G. J. Zissis The Infrared Handbook, Office of Naval Research, Ch. 11, 1978; or Semiconductors and Semimetals: Vol. 12 - Infrared Detectors, ed. R. K. Willardson and A. C. Beer, Academic Press, New York, 1977.

38. K. W. Mitchell, "Optimizing Photodetectors for Radiation Environments", IEEE Trans Nucl. Sci., Vol. NS-24, #6, pp. 2294-2297, Dec. 1977.

39. K. W. Mitchell, "Optimizing Photodetectors for Digital Communications in Radiation Environments", IEEE Trans. Nucl. Sci., Vol. NS-25, #6, pp. 1545-1549, Dec. 1978.

40. A. H. Kalma and W. H. Hardwick, "Radiation Testing of PIN Photodiodes", IEEE Trans. Nucl. Sci., Vol. NS-25, #6, pp. 1483-1488, Dec. 1978.

41. W. H. Hardwick and A. H. Kalma, "Effects of Low-Dose-Rate Radiation on Opto-Electronics Components and Consequences Upon Fiber Optic Data Link Performance", IEEE Trans. Nucl. Sci., Vol. NS-26, pp. 4808-4813, #6, Dec. 1979.

42. A. H. Kalma and R. A. Cesena, "Radiation Testing of Trimetal Infrared Detectors", IEEE Trans. Nucl. Sci., Vol. NS-26, #6, pp. 4833-4839, Dec. 1979.

43. R. Loo, R. C. Knechtli, G. S. Kamath, "Enhanced Annealing of GaAs Solar Cell Radiation Damage", 15th IEEE Photovoltaic Specialists Conference Proceedings, pp. 33-37, IEEE New York, USA, 12-15 May 1981.

44. S. S. Li, W. L. Wang, P. W. Lai, R. Y. Loo, G. S. Kamath and R. C. Knechtli, "Deep-Level Defects, Recombination Mechanisms, and their Correlation to the Performance of Low-Energy Proton-Irradiated AlGaAs-GaAs Solar Cells", IEEE Trans. Elect. Dev., Vol. ED-27, pp. 857-864, April, 1980.

45. R. Loo, L. Goldhammer, B. Anspaugh, R. C. Knechtli, and G. S. Kamath, "Electron and Proton Degradation in AlGaAs-GaAs Solar Cells", 13th IEEE Photovoltaic Specialists Conference - 1978, IEEE Press, New York, USA, pp. 562-572, 1978.

46. J. J. Wiczer, C. E. Barnes, and L. R. Dawson, "Transient Effects of Ionizing Radiation in Si, InGaAsP, GaAlSb, and Ge Photodiodes", Proceedings of the Fiber Optics in the Nuclear Environment Symposium 25-27 March 1980, Vol. II Radiation Physics, pp. 209-222, DNA 5308P-2.

47. J. J. Wiczer, L. R. Dawson, and C. E. Barnes, "Transient Effects of Ionizing Radiation in Photodiodes", IEEE Trans. Nucl. Sci., Vol. NS-28, pp. 4397-4402, Dec. 1981.

48. G. C. Osbourn, L. R. Dawson, and J. J. Wiczer, "Computer Modeling and Radiation Testing of AlGaAs Photodiode Structures", IEEE Trans. Nucl. Sci., Vol. NS-28, #6, pp. 4342-4345, Dec. 1981.

49. J. J. Wiczer, L. R. Dawson, G. C. Osbourn, and C. E. Barnes, "Permanent Damage Effects in Si and AlGaAs/GaAs Photodiodes", IEEE Trans. Nucl. Sci., Vol. NS-29, pp. 1539-1544, Dec. 1982.

50. B. E. Anspaugh and R. G. Downing, "Damage Coefficients and Thermal Annealing of Irradiated Silicon and GaAs Solar Cells", 15th IEEE Photovoltaic Specialists Conference, IEEE Press, New York, USA, pp. 499-504, 1981.

51. W. Luft, "Radiation Effects on High Efficiency Silicon Solar Cells", IEEE Trans. Nucl. Sci., Vol. Ns-23, #6, pp. 1795-1802, Dec. 1976.

52. I. Arimura, J. N. Polky, and W. E. Maher, "Radiation Effects Analysis of a Coherent Laser Detection System", IEEE Trans. Nucl. Sci., Vol. NS-24, pp. 2315-2320, Dec. 1977.

53. J. H. Billington and J. H. Crawford, Radiation Damage in Solids, Princeton University Press, Princeton, New Jersey, 1961.

54. L. W. Ricketss, Fundamentals of Nuclear Hardening of Electronic Equipment, Wiley Interscience, New York, 1972.

55. Radiation Damage and Defects in Semiconductors Conference Proceeding - July 19-21, 1972 at the University of Reading, published by the Institute of Physics, London, England.

56. R. J. Chaffin, Microwave Semiconductor Devices: Fundamentals and Radiation Effects, Wiley-Interscience, New York, 1973.

57. B. L. Gregory, C. W. Gwyn, Radiation Damage in Semiconductor Devices, Vol. 1 and 2, Sandia Laboratories Report SC-M-71-0887, March 1972.

58. For example see the yearly issues of the December (Vol. 6) IEEE Trans on Nuclear Science.

59. J. R. Biard, Optoelectronic Aspects of Avionic Systems, Vol.1 AFAL TR-73-164 & Vol. 2 AFAL TR-75-45, Air Force Avionics Laboratory, Wright-Patterson Air Force Base, Ohio.

60. R. M. Gagliardi and S. Karp, Optical Communications, John Wiley & Sons, New York, 1976.

61. G. H. S. Rokos, "Optical Detection Using Photodiodes", Optoelectronics, Vol. 5, pp. 351-366, 1973.

62. K. J. Soda, C. E. Barnes, and R. A. Kiehl, "The Effect of Gamma Irradition on Optical Isolators", IEEE Trans Nucl. Sci., Vol. NS-22, pp. 2475-2482, Dec. 1975.

63. D. Braeunig, O. Meinhardt, A. Spencker, and H. G. Wagemann, "Radiation Damage in Silicon Photodetectors for Star Sensors in Satellites", Zeitschrift Fuer Angewandte Physik, Vol. 32, pp. 313-318, 1972.

64. A. Spencker and H. G. Wagemann, "Optoelectronic Semiconductor Components under the Action of Ionizing Radiation", Nachrichtentechnische Zeitung, Vol. 26, pp. 155-160, 1973.

65. R. J. Chaffin, "The Effect of Neutron Radiation on an IMPATT Diode", IEEE Trans. Microwave Theory and Techniques, Vol. MIT-17, pp. 119-120, Feb. 1969.

66. R. J. Chaffin, E. P. EerNisse, J. A. Hood, "The Effect of Neutron Irradiation on the TRAPATT Diode", Proc. IEEE, Vol. 57, pp. 2063-2064, Nov. 1969.

67. A. S. Epstein and P. A. Trimmer, "Radiation Damage and Annealing Effects in Photon Coupled Isolators", IEEE Trans. Nucl. Sci., Vol. NS-19, pp. 391-399, Dec. 1972.

68. C. W. Gwyn, D. L. Scharfetter, J. L. Wirth, "The Analysis of Radiation Effects in Semiconductor Junction Devices", IEEE Trans. Nucl. Sci., Vol. NS-14, pp. 153-169, Dec. 1967.

69. R. A. Walters and E. C. Hall, Proc of IEEE Southeastern Region III Conference, Orlando, Florida, p.24, April, 1974.

70. A. R. Lowery and K. D. Friddell, Presented at the IEEE Conf. on Nucl. and Space Radiation Effects, Ann Arbor, Michigan, July, 1965. Issued as report # D2-84071-1 by the Boeing Co.

71. G. C. Osbourn, "Computer Modeling of Radiation Hard AlGaAs Heterojunction Photodiode Structures", IEEE Trans. Nucl. Sci., Vol. NS-28, pp. 4612-4617.

72. J. J. Wiczer, L. R. Dawson, G. C. Osbourn, C. E. Barnes, "Direct Bandgap, Ionizing-Radiation Insensitive, Photodiode Structures", in Fiber Optics In Adverse Environments: SPIE Vol. 296, published by Society of Photo-Optical Instrumentation Engineers, Bellingham, Washington, pp. 95-102, 1982.

V. MULTI-COMPONENT DEVICES AND SYSTEMS CONSIDERATIONS

Having reviewed the radiation damage properties of individual optoelectronic components we now turn our attention to similar effects in multi-component devices. Examples of composite devices and systems made up of optoelectronic elements are: optical isolators containing an LED and detector; transmitters and receivers which contain not only the source and detector but also drive circuits, amplifiers, etc.; pigtailed LEDs, lasers and detectors; and complete fiber optic systems. Following a discussion of radiation effects in the above devices, we will briefly review some actual systems being contemplated for use in radiation environments.

1. OPTICAL ISOLATORS

Epstein and Trimmer (Ref. 1) have studied gamma and neutron irradiation effects in isolators containing both photodiodes and phototransistors. In this work, a separate GaAs emitter was included, but separate detectors were not examined. As expected, the photodiode isolator was much more resistant to both neutron and gamma irradiation. After 10^8 rads, the current transfer ratio, CTR, of the photodiode isolator decreased by an order of magnitude, while the CTR of the phototransistor isolator decreased by 3 to 4 orders of magnitude. Similar changes were observed following a neutron irradiation of 3.7×10^{13} n/cm^2. Thermal annealing was also studied in this work (Ref. 1), and considerable recovery in CTR for gamma-irradiation was observed between 200 and 250° C which corresponds to a prominent annealing

stage in gamma or electron irradiated GaAs. While the phototransistor isolator was much more sensitive to irradiation, it is interesting to note that the CTR's for the two types of isolators were approximately equal after $\Phi = 3.7 \times 10^{13}$ n/cm^2 because of the much larger pre-irradiation CTR of the phototransistor isolator. Consequently, as we have stated earlier in the discussion of LEDs, it is important to consider the pre-irradiation characteristics as well as the radiation hardness when selecting devices.

Soda, et al (Ref.2) studied gamma irradiation effects in photodiode and phototransistor-containing isolators. This study included the simultaneous irradiation and measurement of the individual LEDs and detectors making up the isolators. Based on our review of LED and detector radiation damage effects, it is apparent that the two isolators examined by Soda, et al (Ref.2) are at opposite ends of the radiation sensitivity scale. The Zn diffused GaAs LED/ p-i-n photodiode isolator contained two components that are relatively insensitive to irradiation, while the amphoterically Si doped GaAs LED and phototransistor in the other isolator are both quite sensitive devices. The extent of the degradation in the phototransistor isolator depends on the operating conditions as shown in Figure 5.1. These variations are primarily due to the effectiveness of the ionization-induced surface damage in the phototransistor at differing photocurrents and V_{CE} values. For large LED current and small V_{CE}, that is, the upper family of curves in Figure 5.1, most of the isolator degradation is due to LED damage effects. This can be seen by comparing the irradiated LED

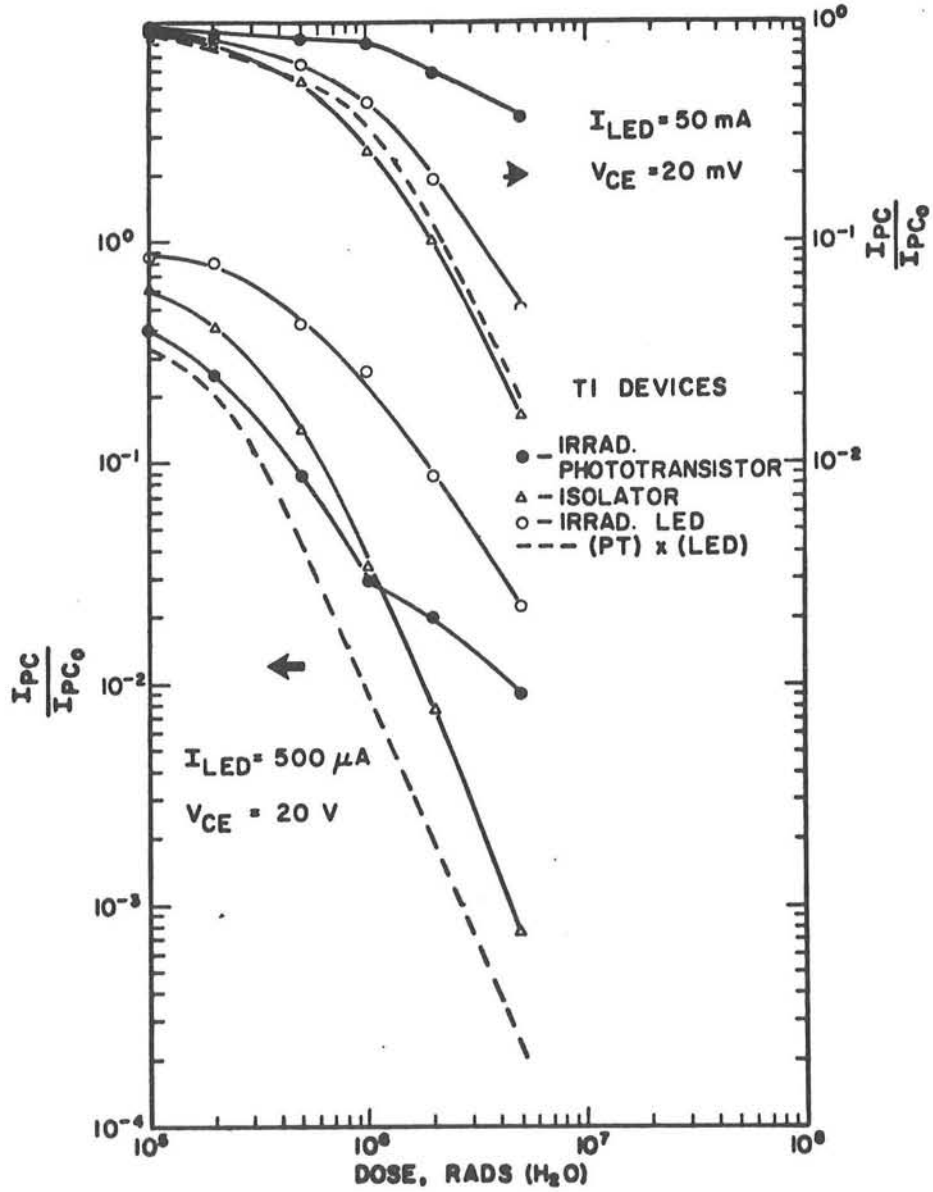

Fig. 5.1 Post-to pre-irradiation (Co^{60} gammas) photocurrent ratios for optical isolators containing amphoterically Si doped GaAs LEDs and Si phototransistors. The operating characteristics for the upper family of curves are for the most radiation resistant conditions. The lower family of curves illustrate the sensitivity of the phototransistor to ionization-induced surface-effects (from K. J. Soda, C. E. Barnes and R. A. Kiehl, IEEE Trans. Nucl. Sci. NS-22, 2475 (1975)).

with that for the irradiated isolator. However, as shown in the lower family of curves, for small LED current and typical operating voltages, the strong isolator degradation is due primarily to phototransistor effects. Note that the LED degradation is approximately the same for both families of curves. These results agree with the computer simulation of the emitter-base depletion layer spreading model which shows that the surface damage is most effective at large V_{CE} and small LED current.

The data in Figure 5.1 also illustrate the value of examining individual components simultaneously along with the isolator. The dashed curves are the products of LED and phototransistor degradation which should approximate the curve for the irradiated isolator. For the upper family the agreement is excellent. The deviation in the lower set of curves is due to fluctuation in the amount of surface damage from one phototransistor to another. Clearly, without the degradation data for the individual components, it would be difficult to determine the mechanisms responsible for isolator degradation.

At Sandia National Laboratories, R. P. Baker has examined neutron damage effects in a phototransistor isolator (TIL 108) similar to that examined by Soda, et al (Ref.2), and a dual channel high reliability isolator (HP 4365) containing photodiodes and amplification circuitry. CTRs as a function of neutron fluence are shown in Figure 5.2 for these devices. Note that the pre-irradiation CTR for the HP 4365 is larger than that for the TIL 108. As neutron irradiation proceeds, the phototransistor isolator degrades

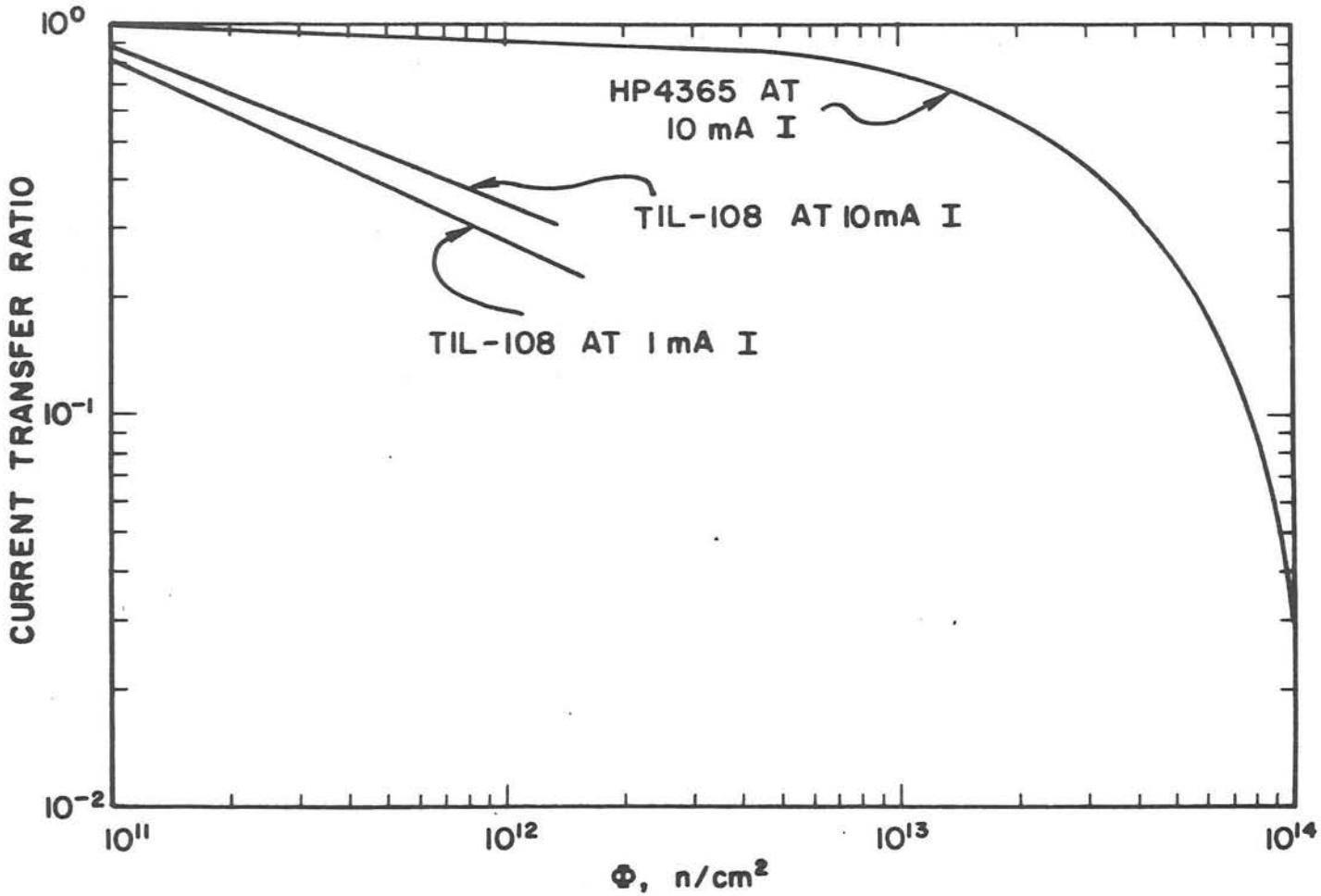

Fig. 5.2 Current transfer ratio as a function of neutron fluence for an optical isolator containing an amphoterically Si doped GaAs LED and a Si phototransistor (TIL-108) and for a dual channel isolator containing GaAsP LEDs and Si photodiodes (HP4365). (courtesy of R. P. Baker, Sandia Laboratories).

rapidly but the HP 4365 is insensitive to irradiation showing little degradation until Φ exceeds 10^{13} n/cm^2. It should be emphasized that this radiation hardness includes the neutron effects on the amplifying transistors. The sudden drop in the CTR for the HP 4365 between 10^{13} n/cm^2 and 10^{14} n/cm^2 was difficult to explain because measurements on individual components were not made.

Measurements in our laboratory (Ref.3) on neutron damage effects in the TIL 107 phototransistor isolator and its individual components show that the amphoterically Si doped GaAs LED degrades almost as rapidly as the phototransistor. Results for the TIL 107 isolator at two different collector currents are shown in Figure 5.3 along with data for other isolators. Note that the degradation rate of the TIL 107, which is quite rapid, does not depend on I_C as it did for gamma irradiated devices. The presence of degradation at the low fluence of 1×10^{11} n/cm^2 is indicative of the combined sensitivities of the LED and phototransistor. Clearly, this is a very poor device for a radiation environment application.

More recently, as part of our study (Ref.4) of radiation effects in long wavelength (1.06 μm) InGaAs LEDs, we have examined both gamma and neutron-induced degradation of isolators made up of InGaAs LEDs and Si photodiodes optimized for detection at 1.06 μm. The neutron degradation of such an isolator is shown in Figure 5.3. Note that this device is relatively insensitive to irradiation in that the reduction in CTR is minimal below 2×10^{14} n/cm^2.

In order to study gamma irradiation effects in the long wavelength isolators, devices were constructed so that they could be

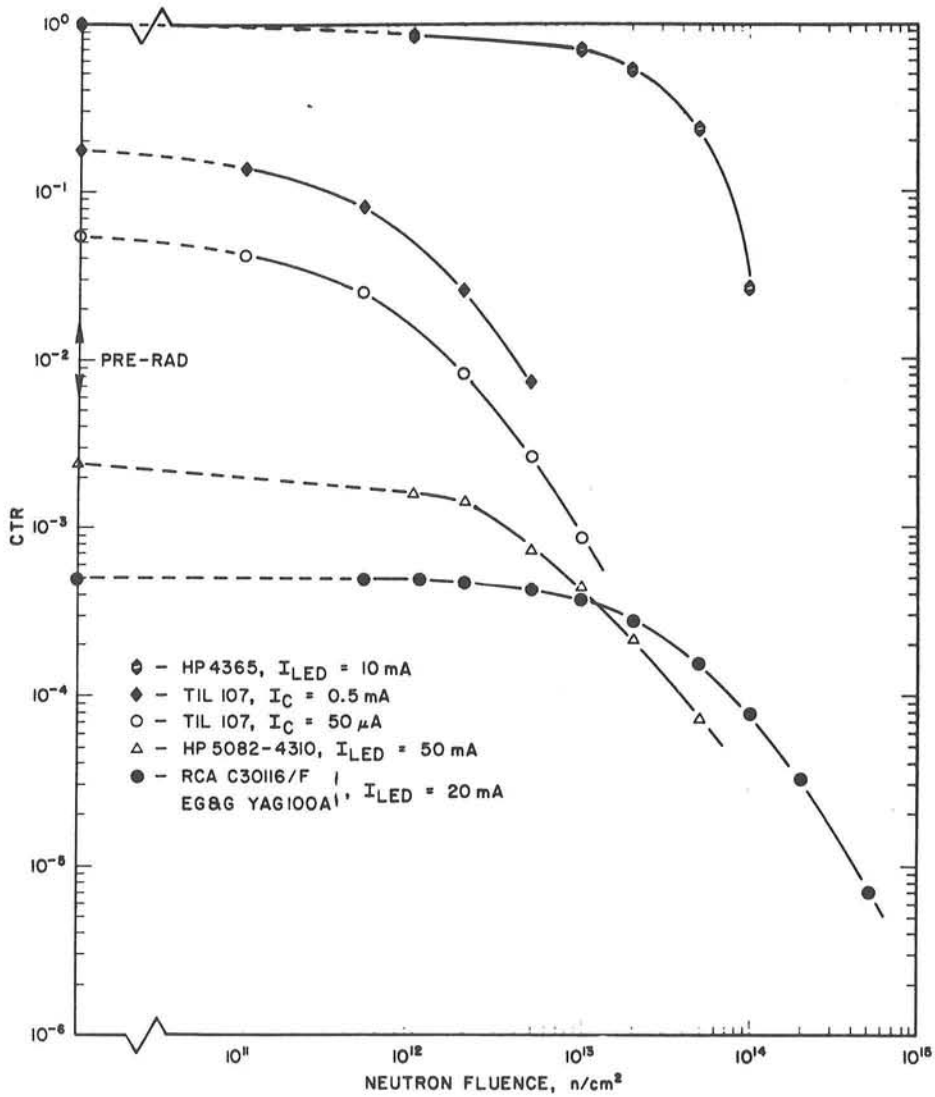

Fig. 5.3 Degradation of current transfer ratios due to neutron irradiation for four types of optical isolators, three of which are commercial devices. For the TIL-107, I_C is the phototransistor collector current. In contrast with the HP 5082-4310 and InGaAs/Si p-i-n photodiode isolators, the TIL-107 and HP 4365 devices possess internal gain.

separated for irradiation of one or both of the components. The results of this type of experiment are shown in detail in Figure 5.4. Data for three isolators are shown: EGGC-1, which was irradiated as a complete isolator without disassembly, LED-3, EGGPD-1, where only the LED was irradiated, and LED-2, EGGPD-2, where only the photodiode was irradiated. The specific emitters and detectors used were as follows: the LEDs are RCA InGaAs devices designated as C30116/F while the photodiodes were obtained from EG&G and are designated as YAG-100A. Results similar to those in Figure 5.4 were obtained when the photodiode portion of the isolator was a similar device obtained from Harshaw Chemical Co. Both types of photodiodes are optimized for 1.06 μm by using appropriate antireflection coatings and thick i regions. Below $\Phi = 5.0 \times 10^6$ rads little change was noted in the current transfer ratio (CTR) for any of the three isolators. Above an LED current of 1 mA, the results clearly indicate that up to a dose of 2.1×10^8 rads essentially all the degradation has occurred in the LED and the photodiode response is unchanged. Bias induced recovery was also studied in the InGaAs emitters. As shown earlier in Figure 1.28, and in Figure 5.4 for LED-3, a 50 mA bias for 45 min. produced significant recovery of the CTR. Therefore, from the point of view of radiation damage, the InGaAs LEDs hold promise for potential use in radiation environments. However, as we have already pointed out, a radiation-hardened LED is of little use if its pre-irradiation power output is very low. It is, therefore, important to note that the typical CTR of 4×10^{-4} for the isolators in

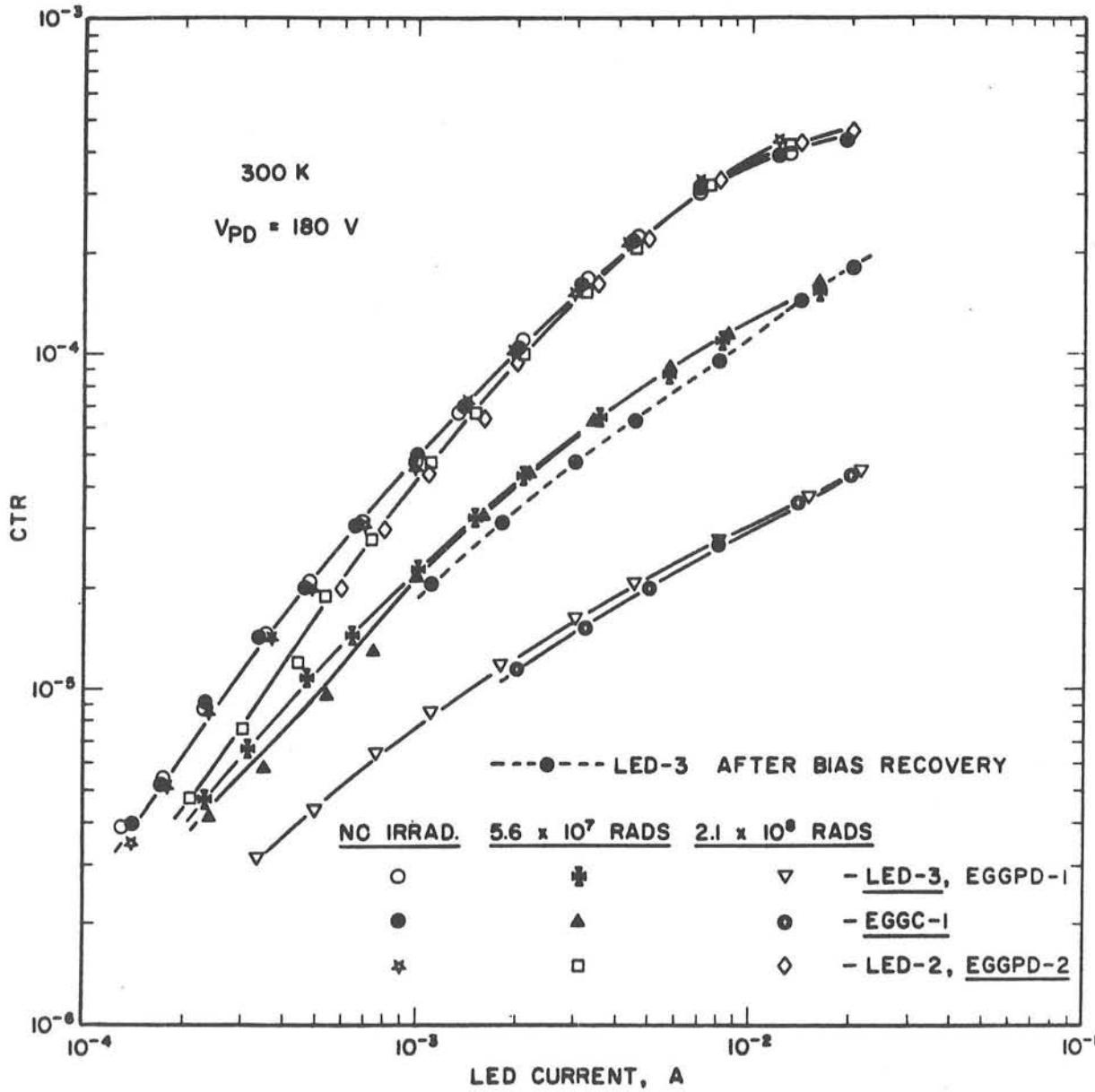

Fig. 5.4 Room temperature current transfer ratio as a function of InGaAs LED current before and after gamma irradiation of the devices underlined. The detectors are EG&G Si photodiodes optimized for 1060 nm, the peak emission wavelength of the InGaAs LEDs. Also shown is the forward bias induced recovery of an InGaAs LED due to a 50 mA bias for 40 min.

Figure 5.4 at realistic operating currents of 10 to 20 mA, is lower than the CTRs of commercial GaAs/photodiode isolators which are typically 1 to 3 x 10^{-3}.

Part of the loss in CTR may be a result of the reduced responsivity of Si detectors at 1.06 μm. Indeed, some of the III-V compound detectors discussed in Section 4 are better suited to operation at this wavelength. Although a partial reduction in responsivity can be expected if these devices are optimized for operation in an ionizing environment, the III-V photodiode structure is more appropriate for detection above 1 μm from both a pre- and post-irradiation point of view than a Si detector.

Comparison with results presented earlier (see Figure 1.38) indicates that the InGaAs emitters are less sensitive to irradiation than the planar GaAs:Zn TIXL-36 but more sensitive than the high radiance LEDs including the Plessey InGaAsP. Consequently, a high radiance LED would be more appropriate for isolator applications requiring radiation exposure. This is especially true if a steady state ionizing environment is anticipated for which our optimized photodiodes are best suited. Recall that the radiation-induced photocurrent in the detector is minimized by reducing detector volume. With a high radiance LED one could reduce detector area without sacrificing current transfer ratio.

2. PIGTAILED DEVICES

The combination of a fiber pigtail and an emitter or detector constitutes a composite device which may require special consideration from the point of view of radiation effects. As an example,

we present calculations of the output of Plessey pigtailed high radiance GaAlAs LEDs assuming a combined exposure to both neutrons and ionizing radiation (Ref.5). For the series of 12 pigtailed LEDs examined in our study (Ref.5), the average measured power outputs prior to irradiation at -45°C, 25°C, and 75°C were 1020 μW, 712 μW, and 530 μW, respectively. Reduced power outputs corresponding to specific neutron fluences were then calculated using the normalized light output degradation curve in Figure 1.38 for the PL-C45 LEDs. The same curve could be used to calculate post-irradiation power outputs at different temperatures since it was shown in this work (Ref.5) that the normalized degradation rate is nearly independent of temperature. Next we linearly superimposed the effects of transient attenuation that were measured in separate pieces of fiber with those of neutron reduced light output. This is valid because our results indicated that neutron irradiation does not affect the fiber pigtail and conversely, ionization does not affect the LED. The reduced power, P(t,T), out of the fiber pigtail in the presence of transient attenuation is computed for a one meter long pigtail using the equations:

$$\alpha(t) = 10 \log \frac{P_{ave}(T)}{P(t,T)} \quad \text{dB/m} \tag{5.1}$$

and

$$P(t,T) = P_{ave}(T)/10^{\alpha(t)/10}, \quad \mu\text{W} \tag{5.2}$$

where $P_{ave}(T)$ is the average power out of the pigtail at a given temperature, T, with no transient attenuation ($\gamma = 0$). These

calculations resulted in the six sets of curves shown in Figure 5.5 for a neutron fluence level, $\phi = 1 \times 10^{14}$ n/cm^2, and two values of dose rate; $\gamma = 4.6 \times 10^9$ rads/sec and $\gamma = 3.7 \times 10^{10}$ rads/sec. For the lower dose rate, the output power is essentially determined by the temperature and the neutron fluence. Even at 20 μs and -45°C the power is down by less than 20%. At one sec, the output is very close to complete recovery at all temperatures. However, for $\gamma = 3.7 \times 10^{10}$ rads/sec the transient attenuation has a strong effect on output. The power output curves at the three temperatures are quite different in shape and exhibit crossover points. These features result from the compensating effects of increasing light output with decreasing temperature and increasing attenuation at a given time with decreasing temperature. While the recovery is far from complete at 1 sec and -45°C, note that after this amount of time recovery is nearly complete at room temperature and above. The data in Figure 5.5 demonstrate that for the largest γ, the power output can drop below 200 μW at early times at all temperatures.

Calculations for three different neutron fluences at room temperature (25°C) are displayed in Figure 5.6. The LED output varies from somewhat less than 100 μW at short times and the largest fluence to the pre-irradiation level of slightly over 700 μW. Note that recovery is nearly complete after 1.0 sec. The data given in Figures 5.5 and 5.6 illustrate that care must be taken in selecting the pigtail fiber and the LED so as to maximize power output for the specific conditions under which the fiber optic system will be used.

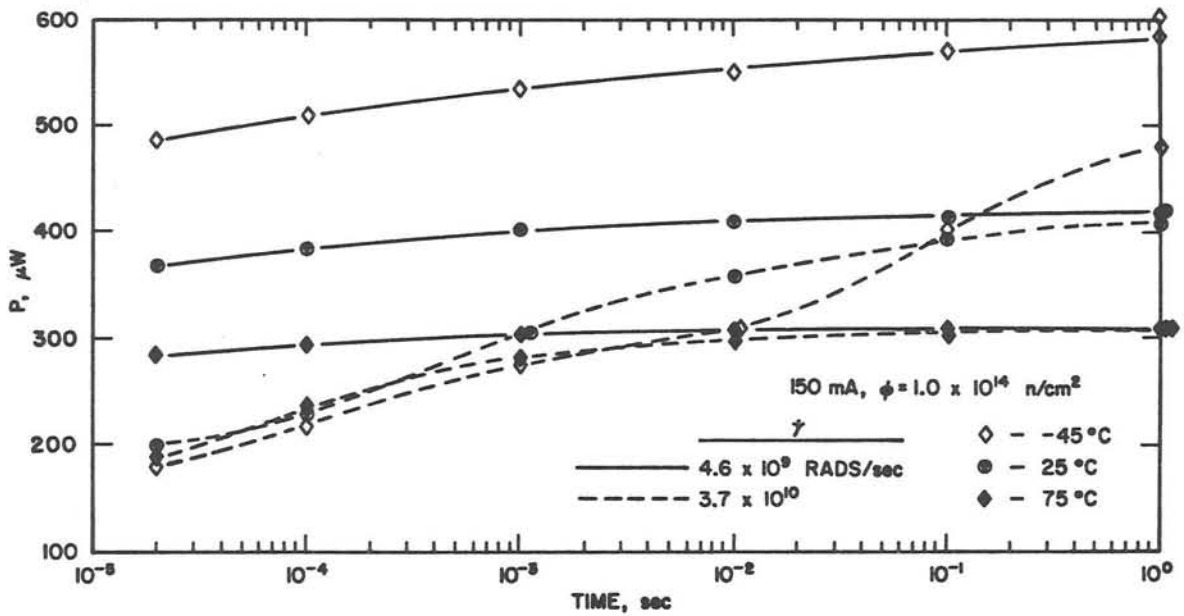

Fig. 5.5 Actual expected average power output at a current of 150mA from the pigtail of a Plessey high radiance GaAℓAs LED as a function of temperature and time after two different $\dot{\gamma}$ value x-ray bursts. The neutron fluence is assumed to be $1.0 \times 10^{14} n/cm^2$ for this case.

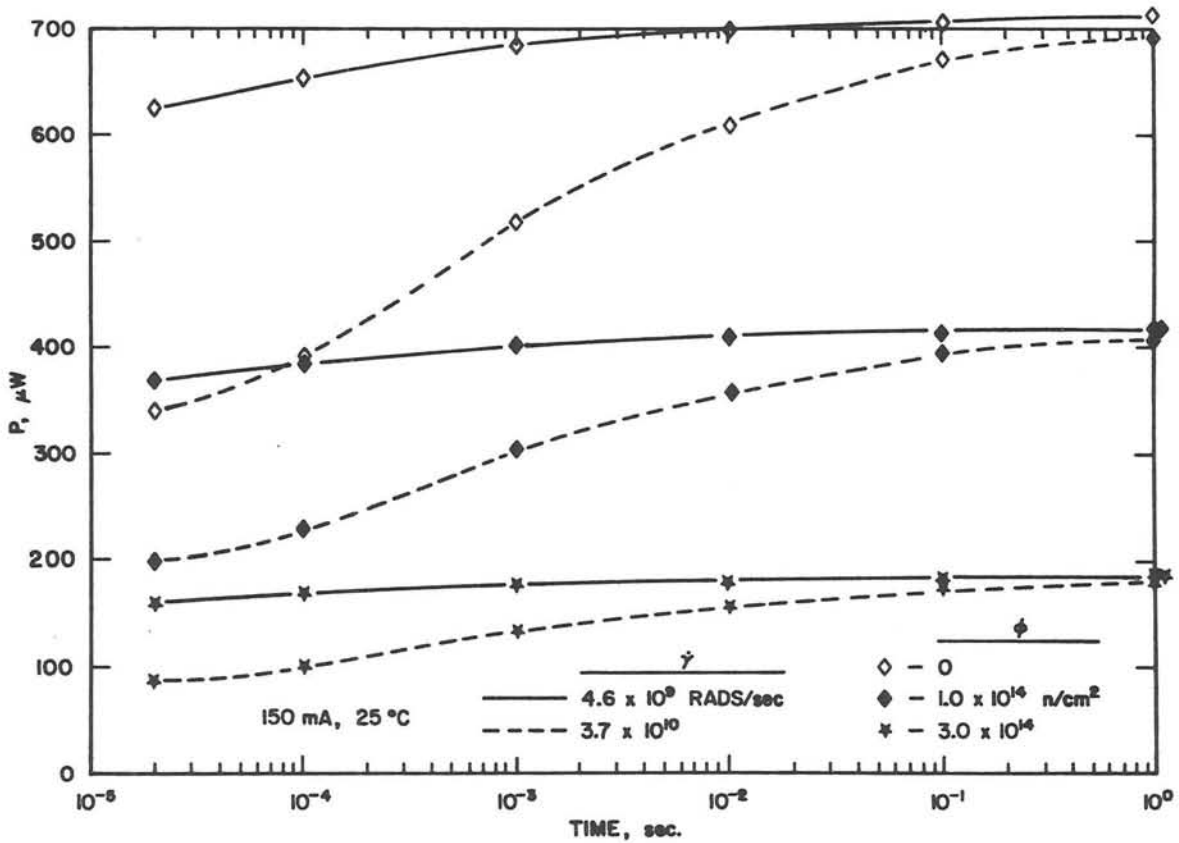

Fig. 5.6 Room temperature data for two values of $\dot{\gamma}$ and three neutron fluence values for a Plessey high radiance GaAℓAs LED with a 1 m long pigtail. The average power output varies from slightly below 100μw to somewhat greater than 700μw.

3. SYSTEMS CONSIDERATIONS

In the intervening years since the first edition of this report, the major emphasis in the fiber optics field has shifted from basic and applied research to engineering development and actual deployment of fiber optic (FO) systems. For many of these systems, there is an existing or anticipated radiation environment through which the system must survive and operate. Any attempt at making a complete and exhaustive list of existing and planned FO systems would not be of particular value because this is such a rapidly expanding field. Consequently, in this Section we will only briefly present examples of such systems.

The field of pulsed power generation is an important applications area for FO systems. Whether one is talking about a flash x-ray machine or an underground nuclear test, high speed acquisition of diagnostic information is often hampered by a hostile environment which can consist of EMP, nuclear radiation, blast and thermal shock, and other detrimental effects. Primarily because of their immunity to EMP effects, FO links can be particularly advantageous in such environments. At Sandia National Labs., examples of such applications are at the HERMES flash x-ray machine and the Pulsed Beam Fusion Accelerator (PBFA). The work at Los Alamos National Labs on radiation effects in fibers, discussed in an earlier Section, has evolved into sophisticated diagnostic tools (Refs. 6-10) for use in underground tests (UGT) and laser fusion experiments. Research has also begun (Ref.11) on the most appropriate FO link for nuclear reactor diagnostics. FO systems are also actively in use at various EMP simulator facilities (Ref.12).

Space-based applications of FO links have many advantages and programs are underway to exploit these attractive features (Refs.13-17). In addition to EMP and EMI immunity and radiation hardness, volume and weight savings and high data rate capabilities are attractive features. Taylor and Thacker (Ref.13), Aukerman, et al (Ref.15), and Kuller and Hanifen (Ref.17) have recently discussed and summarized a variety of potential space applications. It is hoped that a substantial data base for such applications will be developed through experiments such as the Long-Duration Exposure Facility (LDEF) (Ref.16) to be initiated in early 1984. This experiment will include active monitoring of four FO links as well as passive exposure of a variety of optoelectronic components which will be recovered at the termination of the experiment.

Existing and potential military applications of FO systems within the Air Force, Army and Navy are quite numerous and demonstrate a variety of attractive features of these systems. Greenwell has recently summarized a number of these systems (Ref.18) and discussed their vulnerability to nuclear radiation (Ref.19). In addition, Taylor (Ref.20) and Sierak and Druckenmiller (Ref.21) have summarized Air Force FO program development, while Barnoski (Ref.22) and Wichansky, et al (Ref.23) have discussed Army applications. In addition to discussing Navy FO systems projects (Ref.18), Greenwell (Ref.24) has provided a detailed analysis of the FO links employed in the Common Weapon Control System (CWCS) for the Ground Launched Cruise Missile (GLCM), the first tactical

weapons system to employ FO links with a nuclear exposure requirement. Included in this analysis is a link power budget for the FO link which we reproduce in Figure 5.7 and Table I because it is representative of the FO systems analysis one must perform. Shown at the top of Figure 5.7 is a schematic of the GLCM link. This is accompanied in the center of the Figure by the loss budget. At the left is shown the expected power coupled into a fiber from a high radience LED at two temperatures. For the non-nuclear case, the upper set of curves show a reduction in power due to fiber and connector losses to a level of a few microwatts available at the detector. The additional reduction due to the expected nuclear environment is indicated by the lower set of curves. Fortunately, as shown in the lower part of Figure 5.7 and in Table I, even for the worst case (post-nuclear event at low temperature) the power is above the minimum required detector power for a bit error rate less than 1×10^{-9}. It is important to note that without judicious selection of the optoelectronic components using the research data base as a guide, the FO link would not be operable.

In addition to the research cited earlier on optical isolators and pigtailed LEDs, radiation effects studies of more complex FO systems have been conducted. Boeing Aerospace has engaged in an extensive radiation hardened FO link receiver development program for the AFWL (Refs 25 and 26). Their tests included $\dot{\gamma}$, total dose, and neutron exposures of several receiver designs and also complete FO links. It was shown that the various receiver designs demonstrated the hardness levels expected for the FO links.

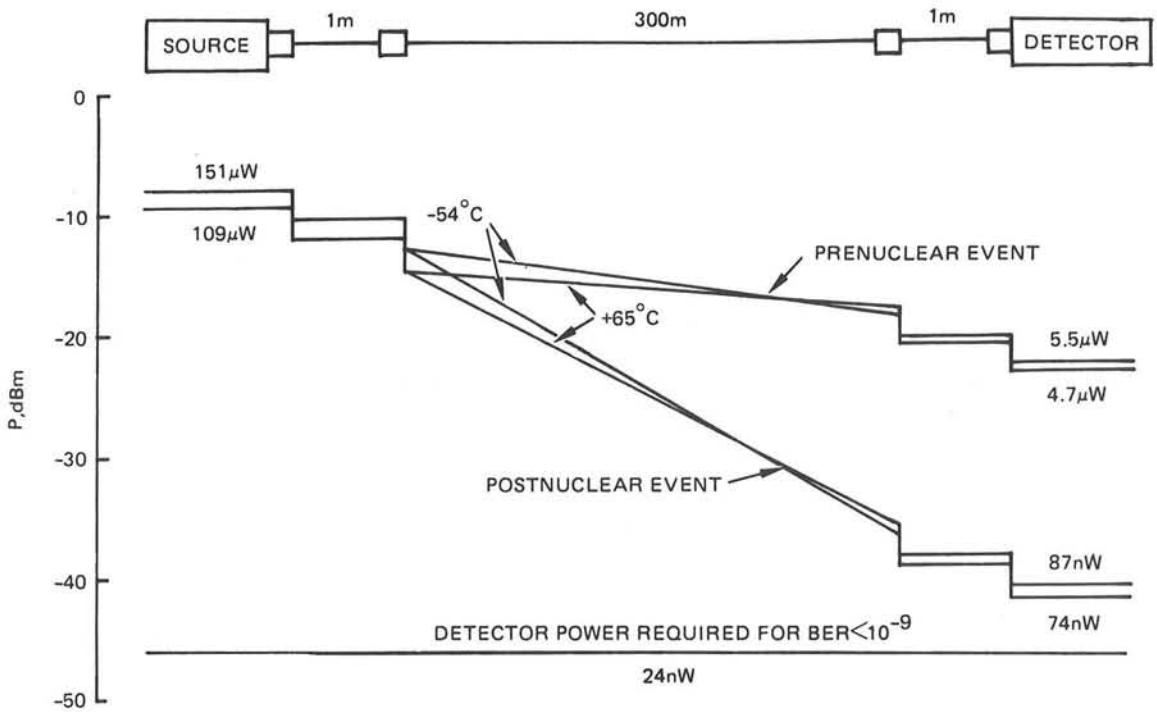

Figure 5.7 Link power budget for the common weapon control system - ground launched cruise missile fiber optic link (from R. A. Greenwell, p. 66 in Laser and Laser Systems Reliability, Proc. of SPIE 328, 1982).

Table I

Link power budget for the common weapon control system (from R. A. Greenwell, p. 66 in Laser and Laser Systems Reliability, Proc. of SPIE 328, 1982).

	Prenuclear Event		Postnuclear Event	
	-54°C	+65°C	-54°C	+65°C
Power coupled from source	-8.2 dBm (151 μW)	-9.6 dBm (109 μW)	-8.2 dBm (151 μW)	-9.6 dBm (109 μW)
Cable loss (300 m)	-5.1 dB	-3.0 dB	-23.1 dB	-21 dB
Connector loss (4 each)	-10 dB	-10 dB	-10 dB	-10 dB
Power coupled to detector	-23.3 dBm (4.7 μW)	-22.6 dBm (5.5 μW)	-41.3 dBm (74 nW)	-40.6 dBm (87 nW)
Power required at detector (BER $\leqslant 10^{-9}$)	-46.2 dBm (24 nW)	-46.2 dBm (24 nW)	-46.2 dBm (24 nW)	-46.2 dBm (24 nW)
Link margin	22.9 dB	23.6 dB	4.9 dB	5.6 dB

However, the choice of optimum receiver design depended on the link characteristics and the anticipated radiation environment. Kincaid (Ref.27) at Lockheed has also done development work on radiation hardened receivers and transmitters. In this study and the Boeing work, the receivers required a few hundred microsec. to recover from high $\dot{\gamma}$ exposure levels (1×10^9 to 1×10^{12} rad/s). For many systems, this time interval is sufficiently short to allow required system turn-on after an ionization burst. Blackburn (Ref.28) and Gilbert (Ref.29) have studied analog FO links for radiation environment applications and predict favorable results on the basis of these studies.

This very brief review of systems studies of FO links for radiation environment applications has not been complete partly because much of this work appears in report form rather than in the open literature. Based on what has appeared, however, one can conclude that future prospects are bright for rapidly expanding usage of FO systems in hostile environments.

4. SUMMARY

A few important general comments can be made based on our review of radiation effects in optoelectronic components and systems. First, although there are many components capable of withstanding significant amounts of radiation, there is no single component of a particular type which is most suitable for all applications. Careful consideration of both non-nuclear requirements and the anticipated hostile environment will usually lead to an FO link design made up of a relatively unique set of components that are optimal for that application. It follows that

the specifications of the non-nuclear performance requirements and the radiation scenario must be well-defined to make an intelligent, well-thought out design.

With regard to radiation effects, one of the most important FO link parameters is the operating wavelength. Its choice restricts the number of material systems (i.e. Si, GaAs, InGaAsP) out of which LEDs, lasers, and detectors can be fabricated. In addition, wavelength selection limits the range of available fiber properties including radiation response. Generally, below an upper limit of approximately 1.6 microns, fiber properties and radiation resistance are better at longer operating wavelengths. Thus, the so-called "second window" at 1.3 microns has many advantages over the 0.82 micron window. As a result, most future long link systems will operate at the second window.

This review of radiation effects in optoelectronics leads us to suggest that the following three problems are the most important for FO links operating in typical radiation environments:

1. Permanent damage effects in LEDs and lasers due to neutron irradiation, or, for space applications, proton irradiation. The neutron-induced defects degrade light output through competing non-radiative recombination.

2. Ionization-induced transient and permanent attenuation in optical fibers. Temporary signal reductions of hundreds of dB can be experienced with an inappropriate fiber.

3. Ionization-induced photocurrents in detectors. These photocurrents are generated by the same physical processes that generate the signal photocurrent. Therefore, it is difficult to separate the two without shielding.

In spite of these problems, based on our review of radiation effects in optoelectronics, we conclude that the application of fiber optics to systems operating in hostile environments has many advantages and will continue to expand rapidly in the future.

5. REFERENCES

1. A. S. Epstein and P. A. Trimmer, "Radiation Damage and Annealing Effects in Photon Coupled Isolators," IEEE Trans. Nuc. Sci. NS-19, No. 6, 391 (1972).
2. K. J. Soda, C. E. Barnes, and R. A. Kiehl, "The Effect of Gamma Irradiation on Optical Isolators," IEEE Trans. Nuc. Sci. NS-22, 2475 (1975).
3. C. E. Barnes and K. W. Mitchell, "Radiation Effects in Optical Emitters and Receivers," p. 248 in Proc. of Fiber Optics and Communications Exposition, Chicago, IL, 1978 (Information Gatekeepers, Brookline, MA, 1978).
4. C. E. Barnes, "Radiation Effects in 1.06 micron InGaAs LEDs and Si Photodiodes," J. Appl. Phys. 50, 5242 (1979).
5. C. E. Barnes, "Radiation Effects in Pigtailed GaAs and GaAlAs LEDs," Air Force Wright Aeronautical Laboratories Report No. AFWAL-TR-81-1086 (Wright Patterson AFB, OH, 1981).
6. J. W. Ogle, P. B. Lyons, L. Looney, L. Hocker, M. A. Nelson, P. A. Zagarino, T. J. Davies, R. D. Simmons, R. Selk, and B. Hopkins, "Improvements to a High-Frequency Fiber-Optic System for Plasma Diagnostics," p.177 in Fiber Optics in Adverse Environments, P. B. Lyons, Ed., Proc. of SPIE 296, 1981, San Diego, CA.
7. D. R. Thayer, P. B. Lyons, L. D. Looney, J. P. Manning, and R. M. Malone, "Preparation, Installation, and Calibration of a 152 Fiber Imaging Experiment at the Nevada Test Site," p. 191 in Ref. 6.

8. R. M. Malone, C. E. Gow, J. P. Manning and D. R. Thayer, "Fiber Optic Imaging System: Calibration," p.195 in Ref. 6.

9. T. H. Tan and A. H. Williams, "Use of Fiber Optics in the CO_2 Laser Fusion Environment," p.164 in Ref. 6.

10. J. L. Longmire and M. E. Thuot, "Fiber Optic Analog and Timing Monitoring System for the Antares Laser Fusion Program," p.219 in Ref. 6.

11. J. K. Partin, J. O. Bolstad, and D. R. Collins, "Real-Time Attenuation of Heated Optical Fibers in a Nuclear Reactor," presented at Photon 83 International Conf. on Optical Fibers and their Applications, May 16-19, 1983, Paris, France.

12. W. M. Caton, "Fiber Optics for Electro-magnetic Pulse (EMP) Simulators," p. 202 in Ref. 6.

13. G. A. Taylor and J. C. Thacker, "Fibre Optics Systems for Space Applications," Optics and Laser Tech., p. 93, April, 1982.

14. G. Evans and J. Leary, "Applications of Semiconductor Lasers in Space Communications," Optical Engineering 22, 247 (1983).

15. L. W. Aukerman, Y. Song, F. L. Vernon, Jr., G. A. Evans, and J. Z. Wilcox, "Radiation Effects on Semiconductor Optical Devices for Space Communications," p.56 in Laser and Laser Systems Reliability, G. A. Evans, Ed., Proc. of SPIE 328, 1982, Los Angeles, CA.

16. A. R. Johnston, L. A. Bergman and E. W. Taylor, "Fiber Optic Experiment for the Shuttle Long-Duration Exposure Facility," p.125 in Ref. 6.

17. W. G. Kuller and D. W. Hanifen, "Space System Survivability," p.72 in Ref. 15.

18. R. A. Greenwell, R. J. Kochanski, and D. N. Williams, "The Navy's Job - Fiber Optics," IFOC, p. 6, July, 1980.

19. R. A. Greenwell, G. H. Baker and W. H. Hardwick, "Fiber Optics in the Nuclear Environment," IFOC, p.19, Sept., 1981.

20. E. W. Taylor, "AFWL Optoelectronic Programs," presented at Tri-Service Working Group Meeting, Sandia National Labs., Oct. 27, 1982, Albuquerque, NM.

21. P. Sierak and R. Druckenmiller, "RADC Fiber Optic Systems Development Program," IFOC, p.19. July, 1980.

22. M. K. Barnoski, "Fiber Systems for the Military Environment," Proc. IEEE 68, 1315 (1980).

23. H. Wichansky, L. U. Dworkin, S. DiVita and A. Mondrick, "Survivability of Army Fiber Optic Systems," p. 110 in Ref. 6.

24. R. A. Greenwell, "Tradeoff Between Laser Diodes and Light-Emitting Diode (LEDs) for the Common Weapon Control System," p.66 in Ref. 15.

25. I. Arimura and R. S. Caldwell, "Radiation Degradation and Recovery in Long Fiber-Optics Data Links," p.175 in Proc. of the Fiber Optics in the Nuclear Environment Symposium, DNA Report no. DNA 5308P-2, March 25, 1980.

26. R. S. Caldwell and A. H. Johnston, "Radiation Hardening Techniques for Fiber Optic Link Receivers," Air Force Weapons Lab. Report no. AFWL-TR-81-45, Nov., 1981.

27. B. E. Kincaid, "Fiber Optic Transmitters and Receivers for Use in High Dose-Rate Ionizing Environments," p.213 in Ref. 6.

28. J. Blackburn, J. Vanderwall, R. Gilbert and V. Holliday, "Wideband Analog Fiber Optic Signal Link for Use in the Space/Radiation Simulator Environment," p.207 in Ref. 6.

29. R. M. Gilbert, "A Radiation-Hardening Scheme for an Analog Fiber-Optic Data Link," p.223 in Ref. 25.

Distribution:

301	P. J. Eicker
1000	J. K. Galt
1100	F. L. Vook
1110	P. S. Peercy
1120	J. B. Gerardo
1130	G. A. Samara
1132	G. C. Osbourn
1140	R. J. Chaffin
1141	G. E. Bulman
1141	L. R. Dawson
1141	D. R. Myers
1141	T. E. Zipperian
1142	C. E. Barnes (75)
1142	R. C. Hughes
1142	J. J. Wiczer (10)
1154	R. M. Biefeld
1234	J. Chang
1600	R. G. Clem
1815	T. Johnson
1845	J. J. Mecholsky
2100	R. L. Gregory
2116	W. J. Barnard
2120	W. R. Dawes, Jr.
2123	A. E. Asselmeier
2123	D. W. Bushmire
2123	I. J. Mirabal
2123	G. R. Schuster
2140	C. F. Gibbon
2150	J. A. Hood
2155	F. N. Coppage
2155	T. A. Fischer
2155	J. E. Gover
2300	J. L. Wirth
2320	J. H. Renken
2330	E. H. Barsis
2335	J. H. Stichman
2360	T. L. Workman
2362	K. R. Hessel
2362	G. E. Clark
2364	T. D. Donham
2364	R. L. Brown
3141	D. Ostrander (Acting) (5)
3151	W. L. Garner (3)
8100	D. M. Olson

For DOE/TIC

3154-4	C. Dalin (25)
8424	M. A. Pound

Second Printing, February 1992

3141 R. E. Martinez (1)